Reduced-Order Models for the Prediction of Unsteady Heat Release in Acoustically Forced Combustion

Christopher R. Martin

Dissertation submitted to the Faculty of the
Virginia Polytechnic Institute and State University
in partial fulfillment of the requirements for the degree of

Doctor of Philosophy
in
Mechanical Engineering

Uri Vandsburger, Chair
Mark Cramer
Christoph Hassa
Mark Paul
Robert West

December 4$^{\text{th}}$, 2009
Blacksburg, Virginia

Keywords: Combustion, Dynamic, Thermo-Acoustic Instabilities

Reduced-Order Models for the Prediction of Unsteady Heat Release in Acoustically Forced Combustion

Christopher R. Martin

ABSTRACT

This work presents novel formulations for models describing acoustically forced combustion in three disjoint regimes; highly turbulent, laminar, and the moderately turbulent flamelet regime. Particular emphasis is placed on simplification of the models to facilitate analytical solutions while still reflecting real phenomenology. Each derivation is treated by beginning with general reacting flow equations, identifying a small subset of physics thought to be dominant in the corresponding regime, and making appropriate simplifications. Each model is non-dimensionalized and both naturally occurring and popular dimensionless parameters are investigated.

The well-stirred reactor (WSR) is used to characterize the highly turbulent regime. It is confirmed that, consistent with the regime to which it is ascribed for static predictions, the WSR is most appropriate to predict the dynamics of chemical kinetics. Both convection time and chemical time dynamics are derived as explicit closed-form functions of dimensionless quantities such as the Damköhler number and several newly defined parameters.

The plug-flow reactor (PFR) is applied to a laminar, burner stabilized flame, using a number of established approaches, but with new attention to developing simple albeit accurate expressions governing the flame's frequency response. The system is studied experimentally using a ceramic honeycomb burner, combusting a methane-air mixture, numerically using a nonlinear FEA solver, and analytically by exact solution of the simplified governing equations. Accurately capturing non-unity Lewis-number effects are essential to capturing both the static and the dynamic response of the flame. It is shown that the flame dynamics can be expressed solely in terms of static quantities.

Finally, a Reynolds-averaged flamelet model is applied to a hypothetical burner stabilized flame with homogeneous, isotropic turbulence. Exact solution with a simplified turbulent reaction model parallels that of the plug flow reactor closely, demonstrating a relation between static quantities and the flame frequency response. Comparison with published experiments using considerably more complex flame geometries yields unexpected similarities in frequency scale, and phase behavior. The observed differences are attributed to specific physical phenomena that were deliberately omitted to simplify the model's derivation.

The following is dedicated to the teachers who touched my life, and in so doing, made this work possible. Though they are many, I am especially grateful to

Vicki Bascom
Miriam Blackwell
Jim Guthrie
Chris Patterson

and to my original teachers,

Brenda and Teddy Martin

Thank you all.

Thanks are due to my committee for their time, their patience, and their guidance. It has been an honor to learn from each of them.

Thanks also to Steve Lepera, the VACCG lab manager, for his aid and his instruction.

Finally, thanks to Joe Ranalli, who shall forever be my original colleague. His contributions through conversations and debate were immeasurable.

Contents

List of Figures

List of Tables

Chapter 1

Introduction

1.1 Motivation

This work is a modest expansion on the vast knowledge still being accumulated on combustion instabilities. Though there already exists a wealth of excellent work detailing the phenomenology of combustion-driven thermo-acoustic instabilities, and though there are already countless artfully derived models, predicting their occurrence and properties remains a formidible challenge. The models and measurements demonstrated herein are developed in the hope that they can contribute to an eventual state of knowledge surrounding combustion instabilities allowing designers to avoid them, accademics to predict and understand them, and gas turbine operators never to have heard of them.

1.1.1 Introduction to thermo-acoustic instabilities

Thermo-acoustic instabilities are a destructive force even to modern gas turbine engines; not only in their negative impact on emissions, performance, and efficiency, but also in destroyed hardware and increased maintenance. These instabilities are self-excited oscillations driven by a dynamic coupling between acoustic oscillations and heat addition to the oscillating fluid. Systems in which these oscillations occur are essentially heat engines that convert thermal energy into acoustic energy.

Combustion systems are particularly appropriate for sustaining such oscillations for a variety of reasons. Intuitively, a system's perpensity for oscillations is linked with the availability of thermal energy; amply available in combustion systems. Additionally, the comparitively low speed of sound in air-breathing systems means that even small systems can exhibit acoustic resonances at frequencies low enough to excite a flame. These conditions are not helped by the fact that efforts to make combustion systems as lossless as possible frequently result in little acoustic damping.

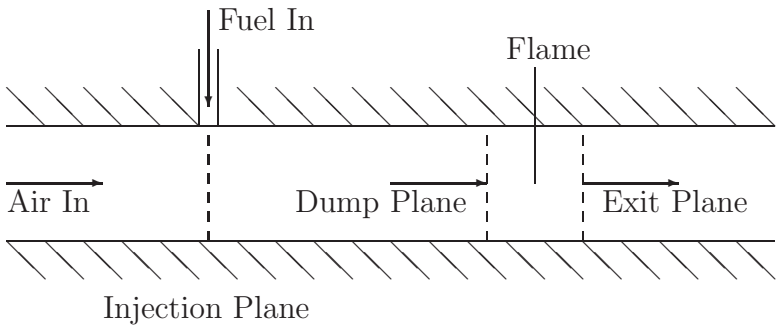

Figure 1.1: A conceptual combustor burning premixed fuel-air

In general, there are three ways an acoustic wave can cause a flame to issue an unsteady heat release. Most intuitively, unsteady velocity at the flame delivers an unsteady supply of fuel and air to the flame, causing the burning rate to fluctuate. As most commonly observed in rocket engines, extremely large pressure fluctuations in the combustor can also affect the reaction rate. In premixed systems, oscillations in pressure or velocity at the fuel injection point can cause uneven mixing that convect to the flame. Practically speaking, only the first and the last typically occur in gas turbine engines.

Figure 1.1 is a crude diagram depicting a premixed combustion system. Fuel is injected some distance upstream of the dump plane where the flame is anchored. Though systems can vary in complexity from a simple tube in a laboratory to a full scale gas turbine, for the most part, this diagram is sufficient to facilitate the discussion of how acoustic waves interact with the combustion process.

One can imagine standing waves of various wavelengths setting up in the tube-like chamber. Which mode of instability is dominant and whether an instability will occur at all is highly dependent on where the maxima and minima of the wave lie. If the boundary conditions are such that a resonant frequency has a velocity maximum coincident with the flame, then acoustic oscillations will likely drive the flame quite strongly. On the other hand, if

the boundary conditions are such that a dominant frequency exhibits a velocity node at a choked fuel inlet, then fuel-air mixture oscillations are likely to be strongly affected by the accoustics. These observations indicate that the acoustics are most compitent to drive the system in certain modes at frequencies determined by the boundary conditions.

The flame is only able to affect an acoustic response by generating a pressure wave due to the unsteady addition of heat. While constant heat addition causes an expansion, so long as it is steady, all oscillations eventually dampen out and relax into a steady open system. Though turbulence causes the flame's heat release to fluctuate, so long as the oscillations are not coherent with the oscillations in the acoustic response (e.g. if they are stochastic), the heat oscillations are as likely to oppose growth of an acoustic response as they are to aid it. Additionally, when the flame is at a pressure node, such as at an open boundary, then it is inept to force a pressure response, so no instability can occur.

1.1.2 Closed-loop modeling

A method for modeling these instabilities that has grown in popularity over the past several decades[15, 18, 24, 38], involves conceptually breaking apart the combustion and acoustic processes, modeling them separately, then combining the models to make predictions on the system's stability. Referred to as "system-level" modeling, it relies on linear system theory to predict the states at which the combustor will exhibit oscillations.

Figure 1.2 shows an example system-level model for the concept combustor in Figure 1.1. Here, the flame's response to equivalence ratio oscillations is treated as a separate model from the flame's response to local velocity oscillations. However, because the system is taken to be linear, their outputs can be summed to yield the total unsteady heat release.

Similarly, the physical system has an acoustic response both at the point of fuel injection

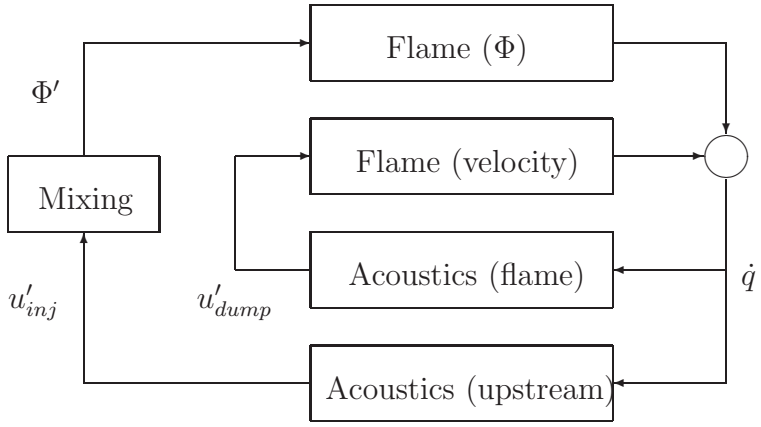

Figure 1.2: Combustion instability system diagram. Signals u'_{inj}, u'_{flame}, $\dot{q}$, and Φ' refer to the acoustic velocity at the injector, acoustic velocity at the flame, heat release rate, and equivalence ratio at the flame respectively.

and local to the flame. The model in Figure 1.2 treats these as two separate models that eventually feed back to the respective flame component models.

Because each of the subsystems is a stable system, the problem is identifying the conditions under which the total closed-loop system becomes unstable. To do this, it necessary to understand how each element of the system varies with the operating conditions.

1.2 Scope and objectives

This work is tailored to extend simple, numerically unimposing models to describe a turbulent flame's unsteady response to acoustic velocity oscillations. Flames are classified in this work as being either laminar or turbulent, and being either inclined or flat.

Turbulent flames imply combustion reactions occurring in the presence of chaotic turbulent oscillations that are decoupled from the acoustic oscillations. While turbulent phenomena can be coupled to acoustic oscillations, this work does not include such effects.

Laminar flames are simply understood to exist in the absence of turbulence. This can be established crudely by the Reynolds number of the flow, but more precisely by ensuring that in the absence of acoustic forcing, the velocity at all points near the flame is steady.

Flat flames are anchored such that they are propagating precisely normally to the direction of a uni-directional flow. Typically this implies that flat flames have to be stabilized on a thermally dissipative burner surface such as a ceramic honeycomb or a porous medium. This classification can only be applied to turbulent flames if one considers the time-averaged propagation and the time-averaged flow field.

Inclined flames are flames that propagate at an angle to the average flow velocity. This includes flames that may have complicated surfaces resulting in a range of propagation angles. Because inclined flame geometry is stable at higher flow rates and typically with fewer losses, inclined flames are heavily studied. Laminar Bunsen flames and turbulent swirl stabilized flames are just two examples of the inclined studies that are discussed in Section 1.3.

The present study investigates flame dynamics in three parts:

1. The limitations of the well-stirred reactor (WSR) are analytically quantified;
2. The importance of spatial effects are investigated in a classical burner-stabilized laminar flame experimentally, numerically, and analytically;
3. The lessons regarding spatial effects are extended to a hypothetical burner-stabilized turbulent flame model, which is solved analytically.

All of these, save the WSR, are flat flames. Though the WSR possesses no distinguishing geometric features and thus can be said to be neither inclined nor flat, the present work shows that its dynamics actually unify quite well with both the flat flames studied herein

and the inclined flames in literature.

Analytical approaches are employed in each part to search for derived quantities relating reactor length scales with the flame's frequency response. Such scalings are a powerful tool to making broad statements about the behavior of flames in general. Thus, the work is concluded with a comparative analysis linking the different flames via their scales.

1.3 Background

1.3.1 History of thermo-acoustic instabilities

Thermo-acoustic phenomena were first noted by Higgins in 1777 in the form of a "singing flame"[63]. Later, some of the earliest records of scientific investigation into thermo-acoustic instabilities were cataloged in Lord Rayleigh's *The Theory of Sound*[55], originally published in 1877. The thermally driven oscillations he listed therein included four distinct phenomena: a thermo-mechanical instability called *Trevelyan's Rocker*, a thermo-acoustic instability that shall be named in this document as *Chladni's Tube* for the acoustician that Rayleigh credited for its discovery, singing that occurs naturally in a *Glassblower's Tube*, and the much celebrated thermo-acoustic instability that occurs in *Rijke's Tube*.

Trevelyan's Rocker An interesting distraction from thermo-acoustic oscillations, this is an indication of the potentially counter-intuitive nature of thermally-driven instabilities. Frequently, as in the case of Trevelyan's Rocker, since the instability results in large-scale oscillations, one is reluctant to investigate the physics of smaller scales to seek an explanation, though that may actually be where the explanation lies.

Trevelyan's Rocker is a hot, metallic isosceles triangular prism with a trench cut in place of

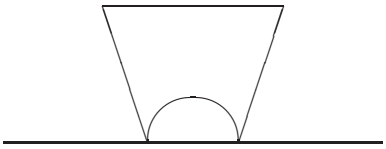

Figure 1.3: A cross-section of Trevelyan's Rocker

the a-symmetric angle, the cross-section of which appears in Figure 1.3. When the metal was heated and placed on a cool lead surface, the device emitted an audible tone. It has subsequently been noted that the pitch is due to rapid rocking oscillations - hence the device's name. It is sufficient to note that there was significant debate as to the cause of the oscillations, the most widely accepted explanation being that alternating thermal expansion and contraction of the lead drove a self-sustaining rocking motion in the prism. Objections to this explanation included that the time-scale associated with transient heating and cooling are much slower than would be necessary to keep up with the frequencies of oscillation observed.

Though discussion on the nature of these oscillations persists, Bhargava and Ghosh[3] have treated the matter with a very simple derivation that agrees sufficiently with empirical observations as to encourage the conclusion. Ultimately, the objections were refuted by noting that when only the *local* heating and cooling at the very small points of contact need be considered, the time scale for thermal decay becomes significantly faster. The lesson to be learned from this endeavor is that these dynamic phenomena defy many of the constructs and intuitions developed around slow or semi-steady phenomena. For this reason it is important to re-investigate many of the preconceived notions surrounding even well-understood phenomena.

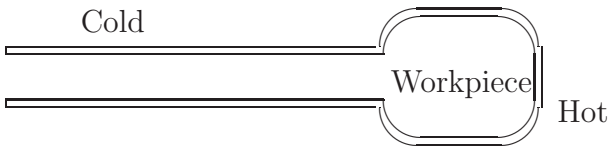

Figure 1.4: The Glass Blower's Tube

Glass Blower's Tube Of the thermo-acoustic instabilities discussed in Rayleigh's book, the relevant physics in the Glass Blower's Tube are the simplest. So, it is with good reason that it is the first of the thermo-acoustic systems to be discussed. This example offers the first glimpse into the physical principles that will remain relevant from one instance of thermo-acoustic coupling to another.

Glass blowers traditionally use a long hollow rod to thrust the work piece into a furnace where the glass is heated until it becomes malleable. The artist blows through the hollow rod to inflate the glass shape into a hollow container. Clearly, the artist is reliant upon the thermal insulation along the length of the rod to maintain a safe temperature at the mouth-piece. Interest among the acoustic community was turned to these devices when glassblowers noticed an audible tone emanating from unattended tubes under some conditions.

Figure 1.4 shows a crude representation of the physical system. The oscillations are caused by unsteady heat transfer to and from the air as it expands and contracts in the tube. At semi-steady-state, any heat transfer from the workpiece to the air inside causes an expansion. As the slightly hotter air expands into the tube, the heat is given up to the cooler walls of the tube, causing a contraction, after which the process is repeated. The phenomenon is, in fact, a naturally occurring heat engine that extracts energy in the form of acoustic oscillations rather than shaft work.

Rijke's Tube Perhaps the most famous of the examples included in Rayleigh's survey of thermally-driven instabilities due to its perceived similitude to the instabilities noted in modern gas turbine engines, Rijke's tube is a favorite for classroom demonstrations and simplified modern stability experiments[13, 28, 40].

The Dutch physicist Pieter Rijke noted that by inserting a heated metallic gauze in an open vertical tube 1/4 the tube's length from the bottom, the emission of a strong tone is audible[55]. The hot gauze transfers heat to the surrounding air, driving a steady current through the tube due to the buoyancy of the heated air. Any slight accelerations in the air velocity cause improved heat transfer, ultimately resulting in enhanced heat addition to the air. Similarly, retarded air velocity deters heat transfer and results in a decline in heat addition. In this manner there is a natural coupling between the acoustics in the tube and the addition of heat to the air in the tube.

Surely one of the primary reasons Rijke's experiment is so popular as an academic curiosity is found in the realization that the phase of the acoustic cycle at which heat is added can be easily adjusted with the vertical position of the gauze in the tube. Thus, it is a simple matter to observe physical limits on stability simply by adjusting the gauze location in the tube.

Chladni's Tube Though it is rarely (if ever) mentioned in the modern combustion literature, Chladni's tube is more relevant to gas turbine thermo-acoustic instabilities than any of the other classic examples in the literature. While both the glassblower's tube and Rijke's tube are thermo-acoustic systems driven by unsteady heat transfer and Trevelyan's rocker is driven by thermo-mechanical coupling, Chladni's tube is unique in the sense that it alone exhibits an instability driven by a flame.

An acoustician famous for his experiments identifying mode-shapes in vibrating plates with

pooling particulates, Chladni is credited as noting (though Higgins is recorded as first noting a similar phenomenon) that a hydrogen flame in a tube produced a pitch similar to the other instabilities. Other experimenters noted that the oscillation could be suppressed by damping the propagation of acoustic waves through the tube supplying the fuel with cotton, while parameters such as the fuel line's length and diameter seemed to matter less. This encouraged what is now a common conclusion: that the propagation of unsteady fuel injection into the flame can drive a thermo-acoustic instability.

Rayleigh Criterion for Stability With regard to these phenomena, in 1878 Sir Rayleigh published both in *The Proceedings of the Royal Institute* and *Nature*, these words which have become the basis for a number of mathematical criteria for thermo-acoustic stability posed since:

> "If heat be periodically communicated to, and abstracted from, a mass of air vibrating (for example) in a cylinder bounded by a piston, the effect produced will depend upon the phase of the vibration at which the transfer of heat takes place. If heat be given to the air at the moment of greatest condensation, or be taken from it at the moment of greatest rarefaction, the vibration is encouraged. On the other hand, if heat be given at the moment of greatest rarefaction, or abstracted at the moment of greatest condensation, the vibration is discouraged. The latter effect takes place of itself when the rapidity of alternation is neither very great nor very small in consequence of radiation; for when air is condensed it becomes hotter, and communicates heat to surrounding bodies. The two extreme cases are exceptional, though for different reasons. In the first, which corresponds to the suppositions of Laplace's theory of the propagation of sound, there is not sufficient time for a sensible transfer to be effected. IN the second, the

> temperature remains nearly constant, and the loss of heat occurs during the process of condensation, and not when the condensation is effected. This case corresponds to Newton's theory of the velocity of sound. When the transfer of heat takes place at the moment of greatest condensation or of greatest rarefaction, the pitch is not affected.
>
> If the air be at its normal density at the moment when the transfer of heat takes place, the vibration is neither encouraged nor discouraged, but the pitch is altered. Thus the pitch is raised if the heat be communicated to the air a quarter period before the phase of greatest condensation; and the pitch is lowered if the heat be communicated a quarter period after the phase of greatest condensation.
>
> In general both kinds of effects are produced by periodic transfer of heat. The pitch is altered, and the vibrations are either encouraged or discouraged. But there is no effect of the second kind if the air concerned be at a loop, i.e. a place where the density does not vary, nor if the communication of heat be the same at any stage of rarefaction as at the corresponding stage of condensation." [55]

The first realization of a mathematical criterion for instability, similar in principle to Rayleigh's qualitative description, is typically credited to Putnam in his study of *Combustion-Driven Oscillations in Industry*[51] and his earlier *Survey of Organ-Pipe Oscillations in Combustion Systems*[50]. Since then, there have been a number of works building upon an reiterating the significance of the conclusion, not the least of which is Culick's communication on the subject [7]. The ultimate result of which is that when acoustic losses are neglected, the flow field will exhibit oscillations that grow in amplitude when

$$\int_V \int \quad p' \cdot q' \quad \mathrm{d}t\mathrm{d}V \quad > \quad 0, \tag{1.1}$$

where p' and q' are the unsteady pressure and heat addition rate (energy per unit time) respectively, and V is the volume of the region where q' and p' are nonzero. There are other forms that include compensation for acoustic losses due to damping or otherwise, but the simple form in Equation 1.1 is by far the most common.

Instabilities in gas turbine engines Modern attention to thermo-acoustic instabilities has been drawn by their prevalence in gas turbine engines. The destructive power of the self-sustained oscillations received prominent note in gas turbine texts such as those of Lefebvre[22] and Putnam[51].

However, modeling and predicting instabilities in even simple systems such as the Rijke tube involves considerable effort[40, 28, 17], with limited generalizablility. In fact, due to the importance of the flame's geometry and the impact the system's geometry has on acoustics, the phenomena observed are frequently peculiar to individual machines. These and other confounding complications make the study of thermo-acoustics an avid focus for research that has persisted into the 21^{st} century.

1.3.2 Phenomenology

Over the last two decades, there have been several excellent review articles that have focused on progress in the area of combustion dynamics as they relate to thermo-acoustics; most notably, by Candel[38], Lieuwen[24], and more recently by Yang et al[15].

Scaling Frequency-dependent phenomena related to the flame's acoustic response have been found to consistently scale with the Strouhal number,

$$Str \equiv \frac{fD}{U}. \tag{1.2}$$

Here, f is the frequency, D is a length scale, and U is a velocity scale.

Figure 1.5 shows data from an experimental investigation by Lohrmann and Büchner investigating a swirl stabilized flame response to acoustic oscillations with respect to varying preheat temperature. The authors indicated that the flame amplitude exhibits a damped resonant response, but exhibits almost pure delay phase dyanmics. Moreover, Lohrmann and Büchner showed that both the magnitude and the phase response collapsed onto a single plot when the frequency axis is scaled by the Strouhal number.

It is also significant that in order to calculate the Strouhal number, Lohrmann and Büchner used the average velocity at the burner exit and the length from the burner exit to the "center of heat release" of the flame. The authors measured the spatially resolved OH radical chemiluminesence as an indication of heat release rate and took the distance separating the burner surface to the centroid of the resulting image as the characteristic length of the flame. This distance succesfully scaled not only the frequency phenomena, but the delay as well; that is, that the delay exhibited by the phase resonse was consistent with the convective delay time from the burner exit to the flame center.

Similar work by Ranalli et. al.[53, 52] indicated that the idea can be extended to an even broader set of operating conditions. Figure 1.6 shows scaled frequency response data from a swirl stabilized combustor at various equivalence ratios and mass flow rates. Though Ranalli still noted the resonant behavior, the he also noted that the phase exhibits slight nuances from pure delay when data is collected at sufficiently high frequencies. Ranalli also used the

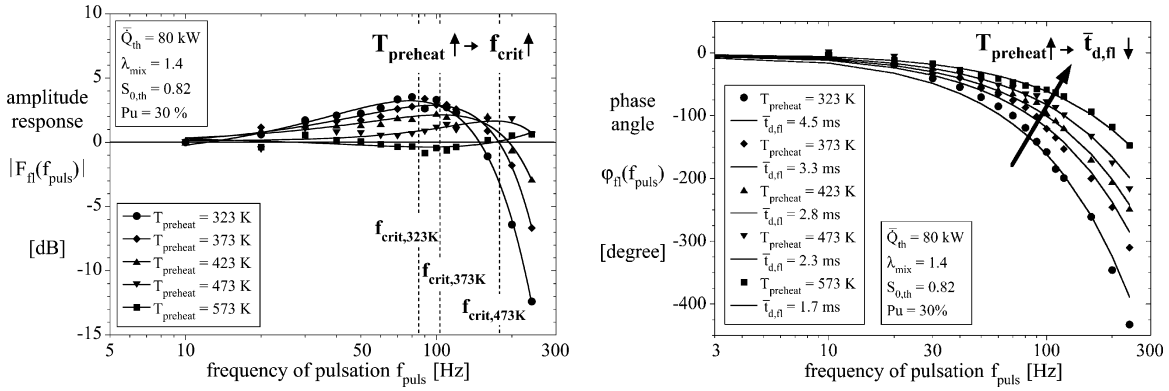

(a) (b)

Figure 1.5: Experimental heat release rate response to velocity oscillations for varying preheat temperatures. (Used with permission[27])

flame centroid with excellent results.

These findings are consistent with the work of Santavicca et. al., who noted that the peak heat release rate of a flame undergoing thermo-acoustic instability is coincident with the moment when shedding vortices reach the flame center [12].

Together, these results help paint a vivid picture of some convected quantity (such as a vortex) forming at the burner exit in response to acoustic oscillations, convecting through the flame, and affecting the heat release rate as it processes. It is quite easy to imagine vortices shedding from the expansion at the combustor inlet, convecting to the flame, and contorting it when they arrive.

Delay Since a sine wave may be expressed arbitrarily in terms of delay or in terms of phase,

$$\sin(\omega(t+\tau)) = \sin(\omega t + \phi),$$

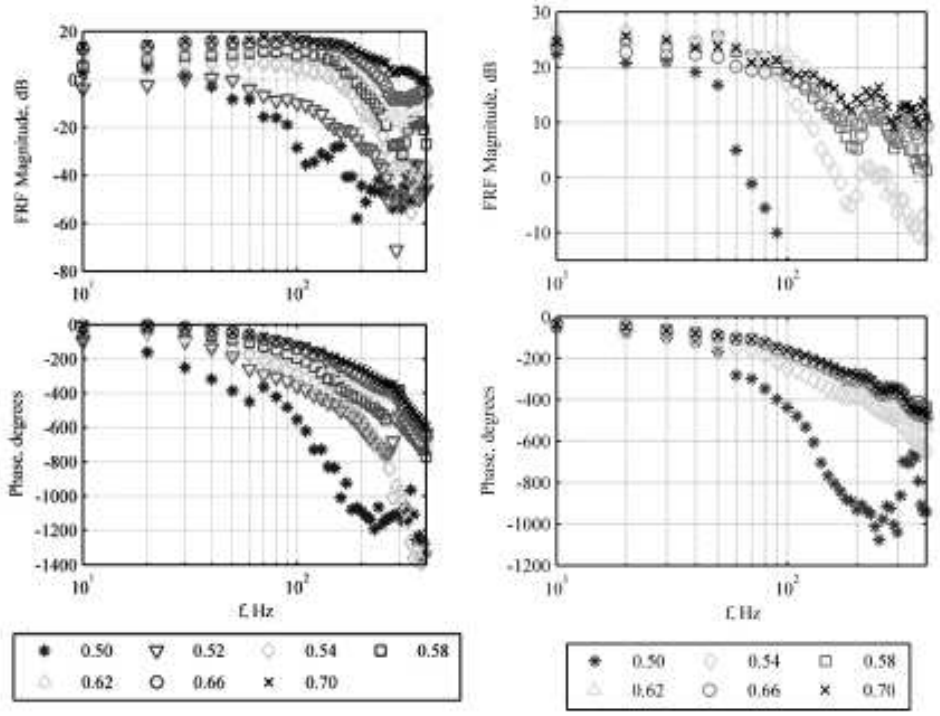

Figure 1.6: Experimental heat release rate response to velocity oscillations for varying equivalence ratio and flow rate. (Used with permission[52])

it is possible to represent delay in terms of phase,

$$\tau = \frac{\phi}{\omega}.$$

Thus, delay manifests itself as a linear decline in phase as a function of frequency. Practically, however, this is quite problematic since phase can arbitrarily have multiples of 2π added without affecting the signal, while delay is an absolute measure in time. This is resolved by the use of group delay,

$$\tau_g = \frac{\mathrm{d}\phi}{\mathrm{d}\omega}. \tag{1.3}$$

Note that when group delay is normalized by the convective delay time, it can be written conveniently in terms of the Strouhal number,

$$\frac{\tau_g U}{L_c} = \frac{U}{2\pi L_c}\frac{\mathrm{d}\phi}{\mathrm{d}f} = (2\pi)^{-1}\frac{\mathrm{d}\phi}{\mathrm{d}Str}. \tag{1.4}$$

Figure 1.7 shows the characteristic phase measured by Ranalli et. al.[54] and the corresponding dimensionless group delay curve. At low frequencies, the delay is roughly half of the convective delay time and after the cutoff frequency (around $Str = 2$), it is roughly one quarter.

On the other hand, Lohrmann and Büchner's data exhibits constant delay across the entire frequency band. However, because their data does not extend very far beyond the cutoff frequencies, it is entirely possible that their flame saw this behavior as well, but they failed to observe it. Also interesting is that they measured a delay consistent with the convection time.

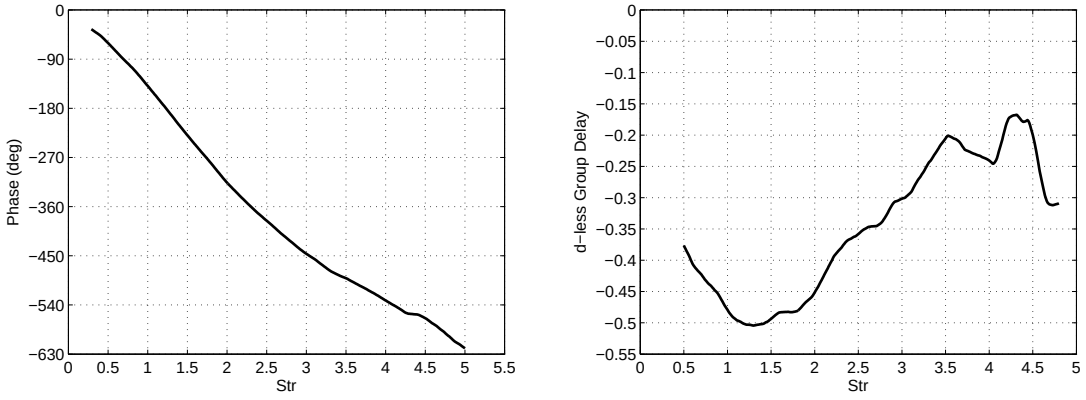

Figure 1.7: Group delay computed from data collected by Ranalli et. al.[54]

Free flames Freely propagating turbulent flames are unusual as topics of study, but offer an opportunity to investigate the conceptual building blocks of more complicated flames. Lawn et. al. investigated a turbulent flame stabilized in an expansion subjected to acoustic forcing. Figure 1.8 shows some of their measurements of the flame's spatial response relative to imposed velocity oscillations. The authors noted that while the freely propagating flame thickness is relatlively constant, its position is strongly affected by the acoustc velocity.

In this geometry, there is no mechanism for the generation of vortices, but there is a mechanism for the generation of scalar waves. As velocity changes at location of intense scalar gradients (such as the temperature gradient at the flame front), the enhanced or retarded convection leads to a local accumulation or depletion of conserved scalar quantities that is then convected with the mean flow. This is the mechanism by which Lawn et. al. found the turbulent flame to move.

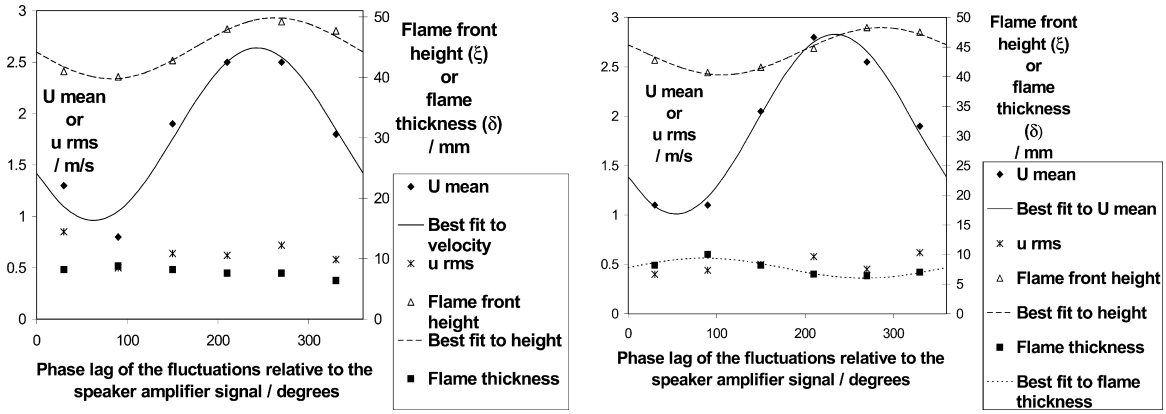

(a) (b)

Figure 1.8: Experimental response of a turbulent flame's position and thickness. (Used with permission[20])

1.3.3 Dynamic well-stirred reactor

The WSR has been the object of countless investigations into the dynamics of chemically reacting flows.

Good progress has been made with the WSR in the field of thermo-acoustic instabilities in gas turbines. Since pressure oscillations in these systems have proven to be a small percentage of the mean[24], the WSR has no dependency on the momentum equation and the dynamics are somewhat simpler than in works when pressure oscillations are important. Liewen et. al. studied the effect of flow rate oscillations[25] as well as mixture oscillations[25]. Park et. al. applied linearized WSRs in a system-level model with simple single-resonance acoustics to predict instabilities[46]. Martin used DC gains predicted by the WSR to predict the onset of instability in a model combustor[32]. This entire field has been recently reviewed by Huang and Yang[15].

Similar parallel efforts with the WSR can be found in chemical engineering fields. For example, Mahmoud and Fahim[29] and Ogawa et. al.[41] both use linearized WSR models to

design and characterize control systems given a particular reactor and reactants. Additionally, Engell and Klatt develop controls for the non-minimum phase behaviors that can be exhibited by the linearized WSR[10].

A number of researchers have also investigated the non-linear characteristics of the WSR. Works by Park and Vlachos[45], Lignola and DiMaio[26], Olsen and Vlachos[42], and Olsen and Epstein[43, 44] detail a wide variety of nonlinear characteristics exhibited by various encarnations of the WSR. These include saddle-node bifurcation behaviors observed in constant-pressure combustion[45], cataloging the existence of stable and unstable orbits in phase space[42], analysis of static[43] and unsteady[44] characteristics, and an investigation of the reactor's initial condition response and its dependence on the model's assumptions[26].

In all cases, great value is placed on modeling the static and the linear reactor behaviors. Olsen and Vlachos[42] exemplified how the reactor's linear behavior local to equilibria offers the first insights into the nearby orbits in phase space[59]. Similarly, the most accurate predictions available regarding thermo-acoustic stability are based on linear stability. This in mind, in this work we discuss general linear characteristics of the WSR and their implications.

1.3.4 Laminar modeling

Though static laminar flames have excellent approximate analytical static solutions, and even a number of similar dynamic approximations, progress with respect to their description has continued even in recent decades.

The challenge of identifying analytical solutions to the laminar flame problem was attacked early on by Hirschfelder[14], and continued by the likes of Liñán[23], Margolis[30], and McIntosh[36]. Researchers achieved great success both by seeking asymptotic solutions as

the reaction activation approaches ∞ and with numerical simulations[30].

Eventually, these works were expanded to investigate dynamic behaviors. For example, Margolis also investigated a laminar flame's transition to turbulence[31]. Of particular interest to the present work, is McIntosh's investigation of non-unity Lewis number affects on burner stabilized flame dynamics[36]. Therein, researchers reported that by breaking the symmetry between the species and energy equations by allowing non-unity Lewis numbers, the flame exhibits second-order dynamic behaviors. The authors predicted the flame to exhibit a resonance and at certain operating conditions, even an instability.

More modern efforts have confirmed and extended this result. McIntosh[60, 34, 33, 35] and others [21, 61, 6] have shown that freely propagating flames also exhibit resonant and even unstable interactions with pressure waves. The key conclusion of these works is that there are natural length and time scales that interact with the period and wavelength of acoustic waves to decide the character of the frequency response.

There has also been progress with respect to burner-stabilized work. McIntosh and Rylands used such models to describe unsteady heat transfer in a Rijke-style burner[37]. Rook et al[56] showed that resonant behaviors can even be predicted for unity lewis number flames by applying laminar flamelet concepts. The authors demonstrated that writing a separate equation for the flamelet motion and making various assumptions as to the internal structure of the flame supplies the added degrees of freedom necessary to demonstrate second-order behaviors.

1.3.5 Flame sheet models

The division of turbulent combustion into regimes, of which the flamelet regime is one, is credited to Borghi[5]. The now famous Borghi diagram[47] acknowledges that the manner

in which turbulent oscillations interact with a propagating flame front is dependent on the relative time and length scales over which the turbulence occurs. Presently, the same notions are being applied to acoustic-flame interactions.

Kaskan performed early experiments showing how freely propagating flames can be contorted by oscillating flow[16]. He measured increased luminosity from a corrugated freely propagating laminar flame subjected to acoustic forcing, and postulated that the increased luminosity corresponded to an increased heat release rate. Thus, he was probably among the first researchers to note that increased flame area corresponds to increased instantaneous heat release rate.

Early unsteady flamelet measurements were made by Blackshear[4] and Merk[39]. These were among the first works identifying the laminar flames as responding with a low-pass character. Merk identified a first-order approximation that mached data to a reasonable approximation.

Since then, more accurate models have been put forth[11, 1], and even validated by experiment by the now famous measurements by Candel et. al.[8, 9].

Baillot[2] also made measurements of an acoustically excited turbulent flat flame.

Chapter 2

Highly Turbulent Combustion

Nomenclature

A ..... Reactor cross-sectional area
$\mathbf{A}$ ..... State matrix
$\mathbf{B}$ ..... Input matrix
c ..... Reaction progress
$\hat{c}$ ..... Specific heat eccentricity
$\mathbf{C}$ ..... Output matrix
C_p ..... Specific heat
Da ..... Damkhöler number
Da_t ..... Turbulent Damkhöler number
e ..... Energy
h ..... Enthalpy
$\mathbf{H}$ ..... Enthalpy vector
I ..... Turbulence intensity
$\mathbf{J}$ ..... Reaction rate jacobian
K ..... Gain
$\dot{m}$ ..... Mass flow
M ..... Reactor mass
MW_i ..... Molecular weight of spec. i
p ..... Pressure
$\mathbf{P}$ ..... Transformation matrix
q_j ..... Reaction rate vector
Q ..... Heat release rate
R ..... Reaction rate
t ..... Time
t_m ..... Residence time ($M/\dot{m}$)
t_t ..... Turbulent time scale
t_r ..... Reaction time scale
T ..... Temperature
u ..... Velocity
$\mathbf{U}$ ..... Input vector
V ..... Reactor volume
$\mathbf{V}$ or $V_{i,j}$ ..... Mass-based rxn. coef.
$\mathbf{X}$ ..... State vector
Y_i ..... Mass fraction of spec. i
$\mathbf{Z}$ ..... Transformed state vector
Γ ..... Reaction rate sensitivity
Δh_f ..... Fuel enthalpy of reaction
ϵ ..... Perturbation amplitude
ζ_i ..... Reaction rate of spec. i
ν', ν'' ..... Reactants and products coef.
ρ ..... Density
τ ..... Dimensionless temperature

2.1 Formulation of the Well-Stirred Reactor

2.1.1 Assumptions and limitations

WSRs have two basic assumptions that have classically been inherent to their formulation;

1. Turbulent mixing in the reactor is so strong that spatial gradients may be ignored,

2. The volume of the reactor is a constant.

These assumptions have been mapped[5, 47] into dimensionless static operating conditions to demonstrate that the WSR is appropriate when the turbulent Damköhler number,

$$Da_t = \frac{t_t}{t_r} \tag{2.1}$$

is much smaller than 1. Here, t_r is the chemical time scale, and t_t is the turbulent time scale, defined by the flame length scale in ratio with the turbulent velocity, $t_t = L/u'$.

2.1.2 Derivation

If spatial gradients are to be ignored in the reactor, then equations governing the mass, temperature, and species mass fractions can be written intuitively from the laws governing conservation of energy and mass.

$$\frac{\mathrm{d}}{\mathrm{d}t}(\rho)\, V = \dot{m}_{in} - \dot{m} \tag{2.2}$$

$$\frac{\mathrm{d}}{\mathrm{d}t}(\rho Y_i)\, V = \dot{m}_{in} Y_{i,in} - \dot{m} Y_i + M\zeta_i \tag{2.3}$$

$$\frac{\mathrm{d}}{\mathrm{d}t}(\rho e)\, V = \dot{m}_{in} e_{in} - \dot{m} e + u_{in} A_{in} p_{in} - uAp. \tag{2.4}$$

Here, V is the reactor volume, M is the mass in the reactor ($M = \rho V$), and e is the fluid internal energy. Subscripts containing *in* indicate properties at the reactor inlet, and are otherwise assumed to be the properties inside the reactor. Momentum is absent since the reactor pressure is not being modeled. The source term, ζ_i is the rate of formation of species i in mass per unit time per unit mass of fluid. Exactly how ζ_i is calculated depends on the chemical kinetic mechanism.

The energy equation Recognizing that $h = e + p/\rho$, Equation 2.4 can be rewritten as

$$\frac{\mathrm{d}}{\mathrm{d}t}(\rho h)\, V - \dot{p}V = \dot{m}_{in} h_{in} - \dot{m} h. \tag{2.5}$$

Now, if the time derivative on the left-hand-side of Equations 2.3 and 2.5 are distributed and the density derivatives are eliminated by substituting Equation 2.2, we are left with

$$\dot{Y}_i M + \dot{m}_{in}\,(Y_i - Y_{i,in}) = M\zeta_i \tag{2.6}$$

$$\dot{h} M + \dot{m}_{in}\,(h - h_{in}) = \frac{1}{\rho}\frac{\mathrm{d}p}{\mathrm{d}t}. \tag{2.7}$$

Again, since the pressure in the reactor is assumed to be both steady and irrelevant to the model, the last term of the energy equation can be neglected. Since the residence time can be defined by $t_m = M/\dot{m}_{in}$, the equations simplify to

$$\dot{Y}_i + {t_m}^{-1}\,(Y_i - Y_{i,in}) = \zeta_i \tag{2.8}$$

$$\dot{h} + {t_m}^{-1}\,(h - h_{in}) = 0. \tag{2.9}$$

Note that the reaction rate still does not appear in the energy equation. We make it appear by writing the mixture's enthalpy in terms of its constituent species, $h = \sum_i Y_i h_i$, and substituting it to get

$$C_p \dot{T} + \sum_i \dot{Y}_i\, h_i + {t_m}^{-1} \left(\sum_i Y_{i,in}\, h_{i,in} - \sum_i Y_i\, h_i \right) = 0 \tag{2.10}$$

Finally, substituting Equation 2.8 to eliminate the time derivatives on Y,

$$C_p \dot{T} + {t_m}^{-1} \sum_i Y_{i,in}\,(h_i - h_{i,in}) = -\sum_i h_i \zeta_i \tag{2.11}$$

The heat release rate can be derived from the source term on the RHS of Equation 2.11, which represents the heat release per unit mass of fluid in the reactor. Multiplying by the mass in the reactor yields

$$Q = -\rho V \sum_i h_i \zeta_i. \tag{2.12}$$

The species equation The conservation of species can be similarly formulated

$$\dot{Y}_i + t_m^{-1} \left(Y_i - Y_{i,in} \right) = \zeta_i, \tag{2.13}$$

where Y_i is the mass fraction of species i, and ζ_i is its rate of formation. Similarly to the energy equation, the three terms that appear represent the specie's accumulation, convection, and generation due to reaction.

General chemical kinetics In general, a chemical mechanism is given as a series of reactions appearing in the form

$$\begin{aligned} &(1) \quad \nu'_{A,1} A + \nu'_{B,1} B + \ldots \rightarrow \nu''_{A,1} A + \nu''_{B,1} B + \ldots \\ &(2) \quad \nu'_{A,2} A + \nu'_{B,2} B + \ldots \rightarrow \nu''_{A,2} A + \nu''_{B,2} B + \ldots \qquad (2.14) \\ &\quad \vdots \qquad (2.15) \end{aligned}$$

so that $\nu'_{i,j}$ and $\nu''_{i,j}$ represent the coefficient of species i on the LHS and RHS (respectively) of reaction step j. Chemical kinetic mechanisms typically define some way of computing the number of reactions per unit time per unit mass of fluid for each of the reaction steps. Given

these rates in a vector, q_j, ζ_i is given by

$$\zeta_i = \sum_j V_{i,j}\ q_j \tag{2.16}$$

when $V_{i,j} = MW_i(\nu''_{i,j} - \nu'_{i,j})$.

2.2 The simple WSR

The first of the reactors we consider herein assumes constant, species-independent specific heat and a single step reaction mechanism. As mentioned above, a number of researchers have considered simplified WSRs in various forms to produce dynamic heat release rate predictions in gas turbine engines.

When the reaction mechanism includes only one step, the formation and depletion of all species occurs proportionally, as determined by the coefficients, $V_{i,1}$. This allows the RHS of Equation 2.11 to be simplified, yielding

$$C_p\dot{T} + t_m^{-1}\sum_i Y_{i,in}\left(h_i - h_{i,in}\right) = -\Delta h_f \zeta_f \tag{2.17a}$$

$$\dot{Y}_i + t_m^{-1}\left(Y_i - Y_{i,in}\right) = \zeta_i. \tag{2.17b}$$

where the fuel heat release is given as a function of reactor temperature by

$$\Delta h_f = \sum_i \frac{V_i}{V_f}\, h_i. \tag{2.18}$$

Here, $V_{i,1}$ is abbreviated to V_i since there is only one reaction step.

With the application of constant and equal specific heats, the energy equation becomes

$$\dot{T} + t_m^{-1}\left(T - T_{in}\right) = -\frac{\Delta h_f}{C_p}\zeta_f \tag{2.19}$$

Since the species equation is independent of the fluid's thermal properties, it is unaffected.

Equations 2.19 and 2.17b are so similar with respect to the state variables that they can be reduced to a single equation on a single state variable. Consider the reaction progress variable employed in the analysis of plug flow reactors by Poinsot and Veynante:

$$T = T_{in} + \Delta T c \tag{2.20}$$

$$Y_i = Y_{i,in} + \Delta Y_i c. \tag{2.21}$$

Here, c is a scalar between 0 and 1 indicating the fractional progress from no combustion to complete exhaustion of the fuel. The ΔT and ΔY_i parameters refer to the change in temperature and mass fraction of species i respectively for "complete" combustion. They can be solved in terms of the enthalpy of reaction and the inlet fuel mass fraction by

$$\Delta T = \frac{\Delta h_f}{C_p} Y_{f,in} \tag{2.22}$$

$$\Delta Y_i = -\frac{V_i}{V_f} Y_{f,in}. \tag{2.23}$$

Thus, the fuel mass fraction is given by $Y_f = (1 - c)Y_{f,in}$. Substituting these quantities into equation 2.19 and 2.17b yields identical equations,

$$\dot{c} + t_m^{-1} c = R(c) \tag{2.24}$$

In Equation 2.24, the function, $R(c)$ has units s^{-1} and is derived from ζ_i by

$$R = \frac{\zeta_i}{\Delta Y_i} \left[= -\frac{\zeta_f}{Y_{f,in}} \right] \tag{2.25}$$

$$= -\frac{\Delta h_f}{C_p \Delta T} \zeta_f. \tag{2.26}$$

It is important to note that dynamic perturbations in mass flow to the reactor will manifest themselves in Equation 2.24 through the appearance of $\dot{m}_0$ in t_m. It can be shown that such perturbations would appear as

$$\dot{c} + t_m^{-1}(1 + \epsilon u)c = R(c), \tag{2.27}$$

where $\epsilon\, u$ is the fractional change in mass flow, $\dot{m}_1/\dot{m}_0$, and ϵ is a positive dimensionless scalar amplitude of the excitation. In this way, the total mass flow is $\dot{m} = \dot{m}_0 + \dot{m}_1(t)$.

Equation 2.27 can be further manipulated by using a non-dimensional time scale, $\hat{t} = t/t_m$. We can also define a non-dimensionalize reaction rate, $\hat{R} = t_r R$, where the chemical time, t_r, is defined, such that $\max(\hat{R}) = 1$. Then, Equation 2.24 can be rewritten as

$$c' + (1 + \epsilon u)c = Da \cdot \hat{R}(c). \tag{2.28}$$

Here, the prime denotes differentiation on $\hat{t}$, and Da is the convective Damköhler number,

$$Da = \frac{t_m}{t_r} = \frac{t_t}{t_r} I = Da_t I. \tag{2.29}$$

The convective Damköhler number differs from the turbulent Damköhler number only in its use of the bulk velocity, $t_m = L/U$, instead of turbulent rms velocity, $t_t = L/u'$. Therefore, the two can be related by the turbulence intensity, $I = u'/U$.

If the reaction progress is further expanded in a Taylor series on ϵ, Equation 2.28 appears

$$\epsilon c_1' + (1 + \epsilon u)(c_0 + \epsilon c_1) + \ldots = Da \cdot \hat{R}(c_0 + \epsilon c_1 + \ldots). \tag{2.30}$$

We obtain equations governing the steady and linear unsteady components of the solution by expanding and grouping like powers of ϵ.

$$c_0 - Da \cdot \hat{R}(c_0) = 0 \tag{2.31}$$

$$c_1' + c_1 \left[1 - Da \cdot \hat{R}'(c_0)\right] = -c_0 u \tag{2.32}$$

Characteristics By assuming constant and equal specific heats with a single-step reaction rate, Equations 2.31 and 2.32 demonstrate that the WSR can be simplified to a first order, single degree of freedom system described by only two parameters. The first and most straightforward is the Damköhler number. Secondly, the shape of the function, $\hat{R}$, also influences the static and especially the dynamic characteristics.

In any discussion of a WSR's characteristics, it is important to begin by noting that there are limits on values of Da for which the model is valid and for which the model even has a solution. The smallest Damköhler number for which there is a solution to Equation 2.31 is referred to as the blowoff point. Mathematically, blowoff can be defined as the condition at which the sensitivity of c_0 relative to changes in Da is infinite or at which the solution is also an inflection point. By differentiating Equation 2.31 with respect to c_0 a little bit of manipulation reveals that the reaction progress and Damköhler number at blowoff are the

solutions to

$$c_{bo}\frac{\hat{R}'(c_{bo})}{\hat{R}(c_{bo})} = 1 \tag{2.33}$$

$$Da_{bo} = \frac{c_{bo}}{\hat{R}(c_{bo})}. \tag{2.34}$$

We can observe by inspection that Da_{bo} will be on the order 1. In fact, Da_{bo} is close to, but slightly less than 1 for most combustion models.

The blowoff limit, $Da > Da_{bo}$, is a hard lower bound on Da. The well known work by Borghi[5] indicates an upper bound since the assumptions inherent to the WSR are only valid when $Da_t \ll 1$. Using Equation 2.29 to relate Da_t to Da, we conclude that the Simple WSR can only be used when

$$Da_{bo} < Da < I. \tag{2.35}$$

This regime only becomes substantial when $I \gg 1$, which is rare in practical combustion systems.

We may characterize the frequency response of heat release rate by deriving an analytical relation between $\dot{m}_1$ and Q_1 in the expansion of heat release rate, $Q = Q_0 + \epsilon Q_1 + \ldots$

Applying a Laplace transform to Equation 2.32 yields the transfer function between u and c_1,

$$\frac{c_1}{u} = \frac{-c_0}{t_m s + (1 - Da \cdot \hat{R}')}. \tag{2.36}$$

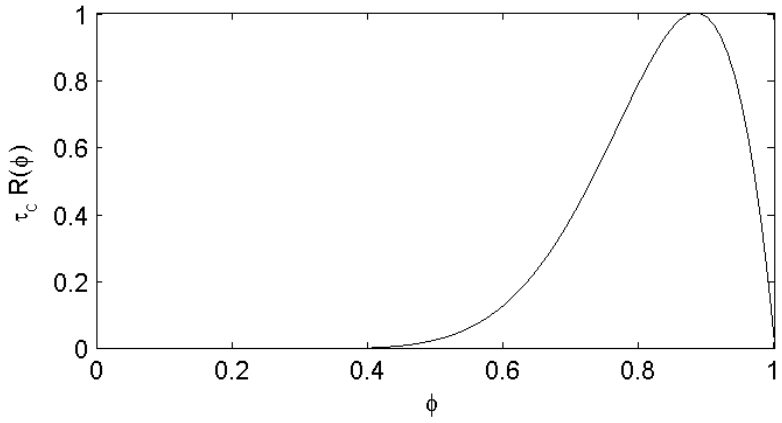

Figure 2.1: A typical reaction rate, $\hat{R} = t_r R$, as a function of c

If we solve for the transfer function between mass flow and heat release, we obtain

$$\frac{Q_1}{\dot{m}_1} = \frac{Q_1}{\dot{m}_0 u} = [C_p \Delta T c_0] \frac{-Da \cdot \hat{R}'}{t_m s + (1 - Da \cdot \hat{R}')}. \tag{2.37}$$

Equation 2.37 exhibits very simple first-order dynamic characteristics shown in Table 2.1. Since the system is only first order, the manner in which it will couple with the surrounding acoustics is completely defined by its cutoff frequency and its DC gain. It is also immediately apparently precisely how important both Da and the shape of $\hat{R}$ are to determining the dynamic response. A typical Arrhenius expression for $\hat{R}$, which we shall use to study Equation 2.37, might look like the curve in Figure 2.1. Its precise shape is dependent on the various empirical parameters used in its definition, so that the characteristics of the WSR will also be implicitly dependent on those parameters as well.

Cutoff frequency Equation 2.37 has a single pole corresponding to a frequency of

$$f_c = (2\pi t_m)^{-1} \left[1 - Da \cdot \hat{R}'(c_0)\right]. \tag{2.38}$$

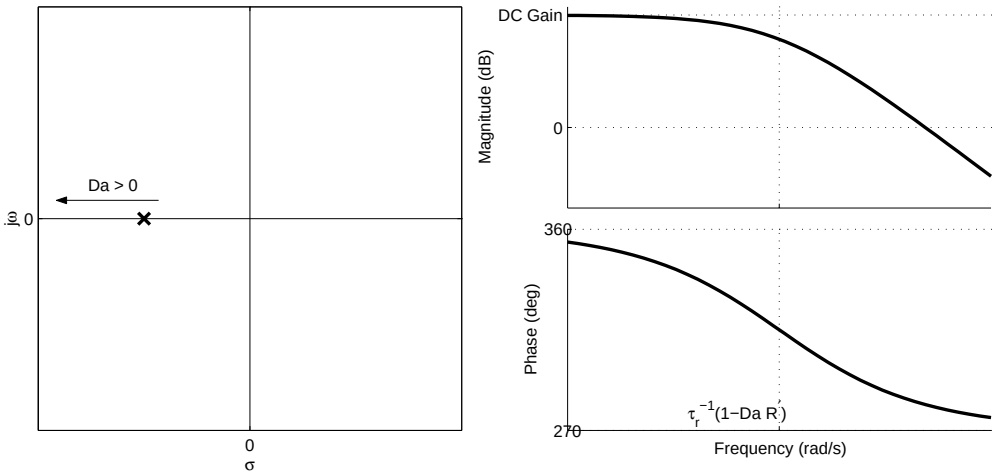

Figure 2.2: Simple WSR root locus and frequency response. The pole trend with respect to Damköhler number is notated on the root locus diagram with a labeled arrow.

The location of the pole in the complex plane and the system's total frequency response is depicted in Figure 2.2.

For large Damköhler numbers, the cutoff frequency is dominated by the second term in the brackets and can therefore be estimated by $-(2\pi t_r)^{-1}\hat{R}'$. It is important to note that *this frequency does not correspond to the chemical time*. Though the chemical time appears as a parameter in the expression, this term can vary anywhere from 0 to 10^2 times *faster* than the chemical time scale, depending on the value of $\hat{R}'(c_0)$. This is the apparent "stiffness" of the flame due to the sensitivity of the reaction rate and not chemical delay. Accepting a single-step reaction mechanism precludes including any real chemical dynamics. Therefore, a Simple WSR's cutoff frequency scales with the chemical time scale for the values of Da for which the WSR is most valid.

These results can be quantified if we use a simplified Arrhenius form for the reaction rate

expression,

$$\hat{R}(c) = A \exp\left(-\frac{T_a}{T}\right)(1-c)^m \tag{2.39}$$

$$T = \Delta T c + T_{in}, \tag{2.40}$$

the parameter, m, defines the reaction rate's sensitivity to the extinction of fuel. Figure 2.3 shows the Strouhal number as a function of Da for various values of m. The dotted lines shows the same curve using the large Damköhler number estimate. This indicates the strong impact that the shape of the reaction rate function can have on the dynamics even for values of the Damköhler number on the order 10. More importantly, Figure 2.3 also indicates that there is no range of Da over which the Simple WSR comes even close to exhibiting cutoff frequencies at a constant value of Str.

DC gain The DC gain of the system is taken as the linear change in reaction rate per change in mass flow to the reactor.

For large Damköhler numbers, the DC gain shown in Table 2.1 can also be simplified. In the limit as $Da \to \infty$, the DC gain approaches $C_p \Delta T c_0$. The total energy per unit mass available from combustion of the incoming mixture is represented by $C_p \Delta T$. Since c_0 indicates the fraction of fuel combusted, $C_p \Delta T c_0$ is the heat release per unit mass of mixture at the current operating condition. As the Damköhler number decreases, however, this intuitive estimate becomes less acurate.

Figure 2.4 shows the DC gain as a function of Damköhler number, normalized by the large-Da gain estimate. The embedded plot shows the minute changes in gain that occur at low Damköhler number with respect to changes in m.

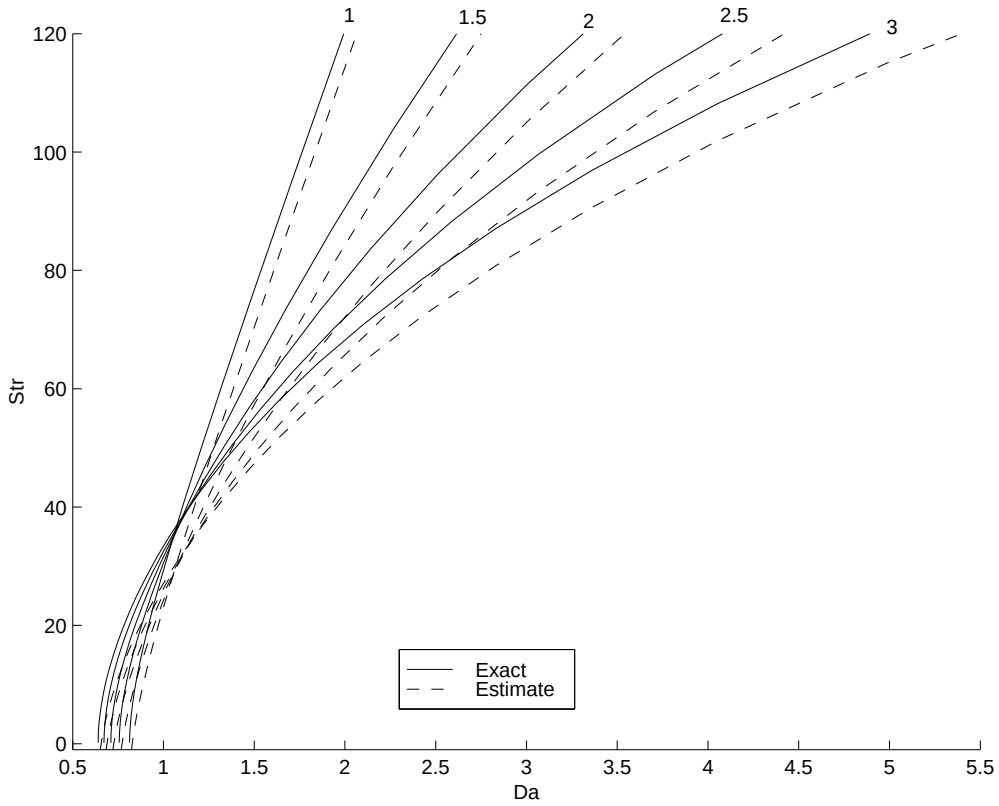

Figure 2.3: Strouhal number ($Str = f_c * t_m$) as a function of Damköhler number for various values of m.

Table 2.1: Dynamic characteristics of the simple WSR. Poles and zeros are reported in real units (rad/s) and the DC gain is also reported in real units (energy/mass). The right-hand column shows the estimated parameters for large Da.

	Explicit	Estimate ($Da \to \infty$)
Poles	$-{t_m}^{-1}\left(1 - Da \cdot \hat{R}'(c_0)\right)$	${t_r}^{-1}\hat{R}'(c_0)$
Zeros	∞	∞
DC Gain	$\dfrac{-Da \cdot \hat{R}'(c_0)}{1 - Da \cdot \hat{R}'(c_0)} C_p \Delta T c_0$	$c_0 C_p \Delta T$

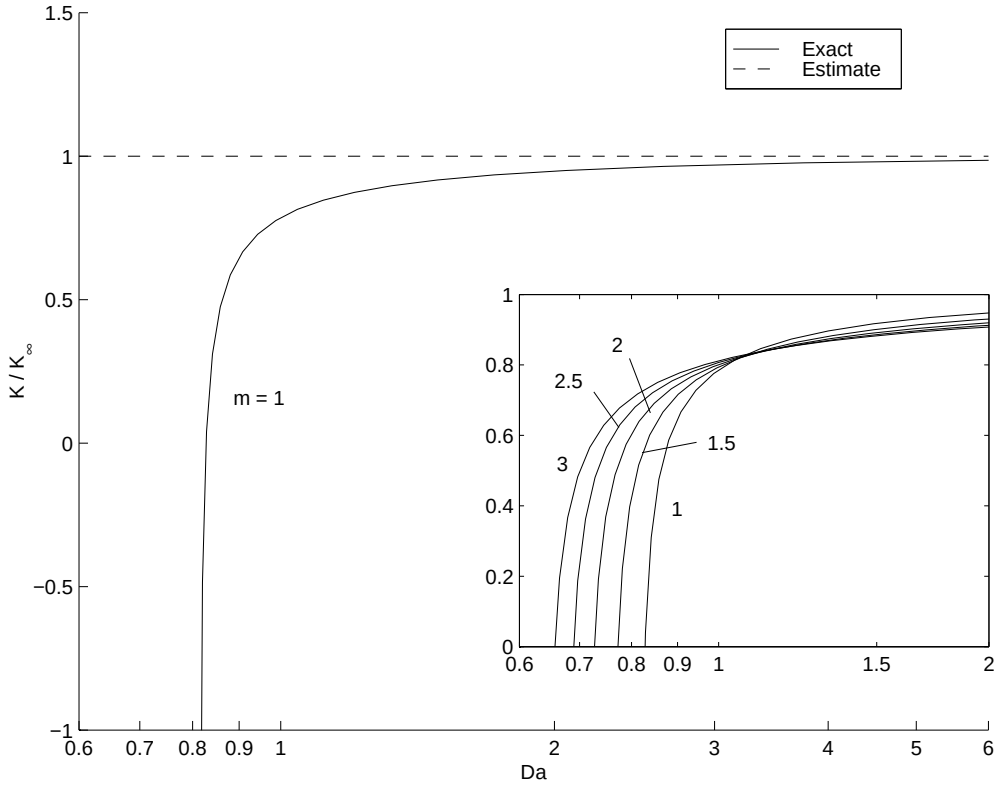

Figure 2.4: DC gain normalized by its asymptotic value ($c_0 C_p \Delta T$) and plotted with respect to Da. The embedded plot shows the gain plotted over narrow ranges of Da for various values of m.

Summary

- DC gain is much less sensitive to the shape of $\hat{R}$ than the cutoff frequency,
- $C_p \Delta T c_0$ is an excellent estimate of DC gain for $Da > \mathcal{O}(10)$,
- Close to blowoff, $\hat{R}'$ changes sign, causing the DC gain to also change sign,
- The Simple WSR's cutoff frequency does not scale like experimental swirl-stabilized flames.

2.3 The non-simple enthalpy WSR

Assuming constant and equal specific heats has long been applied because of the accompanying simplifications. The implications on the static reactor are relatively self evident, but exactly how relaxing this rigid constraint will affect the reactor's dynamics is not obvious from inspection. This will mean a migration from thinking of the enthalpy of species as parallel lines to thinking of enthalpy as a surface with dependencies on the temperature and composition of the fluid.

Since we retain the single-step reaction mechanism, Equations 2.17b and 2.17a apply, but with three very significant differences.

1. The specific heat is a function of both temperature and the fluid composition;
2. the enthalpy terms must remain empirical functions and cannot be further simplified;
3. the enthalpy of reaction, based on its definition in Equation 2.18, is a function of temperature.

Though all three of the above complications apply only to the energy equation, the non-simple enthalpy curves produce an asymmetry in the equations that prevent their collapse into a single equation on reaction progress. As a result, we may define a separate reaction and thermal progress variables, c and τ, such that

$$T = T_0 + \Delta T \tau \tag{2.41}$$

$$Y_i = Y_{i,0} + \Delta Y_i c. \tag{2.42}$$

Similar to the Simple WSR, the progress variables are allowed to vary between 0 and 1 and is assumed to be 0 at the reactor inlet. In this case, ΔY_i has exactly the same definition as in the case of the Simple WSR. Defining ΔT, however, is less trivial.

The enthalpy, which is generally given as a function of temperature and composition,

$$h(T, Y_i) = \sum_i Y_i \; h_i(T_0 + \tau \Delta T), \tag{2.43}$$

can be simplified to

$$h(\tau, c) = (1 - c) \; h_r(\tau) + c \; h_p(\tau), \tag{2.44}$$

where h_r and h_p are the enthalpy curves for the reactants ($c = 0$) and complete-combustion products ($c = 1$) respectively. To obtain the adiabatic temperature rise, ΔT, we enforce that the exiting enthalpy must be equal to the incoming enthalpy, so that for complete combustion,

$$h_r(0) = h_p(1), \tag{2.45}$$

where ΔT is an implicit parameter in the product enthalpy. Generally, the inversion must

be performed numerically.

Nondimensionalizing as in the Simple WSR and substituting back into Equation 2.17a and 2.17b yields

$$(C_p \Delta T)\tau' + (h_r(\tau) - h_r(0)) = \Delta h(\tau) Da \cdot \hat{R}(\tau, c) \tag{2.46a}$$

$$c' + c = Da \cdot \hat{R}(\tau, c). \tag{2.46b}$$

Just as in the Simple WSR, $\hat{R} = t_r (Y_{f,0})^{-1} \zeta_f$. The new parameter, Δh, is given by

$$\Delta h(\tau) = h_r(\tau) - h_p(\tau). \tag{2.47}$$

It is a fortunate consequence to separating thermal and species reaction progress that the model can support not only mass flow perturbations but also perturbations in the incoming composition. Thus, when writing the perturbed equations, we let

$$\dot{m} = \dot{m}_0(1 + \epsilon u(t)) \qquad\qquad c_{inlet} = 0 + \epsilon v(t). \tag{2.48}$$

It is worth commenting that there are as many ways of perturbing the incoming mixture as there are species in the model, while the reaction progress approach will only support perturbations such that $Y_{i,0} = \Delta Y_i v$. Though it is an inherent limitation of reaction progress approaches that mass fractions are not allowed to vary independently, it can be shown with analysis that is tangential to the present discussion, that the relevant dynamics are still accurately represented.

The thusly perturbed reactor equations are

$$C_p \Delta T \epsilon \tau_1' + (1+\epsilon u)\left\{h_r(\tau_0+\epsilon\tau_1) - h_r(0) - \left[\Delta h(\tau) - \Delta h(0)\right]\epsilon v\right\} = \tag{2.49}$$

$$\Delta h(\tau_0+\epsilon\tau_1) Da \cdot \hat{R}(\tau_0+\epsilon\tau_1, c_0+\epsilon c_1) + \ldots \tag{2.50}$$

$$\tag{2.51}$$

$$\epsilon c_1' + (1+\epsilon u)(c_0+\epsilon c_1) - \epsilon v = \tag{2.52}$$

$$Da \cdot \hat{R}(\tau_0+\epsilon\tau_1, c_0+\epsilon c_1) + \ldots. \tag{2.53}$$

After the necessary expansions, isolating like terms of ϵ, and several substitutions, we are left with the steady and linearized unsteady equations of motion. The steady system is given by

$$(1-c_0)h_r(\tau_0) + c_0 h_p(\tau_0) = h_r(0), \tag{2.54a}$$

$$c_0 = Da \cdot \hat{R}(\tau_0, c_0). \tag{2.54b}$$

The classic approach to solving these with minimal iteration is to assume a value for c_0, invert Equation 2.54a to compute the corresponding value for τ_0, and finally use Equation 2.54b to back-calculate the corresponding value of Da. Thus, a mapping can be made between the Damköhler number and the pair, (τ_0, c_0). Otherwise, if Da is specified directly, both equations must be solved numerically and simultaneously.

The dynamic system is given by

$$\tau_1' + \left[1 - \beta Da \cdot \hat{R}_\tau\right]\tau_1 + \left[-\beta Da \cdot \hat{R}_c\right] c_1 = -u\beta c_0 + (\beta - \beta_0)v, \tag{2.55a}$$

$$c_1' + \left[-Da \cdot \hat{R}_\tau\right]\tau_1 + \left[1 - Da \cdot \hat{R}_c\right] c_1 = -uc_0 + v, \tag{2.55b}$$

where β and β_0 are defined as

$$\beta(\tau_0, c_0) = \frac{h_r(\tau_0) - h_p(\tau_0)}{C_p(\tau_0, c_0)\Delta T}, \qquad \beta_0(\tau_0, c_0) = \frac{h_r(0) - h_p(0)}{C_p(\tau_0, c_0)\Delta T}. \tag{2.56}$$

In the case of the Simple WSR, both the static and dynamic equations collapsed conveniently on one another, but the the appearance of a thermal eccentricity, β, produces an asymmetry that prevents further simplification. The thermal eccentricity can be physically interpreted as the ratio of the adiabatic temperature rise assuming constant properties with the actual adiabatic temperature rise. As a result, β is dependent upon the values of τ and c at which the operating conditions are taken. The inlet eccentricity, β_0, appears only as a coefficient of v in the energy equation and accounts for changes in inlet enthalpy as the incoming mixture is varied.

Furthermore, if we take τ_0 to be a function of c_0 via the implicit function theorem, differentiating the energy equation with respect to c_0 yields

$$\frac{\partial h}{\partial \tau}\frac{\mathrm{d}\tau_0}{\mathrm{d}c_0} + \frac{\partial h}{\partial c} = \Delta T C_p \frac{\mathrm{d}\tau_0}{\mathrm{d}c_0} - (h_r - h_p) = 0. \tag{2.57}$$

Therefore,

$$\frac{\mathrm{d}\tau_0}{\mathrm{d}c_0} = \beta. \tag{2.58}$$

Thus, the thermal eccentricity is an indication of how the static solution deviates from the Simple WSR as depicted in Figure 2.5.

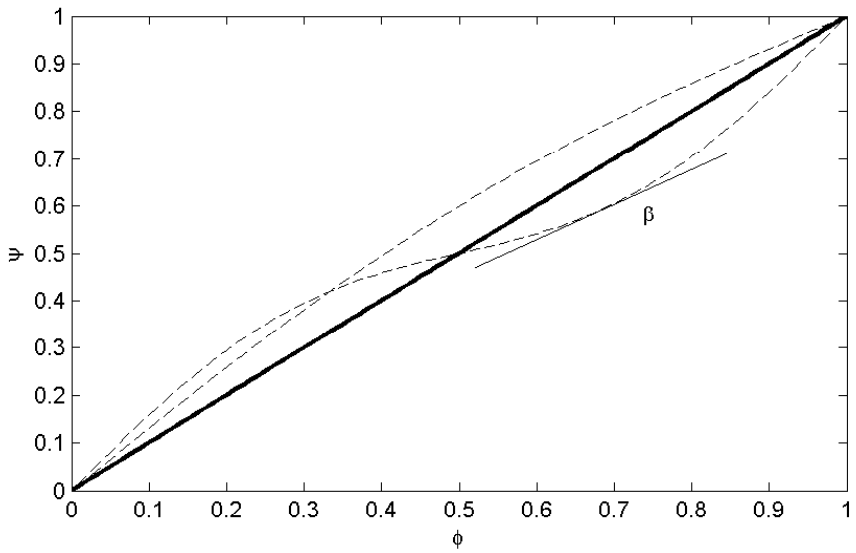

Figure 2.5: Example static solution paths in state space for various hypothetical enthalpy curves.

Heat release Just as with the Simple WSR, the heat release of the model is given by

$$Q = \rho\, V\, \Delta h\, {t_r}^{-1} \hat{R}, \tag{2.59}$$

but now, in addition to considering perturbations in $\hat{R}$, there are also perturbations to Δh that cannot be neglected. The effect is quantified by the expansion of heat release, $Q = Q_0 + \epsilon Q_1 + \ldots$, where

$$Q_0 = \dot{m}_0 \Delta h Da \cdot \hat{R} \tag{2.60a}$$

$$Q_1 = Q_0 \left[\left(\frac{\hat{R}_\tau}{\hat{R}} + \frac{\hat{c}}{\beta} \right) \tau_1 + \frac{\hat{R}_c}{\hat{R}} c_1 \right]. \tag{2.60b}$$

The parameter, $\hat{c}$, is the dimensionless sensitivity of Δh to changes in τ and is defined as

$$\hat{c} = \frac{C_{p,r}(\tau) - C_{p,p}(\tau)}{C_p(\tau, c)}. \tag{2.61}$$

This term has the effect of softening or stiffening the heat release rate's sensitivity to temperature by including perturbations in the temperature-dependent enthalpy of reaction.

It should also be noted that 2.60b implicitly assumes that perturbations in ρ are negligible to determining the dynamic heat release. It can be shown in a tangential analysis that density perturbations generate terms at least two orders of magnitude smaller than the predominant terms, and that their inclusion has no appreciable affect on the combustor dynamics.

State space Equations 2.55 are conveniently expressed in the state space form,

$$\begin{aligned} \mathbf{X}' &= \mathbf{A}\mathbf{X} + \mathbf{B}\mathbf{U} \\ Q &= \mathbf{C}\mathbf{X}, \end{aligned} \tag{2.62}$$

where the vectors, $\mathbf{X}$ and $\mathbf{U}$ are given by

$$\mathbf{X} = \begin{Bmatrix} \tau_1 \\ c_1 \end{Bmatrix} \qquad\qquad \mathbf{U} = \begin{Bmatrix} u \\ v \end{Bmatrix}$$

and the state matricies are formed from Equations 2.55 and 2.60b and are given by

$$\mathbf{B} = \begin{Bmatrix} -\beta c_0 & \beta - \beta_0 \\ -c_0 & 1 \end{Bmatrix} \qquad\qquad \mathbf{C} = Q_0 \begin{Bmatrix} \frac{\hat{R}_\tau}{\hat{R}} + \frac{\hat{c}}{\beta} & \frac{\hat{R}_c}{\hat{R}} \end{Bmatrix} \tag{2.63}$$

$$\mathbf{A} = \left\{ \begin{array}{cc} -1 + \beta Da \cdot \hat{R}_\tau & \beta Da \cdot \hat{R}_c \\ Da \cdot \hat{R}_\tau & -1 + Da \cdot \hat{R}_c \end{array} \right\}. \tag{2.64}$$

A two degree-of-freedom system will exhibit two poles and, at most, one zero. Fortunately, $\mathbf{A}$ is easily diagonalized via the linear transform, $\mathbf{X} = \mathbf{PZ}$, so that

$$\mathbf{Z}' = \mathbf{P}^{-1}\mathbf{APZ} + \mathbf{P}^{-1}\mathbf{BU}. \tag{2.65}$$

In the process of determining an appropriate diagonalizing transform, $\mathbf{P}$, a term, $\Gamma = \hat{R}_\tau \beta + \hat{R}_c$, naturally appears. At this stage, its interpretation is not immediately obvious, but becomes quite significant once the transform is completed. If we select $\mathbf{P}$ such that

$$\mathbf{P} = \frac{1}{\Gamma} \left\{ \begin{array}{cc} \hat{R}_c & \beta \\ -\hat{R}_\tau & 1 \end{array} \right\} \qquad\qquad \mathbf{P}^{-1} = \left\{ \begin{array}{cc} 1 & -\beta \\ \hat{R}_\tau & \hat{R}_c \end{array} \right\}, \tag{2.66}$$

the matrix, $\mathbf{P}^{-1}\mathbf{AP}$, is diagonal, and the system can be divided into two decoupled differential equations,

$$z_1' = -z_1 - \beta_0 v \tag{2.67}$$

$$z_2' = (-1 + Da\Gamma)\, z_2 - c_0 \Gamma u + \left[(\beta - \beta_0)\hat{R}_\tau + \hat{R}_c \right] v. \tag{2.68}$$

The elements of $\mathbf{Z} = \{ z_1 \quad z_2 \}^T$ can be computed in terms of $\mathbf{X}$ by asserting that $\mathbf{Z} = \mathbf{P}^{-1}\mathbf{X}$, resulting in

$$z_1 = \tau_1 - \beta c_1 \tag{2.69}$$

$$z_2 = \hat{R}_\tau \tau_1 + \hat{R}_c c_1. \tag{2.70}$$

Recalling that small changes in the static solution obey $\mathrm{d}\tau_0/\mathrm{d}c_0 = \beta$, changes in z_1 represent perturbations precisely normal to that curve in (c, τ) state space. Thus, if z_1 is constant, then the system is operating parallel to the static curve, and if z_1 is zero, then the system is operating *on* the static curve.

The second transformed state variable, z_2, is simply the unsteady reaction rate. These results also offer a physical interpretation for the parameter, Γ, since when $z_1 = 0$, $z_2 = \Gamma c_1$. Thus, Γ is the Non-simple Enthalpy equivalent of $\hat{R}'$ from the Simple WSR.

To complete the transform, the output, Q, must also be written in terms of $\mathbf{Z}$. Substitution of $\mathbf{X} = \mathbf{PZ}$ into Equation 2.62 yields

$$Q_1 = Q_0 \left\{ \begin{array}{cc} \frac{\hat{c}\hat{R}_c}{\Gamma\beta} & \left(\frac{1}{\hat{R}} + \frac{\hat{c}}{\Gamma}\right) \end{array} \right\} \mathbf{Z}. \tag{2.71}$$

It is also interesting to note that when Δh is constant, Equation 2.71 reduces to $Q_1 = Q_0\, z_2/\hat{R}$. In other words, the fractional change in heat release becomes equal to the fractional change in the reaction rate.

Frequency response to mass flow Because u does not appear in Equation 2.67, when the system is subject to forcing from u, $z_1 = 0$. That is certainly not because a response involving a nontrivial solution for z_1 is disallowed, but simply because, despite the asymmetry in Equations 2.55, the forcing with respect to u does not excite the mode that exhibits that behavior.

Redimensionalizing time and taking the Laplace transform of Equation 2.67, the transfer function between u and z_2 is given by

$$\frac{z_2}{u} = \frac{-c_0\Gamma}{t_m s + (1 - Da\,\Gamma)}. \tag{2.72}$$

Finally, substituting into Equation 2.71, the total transfer function is

$$\frac{Q_1}{\dot{m}_1} = \frac{1}{\dot{m}_0}\frac{Q_1}{u} = \Delta h c_0 \left(1 + \hat{c}\frac{\hat{R}}{\Gamma}\right) \frac{-Da\Gamma}{t_m s + (1 - Da\Gamma)}. \tag{2.73}$$

Equation 2.73 is almost identical to the Simple WSR except for the appearance of Γ instead of $\hat{R}'$ and the appearance of a correction factor $1 + \hat{c}\,\hat{R}/\Gamma$ to account for variations in Δh. If constant and equal specific heats are imposed, β is one and $\hat{c}$ is zero, and we recover the Simple WSR transfer function.

Because the transfer function has only a single high-frequency pole, it can be characterized by its DC gain and cutoff frequency, just as the Simple WSR. These characteristics are summarized in Table 2.2. The cutoff frequency bears the same behavior with respect to Da, but with an added implicit linear dependency on β through Γ.

Frequency response to mixture At first glance, the mixture perturbations have extremely different dynamic characteristics than their mass-flow counterparts. Of the two modes of excitation, mixture perturbations are the only to excite the z_1 mode, which exhibit a pole corresponding to t_m. From the diagonal realization in Equations 2.67 and 2.68, the transfer functions for the state variables with respect to v are

$$\frac{z_1}{v} = \frac{-\beta_0}{t_m s + 1} \tag{2.74}$$

$$\frac{z_2}{v} = \frac{\hat{R}_c}{t_m s + (1 - Da\,\Gamma)}. \tag{2.75}$$

Substituting them into 2.71 and performing the necessary manipulations, we arrive at the

Table 2.2: Dynamic characteristics of the Non-simple Enthalpy, single-step kinetic WSR. Poles and zeros are reported in real units (rad/s) and the DC gain is also reported in real units (energy/mass or energy/s). The right-hand column shows the estimated parameters for large Da and small α.

	Mass	
	Exact	Estimate
Poles	$-{t_m}^{-1}\left(1-Da\,\Gamma\right)$	${t_r}^{-1}\Gamma$
Zeros	∞	∞
DC Gain	$\Delta h c_0\left(1+\hat{c}\dfrac{\hat{R}}{\Gamma}\right)\dfrac{-Da\,\Gamma}{1-Da\,\Gamma}$	$\Delta h c_0\left(1+\hat{c}\dfrac{\hat{R}}{\Gamma}\right)$
	Mixture	
	Exact	Estimate
Poles	$-t_m^{-1}$ $-{t_m}^{-1}\left(1-Da\,\Gamma\right)$	$-t_m^{-1}$ ${t_r}^{-1}\Gamma$
Zeros	$-{t_m}^{-1}\dfrac{1+\alpha+\hat{c}c_0}{1+\alpha}$	$-{t_m}^{-1}(1+\hat{c}c_0)$
DC Gain	$-\dot{m}_0\Delta h\dfrac{\hat{R}_c}{\Gamma}(1+\alpha+\hat{c}c_0)\dfrac{-Da\Gamma}{1-Da\Gamma}$	$-\dot{m}_0\Delta h\dfrac{\hat{R}_c}{\Gamma}(1+\hat{c}c_0)$

Table 2.3: Non-simple Enthalpy WSR parameters, their definitions, and their physical interpretations

Parameter	Definition	Interpretation
α	$\frac{\hat{c}\hat{R}}{\Gamma}\left(1-\frac{\beta_0}{\beta}\right)$	Quantifies the effect of varying thermal eccentricity on WSR zeros.
β	$\frac{h_r - h_p}{C_p \Delta T}$	Thermal Eccentricity: the ratio of actual adiabatic temperature rise to constant-property temperature rise.
Γ	$\hat{R}_\tau \beta + \hat{R}_c$	Reaction Rate Sensitivity: sensitivity of the reaction rate to low-frequency changes in c.
$\hat{c}$	$\frac{C_{p,r} - C_{p,p}}{C_p}$	Specific Heat Eccentricity: dimensionless sensitivity of Δh to changes in τ.

total transfer function,

$$\frac{Q_1}{v} = \dot{m}_0 \Delta h \, Da \, \hat{R}_c \frac{(1+\alpha)\, t_m s + (1+\alpha+\hat{c}\, c_0)}{(t_m s + 1)(t_m s + 1 - Da\, \Gamma)}. \tag{2.76}$$

The parameter, α, appears as a result of the algebraic manipulations required to obtain Equation 2.76 and is given by

$$\alpha = \frac{\hat{c}\hat{R}}{\Gamma}\left(1 - \frac{\beta_0}{\beta}\right). \tag{2.77}$$

This expression quantifies the impact of β variations across τ on the zero location. For most fuels, the Δh bears only a weak dependence on τ. As such, $\beta_0 \approx \beta$ and $\alpha \approx 0$. Furthermore, the impact of this assumption is somewhat mitigated by the appearance of α both numerator terms of Equation 2.76. Inclusion of α is, therefore important when $\hat{c}$ is highly nonzero or when the fuel's heat release is a strong function of τ.

The DC gain, poles, and zeros are summarized in Table 2.2 and depicted in Figure 2.6. Because $z_1 \neq 0$, equivalence ratio perturbations exhibit a true second-order response with a single zero. The high-frequency pole that is present in both the Simple WSR and the Non-simple Enthalpy WSR is still present, but in addition to a low-frequency pole and a nearby zero.

The low-frequency pole corresponds to t_m, regardless of other parameters. This is representative of the classic first order mixing problem that exists even in the absence of chemical reaction. Mass-flow perturbations avoid exciting such a mode altogether, but perturbations in the incoming mixture composition are unavoidably coupled with the mixing process.

The nearby zero, however, threatens to cancel the low-frequency pole. The location of the zero is an artifact of the importance of reaction rate (z_2) over any other parameter in

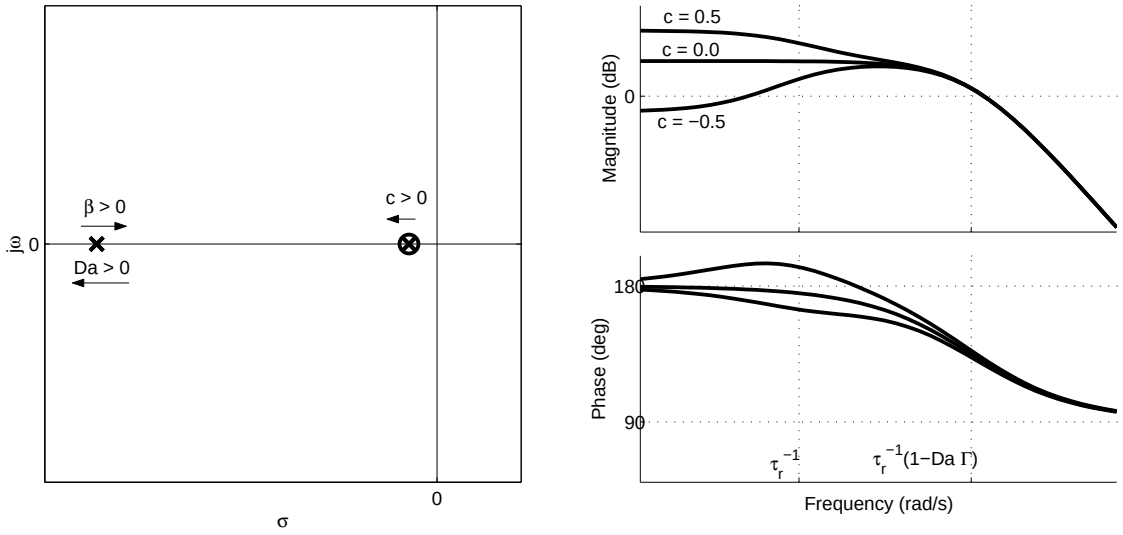

Figure 2.6: Non-simple enthalpy dynamic response to inlet mixture perturbations. The bode diagrams show frequency responses for several values of $\hat{c}$. The root locus plot shows pole and zero locations for $\hat{c} = 0$ with the motions notated by labeled arrows.

determining the heat release rate. Since z_2 only responds with the high-frequency pole, it is only by including a Δh sensitivity to temperature through $\hat{c}$ that the zero moves from -1 and the low-frequency dynamics are revealed.

Figure 2.6 shows the trends in the pole and zero locations and their resulting affects on the frequency response. It should be added that the curves shown on the frequency response plot correspond to abnormally large values for $\hat{c}$. Appendix A shows eccentricities for several common gaseous fuels are on the order 10^{-2} compared to $\hat{c} = 0.5$ used to generate Figure 2.6.

Summary The total dynamic characteristics are summarized in Table 2.2 using dimensionless parameters defined in the above section and summarized in Table 2.3. The chief behaviors of the Non-simple Enthalpy WSR are as follows:

- The Non-simple Enthalpy WSR exhibits one high frequency and one low frequency pole with a single zero.
- Mass-flow perturbations force the zero and the low-frequency pole to cancel, leaving only the high-frequency pole.
- Perturbations in the incoming composition place the zero close to the low-frequency pole. The zero's position is dependent primarily on $\hat{c}$, so that when $\hat{c} = 0$, the zero exactly cancels the pole.
- The high frequency pole exhibits motion identical to the Simple WSR plus an added linear dependence on β.
- The low-frequency pole is always at ${t_m}^{-1}$.
- How severely the low-frequency dynamics affect the frequency response is indicated almost entirely by $\hat{c}$. When $\hat{c} = 0$ the low-frequency dynamics disappear.

2.4 Higher-order chemical kinetics

The inclusion of multi-step chemical kinetics comes with the cost of severe complications to the approach that has thus far provided very broad parametric characterization of the WSR. Firstly, more complicated chemical kinetics introduce multiple reaction pathways and intermediate species so that the species scales, ΔY_i, are no longer well defined. Secondly, there is no longer a single convenient chemical timescale, but multiple chemical timescales so that the Damköhler number is no longer the only relevant parameter. Lastly and the most crippling of all, the system of equations is no longer conveniently analytically diagonalized without selecting a specific reaction mechanism.

Though multistep systems are more complex, there are still a number of simplifications that allow the system to serve as a broad illustration of the relevant dynamics. In a system with n species and a chemical kinetic mechanism with m reaction steps, the various reaction rate tensors and vectors have the following properties:

$$\tilde{\zeta} \in \mathbb{R}^n \qquad \tilde{q} \in \mathbb{R}^m \qquad \mathbf{V} = \{V_{i,j}\} \in \mathbb{R}^{n \times m}$$

If we impose that all species have constant and equal specific heats, then Equation 2.11 and 2.13 can be written

$$\dot{T} + {t_m}^{-1}(T - T_{inlet}) = -\frac{1}{c_p} \sum_i h_i \sum_j V_{i,j}\, q_j \tag{2.78a}$$

$$\dot{Y}_i + {t_m}^{-1}(Y_i - Y_{i,inlet}) = \sum_j V_{i,j}\, q_j \tag{2.78b}$$

From Equation, 2.78a, the temperature rise from each step in the mechanism naturally appears and is conveniently expressed in a vector,

$$\mathbf{H} = \left\{ \frac{\Delta h_j}{c_p} \right\} = \left\{ \frac{1}{c_p} \sum_i h_i V_{i,j} \right\}. \tag{2.79}$$

If we consider the perturbed equations — this time without non-dimensionalizing — we have that

$$\epsilon \dot{T}_1 + {t_m}^{-1}(1 + \epsilon u)(T_0 + \epsilon T_1 - T_{inlet}) = \ldots \tag{2.80}$$

$$- \mathbf{H} \cdot (\mathbf{q} + \epsilon \mathbf{q}_T T_1 + \epsilon \mathbf{q}_\mathbf{Y} \cdot \mathbf{Y}_1) \tag{2.81}$$

$$\epsilon \dot{\mathbf{Y}}_1 + {t_m}^{-1}(1 + \epsilon u)(\mathbf{Y}_0 + \epsilon \mathbf{Y}_1 - \mathbf{Y}_{0,inlet} - \epsilon \mathbf{Y}_{1,inlet}) = \ldots \tag{2.82}$$

$$\mathbf{V} \cdot (\mathbf{q} + \epsilon \mathbf{q}_T T_1 + \epsilon \mathbf{q}_\mathbf{Y} \cdot \mathbf{Y}_1)\,. \tag{2.83}$$

The steady and unsteady state variables can conveniently be grouped into state vectors,

$$\mathbf{X}_0 = \begin{Bmatrix} T_0 \\ \mathbf{Y}_0 \end{Bmatrix} \qquad \mathbf{X}_1 = \begin{Bmatrix} T_1 \\ \mathbf{Y}_1 \end{Bmatrix}.$$

Therefore, by grouping like terms of ϵ, the steady and unsteady equations are

$$\mathbf{X}_0 - \mathbf{X}_{0,inlet} = t_m \mathbf{A}_1 \cdot \mathbf{q} \tag{2.84a}$$

$$\dot{\mathbf{X}}_1 + \left({t_m}^{-1}\mathbf{I} - \mathbf{A}_1 \cdot \mathbf{J} \right) \cdot \mathbf{X}_1 = \mathbf{B} \cdot \mathbf{U}. \tag{2.84b}$$

Here, $\mathbf{A}_1$, $\mathbf{J}$, $\mathbf{B}$, and $\mathbf{U}$ are simplified expressions from the above equations, given by

$$\mathbf{A}_1 = \begin{Bmatrix} -\mathbf{H}^T \\ \mathbf{V} \end{Bmatrix} \qquad \mathbf{J} = \frac{\partial \mathbf{q}}{\partial \mathbf{X}} \qquad \mathbf{U} = \begin{Bmatrix} u \\ \mathbf{Y}_{1,inlet} \end{Bmatrix} \tag{2.85}$$

$$\mathbf{B} = \begin{Bmatrix} -t_m^{-1}(T_0 - T_{0,inlet}) & \mathbf{0} \\ -t_m^{-1}(\mathbf{Y}_0 - \mathbf{Y}_{0,inlet}) & t_m^{-1}\mathbf{I} \end{Bmatrix} \tag{2.86}$$

Some of these vector quantities have important interpretations. The reaction rate Jacobian, $\mathbf{J}$, is the matrix transform between the unsteady state vector, $\mathbf{X}_1$, to the vector of reaction rates. The new input vector, $\mathbf{U}$, includes mass flow perturbations and inlet perturbations for any of the n species and is introduced to the system through the input matrix, $\mathbf{B}$.

The output of the system is obtained by expanding Equation 2.12. After the necessary substitutions, the unsteady heat release rate is

$$Q_1 = -\rho V \mathbf{H} \cdot \mathbf{J} \cdot \mathbf{X}_1. \tag{2.87}$$

Unfortunately, it is not at all clear how the system represented in Equations 2.84b and 2.87 behaves without selecting a specific chemical model. Since the purpose of this analysis is to form broad, useful conclusions regarding the WSR that are independent of particular fuels or kinetic models, limiting conclusions to how the reactor behaves with respect to a specific mechanism would be unacceptably restrictive. We may note with no loss of generality, however, that if the dynamic reaction rates are given by

$$\mathbf{q}_1 = \mathbf{J} \cdot \mathbf{X}_1, \tag{2.88}$$

then Equations 2.84b and 2.87 may be rewritten as

$$\dot{\mathbf{q}}_1 = (-t_m^{-1}\mathbf{I} + \mathbf{J} \cdot \mathbf{A}_1) \cdot \mathbf{q}_1 + \mathbf{J} \cdot \mathbf{B} \cdot \mathbf{U} \tag{2.89a}$$

$$Q_1 = -\rho V \mathbf{H} \cdot \mathbf{q}_1. \tag{2.89b}$$

Equation 2.89 is obtained by multiplying Equation 2.84b by $\mathbf{J}$ from the left and performing the necessary substitutions. This is a state space realization with $\mathbf{q}_1$ as the state vector. This transformation hinges on being able to commute $\mathbf{J}$ in Equation 2.84b using the identity $\mathbf{J} \cdot \mathbf{I} = \mathbf{I} \cdot \mathbf{J}$. If we modified Equation 2.78a to include non-simple enthalpy effects, we would retain eccentricity coefficients in the energy equation and would be left with a diagonal matrix with unequal elements instead of the identity matrix in Equation 2.84b. Since the commutation of matrix multiplication is not allowed when the diagonal matrix cannot be expressed as a scalar multiple of the identity matrix, the transformation fails, and we recover the low-frequency fluid mechanical dynamics observed in the non-simple-enthalpy WSR.

General characteristics Because the matrix, $\mathbf{A}_1$, is utterly dependent on the choice of reaction mechanism, Equation 2.89 still represents a system that can exhibit virtually

any dynamic characteristics. However, the fact that the transformation, $\mathbf{q}_1 = \mathbf{J} \cdot \mathbf{X}_1$, was successful provides a number of important implications.

A successful state space transformation cannot change the input-output relationship, nor subsequently, the transfer function. Since $\mathbf{q}_1 \in \mathbb{R}^m$ and $\mathbf{X}_1 \in \mathbb{R}^{n+1}$, and because m and n are unrelated, the transformation can change the order of the system (the number of poles). The implication is that when the system is expressed as a higher-order system, pole-zero cancellation must occur in the transfer functions so that the total dynamic behavior is preserved. Thus, the order of the system, N, is less than or equal to the smaller of m and $n+1$.

The recognition that $N \leq \min(m, n+1)$ is simply reflective of the fact that the reaction rates cannot vary with more degrees of freedom than there are state variables in the original formulation. Similarly, the species and temperature cannot vary with more degrees of freedom than there are independent reaction rates. It should also be noted that it is still possible, though not likely, that the system can be further reduced in order. This would imply that two or more of the reaction steps are linearly dependent.

The fact that the transformed state of the system can be completely represented by the reaction rates is also extremely suggestive. The transformation on the Non-simple Enthalpy WSR in Section 2.3 exhibited two states. The first was an eccentric state that deviated from the low-frequency operating curve while the second was simply the unsteady reaction rate. Of these two, the former was the only to exhibit the low-frequency dynamics corresponding to the residence time. Equation 2.89 indicates that the Multi-step Chemical Kinetic WSR can be expressed independently of any such state variable. Subsequently the residence time dynamics that the Non-simple Enthalpy WSR exhibited will not appear in the frequency response to Equation 2.84b.

Typical characteristics Typically, these systems will exhibit very high-frequency poles as encountered by Park et. al.[46] and may exhibit zeros in a wide variety of configurations. The poles may be resonant (complex), but are often heavily damped enough to prevent an overshoot response.

Both pole and zero motion will occur with respect to the operating condition, but precisely how is difficult to say. One consistent behavior is that at least one pole will *always* approach the right-half plane as the operating conditions approach blowoff. This corresponds to the approach to the saddle node bifurcation that exists at the blowoff point[42].

We may exemplify these behaviors if we employ the two-step chemical kinetic mechanism proposed by Westbrook and Dryer[64] to include incomplete CO - CO_2 reaction,

$$\mathrm{C}_m\mathrm{O}_n + \left(\frac{n}{2} + \frac{m}{4}\right)\mathrm{O}_2 \rightarrow n\mathrm{CO} + \frac{m}{2}\mathrm{H}_2\mathrm{O} \tag{2.90a}$$

$$\mathrm{CO} + \frac{1}{2}\mathrm{O}_2 \leftrightarrow \mathrm{CO}_2. \tag{2.90b}$$

Reaction 2.90a is one-way, while reaction 2.90b is allowed in reverse. Therefore, the reaction rates from Westbrook and Dryer can be manipulated to the form

$$q_a = A_a \exp\left(-\frac{T_a}{T}\right) Y_{\mathrm{C}_m\mathrm{O}_n}{}^a Y_{\mathrm{O}_2}{}^b \tag{2.91a}$$

$$q_b = A_{b,f} \exp\left(-\frac{T_{b,f}}{T}\right) Y_{\mathrm{CO}} Y_{\mathrm{H}_2\mathrm{O}}{}^{0.5} Y_{\mathrm{O}_2}{}^{0.25} - A_{b,r} \exp\left(-\frac{T_{b,r}}{T}\right) Y_{\mathrm{CO}_2}, \tag{2.91b}$$

wherein the affect of density variations are neglected since reaction rate sensitivity to pressure is not needed.

Figures 2.7 and 2.8 show the response to velocity and equivalence ratio perturbations respec-

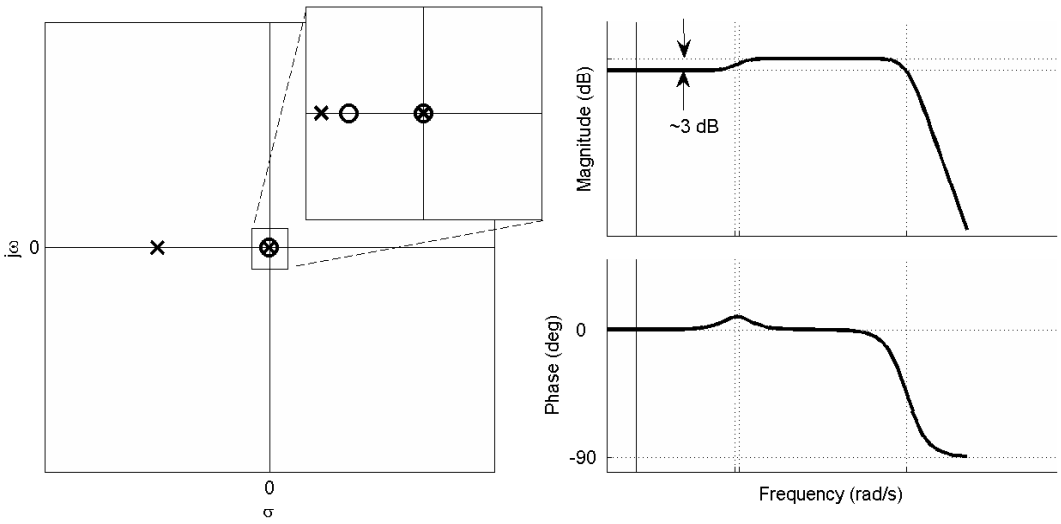

Figure 2.7: Multi-step chemical kinetic model response to velocity input. The stacked pole and zero that appear near the origin are at $-{t_m}^{-1}$, but cancel exactly.

tively of the WSR using the above mechanism. These figures show three poles and two zeros. The low-frequency poles and zeros that appear very close to the origin in both figures are exactly $-{t_m}^{-1}$. Because the thermal eccentricities have been eliminated, they cancel exactly (as we derived via the transformation to Equation 2.89).

The two remaining poles represent the dynamics of the fast and slow chemical reactions at roughly 9×10^{10}rad/s and 2.6×10^{10}rad/s respectively, and are unchanged by the mode of excitation. Only the zero moves between velocity and equivalence ratio excitations, but it is enough to change the character of the response. Just as we discussed in Section 2.2, there is an important distinction between the amount of time it takes for a reaction step to be completed (the chemical time scale) and how quickly that reaction rate will respond to changes in the reactor inputs (the dynamic time scale). While they are related by the fact that a faster reaction will have a faster time constant (shown in 2.2), they are not identical.

The results shown in Figure 2.8 imply that modelers attempting to use the WSR in closed-

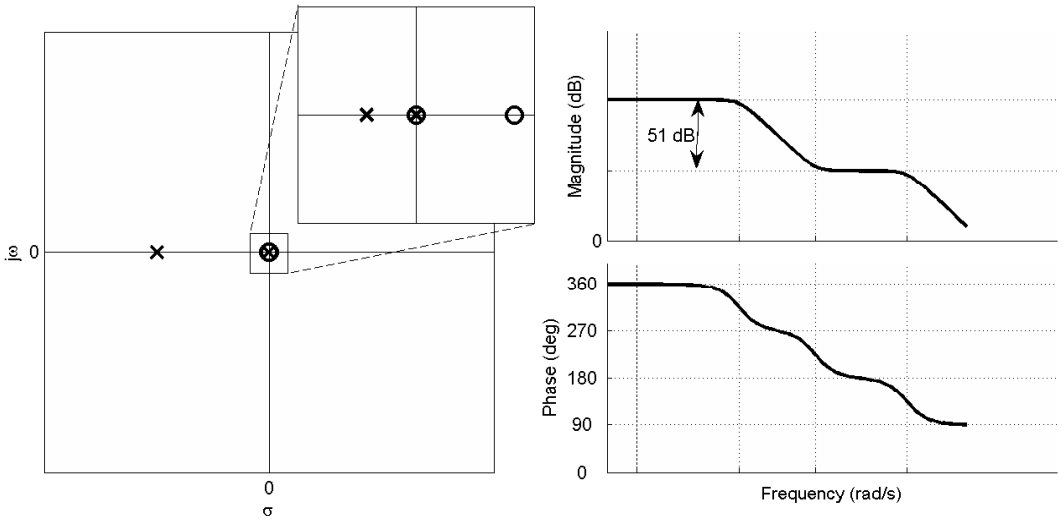

Figure 2.8: Multi-step chemical kinetic model response to equivalence ratio input. The zoomed-in embedded plot is not to scale.

loop systems for predictions on stability must be cautious. The Nyquist and Bode criteria for assessing stability of a closed-loop system as investigated in some detail by Sattelmayer and Polifke [57], make certain assumptions regarding the nature of the system being studied. Among the most typical is that the system is minimum-phase (no zeros in the right-half plane). As Figure 2.8 shows, it is not at all unreasonable, however, for a flame to exhibit non-minimum phase behavior. In this event, even the corrections the authors propose to classical methods [58] might be incapable of accurately assessing stability without first knowing the number of zeros in the right-half plane. If this problem is encountered researchers should reference Engell and Klatt[10].

Chapter 3

1D Laminar Combustion

Nomenclature

General

A ..... Rxn. rate coefficient
c ..... Reaction progress
C_p ..... Specific heat
D_i ..... Total diffusivity of spec. i
h_i ..... Enthalpy of spec. i
Le ..... Lewis number (α/D)
q ..... Expanded d'less rxn. rate
Q ..... Total reaction rate
$\hat{Q}$ ..... D'less reaction rate
R ..... D'less reaction rate
t ..... Time
$\hat{t}$ ..... D'less time (t/t_r)
T ..... Temperature
t_r ..... Reaction time scale
u ..... Velocity
$\hat{u}$ ..... D'less velocity
U ..... Steady velocity
$\hat{U}$ ..... D'less steady velocity
x ..... Position from burner
$\hat{x}$ ..... D'less position (x/δ)
Y_i ..... Mass fraction of spec. i
α ..... Thermal diffusivity
δ ..... Length scale ($\sqrt{\alpha t_r}$)
ΔT ..... Adiabatic temperature rise
ΔY_i ..... Ad. change in spec. i
ζ_i ..... Reaction rate of spec. i
ρ ..... Density
τ ..... D'less temperature
ω ..... Excitation frequency
Ω ..... D'less excitation frequency

Finite element

$E_{i,j}$ ..... Residual i, wght. fn. j
$\mathbf{F}$ ..... Forcing vector
h ..... Element length
$K_{(i,j)}$ ..... Linear stiffness matrix
$\mathbf{L}$ ..... Linear offset vector
$\mathbf{P}$ or $P_{i,j}$ ..... Natural boundary cond.
ϕ_i ..... Interpolation function i
χ ..... D'less pos. in element

Analytical

$b^{\pm}$ ..... Rxn. prog. preheat coef.
B ..... Rxn. prog. flame coef.
c_L ..... Rxn. prog. at flame front
$d^{\pm}$ ..... Temp. preheat wave no.
D ..... Temp. flame wave no.
G ..... Cross-coupling coefficient
J ..... Jump coefficient
$k^{\pm}$ ..... Rxn. prog. preheat wave no.
K ..... Rxn. prog. flame wave no.
L ..... Standoff distance
$\mathbf{M}$ ..... System matrix
$p^{\pm}$ ..... Temp. preheat coefficients
P ..... Temp flame coefficients
β ..... Progress ratio ($\Delta\tau/\Delta c$)
Δc ..... Change in c across flame
$\Delta\tau$ ..... Change in τ across flame
λ ..... Eigenvalue
Λ ..... Steady flame wave number
τ_{ig} ..... Ignition temperature

3.1 Formulation of the Plug Flow Reactor

3.1.1 Assumptions and limitations

The plug flow reactor is a one-dimensional reactor model traditionally used to calculate flame propagation speeds and model uniform burner stabilized flames. Because the dimensionality is limited, it inherently ignores changes in flame area or stretch due to asymmetries. Typically, the PFR includes affects from convection, diffusion, and reaction. Radiation is almost always neglected both because it is very difficult to do accurately since absorption and re-radiation is an inherently multi-dimensional phenomenon, and because numerous works have indicated that its affects are negligible in the flames to which the PFR is most commonly applied.

In this case, I examine a flame stabilized on a burner and excited by unsteady velocity flow through the burner.

3.1.2 Derivation

The one-dimensional reacting flow equations, including the time derivatives that are often neglected for static calculations, are

$$\frac{\partial Y_i}{\partial t} + u\frac{\partial Y_i}{\partial x} - \rho^{-1}\frac{\partial}{\partial x}\rho D_i\frac{\partial Y_i}{\partial x} = \zeta_i \tag{3.1}$$

$$\frac{\partial T}{\partial t} + u\frac{\partial T}{\partial x} - \rho^{-1}\frac{\partial}{\partial x}\rho\alpha\frac{\partial T}{\partial x} = -\frac{1}{C_p}\sum_j h_j\,\zeta_j \tag{3.2}$$

$$\frac{\partial u}{\partial t} + u\frac{\partial u}{\partial x} = -\frac{1}{\rho}\frac{\partial p}{\partial x} \tag{3.3}$$

Here, Y_i is the mass fraction of species i, D_i is the diffusivity of species i, α is the thermal diffusivity, ζ_i is the rate of formation of species i due to chemical reaction in mass per unit time per unit mass of fluid. Time and space are assigned to t and z respectively.

At this point, it is convenient to accept slight deviations from the physical in order to invite mathematical simplicity. The ideal case is for quantities such as diffusivity and velocity to appear as scalar parameters rather than field variables that must be implicitly calculated. McIntosh and later Rook took the same view since they used a density-weighted coordinate system to eliminate derivatives on α and D from the above equations. Additionally, they both took steps to separate the inlet velocity as a parametric superposition with a velocity field variable. In any case, one finds that though the accuracy of the model may be improved by considering diffusivity and velocity to be field variables, the important phenomena are preserved with the assumption that $u = u(t)$ $(u_x = 0)$ and $\alpha = D \cdot Le = \text{const.}$

Note that the total rate of enthalpy generated from chemical reaction in Equation 3.2, given

by

$$Q = -\int_0^\infty \rho \sum_j h_j \zeta_j \mathrm{d}x. \tag{3.4}$$

The heat release rate, aslo called the burning rate, is a measure of the flame's propagation speed and serves as the flame's "output" in response to an unsteady velocity "input".

Reaction progress and dimensionless temperature, c and τ respectively, can be defined such that

$$Y_i(t,x) = Y_{i,in} + \Delta Y_i \; c(t,x) \tag{3.5}$$

$$T(t,x) = T_{in} + \Delta T \; \tau(t,x) \tag{3.6}$$

where the *in* subscripts refer to the values of the corresponding quantities as they enter the region and the Δ operator describes the change in these quantities under complete combustion. With the assumption of constant specific heat, and only single-step chemical kinetics, after some manipulation the energy and species equations reduce to

$$c_t + uc_x - Dc_{xx} = {t_r}^{-1} R(c,\tau) \tag{3.7a}$$

$$\tau_t + u\tau_x - \alpha\tau_{xx} = {t_r}^{-1} R(c,\tau). \tag{3.7b}$$

where the quantity ${t_r}^{-1} R = \zeta_i / \Delta Y_i$. Since the physical system presents no immediately obvious time or length scales, there is no clear choice for the value of t_r until the solution is complete. Since it is only an arbitrary scale at this point, t_r can be selected later based on convenience.

The momentum equation is utterly trivialized by the assumption that velocity is spatially uniform. Even were that not the case, the momentum equation is only useful as a means to

computing pressure; a task that is completely unnecessary given its negligible effect in this particular problem.

The classical approach to select time and length scales offers a convenient non-dimensionalization scheme, $\hat{t} = t/t_r$, $\hat{x} = x/\delta$, where $\delta = \sqrt{\alpha t_r}$. The resulting prototype equations are then

$$\dot{c} + \hat{u}\, c' - \frac{1}{Le}\, c'' = R(c, \tau) \tag{3.8a}$$

$$\dot{\tau} + \hat{u}\, \tau' - \tau'' = R(c, \tau). \tag{3.8b}$$

The non-dimensional velocity ($\hat{u} = u\, {t_r}^{1/2}\, \alpha^{-1/2}$) appears naturally. Dots and primes refer to partial differentiation with respect to $\hat{t}$ and $\hat{x}$ respectively. The only remaining question is the choice of t_r. The classical approach is to define t_r such that $\alpha^{1/2} {t_r}^{-1/2}$ is the laminar flame speed and $\hat{u} = u/S_L$. Unfortunately, this means t_r must be implicitly determined from the solution, but it is a bearable burden.

If the burner is said to be at $\hat{x} = 0$, then the boundary conditions are

$$c(\hat{t}, 0) = 0 \tag{3.9a}$$

$$c'(\hat{t}, \hat{x} \to \infty) = 0 \tag{3.9b}$$

$$\tau(\hat{t}, x) = 0 \tag{3.9c}$$

$$\tau'(\hat{t}, \hat{x} \to \infty) = 0 \tag{3.9d}$$

Lastly, when the same assumptions that were used to obtain Equations 3.7 are applied to the heat release rate in Equation 3.4, one arrives at the dimensionless heat release rate,

$$\hat{Q} \equiv \frac{Q\, t_r\, Y_{f,in}}{\rho C_p \Delta T} = \int_0^\infty R\, \mathrm{d}\hat{x}. \tag{3.10}$$

Thus, $\hat{Q}$ is the ratio of the flame's heat release rate with that of a flame undergoing complete adiabatic combustion.

3.1.3 Expansion

The velocity can be divided into a steady and a small oscillating component, $\hat{u}(\hat{t}) = U + \epsilon \exp(j\hat{t})$. In this way, the amplitude depends on the small dimensionless parameter, ϵ, and it is possible to perform the usual expansions on ϵ.

The solution will take the form

$$c(\epsilon; \hat{t}, \hat{x}) = c_0(\hat{x}) + \epsilon\, c_1(\hat{x})\, \exp\left(j\hat{t}\right) + \mathcal{O}(\epsilon^2) \tag{3.11}$$

$$\tau(\epsilon; \hat{t}, \hat{x}) = \tau_0(\hat{x}) + \epsilon\, \tau_1(\hat{x})\, \exp\left(j\hat{t}\right) + \mathcal{O}(\epsilon^{\in}). \tag{3.12}$$

Substituting into Equations 3.8a and 3.8b,

$$\begin{aligned} &\epsilon \exp\left(j\Omega\hat{t}\right)\, j\Omega\, c_1 + \left(U + \epsilon \exp\left(j\Omega\hat{t}\right)\right)\, \left(c_0' + \epsilon \exp\left(j\Omega\hat{t}\right)\, c_1'\right) - \ldots \\ &\quad \frac{1}{Le}\, \left(c_0'' + \epsilon \exp\left(j\Omega\hat{t}\right)\, c_1''\right) = R(c_0, \tau_0) + \epsilon \exp\left(j\Omega\hat{t}\right) \left(R_c c_1 + R_\tau \tau_1\right) \end{aligned} \tag{3.13a}$$

$$\begin{aligned} &\epsilon \exp\left(j\Omega\hat{t}\right)\, j\Omega\, \tau_1 + \left(U + \epsilon \exp\left(j\Omega\hat{t}\right)\right)\, \left(\tau_0' + \epsilon \exp\left(j\Omega\hat{t}\right)\, \tau_1'\right) - \ldots \\ &\quad \left(\tau_0'' + \epsilon \exp\left(j\Omega\hat{t}\right)\, \tau_1''\right) = R(c_0, \tau_0) + \epsilon \exp\left(j\Omega\hat{t}\right) \left(R_c c_1 + R_\tau \tau_1\right) \end{aligned} \tag{3.13b}$$

To develop the separate equations governing the static and linear dynamic systems, like terms of ϵ from Equations 3.13 must be isolated. Using the principle that corresponding

coefficients of equal polynomials must be equal, the static equations are

$$U\,c_0' - \frac{1}{Le}\,c_0'' = R(c_0, \tau_0) \tag{3.14a}$$

$$U\,\tau_0' - \tau_0'' = R(c_0, \tau_0). \tag{3.14b}$$

Similarly, the dynamic equations are obtained by isolating the ϵ^1 terms. In this case, since a form has already been assumed for the time solution, the equations are in terms of the unknown eigen functions at the given frequency of excitation. They are

$$(j\Omega - R_c)\,c_1 + U\,c_1' - \frac{1}{Le}\,c_1'' = R_\tau \tau_1 - c_0' \tag{3.15a}$$

$$(j\Omega - R_\tau)\,\tau_1 + U\,\tau_1' - \tau_1'' = R_c c_1 - \tau_0'. \tag{3.15b}$$

The static and unsteady heat release rates are found by performing an identical expansion on $\hat{Q}$,

$$\begin{aligned}\hat{Q} &= q_0 + \epsilon q_1 + \mathcal{O}(\epsilon^{\in}) \\ &= \int_0^\infty \left\{R(c_0, \tau_0) + \epsilon\left(R_c c_1 + R_\tau \tau_1\right)\right\} \mathrm{d}\hat{x} + \mathcal{O}(\epsilon^{\in})\end{aligned} \tag{3.16}$$

Thus, the static component of the heat release rate is obtained by equating terms that are independent of ϵ. Substituting the expression for R,

$$\begin{aligned}q_0 &= \int_0^\infty R(c_0, \tau_0)\mathrm{d}\hat{x} \\ &= A\int_L^\infty (1 - c_0)\,.\end{aligned} \tag{3.17}$$

The linear component of the heat release rate is obtained by equating terms that are linear

on ϵ. Substituting the derivatives on R and integrating,

$$\begin{aligned} q_1 &= \int_0^\infty (R_c c_1 + R_\tau \tau_1)\, \mathrm{d}\hat{x} \\ &= A \left\{ \frac{\tau_1(L)}{\tau_0'(L)} \Delta c - \int_L^\infty c_1 \, \mathrm{d}\hat{x} \right\}. \end{aligned} \tag{3.18}$$

3.2 Finite element model

3.2.1 Defining the element

Though the ultimate goal of this effort is the development of novel analytical models governing the flame's dynamics, numerical approaches allow one to adjust the assumptions while observing their affects without re-deriving the solution. In this case, the approach is inherently one-dimensional in space. The primary questions include the effects of Lewis-number and the importance of the reaction rate model.

A one-dimensional finite element system is drastically simpler than its higher-dimensional counterparts. Because the line element is the only type of element possible, one need only decide the number of nodes per element and the size of each element. Just like the elements themselves, the entire domain can only have two boundaries, which drastically simplifies the solution algorithm. The interpolation functions used inside the elements are also drastically less sophisticated, requiring less computational power to integrate and less effort to program.

This investigation uses only linear interpolation and therefore needs only two nodes per element. Figure 3.1 shows a graphical representation of a finite element domain with N elements and n nodes when each element has 2 nodes.

An element, (e), can be defined between two nodes, i and j, as having length $h = x_j - x_i$.

Figure 3.1: Example one-dimensional finite element domain.

Many of the choices that follow are based on convenience and are not necessary choices. They are, however, common convention. Firstly, it is helpful to use a dimensionless coordinate system within the element,

$$\chi = \frac{x - x_i}{h}. \tag{3.19}$$

It is also convenient to use interpolation functions, ϕ_0 and ϕ_1, as depicted in Figure 3.2,

$$\phi_0(\chi) = 1 - \chi \tag{3.20}$$

$$\phi_1(\chi) = \chi.. \tag{3.21}$$

The element and the interpolation functions are depicted in Figure 3.2. Therefore, the variables' solutions inside the element are estimated in terms of the node values by

$$c(\chi) = c_i\,\phi_0(\chi) + c_j\,\phi_1(\chi) \tag{3.22}$$

$$\tau(\chi) = \tau_i\,\phi_0(\chi) + \tau_j\,\phi_1(\chi) \tag{3.23}$$

Derivatives are thus estimated as constant over the element,

$$c' = \frac{\mathrm{d}c}{\mathrm{d}x} = -h^{-1}c_i + h^{-1}c_j \tag{3.24}$$

$$\tau' = \frac{\mathrm{d}\tau}{\mathrm{d}x} = -h^{-1}\tau_i + h^{-1}\tau_j. \tag{3.25}$$

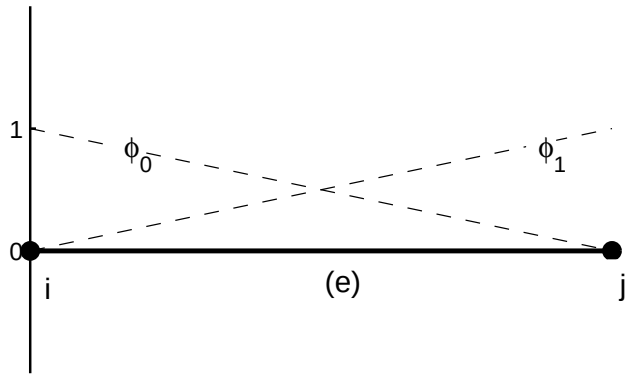

Figure 3.2: A single element and interpolation functions.

Definition of residuals The formulation of the elements is based on the Galerkin method, whereby the interpolation functions are also used as weighting functions to derive weighted residuals. This technique is both simple and can frequently offers numerical advantages over other techniques.

In this particular case, there are two coupled differential operators to be inverted over the element. Thus, the problem can be expressed as

$$g_1(\chi; c, \tau) = f_1(\chi) \tag{3.26}$$

$$g_2(\chi; c, \tau) = f_2(\chi), \tag{3.27}$$

where g_1 and g_2 represent the terms that depend on the unknowns, c and τ, in the species and energy equations respectively. The corresponding f_1 and f_2 functions are "forcing" functions, representing all terms from the same equations that do not depend on c or τ. In general, these can be addressed by the index, s (e.g. g_r and f_r).

Thus, each element is constrained by the energy and species equation with unknowns, τ and c, at each of the nodes. Therefore, with four unknowns, each of the two equations must have

two residuals in order to construct a well defined problem.

Using the Galerkin method, the four residuals are

$$E_{0,r} = h \int_0^1 \phi_r(\chi)\, g_0(\chi; c, \tau) \mathrm{d}\chi \tag{3.28a}$$

$$E_{1,r} = h \int_0^1 \phi_r(\chi)\, g_1(\chi; c, \tau) \mathrm{d}\chi. \tag{3.28b}$$

Similarly, there is a corresponding forcing vector derived from f_r,

$$F_{0,r} = h \int_0^1 \phi_r(\chi)\, f_0(\chi) \tag{3.29a}$$

$$F_{1,r} = h \int_0^1 \phi_r(\chi)\, f_1(\chi), \tag{3.29b}$$

Note that h appears so that the integral is actually over x and not over χ. Though this choice is not absolutely necessary, it prevents disproportionate weighting of small elements. Ultimately, the problem becomes that of finding approximations for c and τ such that

$$E_{s,r} = F_{s,r} \qquad | \qquad r = [0, 1], s = [0, 1] \tag{3.30}$$

Because there are also both static and dynamic equations of motion, the problem is naturally further divided into two subproblems:

1. The nonlinear static problem, governed by Equations 3.14, and

2. The linear dynamic problem, governed by Equation 3.15.

3.2.2 Static element formulation

Developing the static element is helped somewhat by the similarity between Equations 3.14. This section shall, therefore, treat the derivation of residuals from Equation 3.14a with great detail, and the necessary details to generalize the result to Equation 3.14b follow.

Species Beginning with the form of Equation 3.28, the residual for the species equation over element (e) is

$$E_{0,r}^{(e)} = h \int_0^1 \phi_r(\chi) \left[\frac{1}{Le} c_0'' - \hat{U} c_0' + R(c_0, \tau_0) \right] \mathrm{d}\chi. \tag{3.31}$$

Unfortunately, it is still impractical to use the interpolation functions in Equations 3.22 and 3.23 to write the residual in terms of the nodal values since the second derivative on c would vanish. Though this can be accounted for as a jump condition at the boundaries, it is preferable to write a weak formulation; so called because it weakens the requirements on the solution's continuity. This is accomplished by integration by parts,

$$E_{0,r}^{(e)} = h \int_0^1 \left\{ \phi_r(\chi) \left[-\hat{U} c_0' + R \right] - \frac{1}{Le} h^{-1} \frac{\mathrm{d}\phi_r}{\mathrm{d}\chi} c_0' \right\} \mathrm{d}\chi + \frac{1}{Le} \phi_r c_0' \Big|_{\chi=0}^{\chi=1} \tag{3.32}$$

Now, since Equation 3.32 requires only piecewise continuity, it is now practical to substitute the linear interpolation functions, yielding

$$E_{0,r}^{(e)} = h \int_0^1 \left\{ \phi_r \left[-\hat{U} h^{-1} \left(-c_{0,i} + c_{0,j} \right) + R \right] - \frac{1}{Le} h^{-2} \frac{\mathrm{d}\phi_r}{\mathrm{d}\chi} \left(-c_{0,i} + c_{0,j} \right) \right\} \mathrm{d}\chi + P_{0,r}^{(e)}. \tag{3.33}$$

The new parameter, P, represents the so-called "natural" boundary condition, is given by

$$P_{0,r}^{(e)} = \frac{1}{Le}\phi_r c_0' \Big|_{\chi=0}^{\chi=1} = \begin{cases} -\dfrac{1}{Le}c_0'\Big|_{x=x_i}, & r=0 \\ \dfrac{1}{Le}c_0'\Big|_{x=x_j}, & r=1 \end{cases}. \tag{3.34}$$

The natural boundary conditions are used to establish the jump/continuity conditions between neighboring elements. Physically, $P_{0,r}$ represents the mass flux due to diffusion of species through node r. Along the same lines, continuity conditions physically imply that the flux from one element will equal the flux into the neighboring elements.

At this point, it becomes necessary to consider individual cases for r since the result will depend on which residual is being considered. When $r = 0$, the integral in Equation 3.33 can be evaluated to,

$$E_{0,0}^{(e)} = \left(\frac{1}{h\,Le} - \frac{\hat{U}}{2}\right)(-c_{0,i} + c_{0,j}) + h\int_0^1 \phi_0(\chi)\,R\,\mathrm{d}\chi + P_{0,0}^{(e)}. \tag{3.35}$$

Similarly, when $r = 1$,

$$E_{0,1}^{(e)} = -\left(\frac{1}{h\,Le} + \frac{\hat{U}}{2}\right)(-c_{0,i} + c_{0,j}) + h\int_0^1 \phi_1(\chi)\,R\,\mathrm{d}\chi + P_{0,1}^{(e)}. \tag{3.36}$$

Because the system is nonlinear, it will be necessary to iterate on the solution. Newton-Rapson iteration is the most widely used method for multi-dimensional iteration, but it depends on having a linearized form of the error equations. Therefore, it becomes necessary to linearize about an arbitrary guess.

Given a set of guesses for the node values, $\{c_{0,i}, c_{0,j}, \tau_{0,i}, \tau_{0,j}\}^T$, the next set of guesses will be $\{c_{0,i} + \Delta c_{0,i}, c_{0,j} + \Delta c_{0,j}, \tau_{0,i} + \Delta\tau_{0,i}, \tau_{0,j} + \Delta\tau_{0,j}\}^T$. Expanding in a Taylor series about

the changes in the node values,

$$\begin{aligned} E_{0,0}^{(e)} \approx & \left(\frac{1}{h\,Le} - \frac{\hat{U}}{2}\right)(-\Delta c_{0,i} + \Delta c_{0,j}) \\ & + h\int_0^1 \phi_0 \left[\frac{\partial R}{\partial c}\left(\phi_0 \Delta c_{0,i} + \phi_1 \Delta c_{0,j}\right) + \frac{\partial R}{\partial \tau}\left(\phi_0 \Delta \tau_{0,i} + \phi_1 \Delta \tau_{0,j}\right)\right] \mathrm{d}\chi \\ & + \left(\frac{1}{h\,Le} - \frac{\hat{U}}{2}\right)(-c_{0,i} + c_{0,j}) \\ & + h\int_0^1 \phi_0\, R\, \mathrm{d}\chi \\ & + P_{0,0}^{(e)}. \end{aligned} \tag{3.37}$$

$$\begin{aligned} E_{0,1}^{(e)} \approx & -\left(\frac{1}{h\,Le} + \frac{\hat{U}}{2}\right)(-\Delta c_{0,i} + \Delta c_{0,j}) \\ & + h\int_0^1 \phi_1 \left[\frac{\partial R}{\partial c}\left(\phi_0 \Delta c_{0,i} + \phi_1 \Delta c_{0,j}\right) + \frac{\partial R}{\partial \tau}\left(\phi_0 \Delta \tau_{0,i} + \phi_1 \Delta \tau_{0,j}\right)\right] \mathrm{d}\chi \\ & - \left(\frac{1}{h\,Le} + \frac{\hat{U}}{2}\right)(-c_{0,i} + c_{0,j}) \\ & + h\int_0^1 \phi_1\, R\, \mathrm{d}\chi \\ & + P_{0,1}^{(e)}. \end{aligned} \tag{3.38}$$

Energy The residuals for the energy equation are quite similar, only with τ_0 appearing instead of c_0 and the absence of the lewis number constant. Therefore,

$$E_{1,0}^{(e)} = \left(h^{-1} - \frac{\hat{U}}{2}\right)(-\tau_{0,i} + \tau_{0,j}) + h\int_0^1 \phi_0(\chi)\, R\, \mathrm{d}\chi + P_{1,0}^{(e)}. \tag{3.39}$$

$$E_{1,1}^{(e)} = -\left(h^{-1} + \frac{\hat{U}}{2}\right)(-\tau_{0,i} + \tau_{0,j}) + h\int_0^1 \phi_1(\chi)\, R\, \mathrm{d}\chi + P_{1,1}^{(e)}. \tag{3.40}$$

$$\tag{3.41}$$

Similarly, the natural boundary conditions for the energy equation are

$$P_{1,r}^{(e)} = \phi_r \tau_0' \big|_{\chi=0}^{\chi=1} = \begin{cases} -\tau_0'\big|_{x=x_i}, & r=0 \\ \tau_0'\big|_{x=x_j}, & r=1 \end{cases}. \tag{3.42}$$

Finally, when $r=0$, the Taylor expansion for the energy equation results in

$$\begin{aligned} E_{1,0}^{(e)} \approx & \left(h^{-1} - \frac{\hat{U}}{2}\right)(-\Delta\tau_{0,i} + \Delta\tau_{0,j}) \\ & + h\int_0^1 \phi_0 \left[\frac{\partial R}{\partial c}(\phi_0\Delta\tau_{0,i} + \phi_1\Delta\tau_{0,j}) + \frac{\partial R}{\partial \tau}(\phi_0\Delta\tau_{0,i} + \phi_1\Delta\tau_{0,j})\right] \mathrm{d}\chi \\ & + \left(h^{-1} - \frac{\hat{U}}{2}\right)(-\tau_{0,i} + \tau_{0,j}) \\ & + h\int_0^1 \phi_0 R \,\mathrm{d}\chi \\ & + P_{0,0}^{(e)}. \end{aligned} \tag{3.43}$$

When $r=1$, the expansion is

$$\begin{aligned} E_{1,1}^{(e)} \approx & -\left(h^{-1} + \frac{\hat{U}}{2}\right)(-\Delta\tau_{0,i} + \Delta\tau_{0,j}) \\ & + h\int_0^1 \phi_1 \left[\frac{\partial R}{\partial c}(\phi_0\Delta\tau_{0,i} + \phi_1\Delta\tau_{0,j}) + \frac{\partial R}{\partial \tau}(\phi_0\Delta\tau_{0,i} + \phi_1\Delta\tau_{0,j})\right] \mathrm{d}\chi \\ & - \left(h^{-1} + \frac{\hat{U}}{2}\right)(-\tau_{0,i} + \tau_{0,j}) \\ & + h\int_0^1 \phi_1 R \,\mathrm{d}\chi \\ & + P_{0,1}^{(e)}. \end{aligned} \tag{3.44}$$

Matrix realization The linearized residuals can also be expressed in the form

$$\begin{Bmatrix} E_{0,0}^{(e)} \\ E_{0,1}^{(e)} \\ E_{1,0}^{(e)} \\ E_{1,1}^{(e)} \end{Bmatrix} \approx \mathbf{K}^{(e)} \cdot \begin{Bmatrix} \Delta c_{0,i} \\ \Delta c_{0,j} \\ \Delta \tau_{0,i} \\ \Delta \tau_{0,j} \end{Bmatrix} + \mathbf{L}^{(e)} + \mathbf{P}^{(e)} = \mathbf{F}^{(e)}. \tag{3.45}$$

In order of appearance; $\mathbf{K}$, commonly known as the "stiffness matrix", is made up of coefficients of the linear term of a Taylor expansion on the node values; $\mathbf{L}$ is the linear offset vector, containing the constant terms from the Taylor expansion; $\mathbf{P}$ is a vector of the natural boundary conditions; $\mathbf{F}$ is a vector of the "forcing terms" from Equation 3.29.

In the case of the static element, $\mathbf{F}$ is zero since there are no source terms. The natural boundary condition vector is

$$\mathbf{P}^{(e)} = \begin{Bmatrix} P_{0,0}^{(e)} \\ P_{0,1}^{(e)} \\ P_{1,0}^{(e)} \\ P_{0,1}^{(e)} \end{Bmatrix} = \begin{Bmatrix} -(1/Le)c_0'|_{x=x_i} \\ (1/Le)c_0'|_{x=x_j} \\ -\tau_0'|_{x=x_i} \\ \tau_0'|_{x=x_j} \end{Bmatrix}. \tag{3.46}$$

The linear offset vector is

$$\mathbf{L}^{(e)} = \begin{Bmatrix} \left(\frac{1}{h\,Le} - \frac{\hat{U}}{2}\right)(-c_{0,i} + c_{0,j}) + h\int_0^1 \phi_0\, R\,\mathrm{d}\chi \\ -\left(\frac{1}{h\,Le} + \frac{\hat{U}}{2}\right)(-c_{0,i} + c_{0,j}) + h\int_0^1 \phi_1\, R\,\mathrm{d}\chi \\ \left(h^{-1} - \frac{\hat{U}}{2}\right)(-\tau_{0,i} + \tau_{0,j}) + h\int_0^1 \phi_0\, R\,\mathrm{d}\chi \\ -\left(h^{-1} + \frac{\hat{U}}{2}\right)(-\tau_{0,i} + \tau_{0,j}) + h\int_0^1 \phi_1\, R\,\mathrm{d}\chi \end{Bmatrix}. \tag{3.47}$$

Organized by row, the elements of the stiffness matrix are

$$K^{(e)}_{(1,1)} = -\left(\frac{1}{h\,Le} - \frac{\hat{U}}{2}\right) + h\int_0^1 {\phi_0}^2\,\frac{\partial R}{\partial c}\,\mathrm{d}\chi \tag{3.48a}$$

$$K^{(e)}_{(1,2)} = \left(\frac{1}{h\,Le} - \frac{\hat{U}}{2}\right) + h\int_0^1 \phi_0\,\phi_1\,\frac{\partial R}{\partial c}\,\mathrm{d}\chi \tag{3.48b}$$

$$K^{(e)}_{(1,3)} = h\int_0^1 {\phi_0}^2\,\frac{\partial R}{\partial \tau}\mathrm{d}\chi \tag{3.48c}$$

$$K^{(e)}_{(1,4)} = h\int_0^1 \phi_0\,\phi_1\,\frac{\partial R}{\partial \tau}\mathrm{d}\chi \tag{3.48d}$$

$$K^{(e)}_{(2,1)} = \left(\frac{1}{h\,Le} + \frac{\hat{U}}{2}\right) + h\int_0^1 \phi_1\,\phi_0\,\frac{\partial R}{\partial c}\,\mathrm{d}\chi \tag{3.48e}$$

$$K^{(e)}_{(2,2)} = -\left(\frac{1}{h\,Le} + \frac{\hat{U}}{2}\right) + h\int_0^1 {\phi_1}^2\,\frac{\partial R}{\partial c}\,\mathrm{d}\chi \tag{3.48f}$$

$$K^{(e)}_{(2,3)} = h\int_0^1 \phi_1\,\phi_0\,\frac{\partial R}{\partial \tau}\mathrm{d}\chi \tag{3.48g}$$

$$K^{(e)}_{(2,4)} = h\int_0^1 {\phi_1}^2\,\frac{\partial R}{\partial \tau}\mathrm{d}\chi \tag{3.48h}$$

$$\tag{3.48i}$$

$$K^{(e)}_{(3,1)} = h\int_0^1 {\phi_0}^2\,\frac{\partial R}{\partial c}\,\mathrm{d}\chi \tag{3.48j}$$

$$K^{(e)}_{(3,2)} = h\int_0^1 \phi_0\,\phi_1\,\frac{\partial R}{\partial c}\,\mathrm{d}\chi \tag{3.48k}$$

$$K^{(e)}_{(3,3)} = -\left(\frac{1}{h} - \frac{\hat{U}}{2}\right) + h\int_0^1 {\phi_0}^2\,\frac{\partial R}{\partial \tau}\mathrm{d}\chi \tag{3.48l}$$

$$K^{(e)}_{(3,4)} = \left(\frac{1}{h} - \frac{\hat{U}}{2}\right) + h\int_0^1 \phi_0\,\phi_1\,\frac{\partial R}{\partial \tau}\mathrm{d}\chi \tag{3.48m}$$

$$K^{(e)}_{(4,1)} = h \int_0^1 \phi_1 \, \phi_0 \, \frac{\partial R}{\partial c} \, \mathrm{d}\chi \tag{3.48n}$$

$$K^{(e)}_{(4,2)} = h \int_0^1 {\phi_1}^2 \, \frac{\partial R}{\partial c} \, \mathrm{d}\chi \tag{3.48o}$$

$$K^{(e)}_{(4,3)} = \left(\frac{1}{h} + \frac{\hat{U}}{2} \right) + h \int_0^1 \phi_1 \, \phi_0 \, \frac{\partial R}{\partial \tau} \mathrm{d}\chi \tag{3.48p}$$

$$K^{(e)}_{(4,4)} = - \left(\frac{1}{h} + \hat{U} \right) + h \int_0^1 {\phi_1}^2 \, \frac{\partial R}{\partial \tau} \mathrm{d}\chi. \tag{3.48q}$$

The various integrals on R are left unresolved. They can either be estimated by linear interpolation over the element or, since computation time is rarely a concern in a 1-D system, can be more accurately estimated by numerical quadrature. In the present work, they are estimated by numerical quadrature.

3.2.3 Dynamic element formulation

Though the dynamic equations gain a forcing term, the derivation of the dynamic elements is substantially simpler since the governing equations are, in fact, linear. As a result, there is no need to perform a Taylor expansion. In contrast, because of the appearance of c_0' and τ_0' in Equations 3.15a and 3.15b, the forcing vector cannot be ignored.

Species Beginning with the species, the residuals for Equation 3.15a are

$$E^{(e)}_{0,r} = h \int_0^1 \phi_r \left[(j\Omega - R_c) \, c_1 - \frac{1}{Le} c_1'' + \hat{U} c_1' - R_\tau \, \tau_1 \right] \mathrm{d}\chi. \tag{3.49}$$

The second derivative is eliminated in the weak form by applying integration by parts

$$E^{(e)}_{0,r} = h \int_0^1 \left\{ \phi_r \left[(j\Omega - R_c) \, c_1 + \hat{U} c_1' - R_\tau \, \tau_1 \right] + \frac{1}{Le} h^{-1} \frac{\mathrm{d}\phi_r}{\mathrm{d}\chi} c_1' \right\} \mathrm{d}\chi - \frac{1}{Le} \phi_r c_1' \Big|_{\chi=0}^{\chi=1} \tag{3.50}$$

Substituting the interpolation functions,

$$\begin{aligned} E_{0,r}^{(e)} =& h \int_0^1 \{ \dots \\ & \phi_r \left[(j\Omega - R_c) \left(c_{1,i}\phi_0 + c_{1,j}\phi_1 \right) + h^{-1}\hat{U} \left(-c_{1,i} + c_{1,j} \right) - R_\tau \left(\tau_{1,i}\phi_0 + \tau_{1,j}\phi_1 \right) \right] \\ & + \frac{1}{Le} h^{-2} \frac{\mathrm{d}\phi_r}{\mathrm{d}\chi} \left(-c_{1,i} + c_{1,j} \right) \\ \dots \} \, \mathrm{d}\chi & + P_{0,r}^{(e)} \end{aligned} \tag{3.51}$$

Just as in the static element derivation, the natural boundary conditions, P, appear as a consequence of the integration by parts. They are given by

$$P_{0,r}^{(e)} = -\frac{1}{Le} \phi_r c_1' \Big|_{\chi=0}^{\chi=1} = \begin{cases} \dfrac{1}{Le} c_1' \Big|_{x=x_i}, & r = 0 \\ -\dfrac{1}{Le} c_1' \Big|_{x=x_j}, & r = 1 \end{cases} . \tag{3.52}$$

At this point, it becomes necessary to consider cases where $r = 0$ and $r = 1$ separately since the integral in Equation 3.51 will evaluate differently. Beginning with the $r = 0$ case,

$$\begin{aligned} E_{0,0}^{(e)} = & \left(\frac{h}{3} j\Omega - \frac{1}{2}\hat{U} + \frac{1}{h\,Le} - h \int_0^1 {\phi_0}^2 \, R_c \, \mathrm{d}\chi \right) c_{1,i} \\ & + \left(\frac{h}{6} j\Omega + \frac{1}{2}\hat{U} - \frac{1}{h\,Le} - h \int_0^1 \phi_0 \, \phi_1 \, R_c \, \mathrm{d}\chi \right) c_{1,j} \\ & - \left(h \int_0^1 {\phi_0}^2 \, R_\tau \, \mathrm{d}\chi \right) \tau_{1,i} \\ & - \left(h \int_0^1 \phi_0 \, \phi_1 \, R_\tau \, \mathrm{d}\chi \right) \tau_{1,j} + P_{0,0}^{(e)}. \end{aligned} \tag{3.53}$$

When $r = 1$,

$$\begin{aligned} E_{0,1}^{(e)} = &\left(\frac{h}{6}j\Omega - \frac{1}{2}\hat{U} - \frac{1}{h\,Le} - h\int_0^1 \phi_1\,\phi_0\,R_c\,\mathrm{d}\chi\right)c_{1,i} \\ &+ \left(\frac{h}{3}j\Omega + \frac{1}{2}\hat{U} + \frac{1}{h\,Le} - h\int_0^1 {\phi_1}^2\,R_c\,\mathrm{d}\chi\right)c_{1,j} \\ &- \left(h\int_0^1 \phi_1\,\phi_0\,R_\tau\,\mathrm{d}\chi\right)\tau_{1,i} \\ &- \left(h\int_0^1 {\phi_1}^2\,R_\tau\,\mathrm{d}\chi\right)\tau_{1,j} + P_{0,1}^{(e)}. \end{aligned} \tag{3.54}$$

Energy Residuals for the energy equation can be derived using identical steps. In terms of the node values, the residuals for the energy equation are

$$\begin{aligned} E_{1,r}^{(e)} = &h\int_0^1 \{\ldots \\ &\phi_r\left[(j\Omega - R_\tau)\left(\tau_{1,i}\phi_0 + \tau_{1,j}\phi_1\right) + h^{-1}\hat{U}\left(-\tau_{1,i} + \tau_{1,j}\right) - R_c\left(c_{1,i}\phi_0 + c_{1,j}\phi_1\right)\right] \\ &+ h^{-2}\frac{\mathrm{d}\phi_r}{\mathrm{d}\chi}\left(-\tau_{1,i} + \tau_{1,j}\right) \\ \ldots\}\,&\mathrm{d}\chi + P_{1,r}^{(e)}, \end{aligned} \tag{3.55}$$

with natural boundary conditions,

$$P_{1,r}^{(e)} = -\phi_r\tau_1'\big|_{\chi=0}^{\chi=1} = \begin{cases} \tau_1'\big|_{x=x_i}, & r = 0 \\ -\tau_1'\big|_{x=x_j}, & r = 1 \end{cases}. \tag{3.56}$$

Evaluated for the case when $r = 0$,

$$\begin{aligned} E_{1,0}^{(e)} = &\left(\frac{h}{3}j\Omega - \frac{1}{2}\hat{U} + h^{-1} - h\int_0^1 {\phi_0}^2\, R_\tau \,\mathrm{d}\chi\right)\tau_{1,i} \\ &+ \left(\frac{h}{6}j\Omega + \frac{1}{2}\hat{U} - h^{-1} - h\int_0^1 \phi_0\,\phi_1\, R_\tau \,\mathrm{d}\chi\right)\tau_{1,j} \\ &- \left(h\int_0^1 {\phi_0}^2\, R_c \,\mathrm{d}\chi\right)c_{1,i} \\ &- \left(h\int_0^1 \phi_0\,\phi_1\, R_c \,\mathrm{d}\chi\right)c_{1,j} + P_{1,0}^{(e)}. \end{aligned} \tag{3.57}$$

When $r = 1$,

$$\begin{aligned} E_{1,1}^{(e)} = &\left(\frac{h}{6}j\Omega + \frac{1}{2}\hat{U} + h^{-1} - h\int_0^1 \phi_1\,\phi_0\, R_\tau \,\mathrm{d}\chi\right)\tau_{1,i} \\ &+ \left(\frac{h}{3}j\Omega - \frac{1}{2}\hat{U} - h^{-1} - h\int_0^1 {\phi_0}^2\, R_\tau \,\mathrm{d}\chi\right)\tau_{1,j} \\ &- \left(h\int_0^1 \phi_0\,\phi_1\, R_c \,\mathrm{d}\chi\right)c_{1,i} \\ &- \left(h\int_0^1 {\phi_0}^2\, R_c \,\mathrm{d}\chi\right)c_{1,j} + P_{1,1}^{(e)}. \end{aligned} \tag{3.58}$$

Matrix formulation Because the residuals are already linear on the node values, it is possible to form them directly into a matrix realization of the form,

$$\begin{Bmatrix} E_{0,0}^{(e)} \\ E_{0,1}^{(e)} \\ E_{1,0}^{(e)} \\ E_{1,1}^{(e)} \end{Bmatrix} = \mathbf{K}^{(e)} \cdot \begin{Bmatrix} c_{1,i} \\ c_{1,j} \\ \tau_{1,i} \\ \tau_{1,j} \end{Bmatrix} + \mathbf{P}^{(e)} = \mathbf{F}^{(e)}. \tag{3.59}$$

In this form, the vector is of the actual node values instead of changes in the node values as in Equation 3.45. Additionally, the linear offset vector, $\mathbf{L}^{(e)}$, is absent since the system is

already linear and so required no Taylor series.

The natural boundary conditions are

$$\mathbf{P} = \left\{ \begin{array}{c} P_{0,0}^{(e)} \\ P_{0,1}^{(e)} \\ P_{1,0}^{(e)} \\ P_{1,1}^{(e)} \end{array} \right\} = \left\{ \begin{array}{c} -(1/Le)c_1'|_{x=x_i} \\ (1/Le)c_1'|_{x=x_j} \\ -\tau_1'|_{x=x_i} \\ \tau_1'|_{x=x_j} \end{array} \right\}. \tag{3.60}$$

The forcing vector is made up of any terms from Equations 3.15a and 3.15b that are not dependent on the node values. In this case, it is c_0' and τ_0' appear in the species and energy equations respectively. Therefore, the forcing vector is

$$\mathbf{F} = \left\{ \begin{array}{c} h\int_0^1 \phi_0\, c_0' \mathrm{d}\chi \\ h\int_0^1 \phi_1\, c_0' \mathrm{d}\chi \\ h\int_0^1 \phi_0\, \tau_0' \mathrm{d}\chi \\ h\int_0^1 \phi_1\, \tau_0' \mathrm{d}\chi \end{array} \right\} = \left\{ \begin{array}{c} \frac{1}{2}\left(-c_{0,i} + c_{0,j}\right) \\ \frac{1}{2}\left(-c_{0,i} + c_{0,j}\right) \\ \frac{1}{2}\left(-\tau_{0,i} + \tau_{0,j}\right) \\ \frac{1}{2}\left(-\tau_{0,i} + \tau_{0,j}\right) \end{array} \right\}. \tag{3.61}$$

Finally, the stiffness coefficients are taken from the coefficients of node values in Equations 3.53, 3.54, 3.57, and 3.58. Therefore the elements of the stiffness matrix, organized by row, are as follows

$$K_{(1,1)}^{(e)} = \frac{h}{3} j\Omega - \frac{1}{2}\hat{U} + \frac{1}{h\,Le} - h\int_0^1 {\phi_0}^2\, R_c\, \mathrm{d}\chi \tag{3.62a}$$

$$K_{(1,2)}^{(e)} = \frac{h}{6} j\Omega + \frac{1}{2}\hat{U} - \frac{1}{h\,Le} - h\int_0^1 \phi_0\, \phi_1\, R_c\, \mathrm{d}\chi \tag{3.62b}$$

$$K_{(1,3)}^{(e)} = -h\int_0^1 {\phi_0}^2\, R_\tau\, \mathrm{d}\chi \tag{3.62c}$$

$$K_{(1,4)}^{(e)} = -h\int_0^1 \phi_0\, \phi_1\, R_\tau\, \mathrm{d}\chi \tag{3.62d}$$

$$K^{(e)}_{(2,1)} = \frac{h}{6} j\Omega - \frac{1}{2}\hat{U} - \frac{1}{h\,Le} - h\int_0^1 \phi_1\,\phi_0\,R_c\,\mathrm{d}\chi \tag{3.62e}$$

$$K^{(e)}_{(2,2)} = \frac{h}{3} j\Omega + \frac{1}{2}\hat{U} + \frac{1}{h\,Le} - h\int_0^1 {\phi_1}^2\,R_c\,\mathrm{d}\chi \tag{3.62f}$$

$$K^{(e)}_{(2,3)} = -\,h\int_0^1 \phi_1\,\phi_0\,R_\tau\,\mathrm{d}\chi \tag{3.62g}$$

$$K^{(e)}_{(2,4)} = -\,h\int_0^1 {\phi_1}^2\,R_\tau\,\mathrm{d}\chi \tag{3.62h}$$

$$K^{(e)}_{(3,1)} = -\,h\int_0^1 {\phi_0}^2\,R_c\,\mathrm{d}\chi \tag{3.62i}$$

$$K^{(e)}_{(3,2)} = -\,h\int_0^1 \phi_0\,\phi_1\,R_c\,\mathrm{d}\chi \tag{3.62j}$$

$$K^{(e)}_{(3,3)} = \frac{h}{3} j\Omega - \frac{1}{2}\hat{U} + h^{-1} - h\int_0^1 {\phi_0}^2\,R_\tau\,\mathrm{d}\chi \tag{3.62k}$$

$$K^{(e)}_{(3,4)} = \frac{h}{6} j\Omega + \frac{1}{2}\hat{U} - h^{-1} - h\int_0^1 \phi_0\,\phi_1\,R_\tau\,\mathrm{d}\chi \tag{3.62l}$$

$$K^{(e)}_{(4,1)} = -\,h\int_0^1 \phi_0\,\phi_1\,R_c\,\mathrm{d}\chi \tag{3.62m}$$

$$K^{(e)}_{(4,2)} = -\,h\int_0^1 {\phi_0}^2\,R_c\,\mathrm{d}\chi \tag{3.62n}$$

$$K^{(e)}_{(4,3)} = \frac{h}{6} j\Omega - \frac{1}{2}\hat{U} - h^{-1} - h\int_0^1 \phi_1\,\phi_0\,R_\tau\,\mathrm{d}\chi \tag{3.62o}$$

$$K^{(e)}_{(4,4)} = \frac{h}{3} j\Omega + \frac{1}{2}\hat{U} + h^{-1} - h\int_0^1 {\phi_0}^2\,R_\tau\,\mathrm{d}\chi \tag{3.62p}$$

3.2.4 Custom solver

To facilitate this particular effort, a modular solver was written in Matlab. Though the details of its working are beyond the scope of this document, because it is not commercially available, it is worthwhile to mention some of its limitations and features.

Key Limitations:

- *One dimensional:* The solver is inherently one dimensional. Though the matrix inversion process is generalizable, the way the matrix equations are organized and the way the solver is configured requires additional generalization before multi-dimensional grids will be possible.
- *Few pre-defined elements:* Only three elements have been tested on this system; a simple linear convection-diffusion system, a unity-Le flame, and the non-unity-Le flame. The former were only used in preliminary testing of the solver and are not described here.
- *Fixed grid:* The mesh is not adaptive and there is currently no support for adaptive mesh schemes.

Key Features:

- *Configurable setup structure:* The entire solution procedure is highly configurable via a setup structure containing element definitions, the grid arrangement, the iteration convergence criteria, etc...
- *Modular element definition:* Although the user is still required to perform the detailed element definition, the solver accepts a function handle to a function that supplies the stiffness matrix, the linear offset vector, and the forcing vector.
- *Modular convergence criteria:* The solver accepts a function handle to a function for testing convergence in a similar fashion as it accepts the element definition. This is particularly useful when changing between linear and nonlinear elements, or an element with an explicitly defined error.

- *Versatile boundary conditions:* Using a boundary condition specifier function, the user can restrict the necessary degrees of freedom as any legal combination of node values or natural boundary conditions on the domain edges or interior. Alternately, the same tool can be commanded to accept boundary conditions that are dependent on the solution (such as along a convective boundary).

- *Versatile formulations:* The solver can handle any number of simultaneous equations.

3.2.5 FEA results

Up to this point, the element formulations have proceeded with a generalized single-step reaction model. In fact, it is really quite straightforward to write code that treats the reaction model as a modular function rather than an integral part of the governing equations. In this work, the reaction model was given the Arrhenius form,

$$R(c,\tau) = A \exp\left(\frac{-1}{T_0^* + T_d^*\tau}\right)(1-c)\,. \tag{3.63}$$

The dimensionless temperatures are given by

$$T_0^* = \frac{T_0}{T_a} \qquad\qquad T_d^* = \frac{T_\infty - T_0}{T_a}.$$

Here, T_0 is the inlet temperature, T_a is the activation temperature, and T_∞ is the adiabatic flame temperature.

The pre-exponential term, A, is normally determined such that the dimensionless flame speed is $U = 1$. However, that involves either detailed post analysis or a detailed expansion; both of which an unnecessary to the goal of the present effort. Of primary concern is to identify how the flame dynamics behave with respect to statically measurable quantities.

Therefore, A is defined such that when $Le = 1$, the maximum value of R is 1. When $Le = 1$, Equations 3.8 become identical and collapse onto one another. Thus, $c = \tau$. Therefore, the problem of finding the point where R is maximum when $Le = 1$ can be reduced to

$$0 = \frac{\mathrm{d}R(c,c)}{\mathrm{d}c} = A \exp\left(\frac{c-1}{T_0^* + T_d^* c}\right)\left(\frac{T_d^*}{(T_0^* + T_d^* c)^2} - 1\right) \tag{3.64}$$

Therefore,

$$A = R^{-1}(c_{max}, c_{max}) \tag{3.65}$$

when

$$c_{max} = \frac{-(2T_0^* + 1) + \sqrt{4T_d^* + 4T_0^* + 1}}{2T_d^*}. \tag{3.66}$$

This realization for R is successful at guaranteeing that each term in the governing equation remain on the order of unity, but it does not guarantee that the flame speed will be $U = 1$. To the contrary, the dimensionless flame speed will even vary with Lewis number.

Static characteristics Figure 3.3 shows a converged solution when $U = 0.7$ and $Le = 2$. There are a number of features illustrated here that depict general behaviors of the static system.

Note that the species converges precisely to 1, while the temperature is lower. The species consistently converges to 1 since for any other value of c, the reaction rate is non-zero. Since the flow has a Lewis number greater than 1, the energy diffusion is faster than the species diffusion, so the heat lost to the burner out-paces the diffusion of reactants from the burner, causing a decreases in the flame temperature. Figure 3.4 shows the flame temperature as a

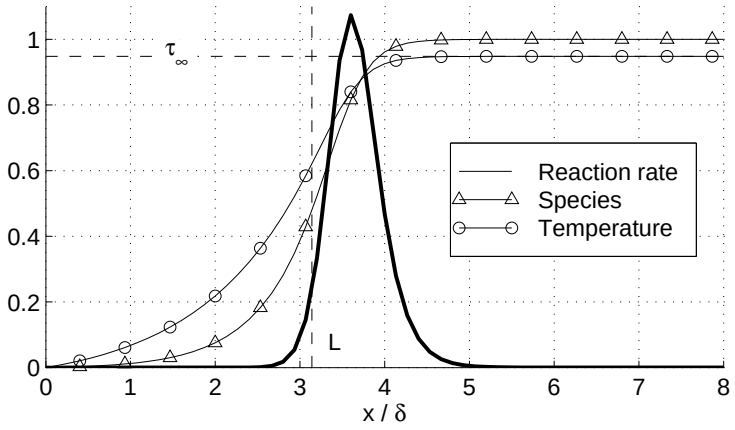

Figure 3.3: Finite element solution for $U = 0.7$ and $Le = 2$.

function of velocity for a variety of Lewis numbers.

Notice that when the Lewis number is less than unity, the flame temperature is higher than the adiabatic temperature. When the diffusion of species out-paces the diffusion of energy, fresh reactants are diffused from the burner faster than heat is lost. Thus, instead of cooling the flame as one might expect, the burner actually increases its temperature. A similar phenomenon can be observed in the flame's total heat release rate shown in Figure 3.5. At low Lewis numbers, the added diffusion at low velocities actually increases the flame's total heat release rate instead of decreasing it.

These behaviors are non-physical consequences of the choice of upstream boundary conditions. Enforcing that $c(t, 0) = 0$ implies that no matter how much diffusion occurs at the burner, the mixture in the premixer is unaffected, when in reality, it is the total mass flow of fuel, $[-\frac{1}{Le}c' + U\,c]_{x=0}$, that is physically determined.

There are, however, two points that make this peculiarity of little concern to the present study. Firstly, the focus is placed on flows where $Le > 1$. In these cases, the diffusion of species is minimized, and even the proper boundary condition is well approximated by

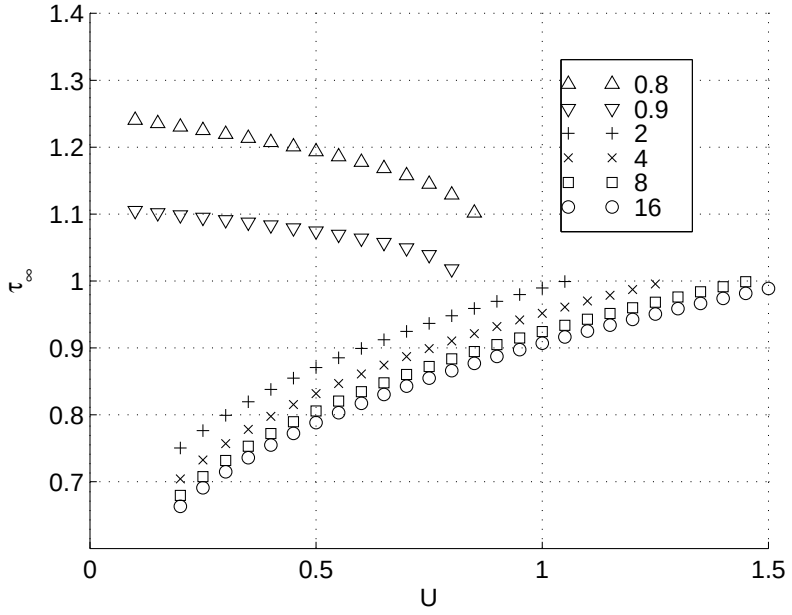

Figure 3.4: Flame temperature as a function of U for various Le.

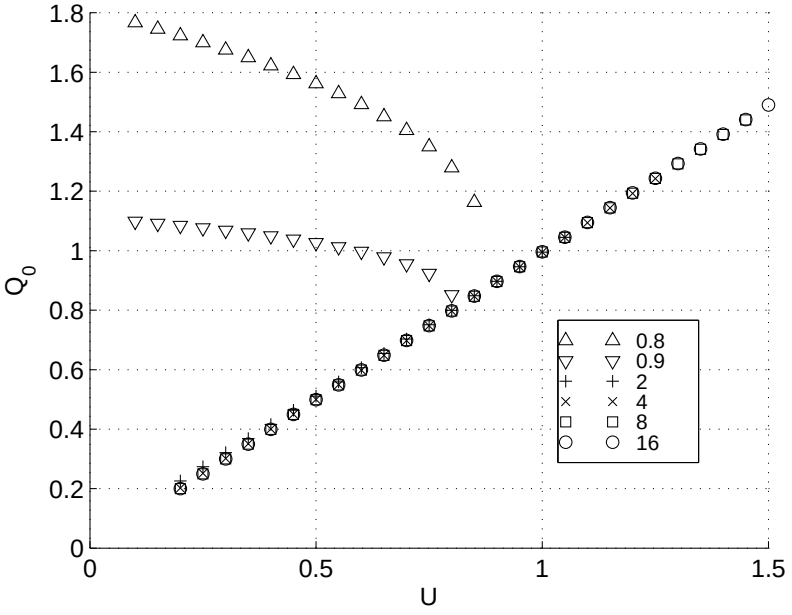

Figure 3.5: Heat release rate as a function of velocity for various Lewis numbers

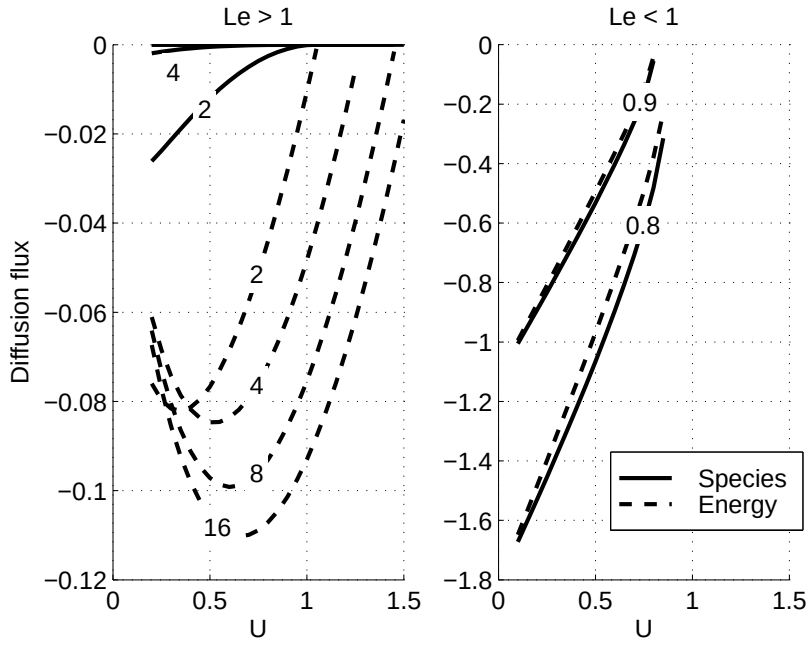

Figure 3.6: Diffusion of species and energy into the burner for high and low Le.

$c(0) = 0$. Secondly, while this argument applies well to the static flow, since the volume upstream of the burner might easily be approximated as large, its composition changes very slowly, so that it is not difficult to accept that it is effectively constant over an acoustic period. Thus, the boundary condition, $c_1(0) = 0$, is in no danger of contradiction. The point is well illustrated in Figure 3.6, where the diffusion of species and energy across the burner is plotted for a variety of operating conditions.

It is possible to asses the flame's so-called standoff distance, L, from the burner by noting the distance between the burner exit and the point where the reaction exceeds a certain threshold. The standoff distance is noted in Figure 3.3. Though in all the following cases, a reaction threshold of $R > 0.1$ is used, Figure 3.3 uses $R > 0.2$ to make the plot more readable. Figure 3.7 shows the standoff distance plotted over velocity.

As the velocity approaches the flame speed (which changes with Lewis number), the flame is

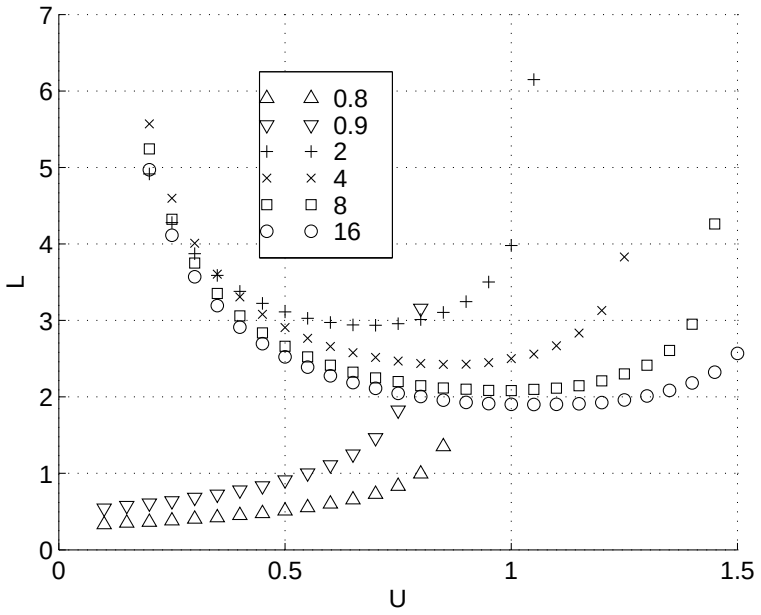

Figure 3.7: Standoff distance as a function of velocity for various Lewis numbers.

pushed farther and farther downstream. Eventually, when the flow exceeds the flame speed, the flame lifts off, and is pushed downstream indefinitely. While this behavior is common at both high and low Lewis numbers, there is a similar behavior that occurs only at high Lewis numbers when velocity approaches zero. When the diffusion of energy is faster than the diffusion of species, convection is relied upon to deliver reactants faster than energy is lost to the burner. As convection decreases, so does the amount of energy the flame can afford to lose to the burner while still igniting; thus, its equilibrium shifts farther away.

Dynamic characteristics: internal structure Figure 3.8 shows a typical magnitude and phase solution for the unsteady system.

The oscillations of both species and temperature peak in the reaction region and decline thereafter. Temperature, however, converges to a steady (although small) value representing dynamic changes in τ_∞. The declining phase in temperature after the reaction region

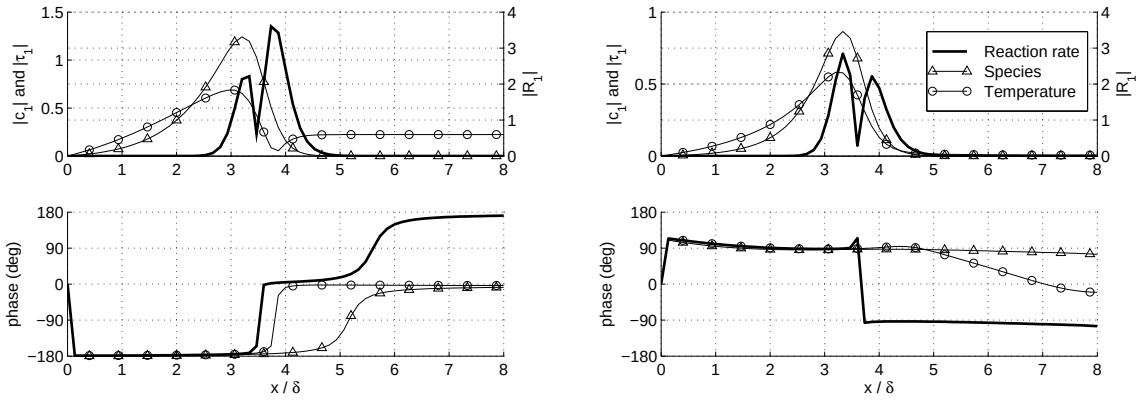

Figure 3.8: Dynamic finite element solution when $U = 0.7$, $Le = 2$, at (a) $\Omega = 0.01$ and (b) $\Omega = 1$. Note that R is plotted on separate axes for convenience.

represents delay as temperature waves leaving the flame are convected downstream.

On the other hand, oscillations in reaction rate exhibit a more sophisticated behavior. There is a peak preceding and proceeding the location where the steady reaction rate peaks, and the unsteady reaction rate vanishes between them. In addition, the reaction rate's phase drops by 180° near the point where the amplitude diminishes, indicating that the oscillations have changed sign.

These characteristics can be explained by considering the predominant components of the reaction rate equation at the various points in space. Figure 3.9 shows the components of the unsteady heat release rate caused by oscillating temperature and species concentrations. At the front of the flame, where there is ample fuel, and the temperature limits the reaction rate, temperature oscillations dominate the response. At the back of the flame, however, where diminishing fuel limits the reaction rate, the oscillating fuel dominates. The point where the transition occurs corresponds to the drop in reaction rate amplitude.

Thus,

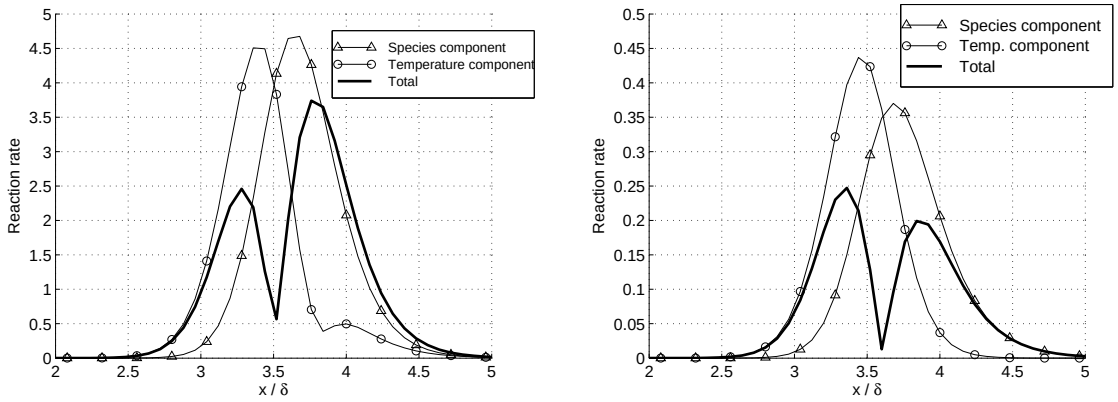

(a) (b)

Figure 3.9: Heat release contribution from oscillating temperature and species compared with the total heat release rate in space. ($U = 0.8$, $Le = 2$, (a) $\Omega = 0.02$, (b) $\Omega = 10$)

1. Upstream of the transition point, the temperature's influence is predominant, and its effect is positive

2. Downstream of the transition point, the species' influence is predominant, and its effect is negative

3. At the transition point, the two are in balance, and their effects cancel.

The importance of these effects to the total heat release response is evident from Equation 3.18. Since the unsteady heat release is determined by integrating the unsteady reaction rate spatially, it is simple to determine exactly how the front and rear dynamics contribute to the overall heat release oscillations. Figure 3.10 shows unsteady heat release transfer functions before and after the maximum static heat release and the corresponding total heat release transfer function.

Though the phases vary significantly over frequency, the front and back transfer functions are consistently out of phase. As frequency increases, the front and back transfer function magnitudes converge, but fall off very slowly. Meanwhile, the total heat release oscillations

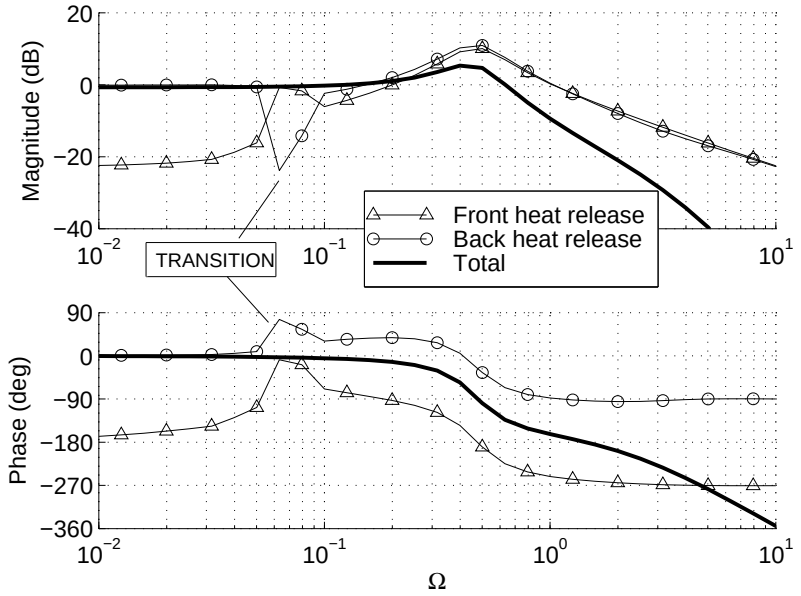

Figure 3.10: Heat release transfer functions in front and behind the static heat release maximum when $Le = 2$, $U = 0.7$.

drop off quite sharply. The implication is that at high frequencies, the total heat release oscillations have diminished, but that the flame itself is oscillating forward and backwards with the flow.

In Figure 3.9, plot (a) shows a rise in temperature oscillations behind the flame that is absent in plot (b). The oscillating heat release rate generates temperature waves that are then convected downstream. At low frequencies, these waves are even allowed to affect the reaction rate and thus, the internal structure of the flame. The jumps labeled "transition" in Figure 3.10 occur when the convection waves are significant enough to move the transition point.

Dynamic characteristics: parametric study Figure 3.10 also demonstrates that the total heat release rate appears very close to being purely second-order in nature; exhibiting

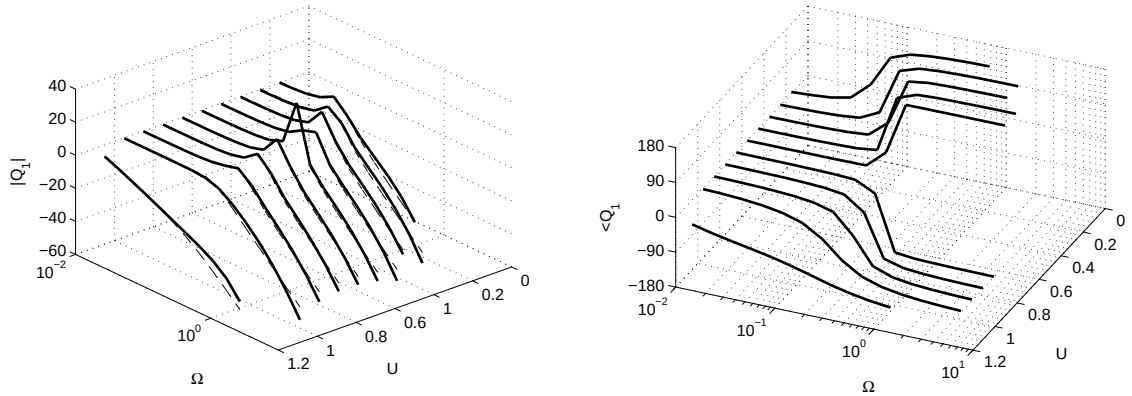

(a) (b)

Figure 3.11: Finite element predicted (a) magnitude and (b) phase of the heat release rate transfer function for various velocities at $Le = 2$. Dotted lines are a second-order fit.

a resonance, corresponding to a 180° drop in phase. Interestingly, it falls off faster than expected and exhibit what appears to be delay at very high frequencies. However, because these effects occur at such low amplitudes, there is excellent cause to consider the predicted response primarily second-order in nature.

Therefore, there are only two parameters that need to be characterized in order to model the flame response; the DC gain, and the complex poles (indicating natural frequency and damping ratio) for the resonance. Figure 3.11 shows the total transfer function for a variety of velocities when $Le = 2$, overplotted with a second-order fit. Over the frequency range shown, the magnitudes are quite close, and the difference in phase between the fits and the model predictions are indistinguishable.

The basic trends are evident in Figure 3.11. The resonance reaches its highest frequency and highest amplitude at moderate velocities and then declines as the flame lifts off on either extreme. It can also be seen from Figure 3.11, that the response is actually over-damped for extreme velocities. However, it is only evident from closer analysis, that the static solution is, in fact, unstable at low velocities. Figure 3.12 shows the root locus path for the various

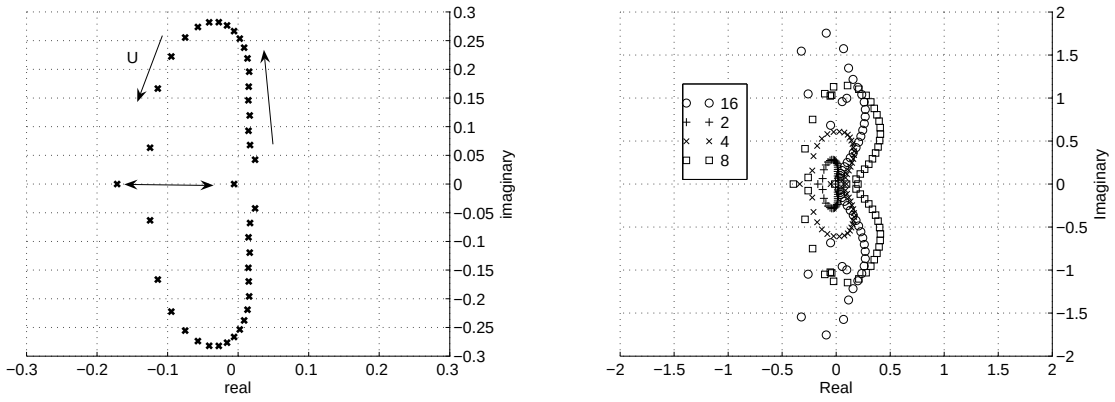

(a) (b)

Figure 3.12: Root loci for (a) $Le = 2$ only and (b) various Lewis numbers.

Lewis numbers as velocity is varied.

This instability, also predicted by McIntosh et. al.[36], corresponds to the point at which the flame's position is limited by the supply of species through convection and not the heat lost to the burner. At high velocities, when the supply of fresh reactants is ample, if the flame is perturbed closer to the burner, it loses more heat, slows, and is eventually returned to its equilibrium. Similarly, perturbations away from the burner reduce the heat loss, accelerate the flame, and it eventually returns to its original location. However, when the flame is species limited, a perturbation toward the burner intensifies the diffusion of species into the flame and accelerates it, causing it to drive further toward the burner. Alternately, perturbations away from the burner reduce the diffusion of species, and only further slow the flame.

Because the distance between the flame front and the burner is of prime importance to stabilizing the flame, it is intuitive that it should play a role in determining the flame's dynamic behavior. That most behaviors are repeated at operating conditions where the flame is lifting off encourages the notion that the cutoff frequency scales with a length scale

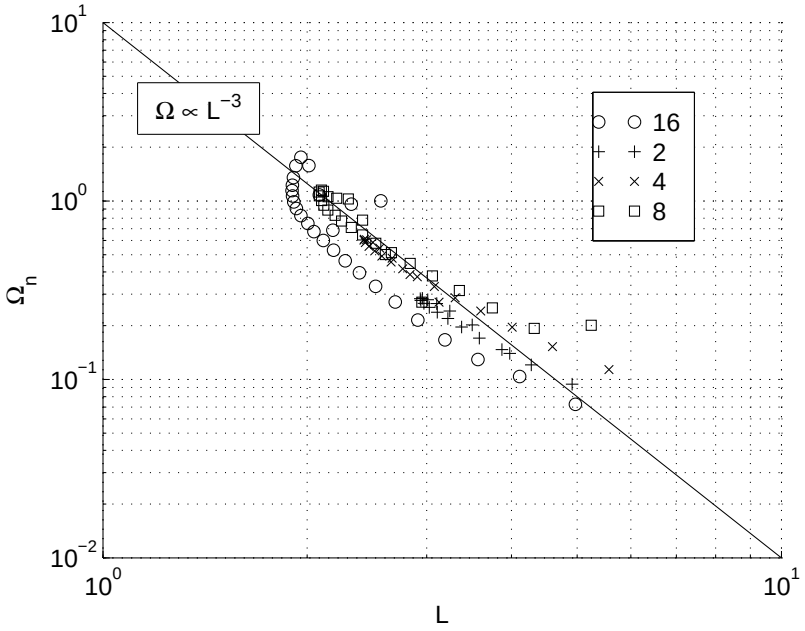

Figure 3.13: Natural frequency as a function of standoff distance.

or set of length scales. Figure 3.13 shows the natural frequency, plotted against the standoff distance, L, for various Lewis numbers. It is clear that there is a characteristic loop that is common to all high-lewis number cases where the flame's cutoff frequency doubles back on itself. Moreover, the points naturally form about a $\Omega_n \propto L^-3$ line.

A note on grid sensitivity To characterize the effect on the system's dependence on the grid density, the total transfer function was calculated at the same operating conditions with a variety of grids. In all tests, the grid was evenly spaced over a domain roughly twice the length of the standoff distance. The results are plotted in Figure 3.14.

All low-frequency points are reproduced with satisfactory precision at low frequencies. However, the responses diverge at high frequencies. Starting with the highest number of nodes and progressing to the lower, the transfer function deviates from the others at lower and lower frequencies. Figure 3.14 indicates that with a 40-node grid, accuracy can be expected

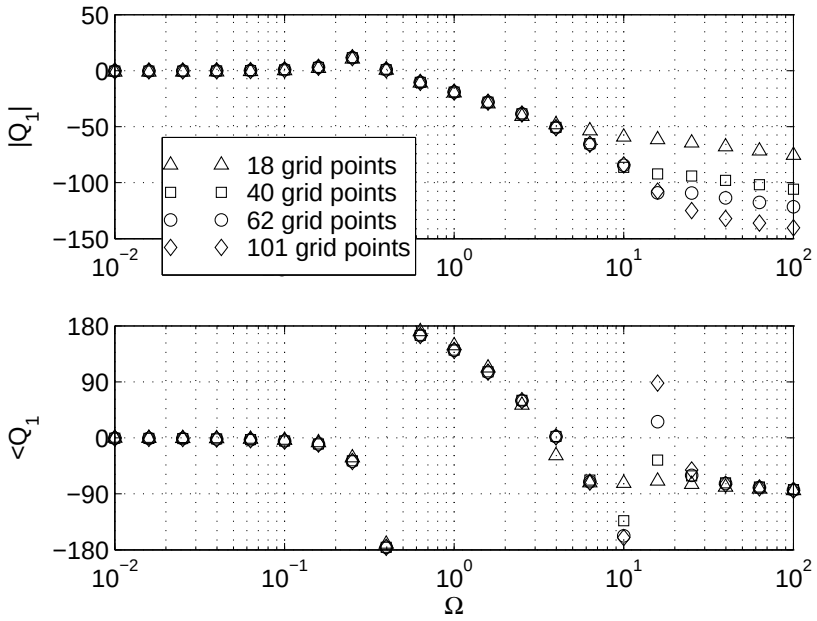

Figure 3.14: Heat release rate transfer functions for various grids at $Le = 2$, $U = 0.7$.

up to -80dB or 10^{-4}.

The frequency at which the model deviates from more accurate grids is found to scale with the residence time in a single element,

$$\Omega_g \propto \frac{U}{h}. \tag{3.67}$$

Thus, exactly how much accuracy can be gained by adding elements into the mesh can be estimated by first predicting the frequency at which the transfer function will be inaccurate and then extrapolating the transfer function's amplitude to that frequency.

All of the calculations presented in this work were performed on a mono-spaced grid in a domain such that the flame is situated as close to the center as possible, so to emulate the conditions under which the grid study was performed. All results were produced with either 100 or 150-element grids.

3.3 Analytical solution

3.3.1 Laminar ignition model

The consistent obstacle to a closed-form solution to these equations is the reaction rate, R. To be as physically accurate as possible, one uses an Arrhenius form,

$$R = A \exp\left(-\frac{\tau_a}{\tau_0 + \tau}\right)(1 - c). \tag{3.68}$$

Here, τ_{in} and τ_a are the inlet and activation temperature respectively, normalized by ΔT.

Though asymptotic solutions to the resulting static system exist, it is possible to glean greater insight from a simpler model. For practical combustion problems, even the adiabatic flame temperature is an order of magnitude below the activation temperature, τ_a, so that the term $\exp(-\tau_a/\tau)$ simply appears very close to zero at low temperatures and then increases sharply at some characteristic ignition temperature. In unity lewis number systems, the ignition model has been shown to give excellent agreement in burning rate predictions[48]. If $h(x)$ is the heaviside function, the ignition model is given by

$$R = A\,(1 - c) \cdot h(\tau - \tau_{ig}) = A\,(1 - c) \begin{cases} 0 & \tau < \tau_{ig} \\ 1 & \tau \geq \tau_{ig} \end{cases}. \tag{3.69}$$

Note that both the ignition model and the Arrhenius models have coefficients, A. These are simply factors to enforce the scaling for t_r. Recall that A must be chosen such that ${t_r}^{-1} R = -\zeta_f / \Delta Y_f$, when t_r is obtained from the flamespeed definition, $S_L = \sqrt{\alpha / t_r}$.

3.3.2 Static solution

The ignition model lends itself to an analytical solution since it quantifies the piecewise simplification that is already typical for laminar flames; that the flame be divided into two regions: a preheat region wherein there is negligible chemical reaction, and a narrow reaction region wherein reaction rate occurs in balance with the transfer of heat to the preheat region. This all hinges on the observation that τ will increase monotonically and will therefore cross τ_{ig} only once. This point in space is $\hat{x} = L$, where L is referred to as the standoff distance.

Though this procedure vastly simplifies the problem, it increases the number of equations to be solved from two to four. Without the addition of new boundary conditions, there is a closure problem. These can be found by ensuring order-0 and order-1 continuity at the interface. By integrating Equation 3.14a for some small distance, $\delta\hat{x}$, on either side of L, we obtain the jump conditions,

$$\lim_{\delta\hat{x}\to 0}\int_{L-\delta\hat{x}}^{L+\delta\hat{x}}\int_0^{\eta}\left\{Uc_0' - \frac{1}{Le}c_0'' = R(c_0,\tau_0)\right\}\mathrm{d}\hat{x}\mathrm{d}\eta$$

$$\frac{1}{Le}\left[c_0\right]_{L^-}^{L^+} = 0 \tag{3.70a}$$

$$\lim_{\delta\hat{x}\to 0}\int_{L-\delta\hat{x}}^{L+\delta\hat{x}}\left\{Uc_0' - \frac{1}{Le}c_0'' = R(c_0,\tau_0)\right\}\mathrm{d}\hat{x}$$

$$\frac{1}{Le}\left[c_0'\right]_{L^-}^{L^+} = 0. \tag{3.70b}$$

Identical integrals for the energy equation yield

$$\left[\tau_0\right]_{L^-}^{L^+} = 0 \tag{3.70c}$$

$$\left[\tau_0'\right]_{L^-}^{L^+} = 0 \tag{3.70d}$$

Therefore, the solution and its derivative are continuous, providing four additional boundary

conditions. Now, with a total of eight boundary conditions on a system of four second-order equations, the problem is closed.

Preheat In the preheat region, where reaction rate is zero, the governing equations are

$$U c_0' - \frac{1}{Le} c_0'' = 0 \tag{3.71a}$$

$$U \tau_0' - \tau_0'' = 0 \tag{3.71b}$$

Integrating and applying boundary conditions 3.9a and 3.9c, the preheat solution is

$$\frac{c_0}{c_L} = \frac{\exp\left(U\, Le\, \hat{x}\right) - 1}{\exp\left(U\, Le\, L\right) - 1} \tag{3.72a}$$

$$\frac{\tau_0}{\tau_{ig}} = \frac{\exp\left(U\, \hat{x}\right) - 1}{\exp\left(U\, L\right) - 1}. \tag{3.72b}$$

In these expressions, L and c_L are unknown parameters that must be obtained by matching the preheat and flame solutions at the jump conditions. As mentioned before, L is the distance from the burner to the point where combustion begins. The later, c_L, is the value of c_0 at L, and is written instead of an integration coefficient since it is a physically relevant parameter.

Flame In the flame region (which actually includes the flame and everything behind it), the governing equations are

$$U c_0' - \frac{1}{Le}\, c_0'' = A - A c_0 \tag{3.73a}$$

$$U \tau_0' - \tau_0'' = A - A c_0 \tag{3.73b}$$

The simplified reaction rate model naturally decouples the species equation from the energy equation, so it is simplest to proceed by solving it first. With boundary conditions 3.9b and 3.70a,

$$c_0 = 1 - \Delta c \exp\left(\Lambda(\hat{x} - L)\right), \tag{3.74}$$

where Δc is $1 - c_L$, and the wave number, Λ, is given by

$$\Lambda = \frac{U\,Le}{2}\left(1 - \sqrt{1 + \frac{4A}{U^2 Le}}\right). \tag{3.75}$$

Equation 3.73a naturally exhibits two wave numbers, but the downstream boundary condition 3.9b eliminates the positive one since it would grow without bound with respect to $\hat{x}$. The jump condition demands continuity with the preheat solution, which is preserved by the implicit appearance of c_L in Δc. Note that at this point both c_L and L are still unknown.

The homogeneous solution to Equation 3.73b also yields two wave numbers. One of them is positive and can be eliminated by boundary condition 3.9d, just as in the solution for c_0. The second wave number is 0, corresponding to a constant. All of the interesting behavior in τ_0 in the flame region is introduced through the particular solution. Substituting3.74, and applying boundary conditions 3.9d and 3.70c, we obtain

$$\tau_0 = \tau_{ig} + \Delta\tau\left[1 - \exp\left(\Lambda(\hat{x} - L)\right)\right], \tag{3.76}$$

where

$$\Delta\tau = \frac{A}{\Lambda^2 - U\Lambda}\,\Delta c = \beta\,\Delta c. \tag{3.77}$$

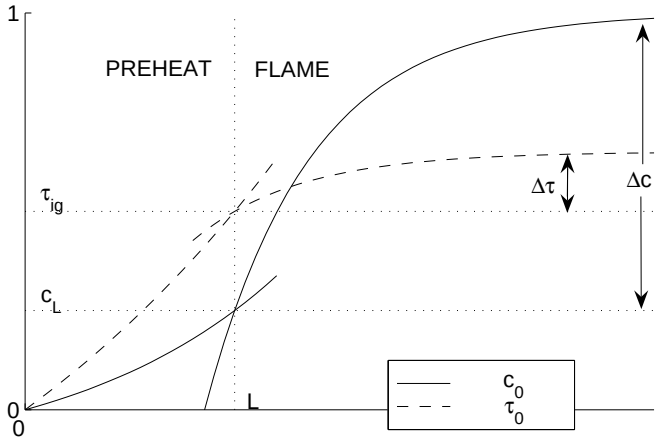

Figure 3.15: Boundary matching problem and parameters depicted.

Similar to Δc, $\Delta\tau$ is defined to be the rise in dimensionless temperature from the flame inlet to the back end of the flame. Unlike c_0, τ_0 does not approach 1 asymptotically. Because the reaction rate decays as $c \to 1$ and is independent of τ, the system naturally demands that $c \to 1$ regardless of lewis number or other transport affects, while there is no such driving force to regulate the temperature. Instead, $\Delta\tau$ is related to Δc by a constant, β, which indicates the temperature rise per unit fuel expended; also taking into account convection and diffusion.

Having solved for the shapes of the curves in the preheat and flame regions and enforced that the values match at the interface, it remains to determine the values for L and c_L that also match the slopes at the interface. Figure 3.15 depicts the matching problem and the relevant parameters. We will show that most if not all of the flame properties can be related to Δc – the fraction of fuel left to be burned at the point when the flame ignites.

Evaluating the derivatives of Equations 3.72a, 3.72b, 3.74, and 3.76 and asserting jump

conditions 3.70b and 3.70d yields

$$(1 - \Delta c)U\, Le\, n(U\, Le\, L) = -\Delta c\, \Lambda \tag{3.78}$$

$$\tau_{ig} U\, n(U\, L) = -\beta\, \Delta c\, \Lambda. \tag{3.79}$$

when the function, n, appears naturally from differentiating the preheat solutions and is defined as

$$n(s) = \frac{\exp(s)}{\exp(s) - 1}. \tag{3.80}$$

Liftoff At all stable operating conditions, the flame rests at some equilibrium standoff distance, L, where the heat lost to the burner is precisely sufficient to reduce the flame speed to match the velocity of the incoming mixture. At operating conditions where $L \to \infty$, the flame is said to have "lifted off". This consistently occurs when the fluid velocity equals or exceeds the adiabatic flame speed, but we will see that it can also happen when $U = 0$.

The reaction rate coefficient was originally implicitly defined with this behavior in mind, so that the non-dimensional velocity is unity when the incoming fluid is equal to the flame speed. Thus, we now use the fact that liftoff must occur when $U = 1$ to derive an explicit definition for A. Since the function $n(s) \to 1$ when $s \to \infty$, when $U = 1$, Equations 3.78 and 3.79 become

$$(1 - \Delta c)\, Le = -\Delta c\, \Lambda \tag{3.81}$$

$$\tau_{ig} = -\beta\, \Delta c\, \Lambda. \tag{3.82}$$

Here, A is introduced implicitly through Λ in Equation 3.75 and β in Equation 3.77. After

some manipulation, we eliminate the unknown, Δc, and arrive at

$$A = \frac{Le}{4}\left[\left(1 + \frac{2\alpha}{Le}\right)^2 - 1\right], \tag{3.83}$$

where

$$\alpha = \frac{\tau_{ig}}{1 - \tau_{ig}}. \tag{3.84}$$

Large Lewis Numbers Since there is no exact solution to Equations 3.78 and 3.79, it becomes necessary to make some approximations in order to complete the solution. There are extremely empowering simplifications to be made with large and small Lewis numbers with acceptable impact on the solution's accuracy. In the case of large Lewis numbers, the quantity $U\,Le\,L$ is large compared to $U\,L$, encouraging the assumption that $n(U\,Le\,L) \approx 1$ in Equation 3.78. This is equivalent to assuming that the diffusion of species through the burner (at $\hat{x} = 0$) is negligible compared with the convection and diffusion of species at the flame interface.

Therefore, after some manipulation, Δc can be written explicitly in terms of the operating conditions,

$$\Delta c = \frac{-U\Lambda}{A}. \tag{3.85}$$

$$L = \frac{1}{U}\ln\left(\frac{1}{1 + \frac{U\tau_{ig}}{\Lambda\beta\Delta c}}\right) \tag{3.86}$$

The results in Equation 3.85 can also be produced by integrating Equation 3.14a and enforcing that $c_0'(0) = 0$.

Small Lewis Numbers When Lewis numbers are smaller than 1, the appearance of $1/Le$ in Equation 3.14a makes diffusion dominate the other modes of transport. Therefore, the assumption that $c'' = 0$ in the preheat region becomes quite good. Therefore, the preheat solution in Equation 3.72a is well approximated by

$$c_0 = c_L \frac{\hat{x}}{L}. \tag{3.87}$$

As a result, Equation 3.78 can be rewritten as

$$\frac{1 - \Delta c}{L} = -\Delta c \Lambda. \tag{3.88}$$

This is identical to expanding n in Equation 3.78 about $Le = 0$.

There is a similar estimate for τ, though less accurate, that gives reasonable accuracy when $Le < 1$. If

$$\tau_0 = \tau_{ig} \frac{\hat{x}}{L}, \tag{3.89}$$

then Equation 3.79 reduces to

$$\frac{\tau_{ig}}{L} = -\beta \Delta c \Lambda. \tag{3.90}$$

Solving Equations 3.88 and 3.90, one obtains the following low-Lewis-number estimates for Δc and L.

$$\Delta c = 1 - \frac{\tau_{ig}}{\beta} \tag{3.91}$$

$$L = -\frac{1}{\Lambda} \left(\frac{\tau_{ig}/\beta}{1 - \tau_{ig}/\beta} \right) \tag{3.92}$$

Static Heat Release Rate Given the solution for c_0 in the flame in Equation 3.74, the steady heat release defined in Equation 3.17 is

$$q_0 = \frac{A\,\Delta c}{-\Lambda}. \tag{3.93}$$

For large Lewis numbers, $\Delta c \approx -U\Lambda/A$, so that $q_0 \approx U$. This result is very intuitive since assuming large Lewis numbers trivializes the diffusion of species. Thus, the only mechanism for delivering species is via convection. Given complete combustion, the heat release rate will be precisely proportional to the rate at which the mixture is delivered to the flame until the flame speed is reached and $q_0 = 1$.

By contrast, for small Lewis numbers, the heat release rate is actually enhanced by the diffusion of fresh reactants through the burner, so that the heat release rate vastly exceeds that of the adiabatic flame. This is possible since the adiabatic flame is infinitely far from the burner, where fast diffusion of species will affect the internal flame structure only. As a source of reactants (the burner) enters the preheat region, the diffusion of species outpaces the diffusion of energy and the burning rate increases accordingly.

Discussion The quality of the estimates are depicted by how well predictions for Δc and L agree with a numerical solution to Equations 3.78 and 3.79. The choice of these two parameters is not arbitrary as understanding their behaviors serves several ends. Apart from being the only remaining unknown parameters in the piecewise solution as formulated above, the reaction progress change across the flame, Δc, has a prominent place in Equations 3.72, 3.74 and 3.76, affording it immense impact on the internal flame structure. Perhaps most compelling, the standoff distance, L, is perhaps the easiest parameter to observe in a physical flame to validate the model.

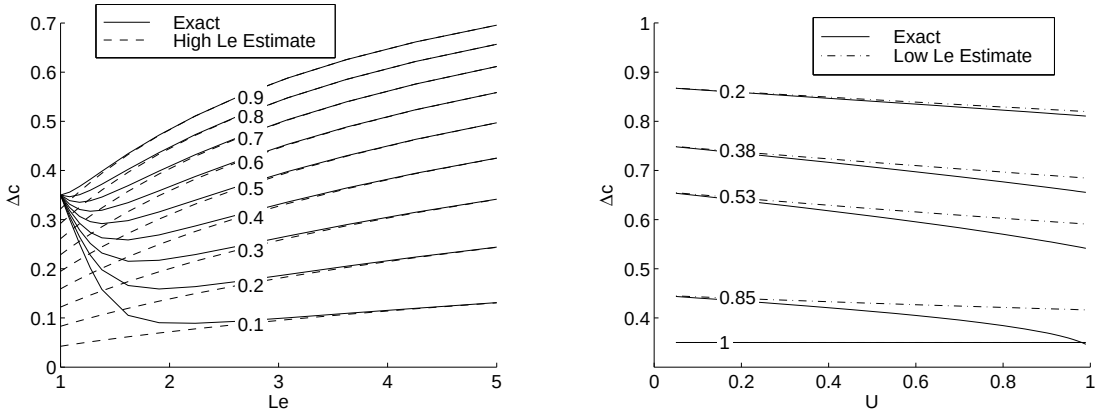

(a) (b)

Figure 3.16: Estimated and exact Δc as a function of Le for various values of U. (a) shows the exact and estimate solutions for large Lewis numbers. (b) shows the same plot for small Lewis numbers.

Figure 3.16 shows Δc plotted against U for various Lewis numbers. When Le is roughly greater than 2, Figure 3.16(a) shows excellent agreement between the high-Le approximation and the exact solution. The high-Le estimate has more trouble predicting the solution at low velocities since as $U \rightarrow 0$, the assumption that the quantity $U\,Le\,L$ is large becomes weaker. Similarly, Figure 3.16(b) shows the low-Le approximation does quite well when Le is below roughly 0.4. The low-Le approximation does poorly at high velocities since as L lengthens, though the fidelity of the reaction progress estimate in Equation 3.87 holds up, the estimate for the preheat temperature in Equation 3.89 becomes quite poor. Were one to accept the added complication of expanding Equation 3.79 to two or more terms, there might be much better agreement over a broader range of U and Le. However, the accuracy presented here is already acceptable to describe the physics at work.

Figure 3.17 shows the high-Le estimate and numerical solutions for standoff distance, as a function of Le for various values of U. For clarity, the results are divided into high- and low-velocity regions. Again, there is excellent agreement above Lewis numbers of 2, and

especially so at high velocities.

It is interesting that for $Le > 1$, $L \to \infty$ not only when U approaches the flame speed, but also as U approaches 0. This can be explained by considering the transport phenomena at work. At any given operating condition, there are six terms in Equations 3.14a, representing a balance of six transport and production mechanisms; diffusion of energy and species, convection of energy and species, and the "source" of energy and species due to chemical reaction. When Le becomes large, the diffusion of species becomes negligible and convection is the only mechanism by which fresh reactants are delivered to the flame. As velocity also approaches zero, the reaction rate *must* also approach zero in order to balance the species equation. The standoff distance becomes relevant when one considers that in the energy equation, the thermal diffusion term is left alone as the convective and reactive terms both approach zero exactly as they do in the species equation. The effect is that thermal diffusion at the burner must also approach zero; which can only happen if the flame (however weak) is infinitely far away.

Of course, when $Le \leq 1$, this behavior no longer occurs. Molecular diffusion catches up with the heat loss to the burner, and a weak flame can theoretically be sustained even at infinitesimal fluid velocities. Figure 3.18 shows the transition in the standoff distance behavior with respect to U over a wide selection of Lewis numbers.

Finally, Figure 3.19 shows the exact and estimate heat release rates plotted against velocity for various Lewis numbers. As shown in the primary figure, solutions at large Lewis numbers converge to the estimate, $q_0 = U$, so that when $Le > 2$, the curves are indistinguishable on these axes.

The small Lewis number solutions shown in the embedded plot are comparatively less sensitive to velocity since diffusion is the primary contributor to the heat release rate. When

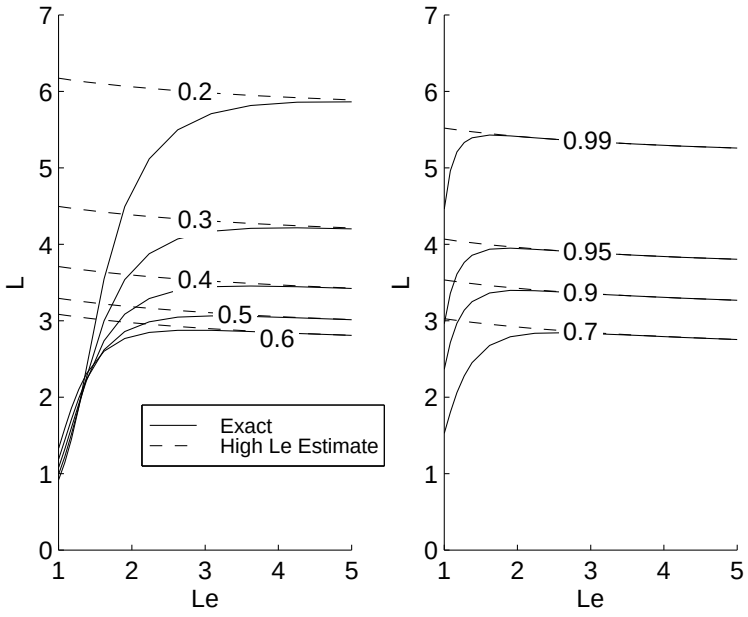

(a)

(b)

Figure 3.17: Estimated and exact L as a function of Le for various values of U. (a) Shows the liftoff at low velocities. (b) Shows the liftoff at high velocities.

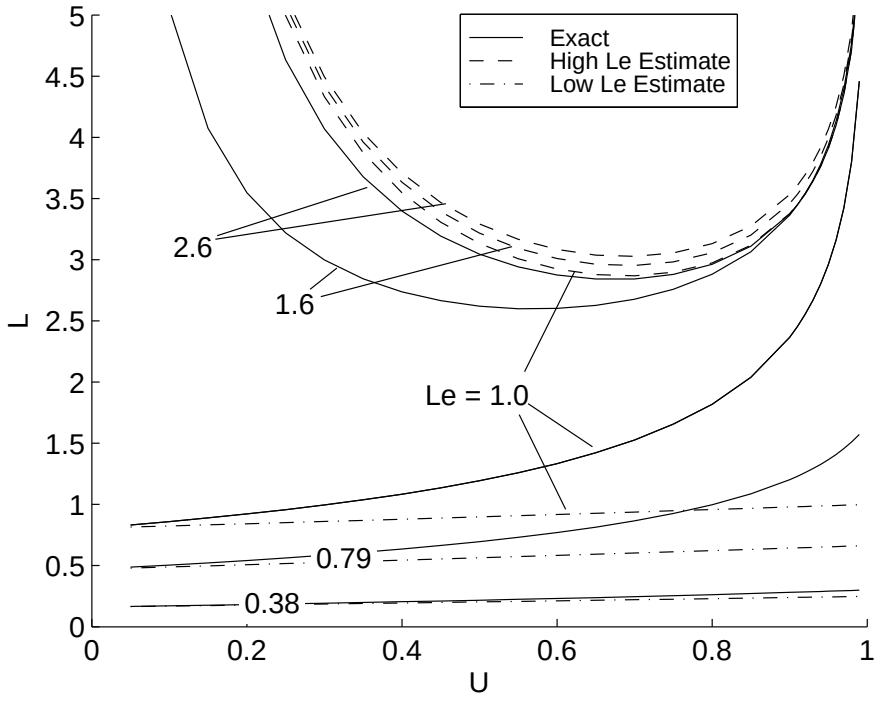

Figure 3.18: Low-Le and high-Le estimates and the exact solution for L as a function of U for selected values of Le.

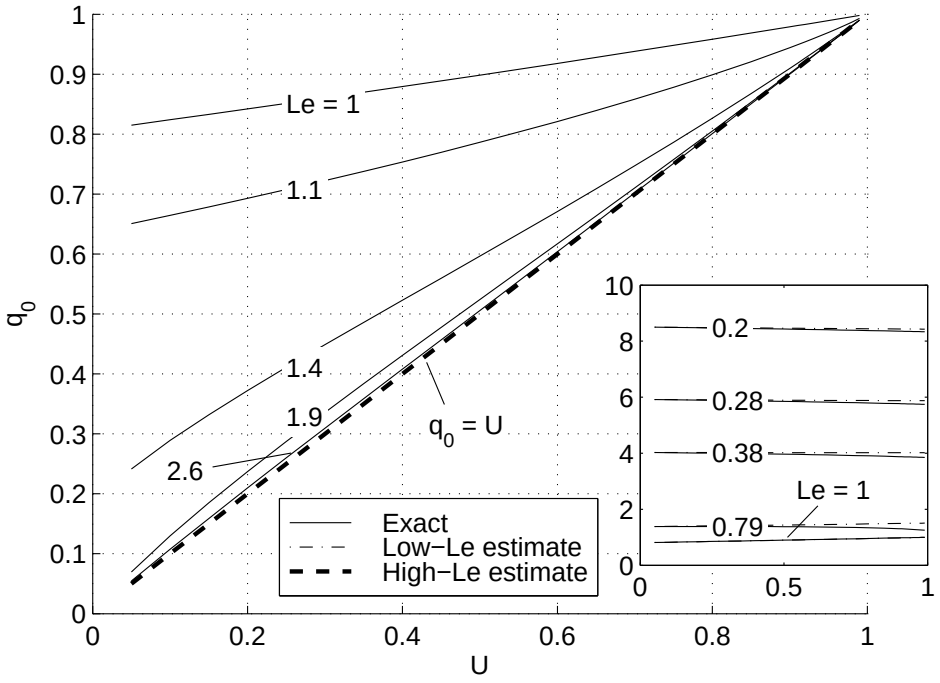

Figure 3.19: Exact and estimate heat release rates for high and low Lewis numbers.

$Le < 0.5$, the heat release rate is, in fact, well estimated by a constant. When increasing velocity does have an appreciable effect, it counter-intuitively reduces the heat release rate. Though increasing velocity also increases the convection of fresh reactants, if pushes the flame downstream and lessens the diffusion of reactants more drastically, thus affecting a net decrease in heat release rate.

3.3.3 Dynamic solution

The dynamic equations can be partitioned into preheat and flame solutions just as were the static equations.

There is, however, an additional complication that appears in the dynamic equations. Equa-

tions 3.15 have terms containing the partial derivatives of reaction rate, R_τ and R_c. Using the definition of R in Equation 3.69, they are

$$R_\tau = A\,\delta(\tau_0 - \tau_{ig})(1 - c_0) \tag{3.94}$$

$$R_c = -A\,h(\tau_0 - \tau_{ig}). \tag{3.95}$$

The impulse function, δ appears due to the discontinuity in R at the ignition temperature. Though that means that R is no longer well defined, it is still integrable. Therefore, we capture the discontinuity using the same approach to the jump conditions as before.

$$\begin{aligned}
&\lim_{\delta\hat{x}\to 0}\int_{L-\delta\hat{x}}^{L+\delta\hat{x}}\int_0^{\eta}\left\{(j\Omega - R_c)\,c_1 + Uc_1' - \frac{1}{Le}c_1'' = R_\tau\tau_1 - c_0''\right\}\mathrm{d}\hat{x}\mathrm{d}\eta \\
&\frac{1}{Le}\left[c_1\right]_{L^-}^{L^+} = 0
\end{aligned} \tag{3.96a}$$

When evaluating the jump condition for c_1', however, the impulse function introduces the first right-hand-side integral that is nonzero. In order to evaluate the integral of the impulse function, we apply a change of variables thusly:

$$\begin{aligned}
&\lim_{\delta\hat{x}\to 0}\int_{L-\delta\hat{x}}^{L+\delta\hat{x}}\left\{(j\Omega - R_c)\,c_1 + Uc_1' - \frac{1}{Le}c_1'' = R_\tau\tau_1 - c_0''\right\}\mathrm{d}\hat{x} \\
&\frac{1}{Le}\left[c_1'\right]_{L^-}^{L^+} = -A\int_{L^-}^{L^+}\delta(\tau_0 - \tau_{ig})\,(1 - c_0)\,\mathrm{d}\hat{x} \\
&\qquad = -A\int_{{\tau_{ig}}^-}^{{\tau_{ig}}^+}\frac{\delta(\tau_0 - \tau_{ig})}{\tau_0'}\,(1 - c_0)\,\mathrm{d}\tau_0 \\
&\qquad = \frac{-A\,\Delta c}{\tau_0'(L)}.
\end{aligned} \tag{3.96b}$$

Following identical procedures with the energy equation, the jump conditions for τ_1 are

$$[\tau_1]_{L^-}^{L^+} = 0 \tag{3.96c}$$

$$[\tau_1']_{L^-}^{L^+} = \frac{-A\,\Delta c}{\tau_0'(L)}. \tag{3.96d}$$

Preheat In the preheat region, the dynamic equations are

$$j\Omega c_1 + U c_1' - \frac{1}{Le} c_1'' = -c_0' \tag{3.97a}$$

$$j\Omega \tau_1 + U \tau_1' - \tau_1'' = -\tau_0'. \tag{3.97b}$$

The source terms on the right hand sides come from the excitation term in the total velocity, $u = U + \epsilon \exp(j\hat{t})$. This term can be satisfied with a particular solution superimposed with a homogeneous solution in the usual way. Since there are two second-order equations, there are four wave numbers,

$$k^{\pm} = \frac{U\,Le}{2}\left(1 \pm \sqrt{1 + \frac{4j\Omega}{U^2 Le}}\right) \tag{3.98}$$

$$d^{\pm} = \frac{U}{2}\left(1 \pm \sqrt{1 + \frac{4j\Omega}{U^2}}\right), \tag{3.99}$$

and the total solution takes the form

$$c_1 = p^+ \exp\left(k^+ (\hat{x} - L)\right) + p^- \exp\left(k^- (\hat{x} - L)\right) - \frac{c_0'}{j\Omega} \tag{3.100a}$$

$$\tau_1 = b^+ \exp\left(d^+ (\hat{x} - L)\right) + b^- \exp\left(d^- (\hat{x} - L)\right) - \frac{\tau_0'}{j\Omega}. \tag{3.100b}$$

Note that the spacial derivatives of the steady solutions, c_0' and τ_0', appear as particular solutions to their respective dynamic equations.

Flame In the flame region, the dynamic equations are

$$(j\Omega + A)\, c_1 + U c_1' - \frac{1}{Le} c_1'' = -c_0' \tag{3.101a}$$

$$j\Omega \tau_1 + U \tau_1' - \tau_1'' = -A c_1 - \tau_0'. \tag{3.101b}$$

The species equation in the flame is quite similar to the species equation in the preheat region, except for the appearance of the reaction rate coefficient, A. The energy equation, however, contains the same term, which couples the two equations. Since τ_1 does not appear in the species equation, c_1 can be solved independently, and then lumped with the particular solution.

Again, there are four wave numbers, but boundary conditions 3.9b and 3.9d imply that those with positive real components have trivial coefficients. The remaining wave numbers are

$$K = \frac{U\, Le}{2}\left(1 - \sqrt{1 + \frac{4(j\Omega + A)}{U^2 Le}}\right) \tag{3.102}$$

$$D = \frac{U}{2}\left(1 - \sqrt{1 + \frac{4j\Omega}{U^2}}\right). \tag{3.103}$$

Thus, the solution in the flame region takes the form

$$c_1 = P \exp\left(K\left(\hat{x} - L\right)\right) - \frac{c_0'}{j\Omega} \tag{3.104a}$$

$$\tau_1 = B \exp\left(D\left(\hat{x} - L\right)\right) + PG \exp\left(K\left(\hat{x} - L\right)\right) - \frac{\tau_0'}{j\Omega}. \tag{3.104b}$$

Notice that c_0' and τ_0' appear as particular solutions just as before. The term, $PG \exp\left(K\left(\hat{x} - L\right)\right)$ is an additional term to the particular solution for τ_1 in response to the appearance of c_1 in

the energy equation. In order to satisfy the system,

$$G = \frac{-A}{j\Omega + UK - K^2}. \tag{3.105}$$

Closure The coefficients, b^+, b^-, p^+, p^-, B, and P, are determined by satisfying the two inlet (Equations 3.9a and 3.9c) and four interfacial jump conditions (Equations 3.96a, 3.96c, 3.96b, and 3.96d). Recall that the downstream boundary conditions are implicitly satisfied by rejecting the downstream wave numbers that grow without bound.

$$p^+ \exp(-k^+ L) + p^- \exp(-k^- L) = \frac{c_0'(0)}{j\Omega} \tag{3.106}$$

$$b^+ \exp(-d^+ L) + b^- \exp(-d^- L) = \frac{\tau_0'(0)}{j\Omega} \tag{3.107}$$

$$P - p^+ - p^- = 0 \tag{3.108}$$

$$B + GP - b^+ - b^- = 0 \tag{3.109}$$

$$\begin{aligned} PK - p^+k^+ - p^- + \frac{c_0''(L^+)}{j\Omega} - \frac{c_0''(L^-)}{j\Omega} \ldots \\ = \frac{-LeA\Delta c}{\tau_0'(L)} \left(b^+ + b^- - \frac{\tau_0'(L)}{j\Omega} \right) \end{aligned} \tag{3.110}$$

$$\begin{aligned} BD + PGK - b^+d^+ - b^-d^- + \frac{\tau_0''(L^+)}{j\Omega} - \frac{\tau_0''(L^-)}{j\Omega} \ldots \\ = \frac{-A\Delta c}{\tau_0'(L)} \left(b^+ + b^- - \frac{\tau_0'(L)}{j\Omega} \right) \end{aligned} \tag{3.111}$$

In writing these constraints, we have implicitly asserted the continuity of the first and second derivatives of the static solutions by allowing certain simplifying cancellations. Notice, however, the appearance of c_0'' and τ_0'' evaluated on either side of the jump condition. These terms do not cancel since there is no continuity constraint beyond the first derivative. However, if

we substitute the static solutions, after some manipulation, we arrive at the conclusion that

$$\frac{c_0''(L^+)}{j\Omega} - \frac{c_0''(L^-)}{j\Omega} = \frac{Le\, A\Delta c}{j\Omega} \tag{3.112a}$$

$$\frac{\tau_0''(L^+)}{j\Omega} - \frac{\tau_0''(L^-)}{j\Omega} = \frac{A\Delta c}{j\Omega}, \tag{3.112b}$$

so that the system can be expressed in the form

$$\mathbf{M} \cdot \begin{Bmatrix} p^+ \\ p^- \\ P \\ b^+ \\ b^- \\ B \end{Bmatrix} = \begin{Bmatrix} c_0'(0)\,/\,j\Omega \\ \tau_0'(0)\,/\,j\Omega \\ 0 \\ 0 \\ 0 \\ 0 \end{Bmatrix} \tag{3.113}$$

when the matrix, $\mathbf{M}$, is given by

$$\mathbf{M} = \ldots$$

$$\begin{Bmatrix} \exp(-k^+L) & \exp(-k^-L) & 0 & 0 & 0 & 0 \\ 0 & 0 & 0 & \exp(-d^+L) & \exp(-d^-L) & 0 \\ -1 & -1 & 1 & 0 & 0 & 0 \\ 0 & 0 & G & -1 & -1 & 1 \\ -k^+ & -k^- & K & -Le\, J & -Le\, J & 0 \\ 0 & 0 & GK & -d^+ - J & -d^- - J & D \end{Bmatrix} \tag{3.114}$$

For brevity, the jump coefficient in Equations 3.110 and 3.111 is represented by $J = -A\Delta c/\tau_0'(L)$.

Unsteady Heat Release Rate Substituting the solution for c_1 and τ_1 from Equations 3.104a and 3.104b into the expression for q_1 in Equation 3.18, we obtain

$$\begin{aligned} q_1 &= -A\left(\frac{B+PG}{\beta\Delta c\lambda}+\frac{\Delta c}{j\Omega}\right)+A\left(\frac{P}{K}+\frac{\Delta c}{j\Omega}\right) \\ &= A\left(-\frac{B+PG}{\beta\Delta c\lambda}+\frac{P}{K}\right). \end{aligned} \tag{3.115}$$

Unfortunately, this form yields little immediate insight into the nature of the flame's dynamic response. It is interesting, however, that the $1/j\Omega$ terms appearing from the particular solutions canceled. Had it not, q_1 would be divergent at low frequencies, where q_1 and the static system's sensitivity, $\partial q_0/\partial U$ (which is seen in Figure 3.19 not to be divergent), must agree.

3.3.4 Analytical results

There are three parameters that dictate the response of dimensionless temperature, τ, and reaction progress, c, to small perturbations in velocity; the steady velocity, U, Lewis number, Le, and the frequency of excitation, Ω. Thus, for a given velocity and Lewis number, there is an eigen function for c_1 and τ_1, each respectively describing the spatial response to perturbations at that frequency. Since the system has been linearized, responses to excitations containing more than a single frequency can be solved by superimposing the individual eigen functions in proportion to and in phase with their respective frequency components in the excitation. Therefore, these eigen functions contain all the information one needs to understand the system and its behaviors.

The trouble is that each eigen function is a function on space, specific to a particular velocity, Lewis number, and frequency triplet. That leaves a four-dimensional variable space, making

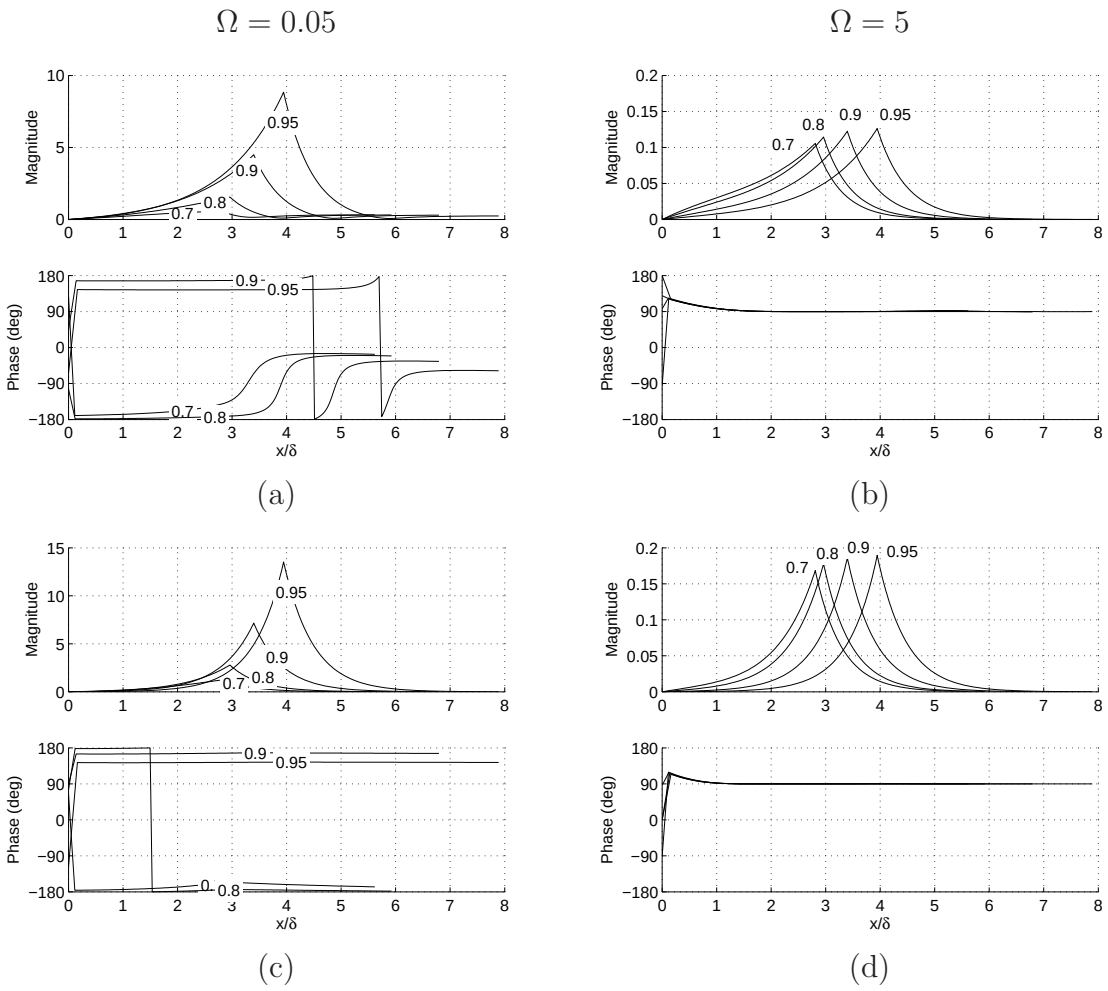

Figure 3.20: τ and c eigen functions for $Le = 2$ at high and low frequencies, and at various velocities. (a) c at $\Omega = 0.05$. (b) c at $\Omega = 5$. (c) τ at $\Omega = 0.05$. (d) τ at $\Omega = 5$.

it quite difficult to visualize the full expanse of the different responses. However, the key elements are outlined in Figures 3.20 and 3.21, by plotting the magnitude and phase of the eigen functions for several velocity conditions at a high and a low Lewis number, and at high and low frequencies. Both to reduce clutter in the plots and to better illustrate the case that will prove of greatest interest later, we elected to show only "large" velocities ($U \geq 0.7$).

High Lewis Numbers Consistent with the static behaviors showcased in Section 3.3.2, dynamic behaviors are relatively consistent with respect to Lewis numbers on the same side of unity. Figure 3.20 shows the eigen functions for τ and c at frequencies $\Omega = 0.05$ and $\Omega = 5.$ when $Le = 2$, where three features are immediately striking;

- At all high-frequency cases, the phase is nearly independent of velocity;
- The strongest difference between τ and c is found in their phases at low frequencies; and
- The low-frequency τ response does not asymptotically approach 0 as $\hat{x} \to \infty$, while the other three do.

As we detail these and more subtle phenomena, it is helpful to envision the perturbed fluid "sloshing" back and forth uniformly and ever so slightly as the bulk makes its way through the reaction region. As the fluid surges and retreats, state of the neighboring fluid that is momentarily whisked into any given point in space is indicated by the spatial derivatives, c_0' and τ_0'. Far before and long after the fluid reaches the flame, these are negligible and so the dynamic responses there mostly decay to zero. Where the reaction is quite intense and these slopes are at their maximum, the dynamic solution's magnitude peaks, and decays on either side.

That the phase is independent of velocity at high frequencies indicates that the excitation out-paces both diffusion and bulk convection, leaving only the process of accumulation and ejection of energy or species as the fluid surges and withdraws. This can also be illustrated mathematically by noting the behavior of the wave numbers in equations 3.103, 3.102, 3.99,

and 3.98,

$$\lim_{\Omega\to\infty} K = \sqrt{j\Omega\, Le} \tag{3.116}$$

$$\lim_{\Omega\to\infty} D = \sqrt{j\Omega} \tag{3.117}$$

$$\lim_{\Omega\to\infty} k^{\pm} = \pm\sqrt{j\Omega\, Le} \tag{3.118}$$

$$\lim_{\Omega\to\infty} d^{\pm} = \pm\sqrt{j\Omega}. \tag{3.119}$$

When the wave numbers no longer vary with velocity, the only remaining implicit dependencies are through the static solutions, c_0, and τ_0, and the standoff distance, L. Since none of these parameters appear in a manner that can strongly influence the phase of the coefficients when the wave numbers have constant real and imaginary components, the phase becomes independent of velocity.

At lower frequencies, there is a more sophisticated behavior to be seen. Before the flame, small increases in velocity enhance the convection of cooler unburned reactants from upstream, causing both the temperature and the reaction progress to drop. Thus, when $\hat{x} < L$, the phase in both low-frequency diagrams is constant near 180 degrees, indicating a negative response.

In the flame, however, the response is quite a bit more complex. There are three processes in inherent competition; convection, diffusion, and generation from reaction. Reaction progress is the simplest to examine since, for large Lewis numbers, the diffusion of species is negligible, leaving only convection and reaction. Additionally, when Lewis numbers are large, the static solution jumps very sharply at the flame front since there is little diffusive transport to smooth out the jump condition. Thus, unsteady convection easily overpowers the unsteady reaction rate to be the dominant physical process. That is illustrated by the near constant 180 degree phases in Figure 3.20, plot *c*. Therefore, increasing velocity convects fresh reactants

downstream, reducing the reaction progress globally.

Temperature, on the other hand, has a more mild response to unsteady convection owing to smoothing effects caused by diffusion, evidenced by the lower amplitudes exhibited by τ. As a result, convection is forced to compete with the reaction within the reaction region. While the convection of cooler upstream fluid attempts to reduce the flame temperature, the corresponding delivery of unburned reactants (which we just established in the last paragraph) intensifies the reaction rate and endeavors to heat the flame. These two processes compete as the fluid progress through the flame until the reaction rate eventually wins, as evidenced by the smooth increase of phase from 180 to 0 in Figure 3.20. Thus, a slow increase in velocity cools the front of the flame and heats the back of the flame, ultimately indicating that the flame is simply shifting backwards to its new equilibrium location.

Lastly, we have to explain why the low frequency solution for τ_1 does not appear to asymptotically approach zero, while the other three solutions do. The answer is linked with the quantity $\Delta\tau$ from the static solution. Low-frequency changes in velocity affect the heat loss to the burner and, consequently, the temperature of the exiting gases. Thus, slow changes in velocity affect corresponding changes in the downstream temperature. At high frequencies, this is no longer true since the forcing is fast enough to allow energy can accumulate and dissipate in the flame. The species, on the other hand, can *never* have downstream affects so long as the flame undergoes complete combustion.

Low Lewis Numbers The response at low Lewis numbers is much less sophisticated than that at high Lewis numbers. Figure 3.21 shows the spatial responses at various velocities when $Le = 0.5$. Though the character of the response is much less dependent on the operating conditions, and there is much less sophisticated phase behavior to be found, there are a number of behaviors from high Lewis numbers that carry over to low Lewis numbers.

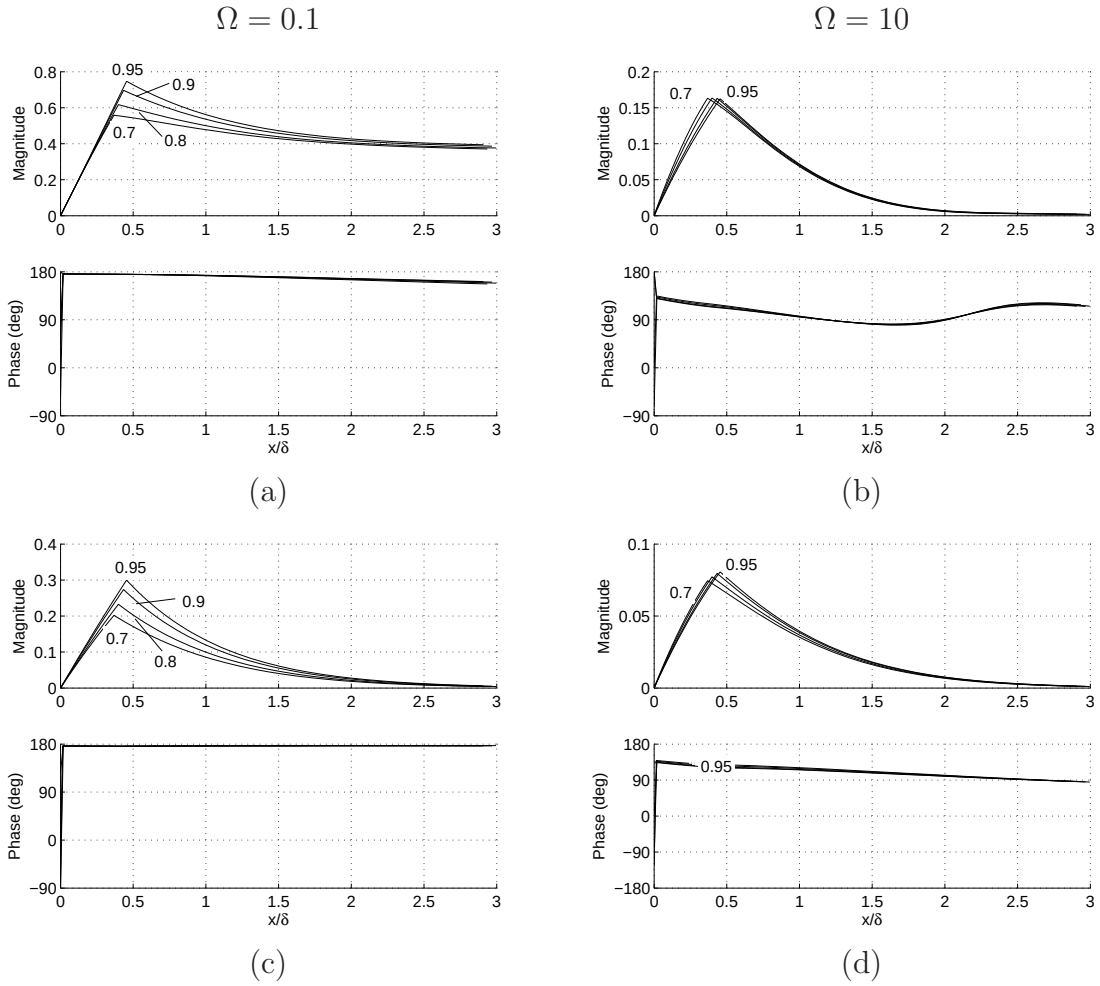

Figure 3.21: τ and c eigen functions for $Le = 0.5$ at high and low frequencies, and at various velocities. (a) c at $\Omega = 0.1$. (b) c at $\Omega = 10$. (c) τ at $\Omega = 0.1$. (d) τ at $\Omega = 10$.

Just as before, temperature oscillations caused by the oscillating reaction rate are convected downstream. At low Lewis numbers, however, they are significantly more intense since the thermal diffusion is too low to smooth them out.

Similarly, the near constant 180° phase observed in the c_1 response at high Lewis numbers is now exhibited by both τ and c. That indicates that at low Lewis numbers, the unsteady convection overpowers all other processes. Thus, at the acoustic velocity's peak, the enhanced convection delivers cool, unburned fuel to the flame, reducing the temperature and reaction progress.

At high frequencies, there is a steady decline in phase as the fluid progresses downstream. That corresponds to waves being convected with the flow. However, at sufficiently high frequencies, their wavelengths are small enough to be destroyed quickly by diffusion.

Frequency response While great insight is gained by examining the spatial responses, the purpose of the present study is to characterize the total heat release response. Calculated from Equation 3.18, Figures 3.22 shows several frequency response functions for the unsteady heat release rate at a constant Lewis number.

At moderate velocities, the flame exhibits a lightly damped resonance. However, as the velocity approaches the flame speed, the response is more heavily damped and at lower frequencies. Though the curves are omitted for clarity, this occurs as the flame lifts off at low velocities as well. Figure 3.23 shows the resonant frequency plotted against the standoff distance for various Lewis numbers.

The response at low Lewis numbers is completely different; exhibiting no resonance at any operating condition, and with more pronounced features at high frequencies. Figure 3.24 shows a plot similar to Figure 3.22, only at $Le = 0.5$.

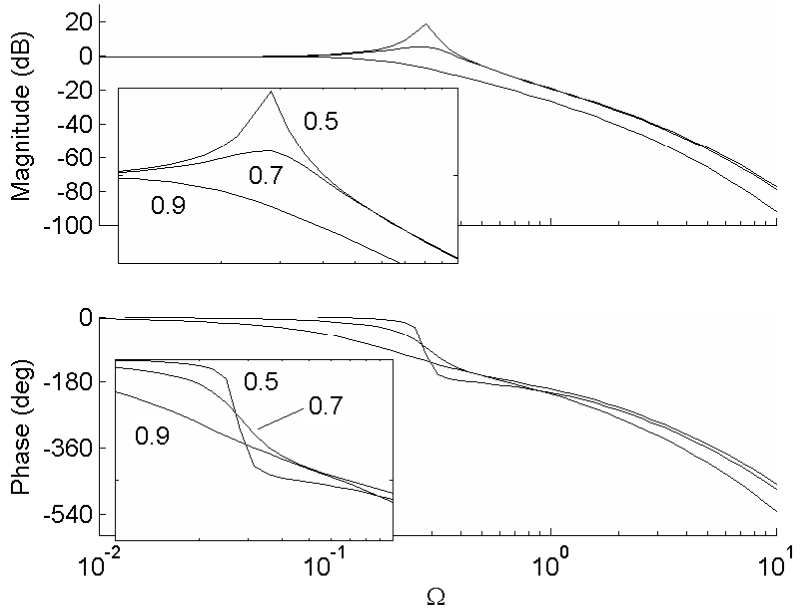

Figure 3.22: Heat release frequency response for various velocities when $Le = 2$.

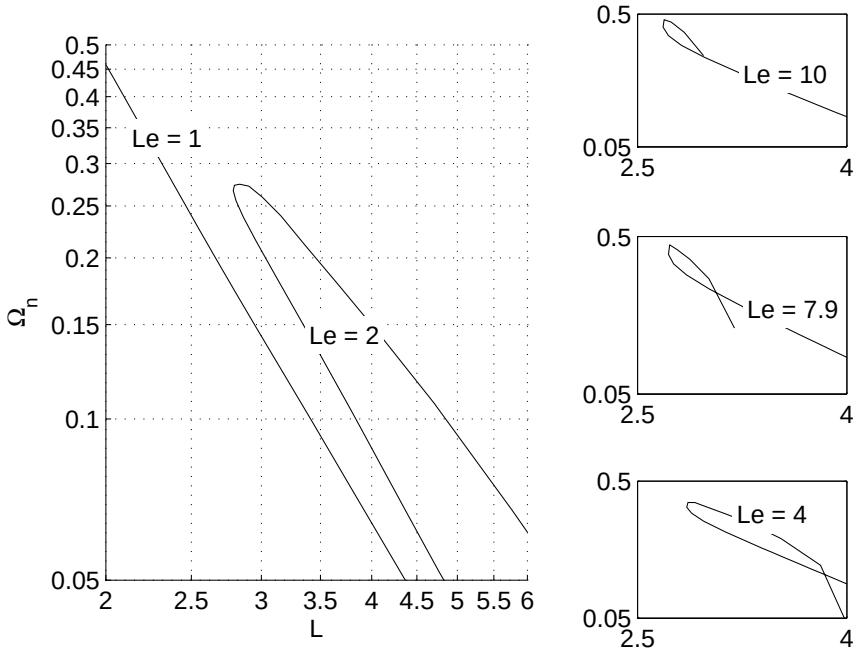

Figure 3.23: Natural frequency plotted against standoff distance for various Lewis numbers.

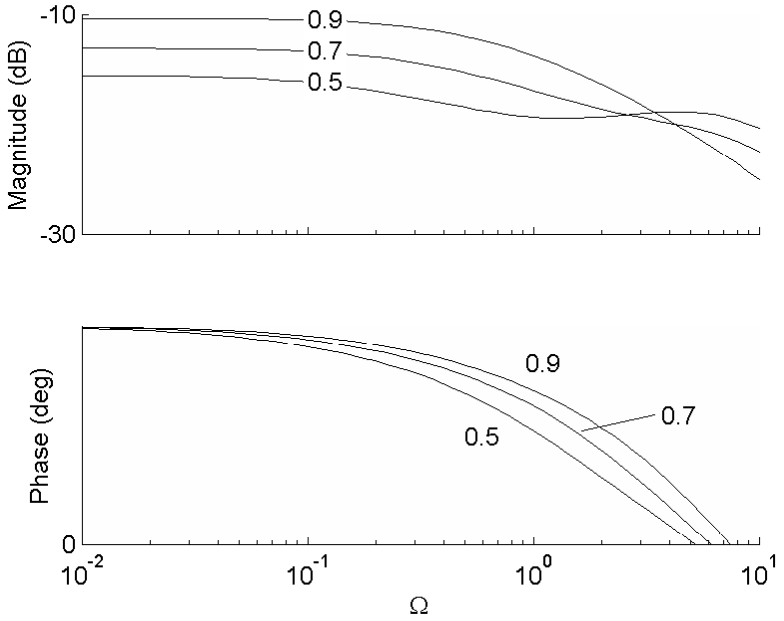

Figure 3.24: Heat release frequency response for various velocities when $Le = 2$.

A note on computing eigenvalues Regardless of the operating condition, there is some critical frequency at which the frequency response changes from its quasi-static character, and begins to exhibit an inherently unsteady response. In the case of the resonance, that is easily characterized by its natural frequency, and in the case of the over-damped behavior at low Lewis numbers, that can be characterized by a low-pass "cutoff" frequency. Regardless, any attempt to understand the affect frequency has on the flame begins and ends with the flame's eigenvalues or "poles".

Because the poles are independent of forcing, they are easiest to identify in the system's initial condition response. Consider the case that the acoustic forcing goes to zero, and

$$c = c_0 + \epsilon\, c_1 \exp(\lambda \hat{t}) + \mathcal{O}(\epsilon^2) \tag{3.120}$$

$$\tau = \tau_0 + \epsilon\, \tau_1 \exp(\lambda \hat{t}) + \mathcal{O}(\epsilon^2), \tag{3.121}$$

where ϵc_1 and $\epsilon \tau_1$ are initial conditions that decay in time. Equations 3.15 become simply

$$(\lambda - R_c)c_1 + \hat{U}\, c_1' - \frac{1}{Le}c_1'' = R_\tau\, \tau_1(\lambda - R_\tau)\tau_1 + \hat{U}\, \tau_1' - \frac{1}{Le}\tau_1'' = R_c\, c_1. \tag{3.122}$$

The significant change is that they are now homogeneous and a function of λ instead of Ω.

All of the same boundary and jump conditions apply, so the matrix, $\mathbf{M}$, is unchanged. However, because the system is now homogeneous, the coefficients are given by

$$\mathbf{M}(\lambda) \cdot \begin{Bmatrix} p^+ \\ p^- \\ P \\ b^+ \\ b^- \\ B \end{Bmatrix} = 0. \tag{3.123}$$

Therefore, the only coefficients that are non-zero in the system's unforced response correspond to λ such that

$$\det(\mathbf{M})(\lambda) = 0. \tag{3.124}$$

Unfortunately, the task of inverting Equation 3.124 is both analytically and numerically daunting. The 6×6 matrix can be simplified to a 4×4 with some work, but unfortunately without really yielding any additional insights. Numerically, the system is extremely stiff inherently multi-dimensional, and even exhibiting "false" poles.

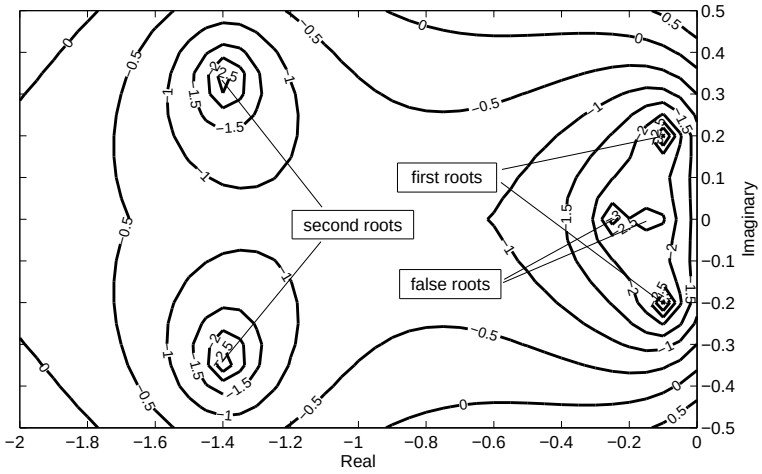

Figure 3.25: Eigenvalue error function, $\log_{10}(\det(\mathbf{M})\det(\mathbf{M})^*)$, over the λ complex plane.

Figure 3.25 is a contour plot for the error function,

$$E = \log_{10}(\det(\mathbf{M}) \cdot \det(\mathbf{M})^*), \tag{3.125}$$

as a function of λ over the complex plane. The first two pair of poles are clearly visible. However, they lie in the middle of a smooth plane with few features to guide a solver to them unless the initial guess were extremely close. Between them, there are local maxima that threaten to drive Newton solvers to infinity.

Additionally, the plane is sloped toward the real axis, where most solvers readily discover one of two false poles. The roots correspond to guesses for λ where $k^+ = k^-$ and $d^+ = d^-$. They represent points where the form of the solution is singular and not actual eigenvalues. Unfortunately they are much easier for a Newton solver to find than the authentic eigenvalues.

3.4 Experiment

3.4.1 Setup and geometry

The experimental effort focused on a honeycomb-stabilized laminar burner combusting methane. The setup is depicted in Figure 3.26. In this arrangement, premixed fuel and are are injected through the quarter-inch NPT fitting at the base of the settling chamber. The flow is homogenized by the copper beads before passing into the plenum, where it is straightened by an aluminum honeycomb, and the turbulence scale limited by a metal screen. After moving through the instrument cavity, the flow finally makes its way through the ceramic honeycomb, where it encounters the flame.

Premixing Prior to entering the settling chamber, methane and air are mixed in a T-style premixer before traveling through more than 1 meter of quarter-inch tubing. The level of turbulence in the mixer is intentionally high to guarantee excellent mixing.

Both the methane and air lines are regulated to steady pressures and their flow rates are controlled by metering valves. Their respective flow rates are measured both by rotometers and by electronic mass flow meters.

(A) Settling Chamber The settling chamber is constructed from a 122mm nominal diameter (5-inch) PVC pipe with a flanged side-branch not shown in Figure 3.26. The side branch holds an acoustic driver, which is sealed to the flange. Incoming reactants enter through the quarter-inch NPT fitting at the base of the chamber, where a diffusion plate (also not pictured) is secured over the inlet. The diffusion plate is a small aluminum plate with two 3mm (1/8-inch) diameter channels cut in a cross on its surface. The intersection is placed directly over the inlet to ensure that any momentum from the incoming mixture is

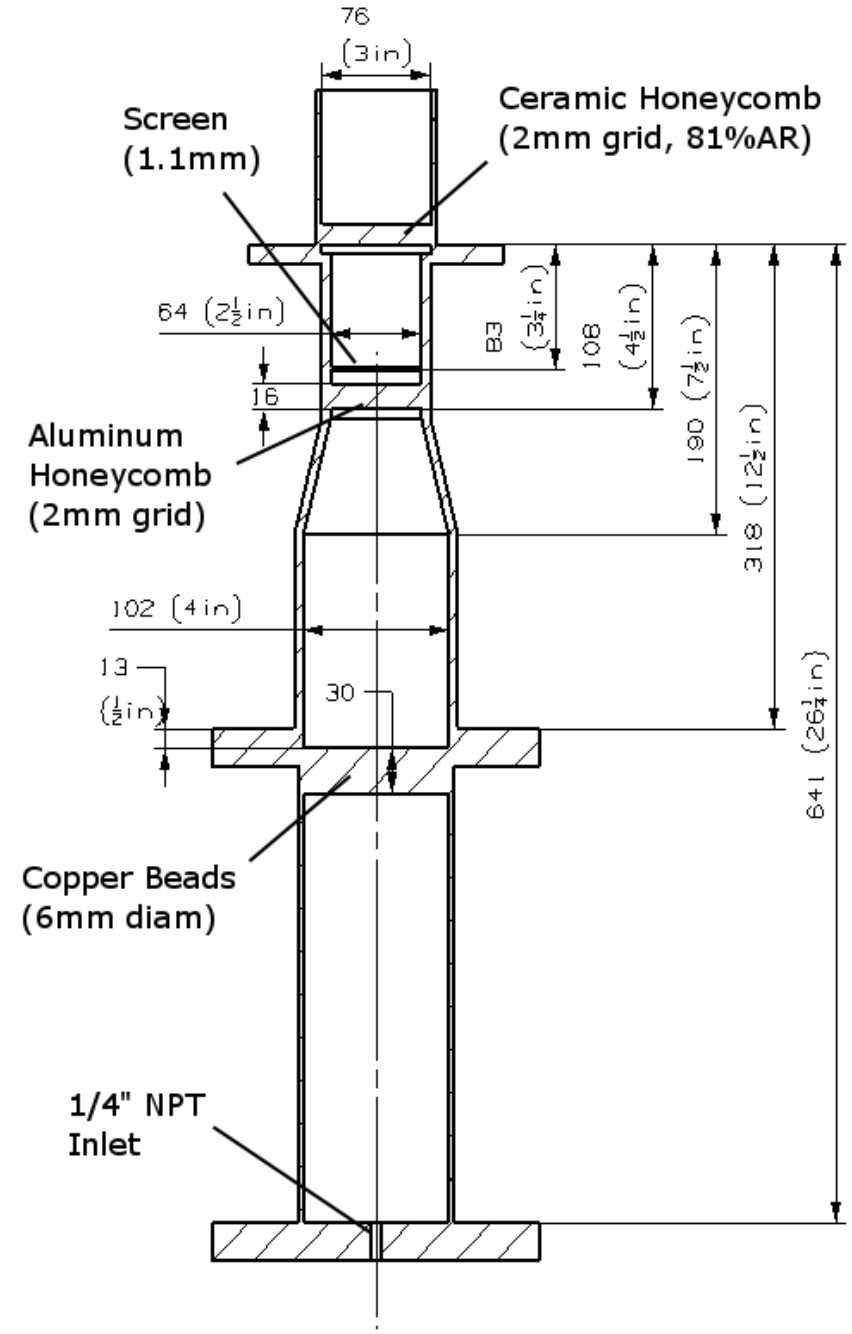

Figure 3.26: Experimental combustor diagram. The marked regions are the (A) settling chamber, (B) plenum, (C) instrument cavity, and (D) burner. All units are in millimeters unless otherwise noted.

lost.

At the top of the settling chamber, a screen is secured to the walls, forming a cup roughly 3cm tall. The cup is filled with 6mm copper beads. These serve both to ensure that the flow is homogeneous and to act as a flame arrester in the event of a flashback.

(B) Plenum The plenum is steel pipe with a bell reducer narrowing its area by 60%. At the top of the plenum, are an aluminum honeycomb with a hexagonal wall pattern and a wire screen. The honeycomb has a length-to-diameter ratio of 9 in order to straighten the flow. The screen is to destroy any surving large-scale structure in the flow.

(C) Instrument chamber There are a number of ports for instrumentation in the space between the screen and the ceramic honeycomb. A hotwire probe is located 42mm (1.75 inches) upstream of the burner surface, and a microphone 55mm (2.25 inches) upstream. The microphone is situated flush with the chamber wall. The hotwire is positioned such that the body of the probe is flush with the chamber wall and the wire is thrust roughly 10mm or so into the flow. This was done to minimize disturbance to the fluid.

(D) Burner The ceramic honeycomb used to stabilize the flame has a square grid with 1.25mm (0.051-inch) spacing and 0.12mm (0.005-inch) wall thickness, causing roughly a 19% area reduction. It is wrapped around its circumference with thermal insulation approximately 2mm thick and pressed into a quartz tube. The quartz tube is separated from the instrument chamber by an insulative ring that helps prevent leakage.

3.4.2 Velocity measurements

Before any confidence can be obtained that the flow is properly laminar, it is necessary to ensure that the flow is entirely laminar, sufficiently homogeneous, and above all steady. The highest Reynolds numbers expected were on the order of 500, so it was certainly reasonable to expect that the flow could be kept laminar.

In order to quantify the matter, the hotwire was secured in a translation stage above the burner and air was pass through the rig at flow rates resembling those of the operating conditions to be tested. The hotwire probe was passed down into the quartz tube and secured approximately 5mm above the ceramic surface. It was then translated across the diameter of the burner. A complete scan was not done.

The flow rates are quantified in three different ways; the rotometer reading, the value in kg/s as reported by the electronic meter, or the average velocity in the instrument chamber. The first two are natural choices, but the last was selected because the actual velocity at the burner cannot be directly measured using the present equipment if a flame is present. Because the ceramic is heated by the flame, it heats the incoming air, and the velocity in the ceramic can be expected to vary inversely with density. Thus, the hot velocity, U_h should be related to the cold-flow velocity, U_c in the instrument chamber by

$$\frac{U_h}{U_c} = \frac{T_h}{T_c}. \tag{3.126}$$

Measurements were taken at three cold-flow velocities; $U_c = 8cm/s$, $U_c = 6cm/s$, and $U_c = 4cm/s$. These were selected to span from the highest to the lowest range of velocities for which tests would be conducted. The anemometer was set to an overheat ratio of 1.1 in order to increase the wire's sensitivity to the small velocities.

Because there was no equipment available to calibrate the hot wire, the profile tests doubled as calibration curves. Over each scan, the voltage varied as a function of radius, so that $V = V(r)$. The velocity at each position in space is related by the unknown calibration polynomial,

$$U(r) = a_0 + \sum_{k=1}^{n} a_k V^k(r). \tag{3.127}$$

Therefore, the average velocity, which is known to be equal to U_c, is given by

$$\begin{aligned} U_c &= a_0 + \sum_{k=1}^{n} \frac{1}{\pi R^2} 2\pi \int_0^R U(r) r \mathrm{d}r \\ &= a_0 + \sum_{k=1}^{n} a_k \frac{1}{R^2} \int_{-R}^{R} V^k(r) |r| \mathrm{d}r \\ &= a_0 + a_1 \overline{V} + a_2 \overline{V^2} + \ldots . \end{aligned} \tag{3.128}$$

Since there are three velocity measurements, the coefficients can be computed for a quadratic fit, and velocities can be computed from the voltages.

Any unsteadiness in the flow was lower in amplitude than the electrical noise in the signal. There was no observable drift in the velocity over the entire span of the test. The flow was deemed sufficiently steady.

Figure 3.27 shows the results of the three tests. The excessively low velocities at the edges are points where the hotwire is directly above the insulation, and little or no flow was expected. All three curves exhibit roughly a 20% variation in velocity over the diameter, and show no blatent asymmetries. However, the nonuniformity drops to roughly 5% within a 4mm diameter.

The non-uniformities are simply the incomplete formation of Poiseuille flow in the instrument

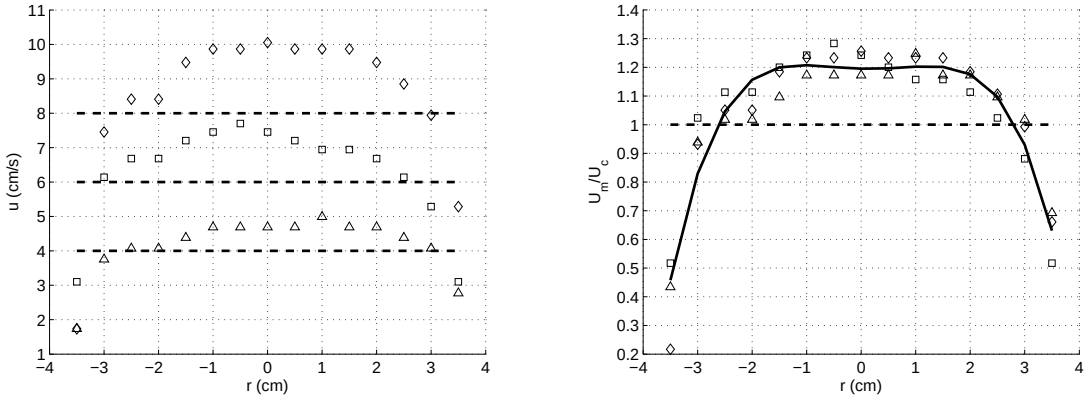

(a) (b)

Figure 3.27: Velocity profile at the burner exit. Measured 5mm above the burner for cold flow at mean velocities of 8cm/s, 6cm/s, and 4cm/s. The mean velocity for each test is marked by a horizontal dotted line. The vertical axes are (a) in absolute units and (b) a fraction of the mean.

chamber. The velocity profile could be further flattened by moving the screen and honeycomb closer to the burner, but that would come at the cost of moving the instrumentation farther from the flame, separated by obstructions that could potentially corrupt the dynamic velocity measurement.

Asymmetry can be quantified by the fourth order fit shown in Figure 3.27,

$$\frac{U}{U_c} = -0.835\left(\frac{r}{R}\right)^4 + 0.104\left(\frac{r}{R}\right)^3 + 0.184\left(\frac{r}{R}\right)^2 - 0.0173\left(\frac{r}{R}\right) + 1.195. \tag{3.129}$$

When the fit is thus normalized, the coefficients can be directly compared since each term varies on the same order of magnitude. The asymmetrical odd terms are less than one eighth the dominant fourth order term.

Since the Poiseuille flow is still largely undeveloped, the profile is fortuitously flat. However, due to the variations that are present at the edges, measurements at the center of the flow should be valued over those at the walls. When a flame is present, the same is doubly true

due to the addition of heat loss to the walls.

3.4.3 Flame position measurements

The flame position relative to the burner was measured using Schlieren imaging. Optical methods are preferable since the presence of a probe could offer a stagnation point on which the flame might stabilize and thus affect the measurement. In addition, the length scales being measured are on the order of fractions of a millimeter, presenting a severely limiting the allowable probe size.

Schlieren imaging is a method for optically detecting density gradients in a flow. A beam of collimated light is passed through a test section and projected onto a screen or focused into a camera. Density gradients in the fluid correspond to gradients in the refractive index of the fluid. Thus, as light passes through locations where intense density gradients are present, it is bent strongly in the direction of the gradient. As the gradient lessens, so does the light's deviation from the collimated path. Before the image is projected, the collimated light is focused to a point. In order to remove the scattered light, a sharp-edged, opaque object or "knife edge" is placed directly next to the focal point. Light that scattered in the direction of the knife edge will miss the focal point and will be incident on the knife. This has the effect of darkening the image where velocity gradients are present.

Figure 3.28 depicts the Schlieren setup. A mercury vapor lamp is focused to a point using a series of lenses and non-focused light was removed with an iris. The trade-off between image clarity and image brightness can be tuned by changing the diameter of the iris; larger diameters allow more light through, but result in a fuzzier image. Because the scales being measured are quite small, image clarity was consistently valued over brightness in these experiments.

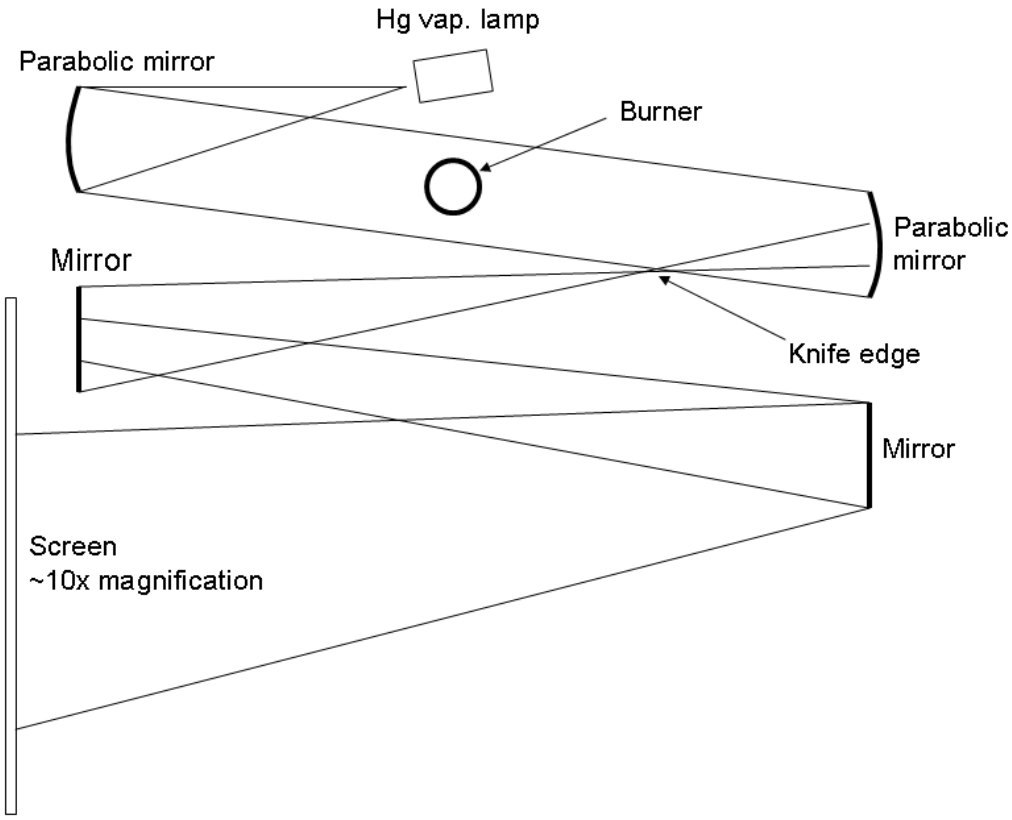

Figure 3.28: A diagram of the Schlieren imaging system used to measure the flame standoff distance.

Collimated beam The lenses and iris are adjusted such that the focal point lies coincident with the focal point of a parabolic mirror. The mirror is tilted to pass collimated light through the experiment, where an identical parabolic mirror receives the beam and focuses it again to a point.

Because the collimated light passes through the cylindrical quartz there is quite a bit of planar scattering, causing a series of undesirable fringe patterns. Along the centerline, however, where the light's path is perpendicular the surface of the quartz, light's course is unchanged. Additionally, because there is no curvature in the vertical direction, the integrity of the vertical measurement is unaffected.

Burner leveling For the measurement to be effective, it is essential that the burner surface be optically parallel to the collimated beam. Since the quartz tube is removed and replaced quite frequently, and since adjustments to any part of the optical setup require complete realignment, it is only natural to adjust the attitude of the burner rather than that of the optics.

The flange joining the settling chamber and the plenum is suspended from a support by two all-threaded rods, allowing manual adjustment of the rig's side-to-side orientation. The to-and-fro motion is controlled by a third, horizontally oriented all-thread rod touching the flange at the base of the settling chamber. The rig's weight presses it against the third rod, whose position determines the attitude of the burner surface relative to the light with very fine adjustment.

It is readily apparent to the naked eye when the burner face is exposed to the collimated beam. The tips of the honeycomb walls are lighted and shadows cast below the tips. Adjustment is easily performed by iteratively lowering the burner face until the shadows just barely overtake the wall tips.

Knife edge A knife edge is positioned beneath the focused point from the second mirror. Its height adjusted the balance between total image brightness and the contrast in the image. This choice proved quite delicate to the experiments, since either extreme rendered the image unreadable.

Additionally, an opaque frame is placed around the focal point to eliminated the light scattered by the quartz tube. Since it is no longer collimated, it deviates strongly from the focal point and is easily blocked at this point.

Magnification The lengths exhibited by the flame varied by fractions of a millimeter. Thus, the image needed to be magnified significantly to make manual measurement practical. Before arriving at the present setup, this was attempted by placing a converging lens between the second parabolic mirror and the knife edge to increase the convergence angle. Unfortunately, the spherical aberrations disrupted to focal point too much to use the knife edge. The present method uses two additional mirrors to allow the image additional distance over which to expand.

The magnification can be estimated by measuring the distance the centerline light path travels from the knife edge to the screen and dividing it by the focal length of the mirror. Because this measurement is not accurate, it was used only to position the mirrors to give approximately a 10× magnification.

An accurate magnification factor was determined by comparing a magnified shadow with the object that cast it. A piece of metal with a rectangular profile was secured next to the burner. Its thickness was measured using a pair of calipers. The corresponding shadow was then measured using calipers. The ratio of heights was found to be 9.0×, indicating that the distance method had severely over-estimated the magnification.

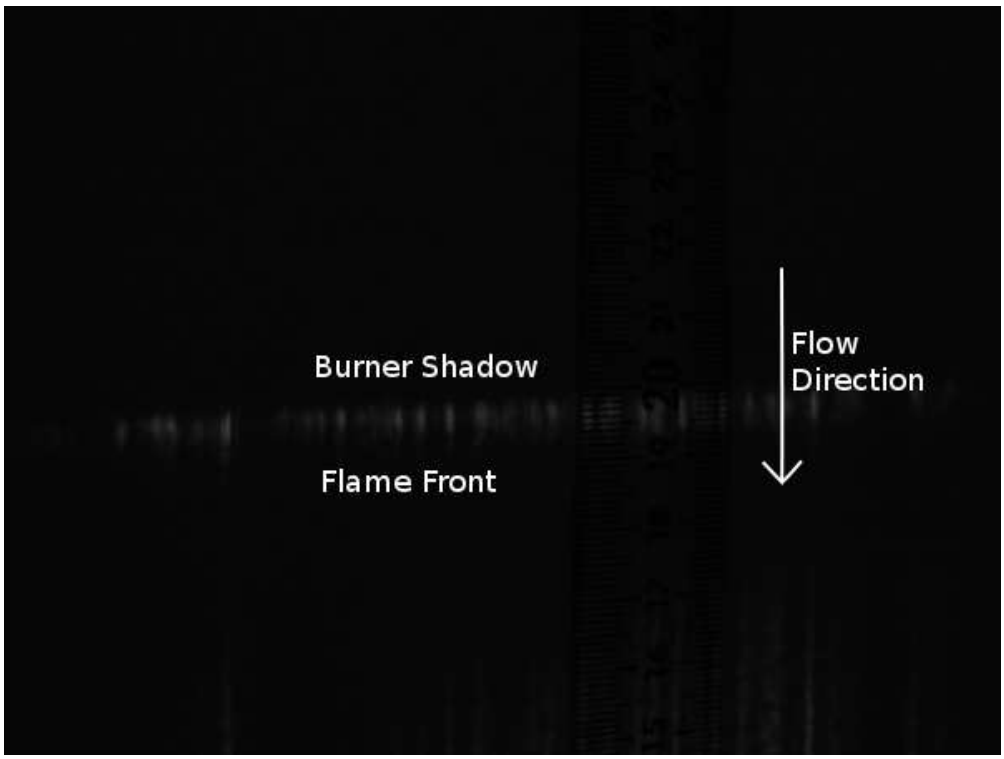

Figure 3.29: Image projected by the Schlieren system.

Figure 3.29 shows a projected image. The image is inverted by the parabolic mirror, so the flow travels from top to bottom. The vertical stripes are interference patterns caused by the curvature of the quartz tube. Below the shadow cast by the burner, there is a bright region followed by a dark region, corresponding to the positive temperature gradient before the flame and the negative temperature gradient after. The model fails to predict the negative temperature gradient because it is caused by heat losses to the ambient air and the quartz tube.

Procedure The standoff distance of methane burning at an equivalence ratio of 0.7, and with various velocities. Since the burner temperature is not regulated, but was expected to impact the flame position, at least five minutes were allowed after each condition was set for the system to reach thermal equilibrium.

Because hysteresis is a concern for such slow thermal systems, to ensure that the five minute settling time was sufficient, special precautions were used. Each test was conducted using one of two different ordering. The first began at low velocities, taking data at every alternate velocity until the maximum velocity was reached. Then, the skipped points were measured in decreasing order. The second was conducted directly in order from low to high velocities. No coherent deviations from the general trend are visible in the data.

The length of the preheat region was measured with a pair of calipers. The calipers were placed against the screen in an open position and gradually narrowed until the shadow cast by the caliper jaws lay adjacent to either side of the bright region in Figure 3.29.

Because the data collection method is prone to error, two tests spanning the operating range were performed on separate days with at most 0.5 cm/s velocity increments. Both the resolution and the repetition reduce the impact of human error. To reduce the degree that the measure of the flame position is subjective, no steps were taken to compare the data until

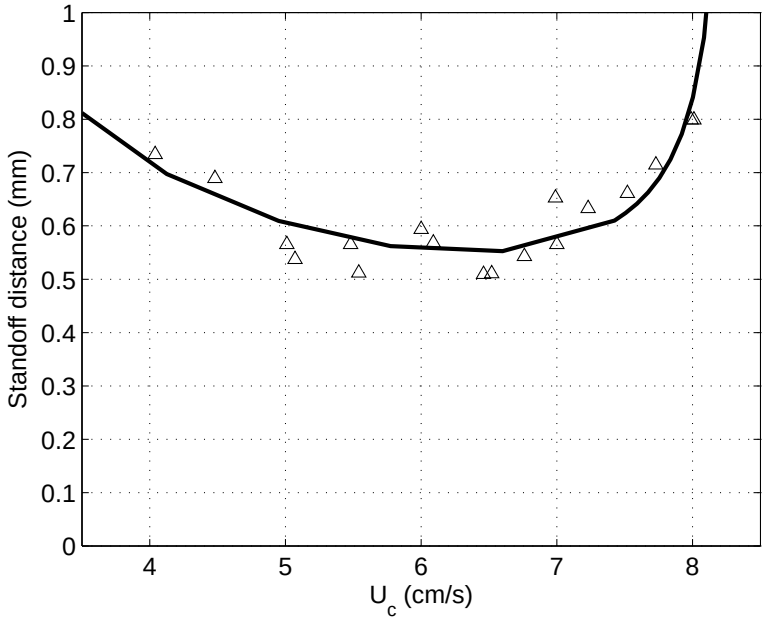

Figure 3.30: Standoff distance data as a function of cold-flow velocity.

after the tests had been completed, so that the researcher was ignorant of the significance of the results he was recording.

Figure 3.30 shows the measured positions in a scatter plot as a function of cold flow velocity. The fit function was selected by reasoning that the flame lifts off at both high and low velocities. Therefore, it is of the form

$$L \approx C \left(\frac{U_c}{U_L} \right)^{-a} \left(1 - \frac{U_c}{U_L} \right)^{-b}. \tag{3.130}$$

Here, U_L is the cold flow velocity at liftoff. Note that C has units of mm. The optimal coefficients are $C = 0.25$, $a = 1.15$, and $b = 0.34$.

The data accurately shows that the flame is quite stable at moderate velocities, but lifts off around $8.25 cm/s$ and $3.75 cm/s$. Liftoff is characterized by a the flame physically separating from the burner face and significantly traveling downstream. It is rare that it will stabilize

downstream, but can be accomplished. More commonly, the flame will simply blow out at either limit.

Should it become critical to future studies, it would be wise to amend the fit to be of the form

$$L \approx C \left(\frac{U_c - U_l}{U_L - U_l} \right)^{-a} \left(\frac{U_L - U_c}{U_L - U_l} \right)^{-b}, \tag{3.131}$$

which accurately incorporates the behavior that the flame also lifts off at the low cold flow velocity, U_l. This was not done in this work because extrapolating the flame's behavior at low velocities is not critical, and because the present models support no theoretical basis for U_l. Further explanation on this disconnect is made in 3.5

3.4.4 Heat release measurements

The heat release of the flame is measured by the intensity of the OH radical chemiluminescence. A lens above the flame focuses light onto a fiber, which delivers the light to a spectrometer, and then a photomultiplier tube (PMT), as depicted in Figure 3.31.

Initial setup During the rig's setup, the lens was focused by disconnecting the fiber from the spectrometer and shining a low power He-Ne laser onto its tip. The light cast on the lens was then projected down onto the burner. The lens was placed such that the image cast onto the burner was centered and roughly 4cm in diameter (corresponding to the region where the velocity profile is flattest).

Since the data acquisition system used in the experiment requires voltage input, the small currents produced by the PMT must be transduced to voltages. This is accomplished by an op-amp circuit. Using an active circuit that is designed to detect with a zero input

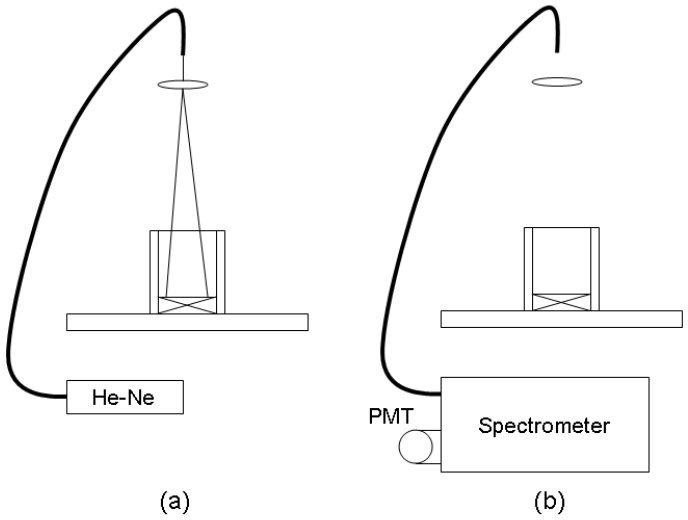

Figure 3.31: A diagram depicting the setup used for heat release rate measurements. (a) Depicts the alignment process. (b) Shows the spectrometer and PMT set up for normal operation.

impedance (requiring no input voltage), as opposed to a simple resistor relieved the PMT from having to drive current against an adverse voltage.

The fiber was aligned in the spectrometer with a twin-axis pivot. Light from a low power He-Ne laser was scattered on the burner surface and the spectrometer was tuned to 633nm; the wavelength produced by He-Ne lasers. The axes of the pivot were manually scanned and currently remain at points where the PMT voltage was maximum.

Spectrum measurements In the absence of forcing, the flame emits a broad spectrum of radiation. In order to verify that the OH radical measurements are detecting the proper peak, a methane flame at equivalence ratio 0.7 and at various velocities was scanned between 250nm and 600nm. In these measurements, the spectrometer is set to scan through the wavelengths at a particular rate while a data acquisition system samples the PMT voltage.

To this end, an acquisition program was written that pauses three seconds while displaying a countdown so that the spectrometer scan can begin in sync with the data acquisition. The program acquires data at 2kHz for 1000 samples, records their average, and repeats the operation once every half second. It accepts the user parameters identifying the beginning and ending wavelengths, as well as the spectrometer's scan rate. From this information, the program logs each data point with its corresponding wavelength. Figure 3.32 shows the result.

The amplitude of the peak indicates the total heat release rate. The relationship is linear, as shown in Figure 3.33.

Dynamic measurement setup The process of measuring a system's linear transfer function as a function of excitation frequency can be conducted using a variety of methods. The measurements presented herein were developed using a sine dwell. In this method, the

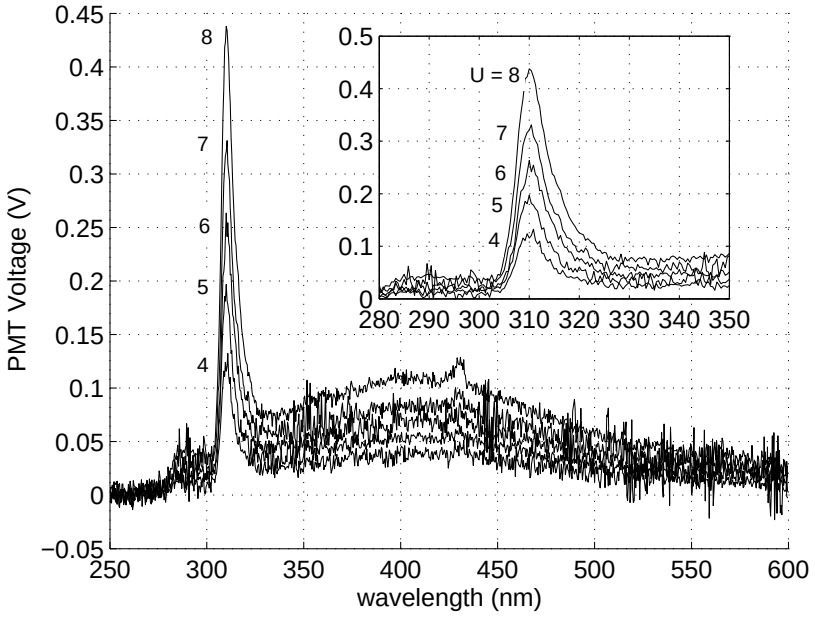

Figure 3.32: Spectral intensities collected at various cold flow rates.

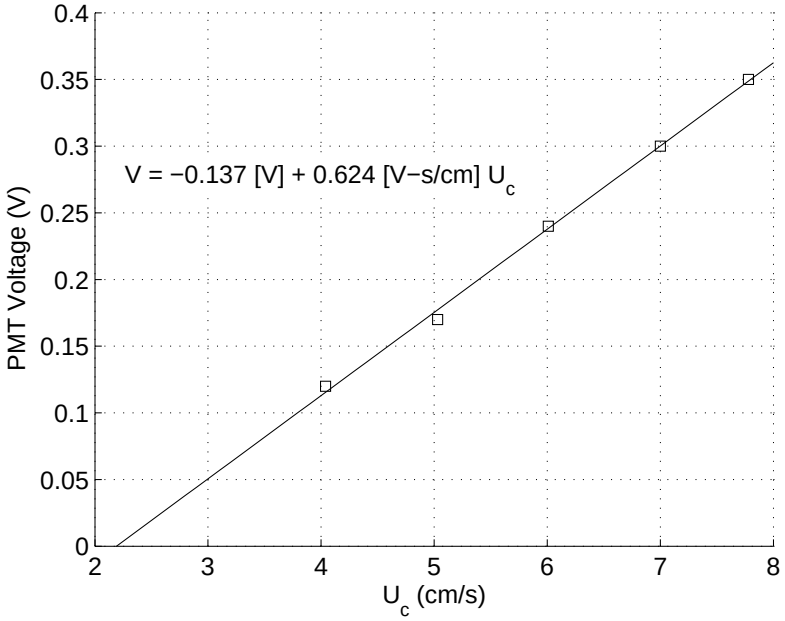

Figure 3.33: PMT voltage at $308nm$ for various cold flow rates.

system is supplied with an input containing energy in only one frequency, and the relative magnitude and phase of the output is measured. This procedure is repeated for each frequency of interest. Though sine dwells consume a great deal of time to collect and analyze, they are advantageous in that the maximize the power per frequency, improving the quality of the data.

The decision as to the amplitude of the dwell is a delicate matter, however, since too low a frequency will decrease the amplitude of the response to the point that noise overwhelms the signal. Meanwhile, too high an input runs the risk of exciting nonlinearities in the system or the sensors; all microphones saturate and hotwires cannot measure reverse flow.

Fortunately, it was found that a wide range of velocity amplitudes gave a consistent response. Transfer functions collected at a variety of frequencies with a variety of speaker excitation amplitudes all converged to similar values. Thus, the limiting factors in this experiment are sensor linearity and the noise floor.

Because of the acoustic properties of both the rig and the speaker, the same voltage into the speaker does not result in the same velocity amplitude at different frequencies. Thus, in order to respect the noise floor and saturation limit, an intermediate velocity amplitude was selected at which the flame had been observed to behave linearly, and where the signal to noise ratio was acceptable, and a system for collecting data was selected such that the same velocity amplitude should be maintained throughout the test. First, this required knowledge of the velocity amplitude relative to the speaker amplitude as a function of frequency.

The data acquisition program developed to record the sine dwell data is automated to cycle through a list of frequencies, record the data from each in a separate file, and then stop. The excitation signal is generated by the computer's sound card, sent through an audio amplifier (which is left at a constant gain for all experiments), and then to the speaker.

In anticipation of needing to adjust the volume at each frequency, it can be configured to load a file, wherein the list of frequencies and their corresponding volumes can be found, or it can be configured to step through a series of equidistant frequencies at a constant volume. The program records a time vector and raw voltages from four channels into ASCII files; the speaker input, the microphone, the hotwire, and the PMT.

With a flame burning at a cold-flow velocity of 6cm/s, the program ran a series of frequencies between 50 and 800 Hz. The signal to the amplifier was also fed back into the data acquisition system, along with the microphone, the hotwire, and the PMT signals. In post processing, the ratio of the amplitudes of the hotwire signal and the excitation were computed at each frequency. Thus, the desired signal volume, V, can be calculated in terms of the desired hotwire amplitude, u_d, with the measured ratio

$$V(f) = \left|\frac{u}{V}\right|^{-1} \cdot u_d. \tag{3.132}$$

The resulting function is shown in Figure 3.34. The rapid change that causes the volume to saturate at 1.00 above 300Hz is due to a rapid decline in the acoustic response at the burner. It is important to note that the plot also saturates at 0.05 at low frequencies. The settling chamber resonates quite well at low frequencies, so the velocity response is quite large, requiring the volume to be as low as possible. Fortunately, neither saturation, nor loss of signal into the noise floor were observed at these frequencies.

Though the data includes frequencies up to 800Hz, the plot is truncated at 400Hz both because the volume continues to saturate at 1.0, and because the system proves to exhibit a very small response above 400Hz.

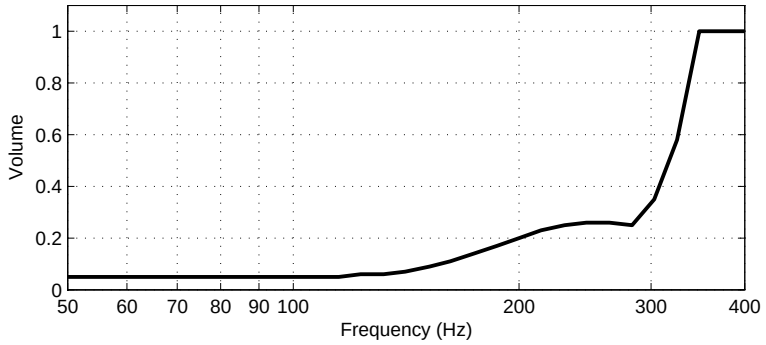

Figure 3.34: The dimensionless volume as a function of frequency to maintain the cold-flow velocity amplitude.

Signal conditioning and data analysis The microphone, hotwire, and PMT signals were filtered by a 2kHz lowpass filter to avoid aliasing. The data acquisition system collected data on the four channels for 10 seconds with a sampling rate of 10kHz.

Between each frequency test, there is a time while the system records the data from the test, during which no excitation is given. Thereafter, the excitation resumes at the next frequency. To ensure that the system has reached quasi-equilibrium, each frequency test begins with a second of continuous excitation during which no data is recorded. Then, the ten second data collection window begins.

The files of each frequency were saved in a folder with a text file describing the test conditions in detail. Each file containing information from a single frequency excitation at a single operating condition was analyzed separately, the relevant information extracted, and the total response function assembled. From the fast Fourier transform (FFT) of each signal, the power spectrum of each signal is computed along with cross spectra, transfer functions, and coherences. Though only a single transfer function calculation is absolutely necessary, these are helpful in debugging problems.

All of the signal properties are averaged by breaking the data for each frequency into equal

Table 3.1: Parameters used in data collection and analysis.

Parameter	**Value**	**Units**
Data collection		
Anti-aliasing cutoff frequency	2	kHz
Sample frequency	10	kHz
Test duration per frequency	10	sec
Excitation time before acquisition begins	1	sec
Analysis		
Points per FFT	8192	points
Maximum frequency in analysis	5	kHz
Frequency resolution in analysis	1.22	Hz
Discarded data between FFTs	0	points
Averages per frequency	12	-
Windowing	None	-
Excitation frequency identification method	spkr. amp.	-

parts, repeating the analysis on each part, and averaging the result. Coherence is calculated based on the statistics of that averaging. During this process, it is possible to reject data points between each part to supply a buffer between the tests, but that was not done.

To assemble a single FRF for the flame at the operating condition of interest, a single data point must be taken from the hotwire-to-PMT transfer function from each frequency test data at the frequency of excitation. Rather than trust that the excitation frequency to be absolutely accurate, the analysis software is capable of identifying the excitation frequency by the point of highest point in the power spectrum on any channel or the point of highest coherence in any transfer function measurement. These tests were analyzed by the power spectrum of the speaker excitation signal.

All of these parameters are summarized in Table 3.1.

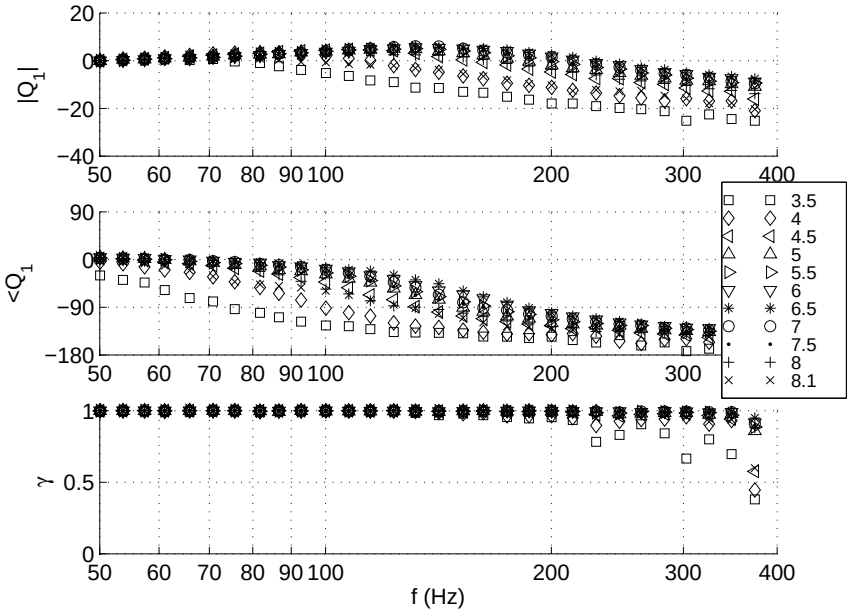

Figure 3.35: Heat release rate transfer functions normalized by their 50Hz amplitude.

3.4.5 Results

The heat release rate response takes the form of a nearly perfect second-order resonance. Note in Figure 3.35 that a slightly damped resonant peak in magnitude is accompanied by a 180° drop in phase, and that the resonance, the magnitude drops off at roughly 20dB per decade. These characteristics are classical indicators for a second-order resonance.

It is a simple matter to fit the data at each velocity condition with a second order model of the form,

$$TF = \frac{1}{s^2 + 2\zeta\omega_n s + \omega_n^2}. \tag{3.133}$$

These fits match the data almost exactly. The resulting trend in natural frequency is shown in Figure 3.36. At either velocity extreme, the cutoff frequency drifts significantly downward.

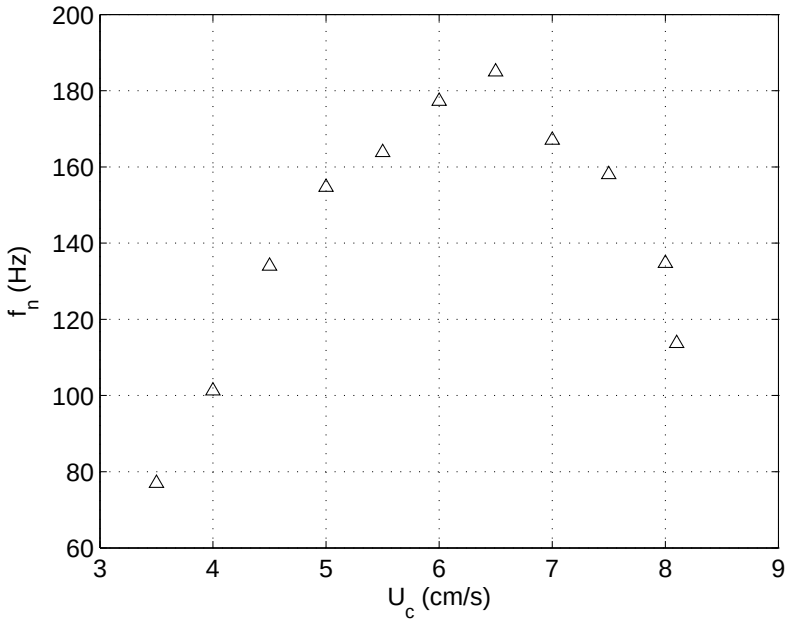

Figure 3.36: Heat release rate transfer functions.

Though it is difficult to see definitively, it is also visible in Figure 3.35, when one notices that the data for $U = 8.1$ and $U = 4$ are almost coincident beside the cluster of the rest of the data to their right.

It is also possible to plot the natural frequencies as a function of the offset distance. Since there is no position data explicitly available, it becomes necessary to interpolate the curve fit from Figure 3.30. The result is shown in log-space in Figure 3.37. There are two distinct legs departing from the cluster of data at the top-left. What is significant is that each of them appears to be following a roughly linear path in log-space, encouraging the notion that a power fit might be appropriate for this type of data.

It is also interesting that as the flame changes its natural frequency, the shape of the curves in Figure 3.35 remains relatively unchanged. In fact, the damping ratios are nearly constant for all cases. Figure 3.38 shows the path in the complex plane taken by the system's poles

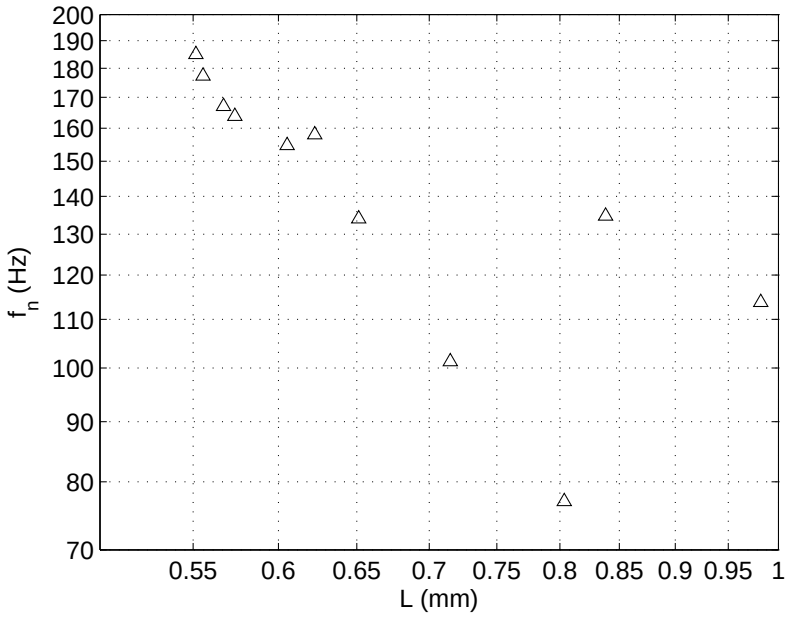

Figure 3.37: Heat release rate transfer functions.

as a function of velocity. The damping ratio remains almost completely constant.

3.5 Comparison

3.5.1 Scaling

In order to compare the finite element model, the analytical model, and the experimental results, it is necessary to first establish a common scale. The experimental data is presented in physical units, while the analytical model is properly normalized relative to the flame speed, and the finite element model is non-dimensionalized by constant time and length scales. Until they are brought into a common scale, it is impossible to comment on their relative accuracy.

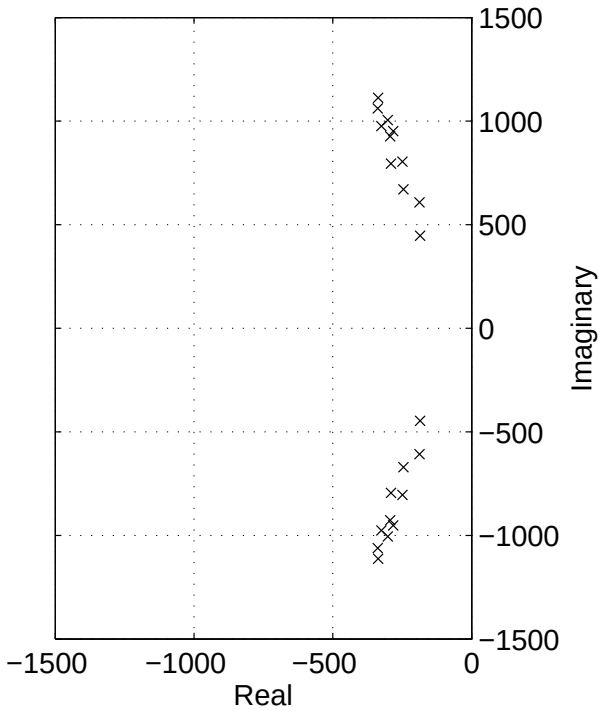

Figure 3.38: Pole root locus with changes in velocity.

To facilitate comment on the models rather than the experiment, the natural choice is to properly reduce the FE model and non-dimensionalize the experimental data. Though it is not done here, it is equally possible to re-dimensionalize the FE and analytical models.

Data Length, frequency, and velocity scales are required in order to reduce the experimental data. From the discussion on non-dimensionalization in Section 3.1, the parameters α and t_r determine all of these,

$$\delta = \sqrt{\alpha t_r} \qquad S_L = \sqrt{\frac{\alpha}{t_r}}$$

$$\hat{t} = \frac{t}{t_r} \qquad \Omega = \omega\, t_r \qquad \hat{x} = \frac{x}{\delta} \qquad \hat{U} = \frac{U}{S_L}.$$

However, because the velocity reported in the experiments is not the *actual* velocity at the flame boundary, the velocity scale derived above is useless. Instead, it is necessary to have some means of scaling the cold flow velocity. With the admittedly generous assumption that the cold flow velocity is proportional to the burner velocity, it is sufficient to identify the velocity at which the flame lifts off. Thus,

$$\hat{U} = \frac{U}{S_L} \approx \frac{U_c}{U_{c,lift}}. \tag{3.134}$$

Table 3.2 lists the values used for the various scales. Note that the time scale is order $10^{-4}s$, though methane is typically characterized by timescales on the order 10^{-3}s [19, 62, 48]. The value was selected in order to match the non-dimensionalized natural frequencies approach the order predicted by the models.

Though it is difficult to confirm, it is entirely possible that this result is quite physical. If the reactants are, in fact, at an elevated temperature as they exit the burner, the reaction

Table 3.2: Values used to non-dimensionalize the laminar flame data.

Parameter		Value	Obtained from
Thermal diffusivity	α	168×10^{-6} m^2/s	Air at 1000K
Chemical time scale	t_r	0.25 ms	Matching
Cold-flow lift-off velocity	U_{lift}	8.25 cm/s	Experimental
Length scale	δ	0.2 mm	$\delta = \sqrt{\alpha\, t_r}$
Frequency scale	ω	5×10^3 rad/s	$1/t_r$

time scale can easily be reduced by an order of magnitude. Which would also accounts for the small flame thickness.

Finite element re-scaling Since the finite element model has already been non-dimensionalized, it must be re-scaled to match the analytical model. Recall that this was not done directly since it is only in post processing that a computation for the flame speed is available. So, the re-scaling of reaction time and subsequently all other scales is based on the calculated liftoff velocity.

If the original choice of reaction time is given by t_r^*, then the corresponding dimensionless parameters are given by

$$\frac{\hat{t}^*}{t} = \frac{1}{t_r^*} \qquad \frac{\hat{U}^*}{U} = \sqrt{\frac{t_r^*}{\alpha}} \qquad \frac{\hat{x}^*}{x} = \frac{1}{\sqrt{\alpha t_r^*}} \qquad \Omega^* = \omega t_r^*.$$

If the choice of reaction time resulting in a flame speed of $\hat{U} = 1$ is t_r, then

$$\frac{\hat{t}}{t} = \frac{1}{t_r} \qquad \frac{\hat{U}}{U} = \sqrt{\frac{t_r}{\alpha}} \qquad \frac{\hat{x}}{x} = \frac{1}{\sqrt{\alpha t_r}} \qquad \Omega = \omega t_r.$$

Table 3.3: Values used to re-scale the finite element model data ($U^*_{lift} = 1.05$)

Parameter		Scaled by	Obtained from
Time	$\hat{t}$	1.1025	$\left(\hat{U}^*_{lift}\right)^2$
Length	L	1.05	U^*_{lift}
Frequency	Ω	0.907	$\left(\hat{U}^*_{lift}\right)^{-2}$

When $U \to S_L$, $\hat{U}$ is unity, and $\hat{U}^*$ is the calculated liftoff velocity, $\hat{U}^*_{lift}$. Therefore,

$$U^*_{lift} = \sqrt{\frac{t^*_r}{t_r}}. \tag{3.135}$$

Therefore, the proper reaction time scaling, t_r, can be determined as a ratio of the old reaction time scale, strictly in terms of the liftoff velocity using the old scale. Similarly, all the other parameters may be defined in ratio with their old values in terms of the liftoff velocity,

$$\frac{\hat{t}}{\hat{t}^*} = \frac{t^*_r}{t_r} = \left(\hat{U}^*_{lift}\right)^2 \tag{3.136}$$

$$\frac{\hat{x}}{\hat{x}^*} = \sqrt{\frac{t^*_r}{t_r}} = \hat{U}^*_{lift} \tag{3.137}$$

$$\frac{\Omega}{\Omega^*} = \frac{t_r}{t^*_r} = \frac{1}{\left(\hat{U}^*_{lift}\right)^2} \tag{3.138}$$

Table 3.3 shows the values used to rescale the finite element data.

3.5.2 Standoff distance

Though the dynamic characteristics of the flame are the primary focus of this endeavor, it is important to compare the static behaviors as well. Because the dynamic calculations inherently depend on the static solution, it is key that it reflect reality.

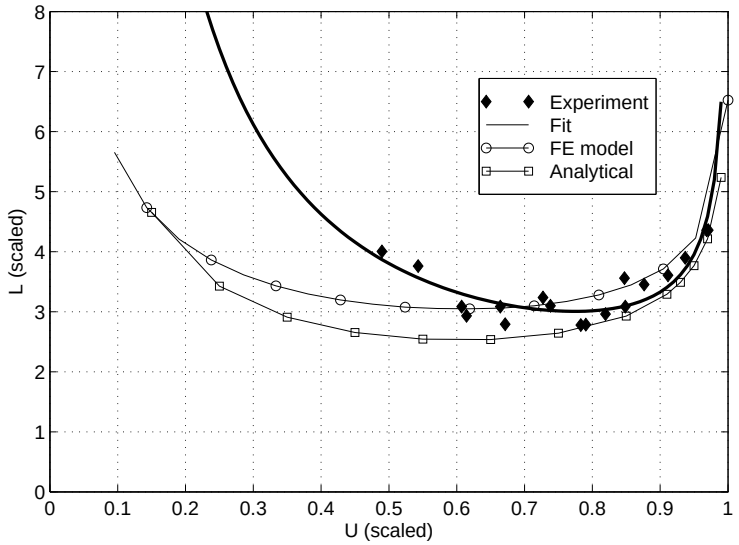

Figure 3.39: Scaled standoff distance with respect to scaled velocity

The standoff distance is, perhaps, the easiest means of validating the static predictions. The diagnostic equipment necessary to measure it is comparatively minimal, it is easily calculated from the FE data, and it is readily solved for in the analytical model. Figure 3.39 shows the three predictions for standoff distance plotted against velocity. Both models used $Le = 2$.

At velocities above roughly 0.5, all three plots are in good agreement, but the experiment diverges from the models severely at low velocities. Recall that these are the velocities at which the flame is highly sensitive to heat loss due to the scarcity of fresh reactants. While these velocities are precisely where the models begin to predict an instability, it will be seen that this is not the explanation for the premature liftoff.

There are two better explanations. Firstly, the assumption governing the velocity scaling could be flawed. It stands to reason that as the flame weakens at low velocities, the burner would cool, reducing the ratio between the cold flow velocity and the burner velocity. On the other hand, at high velocities, when the flame is stronger, additional heat loss to the burner

would result in extra preheat and a greater velocity ratio. Thus, one might even expect the velocity axis to be skewed to the right.

The remaining explanation is that there is additional heat loss not accounted for by the model. Though radiation effects have consistently been concluded to be minor in laminar flames, additional heat transfer to the walls might account for the reduced flame stability. This explanation is particularly tenable when one recalls that the flame is particularly sensitive to heat loss at the low velocities due to the scarcity of reactants to sustain the flame.

The FE and analytical models follow one another quite closely, but with the analytical slightly closer to the burner than the FE model. This can only be attributed to the different reaction model.

3.5.3 Dynamic response

Figure 3.40 shows the three heat release frequency response functions at various velocities. At moderate velocities, the agreement is excellent. Both the damping and natural frequency are accurately predicted.

As the velocity is reduced, however, the disagreement noted in between the standoff distance predictions is mimicked in the frequency response functions. By $U = 0.5$, the models both under predict the damping and over predict the natural frequency; both of which are consistent with the fact that the models have not begun to lift off, while the flame has.

Meanwhile, at $U = 0.9$, the disagreement is more slight, and different in nature. Though the plots do not diverge from one another, the models have both transitioned to become over damped while the experimental data has not.

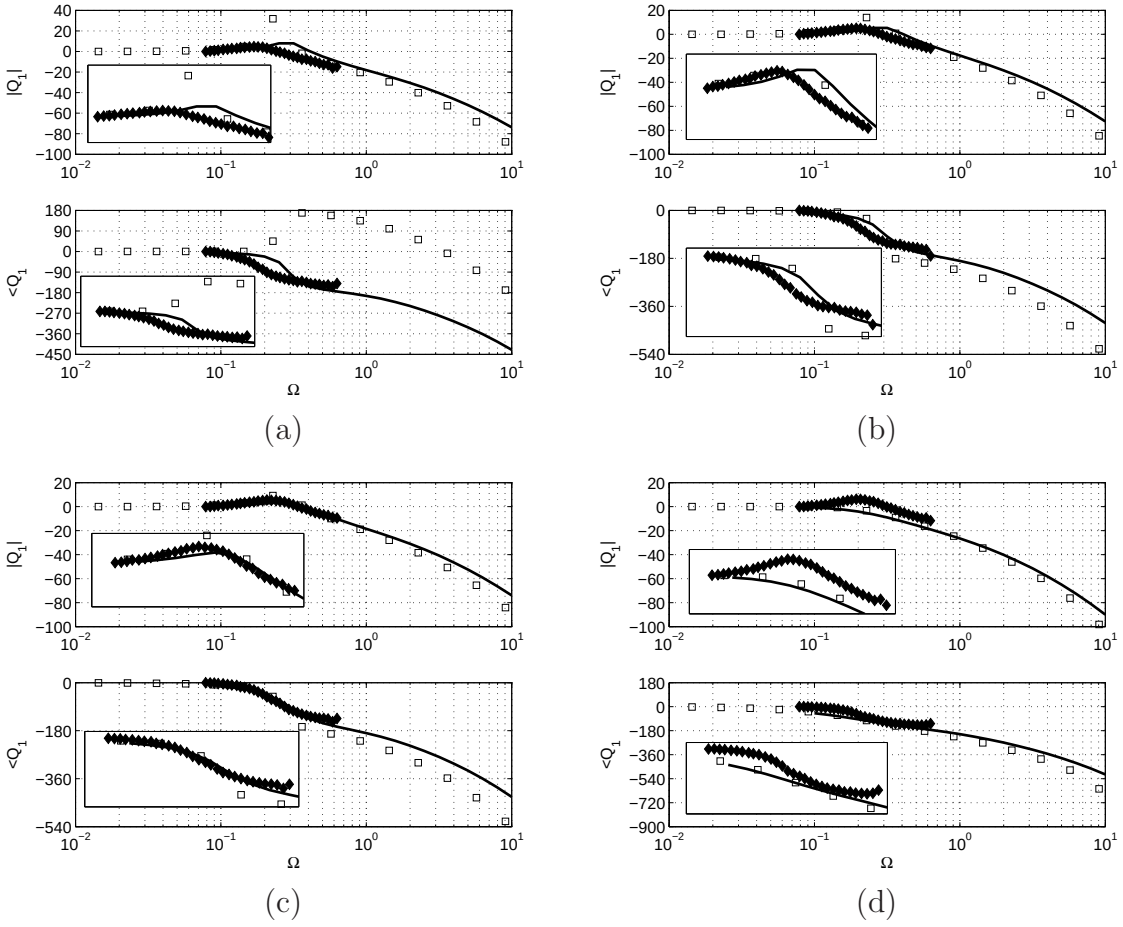

Figure 3.40: Comparison of frequency response data and models. Black diamonds are experimental data, hollow squares are FE model results, and the solid line is the analytical solution. (a) $\hat{U} = 0.5$ (b) $\hat{U} = 0.6$ (c) $\hat{U} = 0.7$ (d) $\hat{U} = 0.9$

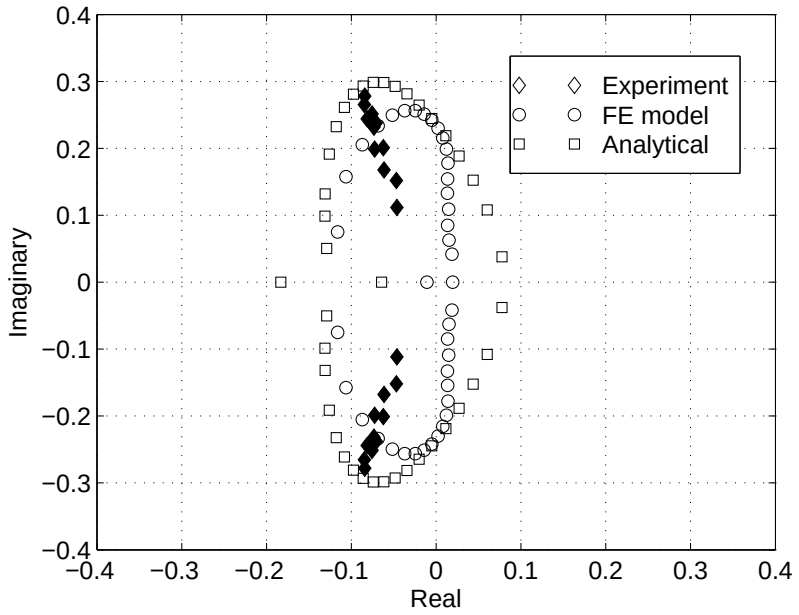

Figure 3.41: Scaled root loci. Models are computed at $Le = 2$.

Instability at low velocities The finite element's rising phase at $U = 0.5$ indicates that it has already gone unstable, while the light damping in the analytical model indicates that it is about to. This is confounding since the data never indicates that the flame is even approaching an instability. Figure 3.41 shows the motion of the resonant poles for the three data sets. Certainly, there is no interpretation of the data's behavior that would indicate that it is tending toward an instability.

It is possible, however, that this can be explained by a poor choice for the burner boundary condition. The models are formulated with the notion that the incoming fluid is at ambient temperature. Certainly it is before it reaches the burner, but after passing through the honeycomb, it has been heated significantly. Since scarcity of energy to sustain the reaction is at the cause for the instability in the first place, it stands to reason that elevated inlet temperatures might be the source of the experiment's stability.

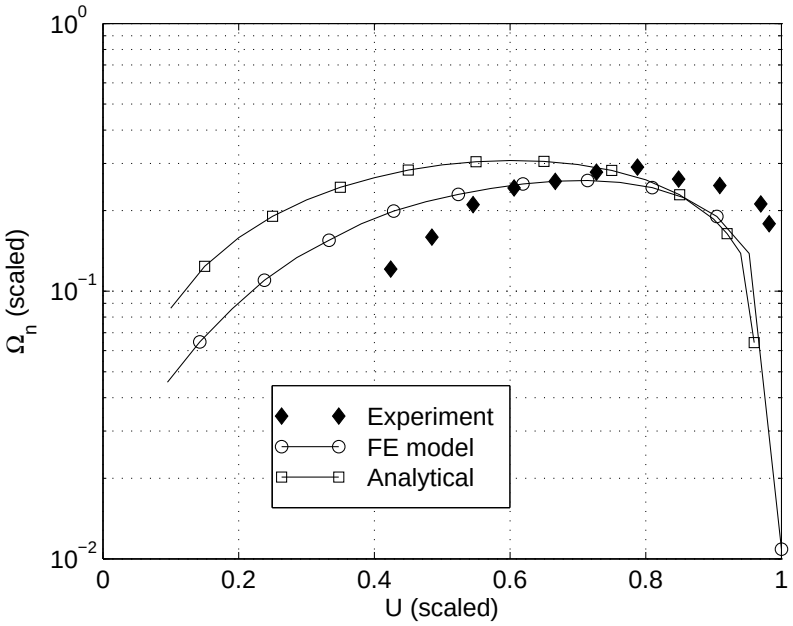

Figure 3.42: Natural frequency as a function of velocity.

Over-damped at high velocities The wide swing in the models' root loci that drives them unstable at low velocities also drives them into the real axis at high velocities. This over-damped behavior is as much a departure from the experimental data as the instability at low velocities. The most probable explanation is the same; that inlet temperature disagreements between the experiment and the models exaggerate the models' pole motion in the complex plane.

Natural frequency behavior Regardless of the disagreement in damping, the natural frequency behaviors are still follows relatively closely. Figure 3.42 shows the natural frequencies plotted against velocity. A disagreement identical in nature to that observed in the standoff distance in Figure 3.39 occurs here. While the experiment agrees quite well with the models at high velocities, it departs quite quickly at low velocities.

If there is doubt that the explanations might be the same, the are asuaged by Figure 3.43.

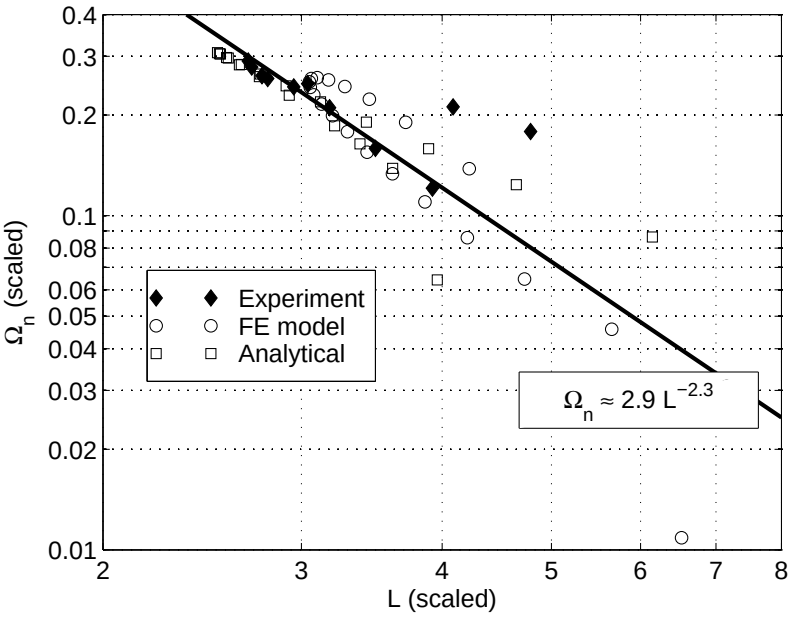

Figure 3.43: Natural frequencies plotted against the standoff distance.

Though the velocity may be skewed, the relationship between standoff distance and natural frequency is unaffected. The three curves are reasonably estimated by the line,

$$\Omega_n = 2.9L^{-2.3}. \tag{3.139}$$

Chapter 4

Moderately Turbulent Combustion

Nomenclature

A ..... Reaction rate coefficient
$B^{(p)\pm}$ ..... Preheat solution coefficients
$B^{(f)\pm}$ ..... Flame solution coefficients
c ..... Reaction progress
c_{ig} ..... D'less ignition parameter
C_p ..... Specific heat
D_i ..... Total diffusivity of spec. i
D_T ..... Turbulent diffusivity
q ..... Expanded d'less heat release
J ..... Jump coefficient $(-A/c_0'|_{L_f})$
$k^{\pm}$ ..... Wave numbers
K ..... DC gain
$\mathcal{L}$ ..... Flame thickness $(L_e - L_f)$
L_c ..... Flame center $(\frac{1}{2}L_f + \frac{1}{2}L_e)$
L_e ..... Flame exhaust location
L_f ..... Flame front location
$\mathbf{M}$ ..... System matrix
$\mathbf{P}$ ..... Boundary condition vector
Q ..... Heat release rate
$\hat{Q}$ ..... D'less heat release rate
R ..... D'less reaction rate
S ..... Turbulent flame speed $(\sqrt{D_T/t_r})$
t ..... Time
$\hat{t}$ ..... D'less time (t/t_r)
t_r ..... Reaction time
T ..... Temperature
$\mathbf{u}$ ..... Velocity vector
$\tilde{\mathbf{u}}$ ..... Incoherent velocity vector
U ..... Steady axial velocty
$\hat{U}$ ..... D'less steady axial velocity
v ..... Acoustic velocity
$\hat{v}$ ..... D'less acoustic velocity
x ..... Position rel. to burner
$\hat{x}$ ..... D'less position (x/δ)
Y_i ..... Mass fraction of spec. i
α ..... Thermal diffusivity
β ... Imag. wave no. component (Im $k^{\pm}$)
δ ..... Diffusion length $(\sqrt{D_T t_r})$
ζ_i ..... Reaction rate of spec. i
λ ..... Eigenvalue
ρ ..... Density
Ω ..... D'less excitation frequency (ωt_r)

4.1 Formulation of the Reynolds-averaged model

4.1.1 Assumptions and Limitations

Analytical solutions for turbulent flow fields rely heavily on simplifying assumptions, since full physical modeling would render an analytical approach absolutely impractical. This can be facilitated by choosing to investigate turbulent effects in geometries that lend themselves to generous simplifications. This study considers a porous-media-stabilized flame with homogeneous, isotropic turbulence. Though the instantaneous flow field (and resultant flame geometry) are far from symmetrical, the statistics that govern both can be taken as purely

one-dimensional. This inherently precludes more complex physics such as vortical structures and propagation of ripples along an inclined flame front, but simplifies the equations to resemble those of a laminar problem.

Additionally, the derivation encourages a number of less intrusive, but very powerful simplifying assumptions:

- That turbulent diffusion of energy and species dominates molecular and thermal diffusion,
- That the unsteady heat release is captured sufficiently over the frequency range of interest by a single-step model, and
- That velocity changes across the flame have a negligible affect on total heat release.

Of these, the last is the most suspect. This assumption is best justified by examining the excellent agreement between the laminar model in Chapter 3 both with the models found in literature that do not include the assumption and with experiment. Though success in laminar models can hardly be taken as absolution for liberties taken with turbulent models, concern can be placated somewhat by the striking similarities between the Reynolds averaged model and laminar models.

4.1.2 Derivation

The equations governing the temperature and the composition of a fluid undergoing combustion are

$$\frac{\partial T}{\partial t} + \mathbf{u} \cdot \nabla T - \nabla \cdot (\alpha \nabla T) = -\frac{\Delta T}{Y_{f,0}} \zeta_f \tag{4.1}$$

$$\frac{\partial Y_i}{\partial t} + \mathbf{u} \cdot \nabla Y_i - \nabla \cdot (D_i \nabla Y_i) = \zeta_i \tag{4.2}$$

when the rate formation of an arbitrary specie, i, can be described by ζ_i in mass formed per unit mass of fluid per unit time. In keeping with typical notation conventions, $\mathbf{u}$ is the fluid velocity vector, D_i is the diffusivity of specie i, α is the thermal diffusivity, and ΔT is the adiabatic temperature rise. It is also important to observe that the use of the fuel reaction rate, ζ_f, to indicate the heat release rate in the energy equation already implies the use of a single-step reaction mechanism.

From these, simplified governing equations can be developed by applying 1) physical constraints on the velocity field and the nature of the turbulence present, 2) non-dimensionalization that exploits specific assumptions regarding dominant processes, and 3) a linear expansion on an imposed acoustic velocity field.

Decomposition of the Velocity Field Though velocity, temperature, species fractions, and reaction rate will vary significantly in time and all three spatial dimensions for even the simplest turbulent flows, statistics describing them may be said to vary only axially for a flow of sufficient homogeneity. Thus, the velocity field can be decomposed into coherent and

stochastic components,

$$\mathbf{u} = \left\{ \begin{array}{c} U(x) + v(x,t) \\ 0 \\ 0 \end{array} \right\} + \tilde{\mathbf{u}} \tag{4.3}$$

Here, U is the steady velocity field, v is the acoustic velocity, and $\tilde{\mathbf{u}}$ is the turbulent velocity with the distinct property that $\langle \tilde{\mathbf{u}} \rangle = 0$. Additionally, great simplicity can be gained by assuming that both the acoustic and steady velocities are not a function of x. In this way, the derivation departs significantly from reality, but with minimal consequences that become clear once the model is complete.

The expected value of Equations 4.1 and 4.2 are

$$\frac{\partial \langle T \rangle}{\partial t} + (U+v)\frac{\partial \langle T \rangle}{\partial x} + \langle \tilde{\mathbf{u}} \cdot \nabla T \rangle - \frac{\partial}{\partial x}\left(\alpha \frac{\partial \langle T \rangle}{\partial x} \right) = -\frac{\Delta T}{Y_{f,0}} \langle \zeta_f \rangle \tag{4.4}$$

$$\frac{\partial \langle Y_i \rangle}{\partial t} + (U+v)\frac{\partial \langle Y_i \rangle}{\partial x} + \langle \tilde{\mathbf{u}} \cdot \nabla Y_i \rangle - \frac{\partial}{\partial x}\left(D_i \frac{\partial \langle Y_i \rangle}{\partial x} \right) = \langle \zeta_i \rangle \tag{4.5}$$

Thus, the governing equations naturally reduce to describe the generation and transport of the expected values for scalar quantities, except for two terms; cross-correlation between turbulent velocity and scalar values and the reaction rate. While the later of the two is a delicate topic that is addressed later, the scalar-velocity cross-correlation is frequently estimated as turbulent defusion, and can be estimated by

$$\langle \tilde{\mathbf{u}} \cdot \nabla T \rangle \approx -\nabla \cdot (D_T \nabla T), \tag{4.6}$$

where D_T is the turbulent diffusivity. Furthermore, if turbulent diffusion dominates molecular and thermal diffusion, then $D_T \gg D_i$ and $D_T \gg \alpha$. Furthermore, the assumption that

turbulence is homogeneous results in equations

$$\frac{\partial\langle T\rangle}{\partial t} + (u+v)\frac{\partial\langle T\rangle}{\partial x} - D_T\frac{\partial^2\langle T\rangle}{\partial x^2} = -\frac{\Delta T}{Y_{f,0}}\langle\zeta_f\rangle \tag{4.7}$$

$$\frac{\partial\langle Y_i\rangle}{\partial t} + (U+v)\frac{\partial\langle Y_i\rangle}{\partial x} - D_T\frac{\partial^2\langle Y_i\rangle}{\partial x^2} = \langle\zeta_i\rangle \tag{4.8}$$

Non-Dimensionalization These equations are conveniently scaled by the scalars' inlet values and their exit values when undergoing complete combustion. If Y_i and T are be written in terms of a single scalar, c,l beginning at 0 at the inlet and terminating at 1,

$$\langle Y_i(t,x)\rangle = Y_{i,0} + \Delta Y_i\,(1 - c(t,x)) \tag{4.9}$$

$$\langle T(t,x)\rangle = T_0 + \Delta T\,c(t,x), \tag{4.10}$$

then the governing equations reduce to a single equation,

$$\frac{\partial c}{\partial t} + (u+v)\frac{\partial c}{\partial x} - D_T\frac{\partial^2 c}{\partial x^2} = \frac{1}{Y_{f,0}}\langle\zeta_f\rangle. \tag{4.11}$$

There are a number of typical scales that can be applied at this point to nondimensionalize the equation. None of them can be rigorously defined at this point, but are instead retroactively constrained based on the solution. Using the reaction time, τ_r, thermal flame length, δ, and the turbulent flame speed, S, the dimensionless time, length, and velocity scales are

$$\hat{t} = \frac{t}{\tau_r} \qquad \hat{x} = \frac{x}{\delta} \qquad \hat{u} = \frac{u}{S}. \tag{4.12}$$

Applied to Equation 4.11,

$$\dot{c} + (\hat{U} + \hat{v})c' - c'' = R(c), \tag{4.13}$$

when the dimensionless reaction rate is given by $R = \tau_r \langle \zeta_f \rangle / Y_{f,0}$, and the dot and prime operations are differentiation in the dimensionless time and space respectively.

Heat release rate Just as in the plug flow reactor, the dimensionless heat release can be defined as

$$\hat{Q} = \frac{t_r \, Y_{f,in}}{\rho C_p \Delta T} Q = \int_0^\infty R \mathrm{d}\hat{x}. \tag{4.14}$$

Recall that the dimensionless heat release rate is heat release as a fraction of the total adiabatic heat release. Thus, the normalization does not change with any of the independent parameters (such as c_{ig} or $\hat{U}$). For more information on the derivation of heat release rate, refer to Section 3.1.2.

4.1.3 Expansion

The acoustic velocity can be expressed as an integral of its spectral components

$$\hat{v}(\hat{t}) = \epsilon \int_{-\infty}^{\infty} a(\Omega) \ \exp\left(j\Omega\hat{t}\right) \mathrm{d}\hat{t} \tag{4.15}$$

or for flows with guaranteed periodicity, Ω_0, a Fourier series of discrete frequencies,

$$\hat{v}(\hat{t}) = \epsilon \sum_{k=-\infty}^{\infty} a_k \ \exp\left(j\Omega_0 k\hat{t}\right). \tag{4.16}$$

Regardless, so long as the expansion only includes linear terms, the solution may always be written as a superposition (or integration) of solutions to the excitation,

$$\hat{v}(\hat{t}) = \epsilon \ \exp\left(j\Omega\hat{t}\right). \tag{4.17}$$

Therefore, the solution may be expressed as an expansion on the excitation amplitude, ϵ,

$$c(\epsilon; \hat{t}, \hat{x}) = c_0(\hat{x}) + \epsilon\, c_1(\hat{x}) \ \exp\left(j\Omega\hat{t}\right) + \mathcal{O}(\epsilon^2). \tag{4.18}$$

Note that the first term has no dependence on $\hat{t}$. When $\epsilon = 0$, there is no excitation and the system is taken to be at steady state. Therefore, this approach neglects affects from initial conditions and assumes that the system has reached quasi-steady-state oscillations. When Equations 4.17 and 4.18 are substituted into Equation 4.13, the steady and linear governing equations are revealed.

$$\hat{U}c_0' - c_0'' = R(c_0) \tag{4.19}$$

$$j\Omega c_1 + \hat{U}c_1' - c_1'' = c_1 \frac{\mathrm{d}R}{\mathrm{d}c}(c_0) - c_0' \tag{4.20}$$

Predictably, the steady solution, c_0, appears as a parameter in the unsteady equation in two locations; the reaction rate sensitivity, $\mathrm{d}R/\mathrm{d}c$, and in the source term, appearing from the expansion of the velocity perturbation, c_0'.

Heat release rate The expansion of the heat release rate continues to parallel the result obtained from the laminar study in Section 3.1.3.

$$\begin{aligned}\hat{Q} &= q_0 + \epsilon q_1 + \mathcal{O}(\epsilon^2) \\ &= \int_0^\infty \{R(c_0) + \epsilon R_c c_1\}\, \mathrm{d}\hat{x} + \mathcal{O}(\epsilon^2)\end{aligned} \tag{4.21}$$

Thus, the static component of the heat release rate is obtained by equating terms that are independent of ϵ. When we substitute the expression for R, we obtain

$$\begin{aligned}q_0 &= \int_0^\infty R(c_0)\mathrm{d}\hat{x} \\ &= A\mathcal{L}.\end{aligned} \tag{4.22}$$

The linear component of the heat release rate is obtained by equating terms that are linear on ϵ. Substituting the derivatives on R and integrating, we obtain that

$$\begin{aligned}q_1 &= \int_0^\infty R_c c_1 \mathrm{d}\hat{x} \\ &= A\int_0^\infty \left(\delta(c_0 - c_{ig}) - \delta(1 - c_0)\right) c_1 \mathrm{d}\hat{x} \\ &= A\left(\frac{c_1}{c_0'}\bigg|_{\hat{x}=L_f} - \frac{c_1}{c_0'}\bigg|_{\hat{x}=L_e}\right).\end{aligned} \tag{4.23}$$

4.1.4 Turbulent ignition model

The piecewise turbulent ignition model can be written in terms of the heaviside function, h, as

$$R(c) = A\, h(c - c_{ig})\, h(1 - c).. \tag{4.24}$$

The discontinuities at c_{ig} and 1 are inherent challenges to using the turbulent ignition model, but using the heaviside functions allows a very natural evaluation of the derivative of R appearing in Equation 4.20,

$$\frac{\mathrm{d}R}{\mathrm{d}c} = A\left[\delta(c - c_{ig}) - \delta(1 - c)\right]. \tag{4.25}$$

From this formulation for R, it is straightforward to arrive at conditions on the continuity of c_0 and c_1 by integrating their respective governing equations. By integrating Equation 4.19 about some point in space, s, over a small distance, η,

$$\begin{aligned} 0 &= \lim_{\eta\to 0}\int_{s-\eta/2}^{s+\eta/2}\left[\hat{U}c_0' - c_0'' - R\right]\mathrm{d}\hat{x} \\ &= \left[\hat{U}c_0 - c_0'\right]_{s^-}^{s^+}. \end{aligned} \tag{4.26}$$

Repeating this process with a double integral,

$$0 = \left[c_0\right]_{s^-}^{s^+}. \tag{4.27}$$

Therefore, both c_0 and c_0' are continuous at all points in space.

However, thanks to the appearance of impulse functions in the reaction rate sensitivity, c_1 must be treated with more care.

$$\begin{aligned} 0 &= \lim_{\eta\to 0}\int_{s-\eta/2}^{s+\eta/2}\left[j\Omega c_1 + \hat{U}c_1' - c_1'' - \frac{\mathrm{d}R}{\mathrm{d}c}c_1 + c_0'\right]\mathrm{d}\hat{x} \\ &= \left[\hat{U}c_1 - c_1'\right]_{s^-}^{s^+} - \int_{c0(s^-)}^{c0(s^+)}\frac{\mathrm{d}R}{\mathrm{d}c}\frac{c_1}{c_0'}\mathrm{d}c_0 \\ &= \left[\hat{U}c_1 - c_1' - \frac{R\,c_1}{c_0'}\right]_{s^-}^{s^+} \end{aligned} \tag{4.28}$$

Similarly to the c_0 continuity, a double integral reveals that

$$0 = [c_1]_{s^-}^{s^+}\,, \tag{4.29}$$

so c_1 is continuous at all points in space.

The first derivative of c_1, however, will have two discontinuities; one at the flame front, where R changes from 0 to A, and one at the flame exit, where R becomes 0 again. The flame front can be defined as the point, $\hat{x} = L_f$, at which $c_0(L_f) = c_{ig}$. The flame exit can be defined as the point at which $c_0(L_e) = c_0(L_e^+) = 1$ and $c_0(L_e^-) < 1$. In other words, the flame exit is the first point in space at which $c_0 = 1$. The discontinuities at these points are, therefore

$$[c_1']_{L_f^-}^{L_f^+} = -A\frac{c_1(L_f)}{c_0'(L_f)} \tag{4.30}$$

$$[c_1']_{L_e^-}^{L_e^+} = A\frac{c_1(L_e)}{c_0'(L_e)} \tag{4.31}$$

4.2 Analytical solution

4.2.1 Static solution

The domain may be conveniently divided into three sub-domains depictied in Figure 4.1; preheat, flame, and equilibrium. The incoming reactants are heated in the preheat region until they reach the ignition temperature, at which point they enter the reaction region. There, the reaction continues until the fuel is exhausted. At that point, the flow enters the equilibrium region, where the reaction has extinguished.

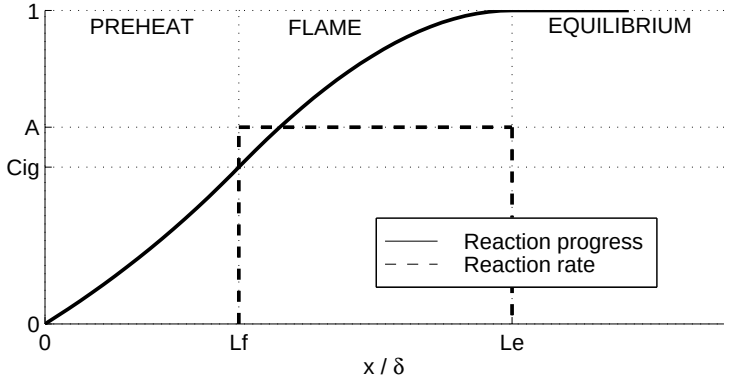

Figure 4.1: A solution for c_0 and the corresponding reaction rate.

Preheat In the preheat region, the reaction rate is zero, simplifying the governing equation to

$$\hat{U}c_0' - c_0'' = 0. \tag{4.32}$$

The boundary conditions are

$$c_0(0) = 0 \qquad\qquad c_0(L_f) = c_{ig}.$$

These are satisfied by

$$c_0 = c_{ig}\frac{\exp(\hat{U}x) - 1}{\exp(\hat{U}L_f) - 1}. \tag{4.33}$$

Equilibrium In the equilibrium region, the governing equation is the same as in the preheat region. The boundary conditions are

$$c_0(L_e) = 1 \qquad\qquad c_0'(\infty) = 0.$$

Therefore, the solution is simply

$$c_0 = 1. \tag{4.34}$$

Flame In the flame, the governing equation is

$$\hat{U}c_0' - c_0'' = A. \tag{4.35}$$

In order to satisfy continuity with the surrounding regions, there are four boundary conditions,

$$c_0(L_f) = c_{ig} \qquad c_0'(L_f) = c_{ig}\hat{U}\frac{\exp(\hat{U}L_f)}{\exp\hat{U}L_f - 1}$$
$$c_0(L_e) = 1 \qquad c_0'(L_e) = 0.$$

Two of these are used to determine the two integration coefficients encountered when solving the governing equation. The other supply the constraints necessary to solve for L_f and L_e.

Using the conditions at L_e to integrate the governing equation,

$$c_0 = 1 - \frac{A}{U^2}\left[\exp\left(U(\hat{x} - L_e)\right) - 1\right] + \frac{A}{U}(\hat{x} - L_e). \tag{4.36}$$

Applying the remaining boundary conditions at L_f,

$$c_{ig} = 1 - \frac{A}{\hat{U}^2}\left[\exp\left(-\hat{U}\mathcal{L}\right) - 1\right] - \frac{A\mathcal{L}}{\hat{U}} \tag{4.37}$$
$$c_{ig}\hat{U}\, n(\hat{U}L_f) = -\frac{A}{\hat{U}}\left[\exp\left(-\hat{U}\mathcal{L}\right) - 1\right], \tag{4.38}$$

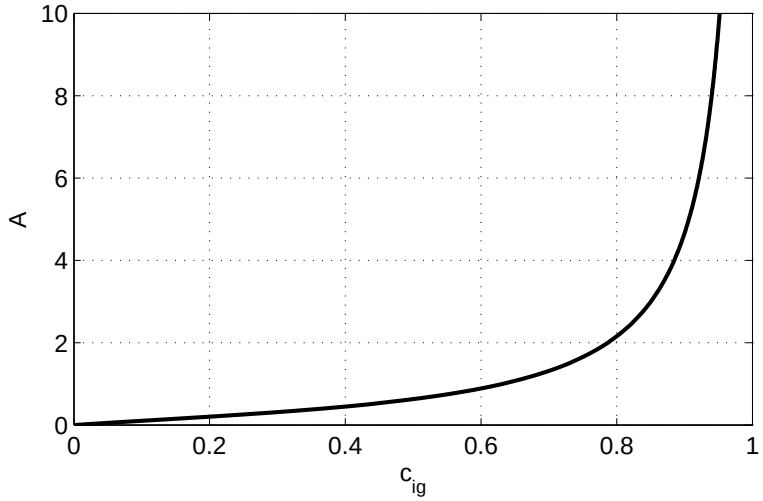

Figure 4.2: Scaled turbulent ignition reaction coefficient, A, with respect to the ignition parameter, c_{ig}.

when $\mathcal{L} = L_e - L_f$ and

$$n(\hat{U}L_f) = \frac{\exp(\hat{U}L_f)}{\exp(\hat{U}L_f) - 1}. \tag{4.39}$$

Firstly, these equations are used to constrain the scaled reaction coefficient, A. Since when $\hat{U} \to 1$, $L_f \to \infty$, Equations 4.37 and 4.38 show that

$$c_{ig} = A\left[1 - \exp\left(\frac{-1}{A}\right)\right]. \tag{4.40}$$

Thus, there is a well defined relationship between the ignition parameter, c_{ig}, and A in order to respect earlier choice of t_r so that the dimensionless flame speed is $\hat{U} = 1$. Unfortunately, if c_{ig} is the specified parameter, then A must be computed iteratively; a task that can be challenging for values of c_{ig} close to unity. Figure 4.2 shows the relationship between c_{ig} and A.

Equations 4.37 and 4.38 are also used to solve for the lengths, L_f and $\mathcal{L}$. Since it does not detract from the insights one might hope to gain from the dynamic model, rather than deriving approximate methods, Equation 4.37 is inverted numerically to yield $\mathcal{L}$. Once $\mathcal{L}$ is computed, L_f is calculated exactly by

$$\begin{aligned} L_f &= \frac{1}{\hat{U}} \ln\left(\frac{r}{r-1}\right) \\ r &= \frac{A}{c_{ig}\hat{U}^2}\left(1 - \exp\left(-\hat{U}\mathcal{L}\right)\right) \end{aligned} \tag{4.41}$$

Figures 4.3 and 4.4 show the resulting flame positions over a wide variable space. It is interesting to note that while the flame thickness is very sensitive to the ignition parameter, it is not particularly sensitive to changes in velocity; particularly for large values of c_{ig}. Conversely, the flame front position, L_f, is almost unaffected by changes in c_{ig}, while strongly dependent on the velocity.

One need only examine the governing equation for an explanation to why $\mathcal{L}$ is weakly sensitive to $\hat{U}$. When one integrates Equation 4.19 over the entire domain, the result is

$$\hat{U} + c_0'|_{x=0} = A\mathcal{L}. \tag{4.42}$$

Intuitively, $\mathcal{L}$, would vary linearly with $\hat{U}$, but because diffusion at the inlet varies almost linearly with velocity for thin flames, the slope of the curve is lessened. As the flame thickens (lower c_{ig} values) and the diffusion at the inlet develops a more complicated relationship to velocity, that affect is obscured.

Repeating a similar exercise, only integrating from the inlet to the flame front yields an

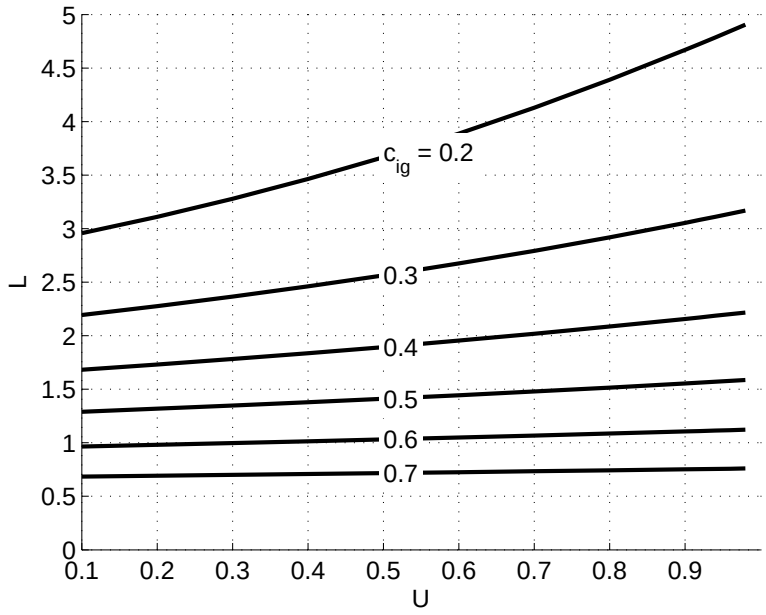

Figure 4.3: Flame thickness, L, plotted against the dimensionless velocity, $\hat{U}$, for various values of the ignition parameter, c_{ig}.

explanation for the flame front's counter-intuitive insensitivity to the ignition parameter.

$$\hat{U}c_{ig} - c_0'|_{x=0}\left(1 - e^{\hat{U}L_f}\right) = 0. \tag{4.43}$$

Since c_0' also varies roughly linearly with c_{ig}, it can be canceled from every term, and velocity is the only remaining significant influence on L_f.

4.2.2 Dynamic solution

Unlike the static system, the first expansion of the governing equation is the same in all regimes,

$$j\Omega c_1 + \hat{U}c_1' - c_1'' = -c_0'. \tag{4.44}$$

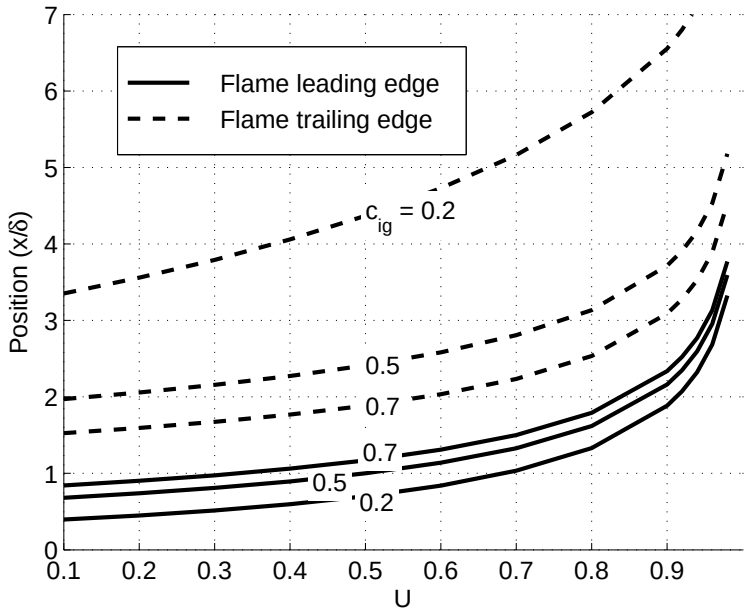

Figure 4.4: Flame front, L_f, and exit, L_e, positions plotted against the dimensionless velocity, $\hat{U}$, for various values of the ignition parameter, c_{ig}.

The reaction rate affects enter the dynamic equation through the jump conditions in Equations 4.30 and 4.31. As a result, the same wave numbers are valid at all points in the domain

$$k^{\pm} = \frac{\hat{U}}{2}\left[1 \pm \sqrt{1 + \frac{4j\Omega}{\hat{U}^2}}\right]. \tag{4.45}$$

The solution in each of the three domains is of the form

$$c_1^{(p)} = B^{(p)+}\exp\left(k^{+}\hat{x}\right) + B^{(p)-}\exp\left(k^{-}\hat{x}\right) - \frac{c_0'}{j\Omega} \tag{4.46}$$

$$c_1^{(f)} = B^{(f)+}\exp\left(k^{+}\left(\hat{x} - L_e\right)\right) + B^{(f)-}\exp\left(k^{-}\left(\hat{x} - L_e\right)\right) - \frac{c_0'}{j\Omega} \tag{4.47}$$

$$c_1^{(e)} = 0 \tag{4.48}$$

The B coefficients are solved for by applying the boundary and jump conditions. At the reactor inlet,

$$\begin{aligned} 0 &= c_1(x=0) \\ &= B^{(p)+} + B^{(p)+} - \frac{c_0'(0)}{j\Omega}. \end{aligned} \tag{4.49}$$

The reactor exit conditions are already satisfied by Equation 4.48, so all that remains are the jump conditions. At the flame front, continuity indicates that

$$\begin{aligned} 0 =& c_1(x=L_f^+) - c_1(x=L_f^-) \\ 0 =& B^{(f)+}\exp\left(-k^+\mathcal{L}\right) + B^{(f)-}\exp\left(-k^-\mathcal{L}\right) \\ & - B^{(p)+}\exp\left(k^+L_f\right) - B^{(p)-}\exp\left(k^-L_f\right) \end{aligned} \tag{4.50}$$

and the jump condition indicates that

$$\begin{aligned} Jc_1(L_f) &= c_1'(x=L_f^+) - c_1'(x=L_f^-) \\ J\left\{B^{(f)+}\exp\left(-k^+\mathcal{L}\right) + B^{(f)-}\exp\left(-k^-\mathcal{L}\right)\right\} &= k^+B^{(f)+}\exp\left(-k^+\mathcal{L}\right) + k^-B^{(f)-}\exp\left(-k^-\mathcal{L}\right) \\ & - k^+B^{(p)+}\exp\left(k^+L_f\right) - k^-B^{(p)-}\exp\left(k^-L_f\right) \end{aligned} \tag{4.51}$$

when $J = -A/c_0'(L_f)$. Note that the particular solution, c_0' does not appear in Equation 4.51. The particular terms cancel owing to the identity,

$$A = c_1''(L_f^+) - c_1''(L_f^-), \tag{4.52}$$

which can be derived from Equation 4.20.

At the flame exit, continuity dictates that

$$\begin{aligned} 0 =& c_1(x = L_e^+) - c_1(x = L_e^-) \\ 0 =& B^{(f)+} + B^{(f)-}. \end{aligned} \tag{4.53}$$

It is a simple matter to show that the remaining jump condition is automatically satisfied when these conditions are met and is redundant. Therefore, Equations 4.49, 4.50, 4.51, and 4.53 represent four equations on four unknowns, which are naturally expressible in the form

$$\mathbf{P}(\Omega) \cdot \mathbf{M}(\Omega)^{-1} = \left\{ \begin{array}{c} B^{(p)+} \\ B^{(p)-} \\ B^{(f)+} \\ B^{(f)-} \end{array} \right\} \tag{4.54}$$

when

$$\mathbf{M} = \left\{ \begin{array}{cccc} 1 & 1 & 0 & 0 \\ -e^{k^+ L_f} & -e^{k^- L_f} & e^{-k^+ \mathcal{L}} & e^{-k^- \mathcal{L}} \\ -k^+ e^{k^+ L_f} & -k^- e^{k^- L_f} & (k^+ - J)e^{-k^+ \mathcal{L}} & (k^- - J)e^{-k^- \mathcal{L}} \\ 0 & 0 & 1 & 1 \end{array} \right\} \tag{4.55}$$

and

$$\mathbf{P} = \left\{ \begin{array}{c} \frac{c_0'(0)}{j\Omega} \\ 0 \\ 0 \\ 0 \end{array} \right\}. \tag{4.56}$$

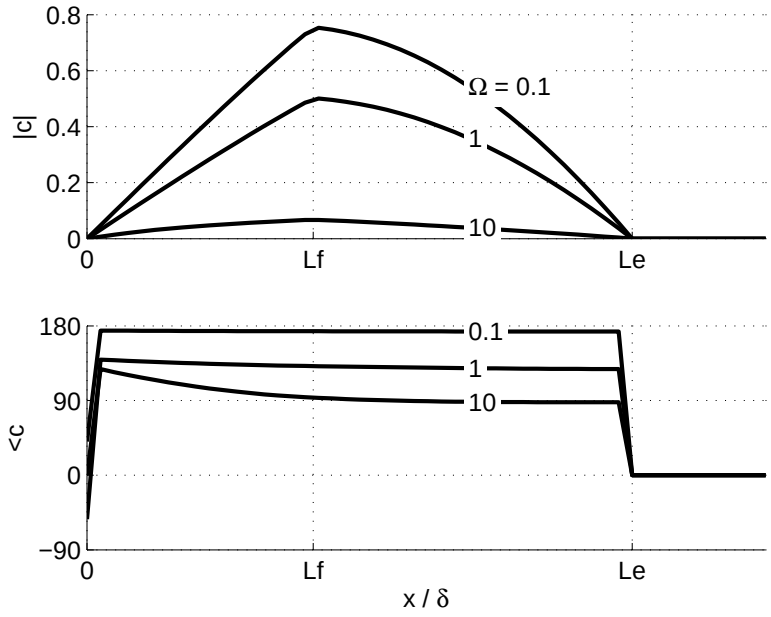

Figure 4.5: The c_1 field response to various frequencies.

Thus, this solution approach allows the dynamic flame response to be computed as a function of the excitation frequency. Figure 4.5 shows the solution for for various values of Ω, plotted with respect to $\hat{x}$.

Low-frequency singularity The work is not done, however, because Equation 4.54 exhibits a singularity as $\Omega \to 0$. At first glance it might be inferred that the low-frequency response is simply infinite, but this is not true. The low-frequency response must be identical to the static solution's sensitivity to velocity changes; wich is quite finite. Upon closer examination, it is readily apparent that the particular solution, $c_0'/(j\Omega)$, implicitly assumes that Ω is non-zero.

Therefore, it becomes necessary to repeat the solution for the special case that $\Omega = 0$. If approach succeeds, then the special solution will be consistent with the ordinary solution at small frequencies.

The new governing equation is

$$\hat{U}c_1' - c_1'' = -c_0', \tag{4.57}$$

Consider solutions of the form

$$c_1^{(p)} = B^{(p)+}\exp\left(\hat{U}\hat{x}\right) + B^{(p)-} + a^{(p)}\,\hat{x}\,c_0' + b^{(p)}\,\hat{x} \tag{4.58}$$

$$c_1^{(f)} = B^{(f)+}\exp\left(\hat{U}\,(\hat{x} - L_e)\right) + B^{(f)-} + a^{(f)}\,\hat{x}\,c_0' + b^{(f)}\,\,(\hat{x} - L_e) \tag{4.59}$$

$$c_1^{(e)} = 0. \tag{4.60}$$

In both the preheat and flame regions, substituting the particular solutions into Equation 4.57 yields

$$a\hat{U}c_0' - 2ac_0'' + \hat{U}b = -c_0' \tag{4.61}$$

Without incorporating additional knowledge of c_0, this is an over-constrained problem since there are three independent functions (a constant, and two derivatives of c_0), but only two coefficients with which to satisfy the equation. However, Equation 4.19, can be used to relate c_0'' to c_0' and constant terms in the various regions.

In the preheat region, $c_0'' = \hat{U}c_0'$. After substitution into Equation 4.61, the preheat particular

solution is satisfied by

$$a^{(p)} = \frac{1}{\hat{U}} \qquad\qquad b^{(p)} = 0. \tag{4.62}$$

In the flame region, $c_0'' = \hat{U}c_0' - A$. Similar substitution into Equation 4.61 yields

$$a^{(f)} = \frac{1}{\hat{U}} \qquad\qquad b^{(f)} = -\frac{2A}{\hat{U}^2}. \tag{4.63}$$

The remaining homogeneous coefficients are determined just as before; by applying boundary and jump conditions. The inlet boundary condition states that

$$\begin{aligned} 0 &= c_1(x = 0) \\ &= B^{(p)+} + B^{(p)+}. \end{aligned} \tag{4.64}$$

Again, the reactor exit conditions are already satisfied, so the jump conditions provide the remaining constraints.

$$\begin{aligned} 0 =& c_1(x = L_f^+) - c_1(x = L_f^-) \\ 0 =& B^{(f)+} \exp\left(-\hat{U}\mathcal{L}\right) + B^{(f)-} \\ & - B^{(p)+} \exp\left(\hat{U}L_f\right) - B^{(p)-} + \frac{2A\mathcal{L}}{\hat{U}^2} \end{aligned} \tag{4.65}$$

In this instance, the particular solution on either side of the discontinuity no longer cancels,

so that an additional term appears. Something similar happens in the jump condition,

$$\begin{aligned} Jc_1(L_f) &= c_1'(x = L_f^+) - c_1'(x = L_f^-) \\ J\left\{B^{(p)+}\exp\left(\hat{U}L_f\right) + B^{(p)-}\right\} &= \hat{U}B^{(f)+}\exp\left(-\hat{U}\mathcal{L}\right) \\ &\quad - \hat{U}B^{(p)+}\exp\left(\hat{U}L_f\right) - \frac{2A}{\hat{U}^2} \end{aligned} \tag{4.66}$$

when $J = -A/c_0'(L_f)$. Though cancellation removes the particular solution from the jump condition, the discontinuity in the particular leaves the term $2A/\hat{U}^2$ on the right-hand side. Meanwhile, just like in the general solution, the final continuity condition at the flame exit states that

$$\begin{aligned} 0 =& c_1(x = L_e^+) - c_1(x = L_e^-) \\ 0 =& B^{(f)+} + B^{(f)-}. \end{aligned} \tag{4.67}$$

Therefore, there is a modified matrix relationship for the special case when $\Omega = 0$,

$$\mathbf{M} = \begin{Bmatrix} 1 & 1 & 0 & 0 \\ -e^{\hat{U}L_f} & -1 & e^{-\hat{U}\mathcal{L}} & 1 \\ -(\hat{U}+J)e^{\hat{U}L_f} & -J & \hat{U}e^{-\hat{U}\mathcal{L}} & 0 \\ 0 & 0 & 1 & 1 \end{Bmatrix} \tag{4.68}$$

and

$$\mathbf{P} = \left\{ \begin{array}{c} 0 \\ -\frac{2A\mathcal{L}}{\hat{U}^2} \\ \frac{2A}{\hat{U}^2} \\ 0 \end{array} \right\}. \tag{4.69}$$

Heat release response From Equation 4.23 of Section 4.1.3, the dynamic heat release rate is dependent on the ratio c_1/c_0' evaluated at the flame front and the flame exit. At the flame front, this is quite straightforward. So long as Ω is nonzero,

$$\left.\frac{c_1}{c_0'}\right|_{x=L_f} = -\frac{J}{A}\left\{B^{(f)+}\exp\left(-k^+\mathcal{L}\right) + B^{(f)-}\exp\left(-k^-\mathcal{L}\right)\right\} - \frac{1}{j\Omega}. \tag{4.70}$$

Recall that J is the jump coefficient, defined in the text on page 180.

However, at the flame exit, both c_1 and c_0' approach zero, thus requiring the application of L'Hôpital's rule.

$$\left.\frac{c_1}{c_0'}\right|_{x=L_e} \rightarrow \left.\frac{c_1'}{c_0''}\right|_{x=L_e} = \frac{k^+B^{(f)+} + k^-B^{(f)-}}{-A} - \frac{1}{j\Omega}. \tag{4.71}$$

Substituting into Equation 4.23, the unsteady heat release rate is given by

$$\hat{q_1} = \left(-k^+ + J\exp\left(-k^+\mathcal{L}\right)\right)B^{(f)+} + \left(-k^- + J\exp\left(-k^-\mathcal{L}\right)\right)B^{(f)-}. \tag{4.72}$$

Figure 4.6 shows the magnitude, phase, and group delay for the unsteady heat release rate response to acoustic oscillations as a function of frequency for various operating conditions.

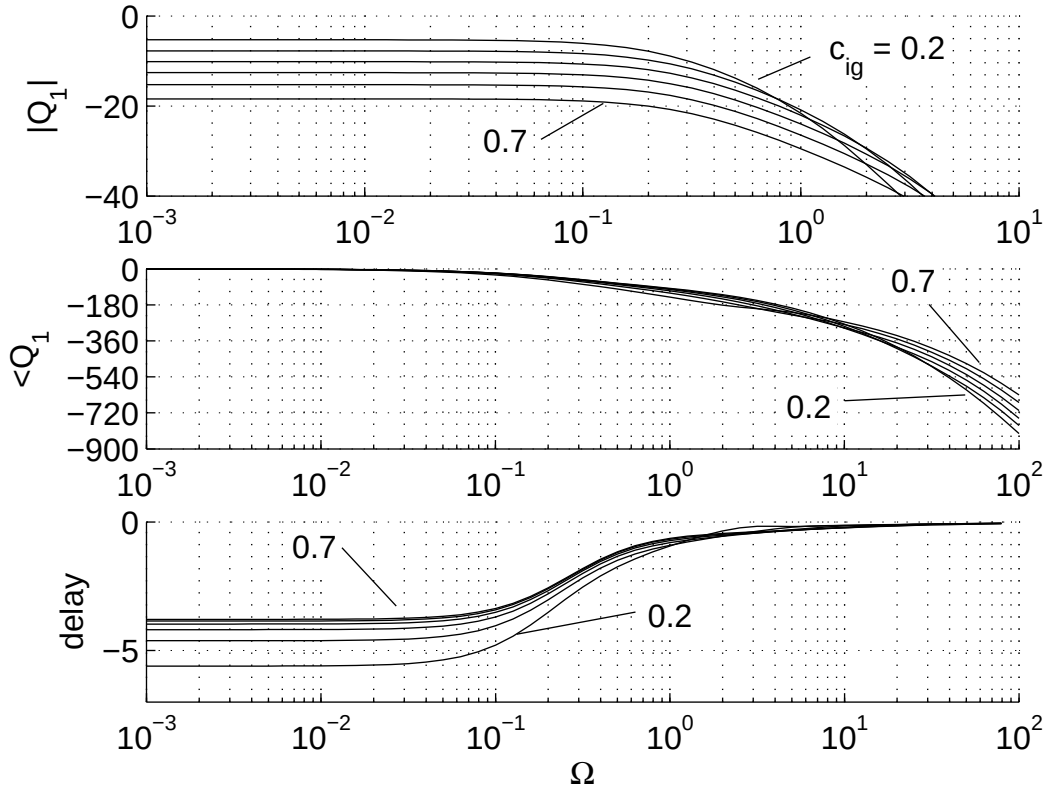

Figure 4.6: Heat release rate response to velocity inputs. Shown at $\hat{U} = 0.8$ and various values of c_{ig}.

4.2.3 Eigenvalues

It is evident from the character of the heat release frequency response in Figure 4.6, that there is one dominant frequency at which the response changes. It is possible, however, that there are more characteristic frequencies whose affects are simply less pronounced. These frequencies are determined by the eigenvalues or poles of the system.

Thus far, the entire analysis is predicated on the character of the excitation and not on the system itself. It is possible, however, with minimal difficulty, to consider the case that there is no excitation and that the only source of dynamics is from decaying initial conditions. Thus, instead of writing the solution in terms of $\exp\left(j\Omega\hat{t}\right)$, one writes

$$c = c_0 + \epsilon c_1 \exp\left(\lambda\hat{t}\right) + \mathcal{O}(\epsilon^2). \tag{4.73}$$

The acoustic excitation, $\hat{v}$, is taken to be zero, so that the c_0' term in Equation 4.20 vanishes and all of the instances of the particular solution in the previous sections are removed. That leaves the problem of solving

$$\dot{c}_1 + \hat{U}c_1' - c_1'' = 0, \tag{4.74}$$

subject to initial conditions. For the moment, since there are no particular initial conditions that are of interest, there is no need to specify them.

The problem must, however, obey identical boundary and jump conditions. Without the

forcing term, however, the problem becomes

$$\mathbf{0} = \mathbf{M}(\lambda) \cdot \begin{Bmatrix} B^{(p)+} \\ B^{(p)-} \\ B^{(f)+} \\ B^{(f)-} \end{Bmatrix}. \tag{4.75}$$

Here, $\mathbf{M}$ is the same function as from Equation 4.55, only λ has been substituted for the instances of $j\Omega$.

Because of the lack of forcing, $\mathbf{P}$ from Equation 4.54 is now the zero vector. Therefore, the only values of λ for which a non-trivial solution is allowed is when $\mathbf{M}$ is singular. Thus, λ is an eigenvalue of the flame when

$$\det\left(\mathbf{M}(\lambda)\right) = 0. \tag{4.76}$$

After considerable manipulation, it is possible to show that 4.76 can be reduced to

$$0 = f_1 = J\sinh(\beta\mathcal{L})\sinh(\beta L_f) + \beta\sinh(\beta L_e) \tag{4.77}$$

when

$$\beta = \sqrt{\frac{\hat{U}^2}{4} + \lambda} \qquad\qquad J = \frac{-\hat{U}}{1 - \exp\left(-\hat{U}\mathcal{L}\right)} \tag{4.78}$$

For a detailed derivation of Equation 4.77, see Appendix B.

Numerical considerations Equation 4.77 is highly nonlinear and upon examination it even has a number of properties that make it undesirable from a standpoint of numerical

inversion. Since the governing equation is only first order in time, it is reasonable to limit values of λ to be real, but β is still allowed to transition to be imaginary. That means for $\lambda < -\hat{U}^2/4$, the hyperbolic sines will transition to be ordinary sines and the entire problem becomes oscillatory. Thus, there will be local maxima and minima from which a Newton algorithm is unlikely to recover.

Additionally, $\beta = 0$ is always a solution. This corresponds to the special case when $k^+ = k^-$, and the assumed form of the solution becomes linearly dependent and not to an actual eigenvalue.

Both of these issues can be avoided by instead considering the criterion,

$$0 = f_2 = \frac{J \sinh(\beta \mathcal{L}) \sinh(\beta L_f)}{\beta \sinh(\beta L_e)} + 1. \tag{4.79}$$

At first glance, this would seem to make the problem worse since there is now a singularity when $\beta = 0$, and there are periodic singularities when βL_e is a multiple of π.

Figure 4.7 shows f_1 and f_2 plotted over λ. Not only does f_2 no longer predict the false root, but because the singularity there is appears as $\mathcal{O}(\beta^2)/\mathcal{O}(\beta^2)$, points near it approach a finite value smoothly. It is a simple matter to detect β's proximity to zero and implement L'Hôpital's rule when necessary.

On the other hand, the singularities can be changed from a numerical challenge to a numerical advantage. They occur at the points

$$\beta_n^{(s)} = j\pi L_e n, \tag{4.80}$$

when $n > 0$. When neighboring singularities approach opposite extrema, continuity between them guarantees that they bracket a solution. For even extremely stiff functions, there are

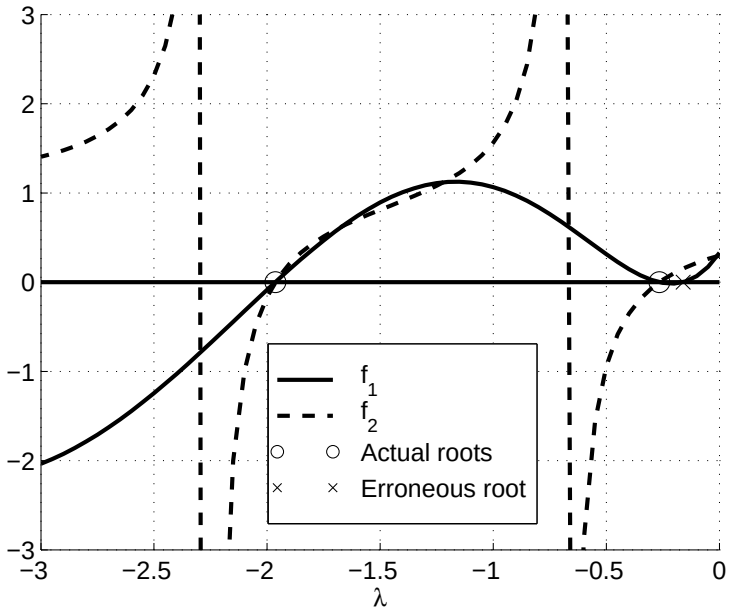

Figure 4.7: Eigenvalue error functions plotted against the eigenvalue, λ, when $\hat{U} = 0.8$ and $c_{ig} = 0.3$.

well established methods for guaranteed convergence to a bracketed solution. Figure 4.8 shows the first two eigenvalues over $\hat{U}$.

4.3 Results and discussion

4.3.1 Low-frequency behaviors

Low-frequency responses can be characterized by the DC gain. The term low-frequency implies that the response occurs at frequencies low enough to ignore all dynamics. That implies that the transfer function that describes the linear relationship between input and output becomes purely real; possessing a phase of 0 or 180 degrees, corresponding to a positive or negative gain respectively. Qualitatively, the DC gain describes the sensitivity of

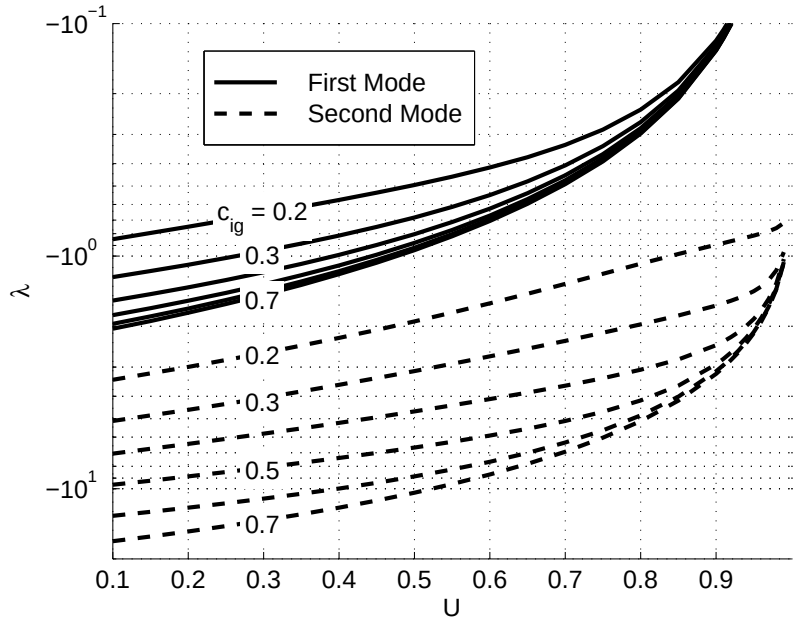

Figure 4.8: First and second eigenvalues plotted against $\hat{U}$ for various values of c_{ig}.

the system to slow changes in the input.

The DC gain can be calculated two ways. By definition, the DC gain is simply the amplitude of the transfer function as $\Omega \to 0$, so the derivation devoted to low-frequency behaviors in section 4.2.2 becomes quite useful. Repeating the heat release derivation yielding Equation 4.72 for the low-frequency case yields

$$\begin{aligned} K = \lim_{\Omega \to 0} q_1 =& A \left(- \frac{c_1}{c_0'}\bigg|_{\hat{x}=L_f} + \frac{c_1'}{c_0''}\bigg|_{\hat{x}=L_e} \right) \\ =& \hat{U} B^{(f)+} + b^{(f)} + a^{(f)} \mathcal{L} - \frac{B^{(f)+} \exp(-\hat{U}\mathcal{L}) + B^{(f)-} - b^{(f)} \mathcal{L}}{1/\hat{U} \left[1 - \exp(-\hat{U}\mathcal{L}) \right]} \end{aligned} \tag{4.81}$$

Figure 4.9 shows the resulting gains for a wide variety of operating conditions.

Since DC gain is a system characteristic in the absence of dynamics, it can alternately be calculated from the static model as the sensitivity of the total heat release rate to changes

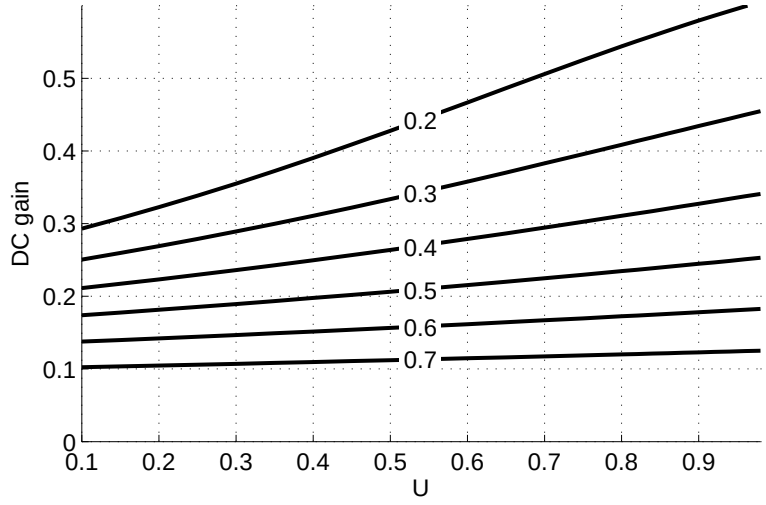

Figure 4.9: DC gain plotted against $\hat{U}$ for various values of c_{ig}.

in velocity,

$$K = \frac{\partial q_0}{\partial \hat{U}}. \tag{4.82}$$

Figure 4.10 shows the steady heat release rate, calculated from Equation 4.22. Observe that the gains calculated in Figure 4.9 are consistent with the slopes of the curves in Figure 4.10.

Figure 4.10 is also identical to Figure 4.3, but with different units. That is a consequence of the ignition model. As already established in Equation 4.22, assuming a constant reaction rate intensity implies that the heat release rate is simply proportional to the flame thickness. This turns out to be true not only statically, but instantaneously as well. Thus, the flame heat release dynamics are identical to the flame size dynamics, just as measured by Ranalli et. al.[53].

At first glance, it is counter intuitive that the heat release curve does not intersect zero at zero velocity. However, as discussed in Section 3.2.2 and shown in Equation 4.42, even in the

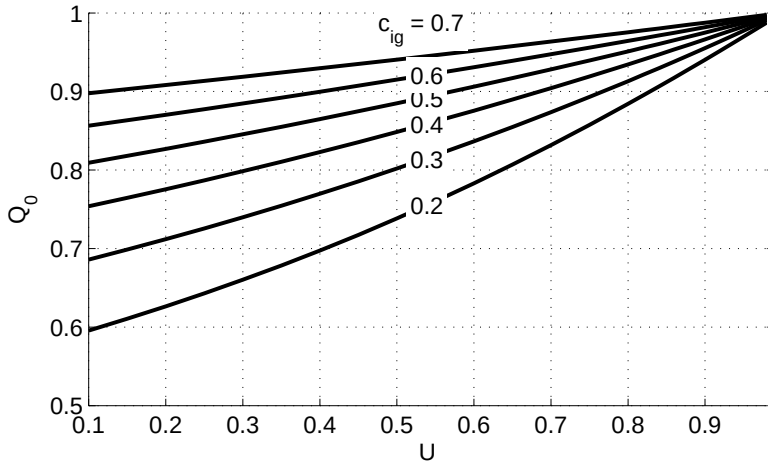

Figure 4.10: Heat release rate plotted against $\hat{U}$ for various values of c_{ig}.

absence of convection, the flame is sustained by the diffusion of species. The flame position is determined by a balance between convection and diffusion. Fresh reactants must be supplied to the flame at a rate sufficient to sustain the rate at which energy is lost. When $\hat{U} = 1$, the flame is infinitely far from the burner, and convection is the only remaining force driving reactants and energy in and out of the flame. However, as velocity diminishes, reactants are instead supplied by diffusion from the burner, and temperature is similarly lost to the burner. For flames with low lewis numbers, the delivery of species is sufficient to sustain the reaction.

Since this means the heat release rate curve never reaches zero, it is flatter than if it did. Ultimately, that has the effect of lessening (sometimes severely) the DC gain from that of high lewis number flames. In reality, the intensity of the turbulent mixing and therefore the diffusivity will also change with velocity, so determining the *actual* path in the parameter space as velocity is varied might yield yet more complicated behaviors.

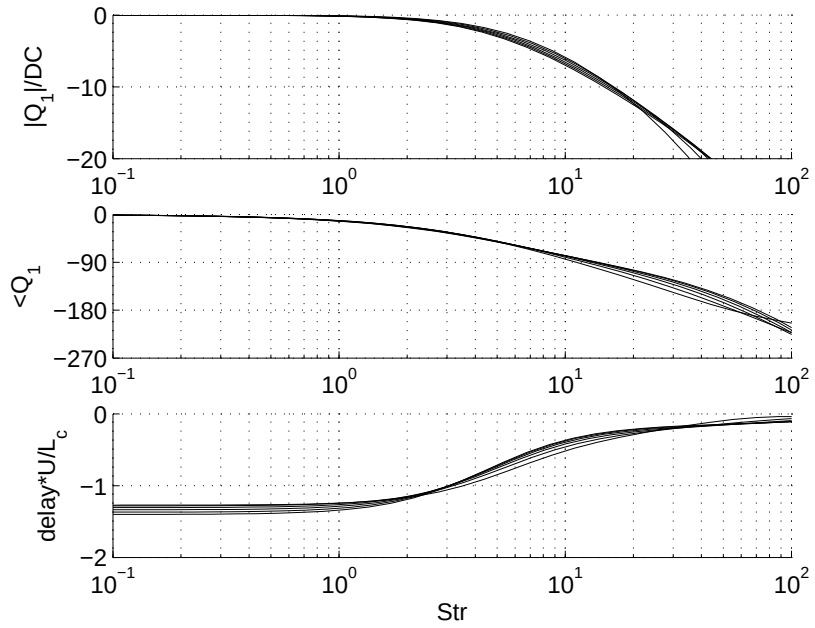

Figure 4.11: Heat release transfer function scaled by Strouhal number for various values of c_{ig} at $\hat{U} = 0.8$.

4.3.2 Frequency scaling

Since so many turbulent flames have been observed to scale well with the Strouhal number, it is only natural to see how frequency phenomena in the present model scales. Figure 4.11 shows the heat release rate transfer function plotted against the Strouhal number, $Str = 2\pi L_c \Omega / \hat{U}$. The magnitudes collapse quite nicely, and even the delay seems to scale well with the convective time.

Though the scaling appears to be successful, comparison at multiple velocities is not so successful. Figure 4.12 shows the Strouhal number computed from the first two eigenvalues, $Str = 2\pi L_c \lambda / \hat{U}$ for a wide variety of operating conditions. A successful scaling would reduce the set of curves to a single horizontal line. However, it is clear that the Strouhal number only captures affects from varying c_{ig}.

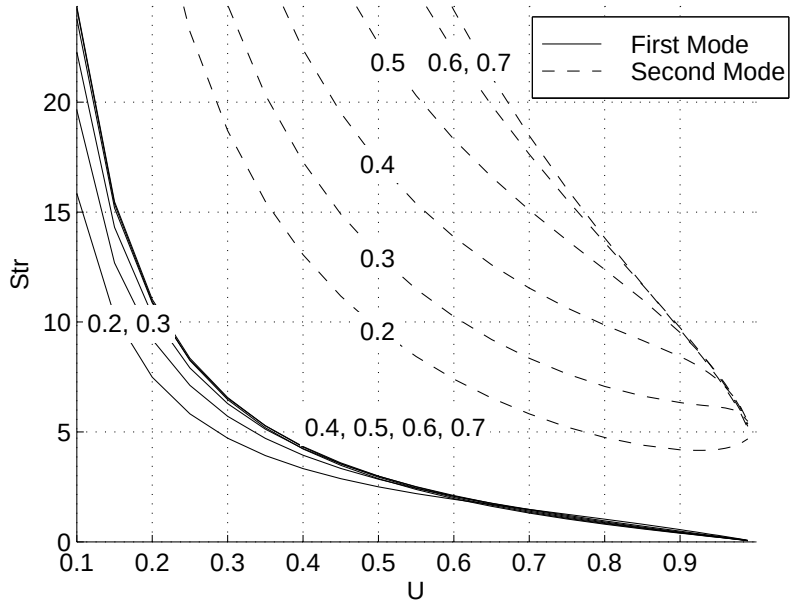

Figure 4.12: Eigenvalues scaled by the Strouhal number, $Str = 2\pi L_c \lambda / \hat{U}$, as a function of velocity for various values of c_{ig}.

Figures 4.13 and 4.14 show transfer functions at $\hat{U} = 0.5$ and $\hat{U} = 0.8$ respectively where the frequency has been scaled by λ_1 instead. As one would expect, the cutoffs are precisely at $\Omega/\lambda_1 = 1$. The dotted lines represent the response of a first-order system with an eigenvalue at λ_1. The agreement between the model and the first order system is reasonable at low and even moderate frequencies. However, the model deviates significantly from the first-order system at frequencies above λ_2.

The implication is that the underlying dynamics are more complicated than the convective delay. Though λ can be implicitly related to the flame's length scales, the relationship is more sophisticated than convection alone. Since the use of the Strouhal number is taken from the study of inclined flames such as those stabilized by swirl or by bluff bodies, it can be little surprise that its application to this model has only limited success.

The present model might be extended to include the dynamics relevant to inclined flames

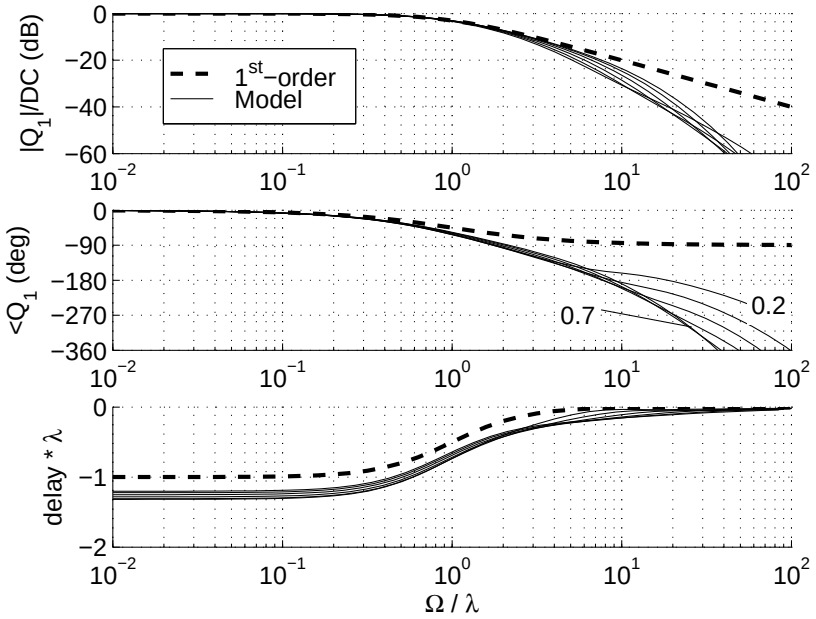

Figure 4.13: Heat release transfer function scaled by the first eigenvalue, λ_1, at $\hat{U} = 0.5$.

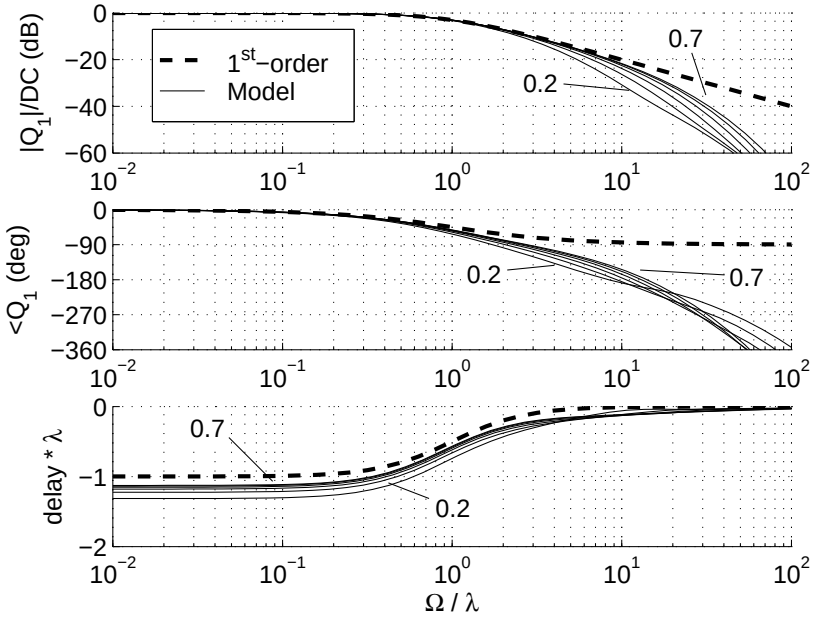

Figure 4.14: Heat release transfer function scaled by the first eigenvalue, λ_1, at $\hat{U} = 0.8$.

in several ways. Most intuitively, an additional spatial dimension could be added and the boundary conditions modified to allow for the propagation of waves along the flame front. On the other hand, to retain the simplicity of a single spatial dimension, an inclined flame might be thought of as having some average axial reaction progress similar to that of the current model, but excited by a new mode of forcing. Instead of driving the flame with velocity directly, the effect of coherent structures such as rich mixtures or vortices could be modeled as a region of enhanced reaction that is convolved through the flame. Certainly the former is the more physical of the two, but the latter preserves the desirable simplicity of the current approach.

4.3.3 Delay

Delay seems to be a consistent component of a flame's acoustic response. This is linked with the time required for coherent structures in the flow forced by the acoustic oscillations to reach the flame's center[53, 27]. That this model seems to exhibit similar low-frequency delay is puzzling since there is no inherent support for vortex or scalar wave convection that might cause delay.

Further investigation shows that though the delay seems to scale fairly well with the convection time in Figure 4.6, this is, in fact, a coincidence. In general, the low-frequency delay is completely unrelated to the convective delay time. Instead, the delay is completely consistent with ordinary over-damped dynamics.

Figure 4.13 and 4.14 show the delay scaled by λ_1 instead of the convection time. While the scaling is quite consistent, and the behaviors are quite similar, the first-order estimate is not precise. It is clear that the actual low-frequency delay is significantly higher than that of the first-order estimate.

It is actually quite straightforward to show why this occurs. Consider the first-order system is over the form

$$G_1 = \frac{1}{j\Omega/\lambda_1 - 1}. \tag{4.83}$$

Its low-frequency group delay of Equation 4.83 is given by

$$\begin{aligned} t_1 &= \lim_{\Omega \to 0} -\frac{\mathrm{d}\phi_1}{\mathrm{d}\Omega} \\ &= \lim_{\Omega \to 0} \frac{\mathrm{d}}{\mathrm{d}\Omega} \arctan(\Omega/\lambda_1) \\ &= \lim_{\Omega \to 0} \frac{1/\lambda_1}{1 + (\Omega/\lambda)^2} \\ &= 1/\lambda_1. \end{aligned} \tag{4.84}$$

Similarly, a system containing the first two poles might be given by

$$G_2 = \frac{1}{(j\Omega/\lambda_1 - 1)(j\Omega/\lambda_2 - 1)}, \tag{4.85}$$

with low-frequency delay given by

$$\begin{aligned} t_2 &= \lim_{\Omega \to 0} -\frac{\mathrm{d}\phi_2}{\mathrm{d}\Omega} \\ &= \lim_{\Omega \to 0} \frac{\mathrm{d}}{\mathrm{d}\Omega} \{\arctan(\Omega/\lambda_1) + \arctan(\Omega/\lambda_2)\} \\ &= 1/\lambda_1 + 1/\lambda_2. \end{aligned} \tag{4.86}$$

It seems reasonable to postulate that the actual delay exhibited by the system is calculated

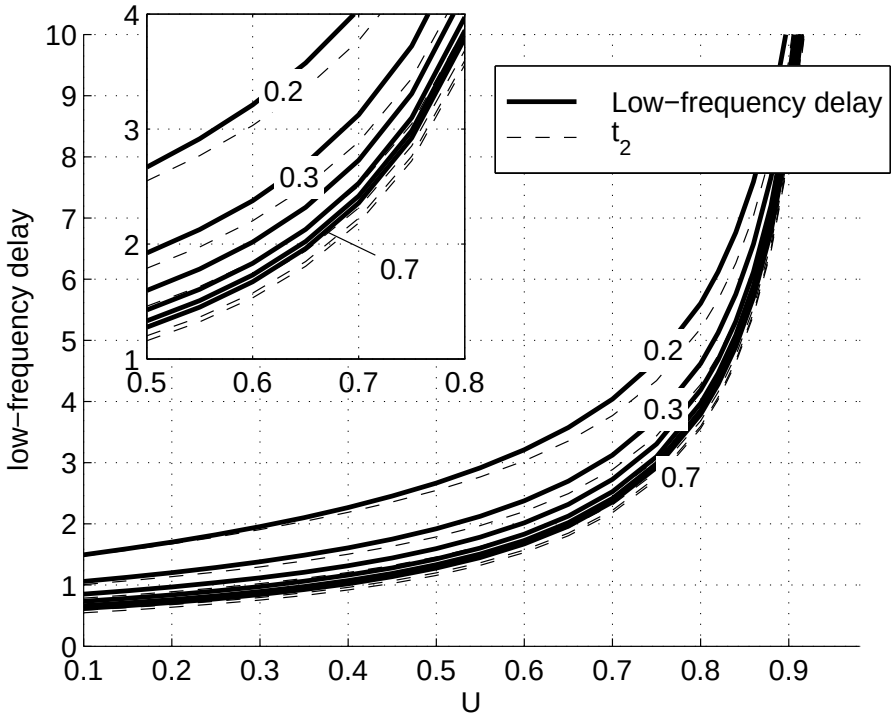

Figure 4.15: Low-frequency delay and the t_2 estimate plotted against $\hat{U}$ for various values of c_{ig}.

by the infinite series,

$$t_\infty = \sum_{n=1}^{\infty} \frac{1}{\lambda_n}. \tag{4.87}$$

It is important to note that this formulation excludes the possibility of zeros that would also affect the low-frequency delay. Since the present work includes no proof that the flame transfer function has no zeros, this is not a safe assumption. However, 4.87 does seem to represent the delay quite well. Figure 4.15 shows the model's low-frequency delay plotted with the t_2 delay.

This revelation actually allows for a general form approximating the flame transfer function. Precluding the discovery of some heretofore undiscovered system zeros, the total heat release

transfer function can be written in the form

$$\frac{q_1}{\hat{v}} = K \prod_{n=1}^{\infty} \frac{1}{s/\lambda_n - 1}. \tag{4.88}$$

4.3.4 Comparison with experiments

Though the model does not exhibit the same behaviors exhibited by flames with more complicated geometries, there is also data available in literature describing the dynamic behavior of flat turbulent flames. The study conducted by Lawn et. al. on a turbulent flame's response to normal acoustic excitation provides just such insights. The authors stabilized a normally propagating turbulent flame in a conical expansion, where they excited the flame with an acoustic driver. This corresponds to the case that $\hat{U} \to 1$.

The authors recorded, among other things, the response of the flame's leading and trailing edges with respect to acoustic excitation. They noted that the flame front responded with large oscillations, while the flame thickness varied very little if at all.

It is quite convenient to compare the model's prediction with these observations. The leading edge is defined as L_f, such that

$$c(L_f) = c_{ig}. \tag{4.89}$$

However, acknowledging that L_f will fluctuate, it becomes possible to expand it as well with respect to ϵ, so that $L_f = L_{f,0} + \epsilon L_{f,1} + \mathcal{O}(\epsilon^2)$. Expanding Equation 4.89,

$$c(L_f) = c_0(L_{f,0}) + \epsilon c_1(L_{f,0}) + \epsilon c_0'(L_{f,0}) L_{f,1}. \tag{4.90}$$

Because c_{ig} does not scale with ϵ, its coefficients must sum to zero. Therefore,

$$L_{f,1} = -\left.\frac{c_1}{c_0'}\right|_{x=L_{f,0}}. \tag{4.91}$$

Observe that Equation 4.91 is the negative of the first term in the heat release rate in Equation 4.23. This is intuitive since $q_1 = A\mathcal{L} = A(-L_f + L_e)$. It comes as no surprise, then, that after repeating these steps for L_e, one obtains

$$L_{e,1} = -\left.\frac{c_1}{c_0'}\right|_{x=L_{e,0}}. \tag{4.92}$$

Figure 4.16 shows transfer functions for the leading and trailing edge positions for various velocities. Note that when the velocity is low, L_f has little response, while L_e has a very significant response, indicating that the flame thickness is varying significantly. As the velocity increases, and the flame is pushed farther downstream, the response of L_f and L_e approach one another, indicating that the flame thickness (and subsequently the heat release) exhibits a diminishing response.

When the flame is close to the burner, its position is determined more and more by diffusive processes and less by convection. However, as the flame is pressed away from the burner, the position is only loosely constrained. In fact, as $\hat{U} \to 1$, the DC gain of the $L_{f,1}$ transfer function is infinite since there are absolutely no remaining physical processes determining the flame position. In effect, the flame is, instead, propagating at its flame speed while utterly unaware of the fluid's motion relative to laboratory coordinates.

4.3.5 Summary

The Reynolds averaged model presents the following key traits:

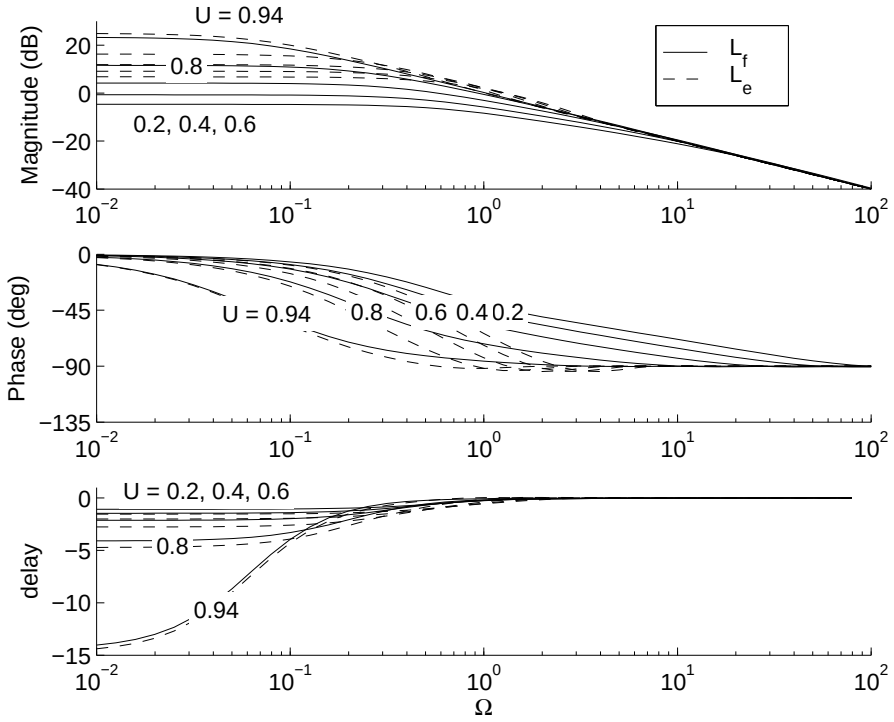

Figure 4.16: Leading and trailing edge transfer functions for various values of $\hat{U}$.

- Equation 4.79 indicates that a flame that obeys the underlying assumptions of the model will exhibit a cutoff frequency that can be determined knowing only the fluid velocity and the steady flame position;
- The magnitude behaves roughly like a first-order low-pass system, but with faster rolloff;
- The phase exhibits low-frequency delay behavior resembling, but actually more complicated than a first-order system;
- Strouhal frequency scaling fails with respect to change in velocity, but succeeds with respect to changes in c_{ig};
- Convective delay scaling fails altogether;
- Delay actually scales with the eigenvalues;
- The flame seems to be well approximated by a system of the form;
- The system does not appear to exhibit dynamic behavior consistent with zeros.

The following conclusions can be drawn from these observations:

1. The relationship between the flame geometry and its frequency response is more sophisticated than that of swirl stabilized flames that scale with only the Strouhal number;
2. The model's predominant dynamics are not convective in nature, but instead obey the relaxation of a standing wave;
3. The convective phenomena present in inclined flames such as swirl stabilized flames are caused by phenomenology absent in the present model;
4. Flat flames seem to be well represented by the present model;

5. If the system actually exhibits no zeros, then the transfer function can be written as

$$\frac{q_1}{\hat{v}} = K \prod_{n=1}^{\infty} \frac{1}{s/\lambda_n - 1} \tag{4.93}$$

Chapter 5

Conclusions

5.1 The Bhorgi diagram

The findings of the previous chapters are best understood within the context of the scaling techniques typically used to construct the Bhorgi diagram. The so-called Bhorgi diagram is derived from the notion that a static flame's character can by the relationship between the turbulence time scales and the reaction time scales[47].

Kolmogorov scales In a turbulent flow, the unsteady turbulent features occupy a certain rage between the integral scale, (L, t_L), and the Kolmogorov scale, (η, t_η). The integral scale is on the same order of magnitude as the geometric features of the steady flow such as the combustor diameter. The Kolmogorov scale is, by definition, the smallest scale at which turbulent features survive before being destroyed by viscous losses. Between the two extremes, there is a point where the turbulent eddies take on a character that is independent of the integral scale geometry and is universal to all flows.[49]

The velocity at each length scale, is simply related to the length and time scales by $u_l = l/t_l$. Therefore, there is a Reynold's number at each length scale, given by

$$Re_l = \frac{u_l l}{\nu} = \frac{l^2}{t_l \nu}. \tag{5.1}$$

There are two constraints used to relate the Kolmogorov scales to the integral scales. Firstly, the smallest scalles will occur when the momentum and viscous forces ballance, and $Re_\eta = 1$. The second constraint is taken from the idea of the "energy cascade". That is, that the only source of energy lies in the integral length scales and that the smaller scales draw their energy

from those. The rate of dissipation is, therefore, equal across all the scales,

$$\epsilon = \frac{{u_l}^2}{t_l} = \frac{{u_l}^3}{l} = \frac{{u_\eta}^3}{\eta}. \tag{5.2}$$

Therefore, the Kolmogorov scales can be written in terms of the integral scales as

$$\frac{\eta}{L} = {Re_L}^{-3/4} \tag{5.3}$$

$$\frac{t_\eta}{t_L} = {Re_L}^{-1/2} \tag{5.4}$$

$$\frac{u_\eta}{u_L} = {Re_L}^{-1/4}. \tag{5.5}$$

Therefore, for fully turbulent flows ($Re > 10^4$), the Kolmogorov velocity, length, and time are much smaller than the respective integral scales, indicating that turbulent motions are present on a very wide range of scales.

Damköhler and Karlovitz number The way in which the two extreme scales present in turbulence relates to the scales relevant to the flame are represented by two corresponding dimensionless numbers; the Damköhler and Karlovitz numbers.

The Damköhler number relates the convection times to the chemical times in a flame. Therefore, the Damköhler number can be written at any length scale, $Da_l = t_l/t_r$. However, it is typically written at the integral length scale, so that when no length is specified,

$$Da = \frac{t_L}{t_r} = \left(\frac{L}{\delta}\right)\left(\frac{u_L}{S_L}\right)^{-1}. \tag{5.6}$$

The Karlovitz number is identical in that it describes a ratio of convective to reactive time

scales, but it is defined at the Kolmogorov scales instead of the integral scales,

$$Ka = {Da_\eta}^{-1} = \frac{\delta/S_L}{L/u_L} Re_L^{1/2}. \tag{5.7}$$

Thus, together, the Karlovitz and the Damköhler numbers describe how the chemical reaction compares with the full range of turbulent time scales. When $Da < 1$, even the slowest of the turbulent transport times is faster than the chemical time. On the other hand, when $Ka > 1$, even the fastest of the turbulent transport times is slower than the chemical time. Both extremes imply that the turbulent processes may be decoupled from the chemical ones.

The Bhorgi diagram The classical Bhorgi diagram considers the space described the dimensionless turbulence intensity , u_L/S_L, and the dimensionless turbulence length scale, L/δ. These two dimensionless parameters are explicitly present in Equation 5.6. The Karlovitz number, on the other hand requires some additional manipulation before it can be expressed thusly.

Because the kinematic viscosity is on the same order of magnitude as the fluid's thermal diffusivity, the Reynold's number can also be approximated as

$$Re_L = \frac{u_L L}{\nu} \approx \left(\frac{u_L}{S_L}\right)\left(\frac{L}{\delta}\right).$$

Therefore, the Karlovitz number can also be written

$$Ka = \left(\frac{u_L}{S_L}\right)^{3/2}\left(\frac{L}{\delta}\right)^{-1/2}. \tag{5.8}$$

Figure 5.1 shows the classical Bhorgi diagram with lines of $Da = 1$ and $Ka = 1$ marked. Regions are makred by physical characteristics of flames that are observed there and the

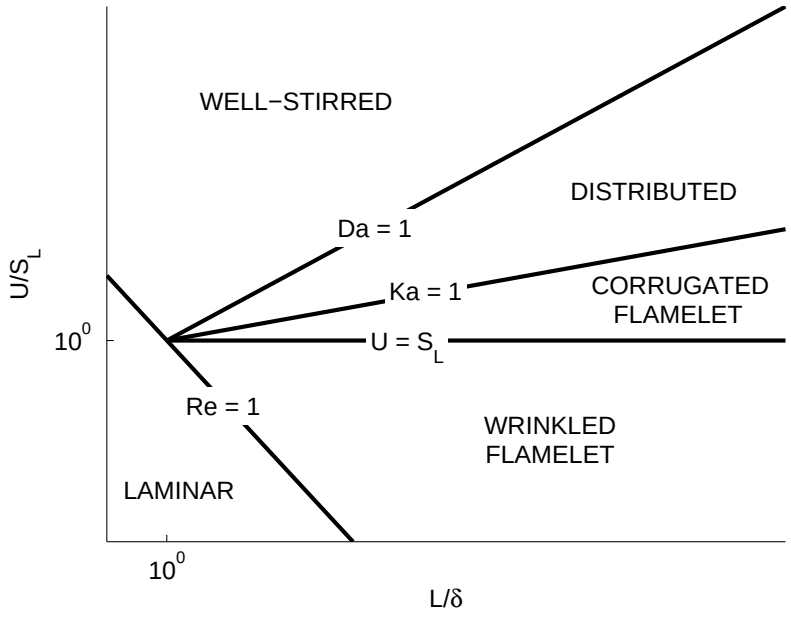

Figure 5.1: Classical Bhorgi diagram.

corresponding models that are most appropriate to them.

At the bottom of the diagram, the turbulence intensity is quite low, so the reaction region is a thin sheet that is convected with the unsteady flow. As the turbulence intensity increases, the turbulent velocity eventually out-paces the flame speed and it becomes possible for the turbulence to cause local extinctions in the corrugated flamelet region. As the turbulence intensifies still higher, the slowest of the turbulence scales out-paces the reaction time, and the reaction region is thickened by the transport of intermediate species and energy from the flame center. Lastly, as even the integral scales out-pace the reaction time scale, the intensity of the mixing overwhelms the reaction time scale, and the reaction region expands to occupy a large region and is considered well mixed.

5.2 Summary of turbulence regimes

Chapters 2, 3, and 4 establish frequency response funcitons of various flame heat release rates in resposne to velocity oscillations. In each case, there is some critical dimensionless frequency, Ω_c, below which the flame's response is quasi-static, and above which the response exhibits a declining amplitude with significantly decreasing phase.

The following discussion reviews the results of the previous chapters and connects them conceptually with the prevalent literature.

5.2.1 Highly turbulent

The highly turbulent regime is approximated by the well-stirred reactor (WSR), which, depending on the mode of forcing and the thermodynamic properties of the species present, exhibits dynamic events at two frequency scales; one consistent with the chemical time scale and one consistent with the residence time.

Major behaviors While the WSR is capable of exhibiting dynamics on the residence time scale, regardless of the forcing they are minor in comparison with those at the chemical time scale. Regardless of the forcing and reagrdless of the the species involved, the most significant dynaic event occurs around the dimensionless frequency, Ω,

$$\Omega = t_r\omega \approx R' \approx \mathcal{O}(1). \tag{5.9}$$

While there is some variation about the curve $\Omega \approx 1$ since it is only an order-of-magnitude approximation, it is valid over a very wide range of conditions, making it quite powerful despite its limited accuracy.

Minor behaviors The low-frequency events are exhibited only when the system is forced through incoming misture oscillations and only when the species present exhibit excentric enthalpies. The severity of the dynamics associated with these processes is determined by the severity of the excentricity of the species' enthalpies. For typcial values, the event is extremely minor and is of little importance in determining the system's dynamic response.

These events scale exactly,

$$\Omega = t_r \omega = \frac{t_r}{t_m} = Da. \tag{5.10}$$

Chapter 2 focusses on the case where the residence time, t_m is independent of the turbulence scale, t_L. In reality,

Comparitive scales The WSR's transition from a quasi-static response to a truely dynamic response occurs at frequencies corresponding to the reaction time scale, t_r. Though the residence time scale, t_m, can absolutely be slower, its affects are minor when they occur at all, and can actually be neglected from the model with little loss in acuracy.

Figure 5.2 depicts the WSR's turbulent and reaction time scales on parallel frequency and time axes. For the WSR, the reaction time scale is longer than the slowest of the turbulent time scales, by the nature of the Damköhler number restriction,

$$Da_t = \frac{t_L}{t_r} < 1. \tag{5.11}$$

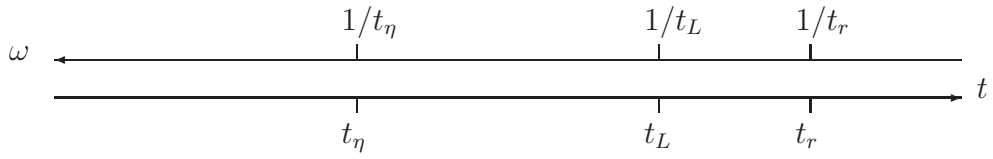

Figure 5.2: Well stirred regime reaction, integral, and Kolmogorov scales depicted on time and frequency axes.

5.2.2 Moderately turbulent

Together with the findings of Chapter 4 and the results shown in literature, there are two frequency scales that might be exhibited by a turbulent flame depending on its means of stabilization. Like laminar flames, inclined flames demonstrate a completely different frequency scaling than do burner-stabilized flames.

Inclined flames From literature, there is the well-established Strouhal number scaling valid for both bluff body and swirl stabilized flames,

$$Str = \frac{L\omega_c}{U} \approx 1, \tag{5.12}$$

where L is the distance from the burner outlet to the center of heat release of the flame cone (integral length scale), U is the unburned gas velocity, and ω_c is the critical frequency. However, taking advantage of the definition of flame speed, it is possible to write

$$\frac{\omega_c L}{U} = \frac{\omega_c t_r S_L L}{\delta U} = \Omega_c \frac{L/\delta}{U/S_L} \tag{5.13}$$

Thus, Ω_c scales explicitly in terms of the dimensionless length and velocity scales

$$\begin{aligned}\Omega_c &\propto \left(\frac{U}{S_L}\right)\left(\frac{L}{\delta}\right)^{-1} \\ &= Da^{-1}\end{aligned} \tag{5.14}$$

Flat flames The present work also shows that the critical frequency of a burner-stabilized flame scales very crudely as a power of the flame's distance to the burner, L, so that

$$\Omega_c = \omega t_r \propto \left(\frac{L}{\delta_t}\right)^m. \tag{5.15}$$

Here, δ_t is the turbulent diffusion length scale from Chapter 4. The exponent, m,

It can be related to the laminar length scale through its definition,

$$\delta_t = \sqrt{D_t t_r} = \delta\sqrt{\frac{D_t}{\alpha}}. \tag{5.16}$$

From Taylor's theory of turbulent diffusion[49], D_t scales like the multiple of the integral velocity and length scales, UL. Therefore, the critical frequency scales

$$\begin{aligned}\Omega_c &\propto \left(\frac{L}{\delta}\right)^m \left(\frac{UL}{\alpha}\right)^{-m/2} \\ &= \left(\frac{L}{\delta}\right)^{m/2} \left(\frac{U}{S_L}\right)^{-m/2} \\ &= Da^{m/2}.\end{aligned} \tag{5.17}$$

Comparative scales Figure 5.3 shows the relevant time and frequency scales on parallel axes. There are three time scales of primary interest; the reaction time, the integral time, and the burner stabilized time, t_b.

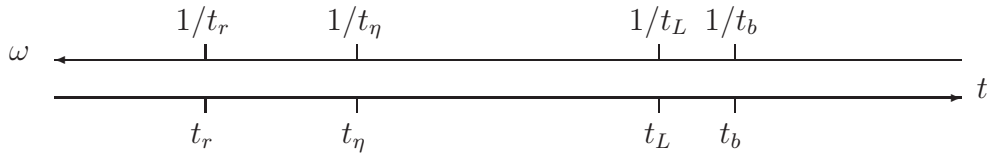

Figure 5.3: Flamelet regime reaction, integral, and Kolmogorov scales depicted on time and frequency axes.

Because these scalings are derived on the premise that the integral scales are comparable to the mean scales, the integral scale is coincident with the Strouhal scaling for inclined flames. This is easily verified by inspection of Equation 5.12.

The burner-stabilized time scale, t_b, is taken from Equation 5.17. Whether it is greater or less than the integral time scale depends on the value of m. Since $Da > 1$ in these regimes, when $m < -2$, the burner time scale is slower than the integral time scale, and the converse is also true. Regardless, the burner time scale is not far from the integral time scale.

By virtue of the flamelet and distributed flame regimes, the reaction time is faster than the integral scale. The implication is that reaction dynamics are sufficiently fast in this regime to be considered quasi-steady relative to the integral and burner dynamics.

5.2.3 Laminar

Laminar flames are also shown both in literature and in the present work to exhibit two frequency responses depending on the stabilization mechanism. Inclined flames such as V- and inverted-V-shaped flames exhibit a Strouhal number scaling, while the burner stabilized flame transfer function scales with the flame distance to the burner, L,

$$\Omega_c \propto \left(\frac{L}{\delta}\right)^m. \tag{5.18}$$

Chapter 3 demonstrates that typical values for m may range from -2 to -3.

Unlike the results of the WSR and Reynolds-averaged model, the laminar frequencies bear no dependence on the turbulent scales since the static length and velocity scales no longer have any bearing on the turbulence scales (which are neglegibly small).

5.3 Comparisons

The frequency scales exhibited by each of the models can be represented by a third axis on the Bhorgi diagram indicating the frequency of excitation. From the previous section, it is clear that there are critical frequencies at which the quasi-static response at low frequencies transitions to the dynamic response characterized by declining amplitude and increasing phase lag at high frequencies. When this critical frequency is depicted on the frequency axis over the various turbulence regimes, it is a surface bounding the static and dynamic regions.

The shape of the surface is obtained from the dominant dynamics of each regime. The well-stirred regime obeys Equation 5.9. The flamelet regime obeys either Equation 5.17 or 5.14 depending on the geometry. Because viscosity already dominates the momentum forces at integral scale in the laminar regime, incoherent turbulent effects are irrelevant there.

The behavior in the distributed regime is uncertain given the present work, but it is reasonable to hypothesize that the flamelet-regime scaling would remain valid there since the anticipated physical processes are quite similar. An inclined flame in the distributed regime should still have the same potential for trans-axial wave propagation. Though the damping might increase as the flame thickness approaches the wavelength of ripples propagating along the flame, the fundamental frequency can reasonably be expected to remain unchanged. Similarly, it is unclear how a burner-stabilized flame model should be any different from the

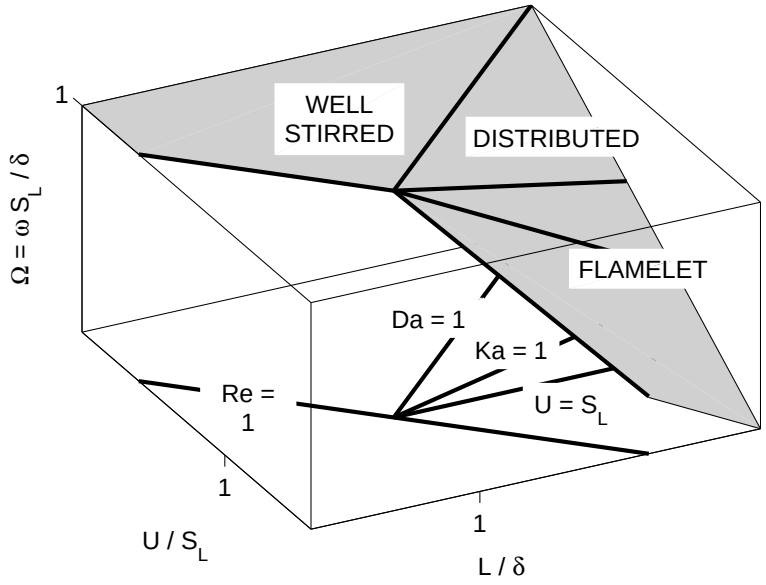

Figure 5.4: The extended Bhorgi diagram for inclined flames (Strouhal scaling).

Reynold's averaged model presented in Chapter 4.

Figure 5.4 shows the resulting surface for inclined flames. Though the Strouhal number scaling and the well-stirred scale are developed from completely independent arguments, that they form a piecewise-continuous surface somewhat substantiates the argument that the distributed regime should maintain the scaling of the flamelet regime.

The surface depicted in Figure 5.4 forms a flat plane that bends sharply along the $Da = 1$ line and descends at a constant rate in log space. Thus, it is convenient to re-orient the Bhorgi diagram so that instead of length and velocity, the axes are the Damköhler number and the Reynold's number. So long as the Reynold's number is greater than unity, the profile of the surface does not change from that of Figure 5.5

Figure 5.5 also shows the profile of the length-scaled burner stabilized flame dynamics for several values of m. Note that when $m = -2$, the Strouhal number scaling and the length

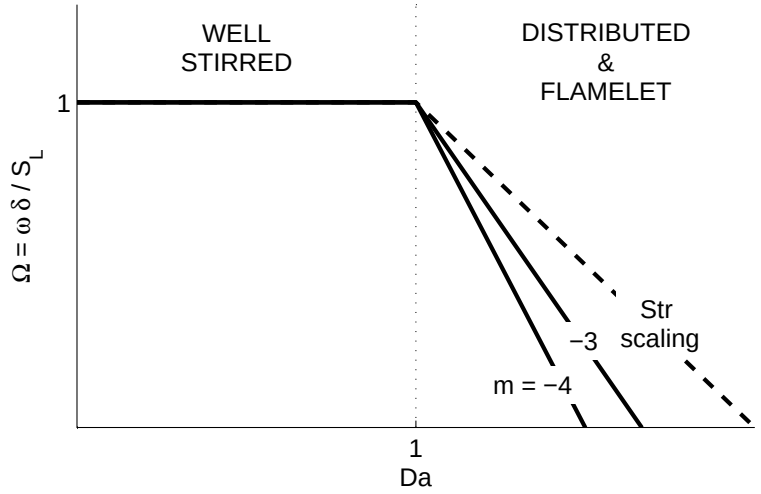

Figure 5.5: A profile of the extended Bhorgi diagram along a line of constant Reynold's number. Both the Strouhal scaling for inclined flames and length scaling for burner-stabilized flames are shown.

scaling are coincident. Despite the fact that the burner-stabilized dynamics are driven by different physical processes than the inclined flame dynamics, their characteristics scale quite similarly.

5.4 Future work

The key result of this work is that there are distinct frequency scales relevant to inclined and flat flames. Though these behaviors are characterized here, more work is needed to describe the transition between them. There are a number of steps that could be taken to accomplish exactly such a characterization while also further unifying the results with existing literature;

1. An experimental study into the laminar transition from burner-stabilized to inclined flame behavior,

2. Extension of the laminar model to include two spatial dimensions to support trans-axial

wave propagation,

3. An experimental study into turbulent burner-stabilized and inclined flames,

4. Similar extension of the Reynolds-averaged model to include two spatial dimesions,

1. Laminar experimental study The existing experimental setup in Chapter 3 could be modified with a solid ring along the quartz tube where the flame could stabilize as it begins to lift from the burner. In this way, the behaviors characterized in Chapter 3 could be extended to observe the transition from burner-stabilized to inclined flames.

Great care would need to be taken to select the size and location of the ring. Too-large a ring placed too far upstream would affect the burner-anchored flame, and too small a ring placed too far downstream might fail to anchor the flame or allow a jump rather than a smooth transition.

2. Laminar model extension By adding a second dimension to the laminar model, it should be feasible to identify two wave numbers; one describing waves passing normal to the flame, and one describing waves propagating along the flame front. The results from literature that scale with Strouhal number all rely on waves propagating along the flame front that are absent in the present work while neglecting the flame's "internal" response that is considered in the present work. A model unifying the two could describe the transition from burner-stabilized to inclined flame response.

3. Turbulent experimental study A burner with grid-generated turbulence could be used to stabilize a flame on the burner surface and observe the acoustic transition that occurs as the mechanism for stabilization transitions. The scale and intensity of the turbulence

could be adjusted by changing the dimensions of the grid and characterized by pressure measurements.

The system could be excited by an upstream acoustic driver, with upstream hotwire measurements, and OH radical chemiluminsence measurements. Ideally, the flame could be stabilized in such a way that even the inclined flame adopts an inherently two-dimensional geometry, preventing the need for complicated imaging, but if a conical flame is all that is practical, the turbulent flame thickness can be assessed by ensemble-averaged PLIF measurements.

4. Turbulent model extension With the addition of trans-axial gradients, it should be possible to calculate a natural frequency for wave phenomena in that direction as well. Based on the results in literature, there is every reason to expect that it will obey the Strouhal scaling.

The key question to this investigation would be to understand the effect the turbulent flame thickness has on the inclined flame. Since most of the modern models that are used to construct arguments for turbulent flames neglect turbulent oscillations, understanding the importance the turbulence has on the frequency response would contribute a great deal to generalizing or establishing limits on models in literature.

Bibliography

[1] F. Baillot, D. Durox, and R. Prud'homme. Experimental study of a premixed vibrating flame. *Combustion and Flame*, 88:149–168, 1992.

[2] R. Becker and R. Günther. In *Proceedings of the Combustion Institute*, 1971.

[3] S. Bhargava and R. N. Ghosh. Note on Trevelyan's rocker. *Phys. Rev.*, 22(5):517–521, Nov 1923.

[4] P. Blackshear. In *Proceedings of the Combustion Institute*, 1953.

[5] R. Borghi. On the structure of turbulent premixed flames. *Recent Advances in Aeronautical Science*, pages 117–138, 1984.

[6] P. Clavin, P. Pelce, and L. He. One-dimensional vibratory instability of planar flames propagating in tubes. *Journal of Fluid Mechanics*, 216:299–322, 1990.

[7] F. Culick. A note on Rayleigh's criterion. *Combustion Science and Technology*, 56:159–166, 1987.

[8] S. Ducruix, D. Durox, and S. Candel. Theoretical and experimental determination of the transfer function of a laminar flame. In *Proceedings of the Combustion Institute*, 2000.

[9] D. Durox, T. Schuller, N. Noiray, and S. Candel. Experimental analysisof flame transfer functions for different flame geometries. In *Proceedings of the Combustion Institute*, volume 32, pages 1391–1398, 2008.

[10] S. Engell and K. Klatt. Nonlinear control of non-minimum phase CSTR. In *American Control Conference*, 1993.

[11] M. Fleifil, A. Annaswamy, Z. Ghoneim, and A. Ghoniem. Response of a laminar premixed flame to flow oscillations: a kinematic model and thermo-acoustic instability results. *Combustion and Flame*, 106:487–510, 1996.

[12] E. D. Gonzalez-Juez, J. G. Lee, and D. A. Santavicca. A study of combustion instabilities driven by flame-vortex interactions. In *41st AIAA/ASME/SAE/ASEE Joint Propulsion Conference & Exhibit*, 2005.

[13] A. Greenwood. Implementation of adaptive filter algorithms for the suppression of thermoacousticinstabilities. Master's thesis, Virginia Polytechnic Institute & State University, 2003.

[14] O. Hirschfelder, C. Curtiss, and D. Campbell. In *Fourth symposium (international) on combustion*, page 190. Williams and Wilkins, 1953.

[15] Y. Huang and V. Yang. Dynamics and stability of lean-premixed swirl-stabilized combustion. *Progress in Energy and Combustion Science*, 35:293–364, 2009.

[16] W. Kaskan. An investigation of vibrating flames.

[17] V. Khanna. *A Study of the Dynamics of Laminar and Turbulent Fully and Partially Premixed Flames*. PhD thesis, Virginia Polytechnic Institute & State University, 2001.

[18] Kiel. Review of advances in combustion control, actuation, sensing, modeling, and related technologies for air breathing gas turbines. In *AIAA paper 2001-0481*, 2001.

[19] K. K. Kuo. *Principles of Combustion*. John Wiley & Sons, Inc., Hoboken, second edition, 2005.

[20] C. Lawn, T. Williams, and R. Schefer. The response of turbulent premixed flames to normal acoustic excitation. In *Proceedings of the Combustion Institute*, volume 30, pages 1749–1756, 2005.

[21] G. Ledder and A. Kapila. The response of premixed flames to pressure perturbations. *Combustion Science and Technology*, 76:21–44, 1991.

[22] A. Lefebvre. *Gas Turbine Combustion*. Taylor and Francis, Ann Arbor, MI, 2 edition, 1999.

[23] P. Libby, A. L. nán, and F. Williams. Strained premixed laminar flames with nonunity lewis numbers. *combustion science and technology*, 34:257–293, 1983.

[24] T. Lieuwen. Modeling premixed combustion - acoustic wave interactions: A review. *AIAA Journal of Propulsion and Power*, 19:765–781, 2003.

[25] T. Lieuwen and B. T. Zinn. The role of equivalence ratio oscillations in driving combustion instabilitiesin low nox turbines. In *Proceedings of the 27th International Symposium on Combustion*, pages 1809–1816, 1998a.

[26] Lignola and DiMaio. Some remarks on modeling the CSTR combustion processes. *Combustion and Flame*, 80:256–263, 1990.

[27] M. Lohrmann and H. Büchner. Prediction of stability limits for LP and LPP gas turbine combustors. *Combustion Science and Technology*, 177:2243–2273, 2005.

[28] D. Losh. Linear stability analysis of a Rijke tube and modeling of turbulent combustion using dynamic well-stirred reactors. Master's thesis, Virginia Polytechnic Institute & State University, 2004.

[29] M. Mahmoud and M. Fahim. Closed-loop performance of inearized CSTR models. In *IFAC Proceedings Series, Automation and Control in Petroleum, Petrochemical, and Desalination Industries*, pages 25–28, 1986.

[30] S. Margolis. Theoretical analysis of steady, nonadiabatic premixed laminar flames. *Quarterly of Applied Mathematics*, 1980.

[31] S. Margolis and B. Matkowsky. Nonlinear stability and bifurcation in the transition from laminar to turbulent flame propagation. *Combustion Science and Technology*, 34:45–77, 1983.

[32] C. Martin. Systematic prediction and parametric characterization of thermo-acousticinstabilities in premixed gas tubine combustors. Master's thesis, Virginia Polytechnic Institute & State University, Blacksburg, VA, 2006.

[33] A. McIntosh. Pressure disturbances of different length scales interacting with conventional flames. *Combustion Science and Technology*, 75:287–309, 1991.

[34] A. McIntosh. The linearized response of the mass burning rate of a premixed flame to rapid pressure change. *Combustion Science and Technology*, 91:329–346, 1993.

[35] A. McIntosh. Deflagration fronts and compressibility. *Philosophical Transactions of the Royal Society, London*, A:3523–3538, 1999.

[36] A. McIntosh and J. Clarke. Second order theory of unsteady burner-anchored flames with arbitrary lewis number. *Combustion Science and Technology*, 38:161–196, 1984.

[37] A. McIntosh and S. Rylands. A model of heat transfer in Rijke tube burners. *Combustion Science and Technology*, 113-114:273–289, 1996.

[38] K. McManus, T. Poinsot, and S. Candel. A review of active control of combustion instabilities. *Progress in Energy and Combustion Science*, 19:1–29, 1993.

[39] J. Merk. In *Proceedings of the combustion institute*, 1956.

[40] L. Nord. A thermoacoustic characterization of a Rijke-type tube combustor. Master's thesis, Virginia Polytechnic Institute & State University, 2001.

[41] M. Ogawa, H. Yamamoto, T. Itch, and T. Katayama. Tracking controller design for a nonlinear CSTR using exact linearization. In *Proceedings of the International Conference on Industrial Electrical Control and Instrumentation*, number 3, pages 2229–2234, 1991.

[42] Olsen and Vlachos. A complete P-T diagram for air oxidation of H_2 in a cstr. *Jounral of Physics: Chemistry A.*, 103:7990–7999, 1999.

[43] R. Olsen and I. Epstein. Bifurcation analysis of chemical reaction mechanisms i. steady state bifurcation structure. *Journal of Chemical Physics*, 94:3083–95, 1991.

[44] R. Olsen and I. Epstein. Bifurcation analysis of chemical reaction mechanisms ii. Hopf bifurcation analysis. *Journal of Chemical Physics*, 98:2805–22, 1993.

[45] Park and Vlachos. Kinetically driven instabilities and selectivities in methane oxidation. *AICHE Journal*, 43:2083–2095, 1997.

[46] S. Park, A. Annasway, and A. Ghoniem. Heat release dynamics modeling of kinetically controlled burning. *Combustion and Flame*, 128:217–231, 2002.

[47] N. Peters. Flamelet concepts in turbulent combustion. *Proceedings of the Combustion Institute*, pages 1231–1250, 1986.

[48] T. Poinsot and D. Veynante. *Theoretical and Numerical Combustion*. R.T. Edwards Inc., 2001.

[49] S. Pope. *Turbulent Flows*. Cambridge university press, Cambridge, UK, 2001.

[50] A. Putnam and W. Dennis. Survey of organ-pipe oscillations in combustion systems. *Acoustical Society of America*, 28(2), 1956.

[51] A. A. Putnam. *Combustion-Driven Oscillations in Industry*. American Elsevier Pub. Co., New York, 1971.

[52] J. Ranalli, C. Martin, P. Black, U. Vandsburger, and R. West. Measurement of flame transfer functions in swirl-stabilized, lean-premixed combustion. *AIAA Journal of Propulsion and Power*, 25:1350–1354, 2009.

[53] J. Ranalli, C. Martin, and U. Vandsburger. Measurements of ensemble averaged flame dynamics using spatially resolved analysis. Publication Pending, 2009.

[54] J. Ranalli, C. Martin, and U. Vandsburger. Prediction of thermo-acoustic instabilities by application of linear Bode analysis. Publication Pending, 2009.

[55] J. Rayleigh. *The Theory of Sound*. Dover Publications, New York, second edition, 1945.

[56] R. Rook, L. P. H. D. Goey, L. M. T. Somers, K. R. A. M. Schreel, and R. Parchen. Response of burner stabilized flat flames to acoustic perturbations. *Combustion Theory and Modelling*, 6:223–242, 2002.

[57] T. Sattelmayer and W. Polifke. Assessment of methods for the computation of the linear stability of combustors. *Combustion Science and Technology*, 175:453–476, 2003.

[58] T. Sattelmayer and W. Polifke. A novel method for the computation of the linear stability of combustors. *Combustion Science and Technology*, 175:477–497, 2003.

[59] S. Strogatz. *Nonlinear Dynamics And Chaos*. Westview Press, 1994.

[60] O. Teerling, A. Mcintosh, and J. Brindley. Pressure wave excitation of natural flame frequencies. *Combustion Theory and Modeling*, 11(1):147–164, 2007.

[61] O. Teerling, A. McIntosh, and J. Brindley. pressure wave excitation of natural flame frequencies. *Combustion Theory and Modelling*, 11(1):147–164, 2007.

[62] S. R. Turns. *An Introduction to Combustion*. McGraw Hill, New York, second edition, 2000.

[63] J. Tyndal. *Sound*. D. Appleton & Co., New York, 1897.

[64] C. Westbrook and F. Dryer. Simplified reaction mechanisms for the oxidation of hydrocarbon fuels in flames. *Combustion Science and Technology*, 27:31–43, 1981.

Appendix A

Thermal eccentricities for common fuels

Table A.1: Eccentricities for various fuels under stoichiometric, adiabatic combustion, with $T_{inlet} = 300K$

Fuel	Symb.	$\hat{c}$	β
Hydrogen	H_2	0.012	0.950
Methane	CH_4	0.016	0.873
Ethane	C_2H_6	0.010	0.873
Propane	C_3H_8	0.011	0.874

Though the values of $\hat{c}$ and β depend on the precise temperature and composition, a reasonable idea of the orders of magnitude involved may be drawn from their values under complete stoichiometric combustion at the adiabatic flame temperature. Thus, using the JANAF tables, wherein $C_p = C_p(T, \mathbf{Y})$, we may compute stoichiometric values for $\hat{c}$ and β when $\mathbf{Y}_{inlet}$ is a stoichiometric air-fuel mixture and the product mixture is given by

$$\mathbf{Y} = \mathbf{Y}_{inlet} + \mathbf{V} Y_{f,inlet} / V_f. \tag{A.1}$$

Finally, the stoichiometric, adiabatic values for $\hat{c}$ and β are given by

$$\hat{c} = \frac{C_p(T_{ad}, \mathbf{Y}_{inlet}) - C_p(T_{ad}, \mathbf{Y})}{C_p(T_{ad}, \mathbf{Y}_{inlet})} \qquad \beta = \frac{h(T_{ad}, \mathbf{Y}_{inlet}) - h(T_{ad}, \mathbf{Y})}{C_p(T_{ad}, \mathbf{Y})(T_{ad} - T_{inlet})}.$$

Table A.1 shows $\hat{c}$ and β for various common gaseous fuels with an inlet temperature of 300K. The remarkable similarity between fuels is destroyed if we consider non-complete combustion or vary the inlet temperature. Methane can even be made to exhibit a negative $\hat{c}$.

In general, however, β remains relatively close to 1 and $\hat{c}$ remains quite close to 0. This is due to the fact that the reacting species only constitute a small fraction (even at stoichiometric conditions) of the fluid. As the incoming mixture becomes further and further from stoichiometric (rich or lean), the reacting species will constitute an even smaller fraction of the mixture and the eccentricities will be on an even smaller order of magnitude. The

stoichiometric case is, in fact, the most eccentric case.

Appendix B

Eigenvalues for the Reynolds Averaged Flame

Section 4.2.3 shows that the eigenvalue problem for the Reynolds averaged flame is to find λ such that

$$\det(\mathbf{M}(\lambda)) = 0, \tag{B.1}$$

when

$$\mathbf{M} = \begin{Bmatrix} 1 & 1 & 0 & 0 \\ -e^{k^+ L_f} & -e^{k^- L_f} & e^{-k^+ \mathcal{L}} & e^{-k^- \mathcal{L}} \\ -k^+ e^{k^+ L_f} & -k^- e^{k^- L_f} & (k^+ - J)e^{-k^+ \mathcal{L}} & (k^- - J)e^{-k^- \mathcal{L}} \\ 0 & 0 & 1 & 1 \end{Bmatrix}, \tag{B.2}$$

and

$$k^{\pm} = \frac{\hat{U}}{2}\left(1 \pm \sqrt{1 - \frac{4\lambda}{\hat{U}^2}}\right) \qquad\qquad J = \frac{\hat{U}}{1 - \exp\left(-\hat{U}\mathcal{L}\right)}$$

However, this problem can be reduced by using a series of row manipulations to reduce the size of $\mathbf{M}$ until it is more manageable. To that end, it will become convenient to define two parameters,

$$\alpha = \frac{\hat{U}}{2} \tag{B.3}$$

$$\beta = \sqrt{\frac{\hat{U}^2}{4} - \lambda} \tag{B.4}$$

such that the wave number can be written as

$$k^{\pm} = \alpha \pm \beta. \tag{B.5}$$

Using Gaussian elimination, it is possible to modify $\mathbf{M}$ without affecting its zero determinant. The following series of row manipulations provides a more manageable form of $\mathbf{M}$:

1. (Row1) $\times\, e^{k^- L_f} + $ (Row2) $\rightarrow$ (Row2) Eliminates element (2,2)
2. (Row1) $\times\, k^- e^{k^- L_f} + $ (Row3) $\rightarrow$ (Row3) Eliminates element (3,2)
3. (Row4) $\times\, -e^{-k^- \mathcal{L}} + $ (Row2) $\rightarrow$ (Row2) Eliminates element (2,4)
4. (Row4) $\times\, -(k^- - J)e^{-k^- \mathcal{L}} + $ (Row3) $\rightarrow$ (Row3) Eliminates element (3,4)

The result is that

$$\left\{ \begin{array}{cccc} 1 & 1 & 0 & 0 \\ -e^{k^+ L_f} + e^{k^- L_f} & 0 & e^{-k^+ \mathcal{L}} - e^{-k^- \mathcal{L}} & 0 \\ -k^+ e^{k^+ L_f} + k^- e^{k^- L_f} & 0 & (k^+ - J)e^{-k^+ \mathcal{L}} - (k^- - J)e^{-k^- \mathcal{L}} & 0 \\ 0 & 0 & 1 & 1 \end{array} \right\} \tag{B.6}$$

Simply by rearranging the columns and rows, the matrix becomes

$$\left\{ \begin{array}{cccc} -e^{k^+ L_f} + e^{k^- L_f} & e^{-k^+ \mathcal{L}} - e^{-k^- \mathcal{L}} & 0 & 0 \\ -k^+ e^{k^+ L_f} + k^- e^{k^- L_f} & (k^+ - J)e^{-k^+ \mathcal{L}} - (k^- - J)e^{-k^- \mathcal{L}} & 0 & 0 \\ 1 & 0 & 1 & 0 \\ 0 & 1 & 0 & 1 \end{array} \right\}, \tag{B.7}$$

and it is readily apparent that the matrix can be segmented such that the problem reduces to $\det(\tilde{\mathbf{M}}) = 0$, when

$$\tilde{\mathbf{M}} = \left\{ \begin{array}{cc} -e^{k^+ L_f} + e^{k^- L_f} & e^{-k^+ \mathcal{L}} - e^{-k^- \mathcal{L}} \\ -k^+ e^{k^+ L_f} + k^- e^{k^- L_f} & (k^+ - J)e^{-k^+ \mathcal{L}} - (k^- - J)e^{-k^- \mathcal{L}} \end{array} \right\}. \tag{B.8}$$

At this point, it is convenient to apply Equations B.3 and B.4. Note that because

$$e^{k^{\pm}} = e^{\alpha}\, e^{\pm\beta}, \tag{B.9}$$

the term, $\exp(\alpha)$ can be factored out as a scalar and effectively removed from the problem. Consider the following simplification for the resulting element (2,2) of $\tilde{\mathbf{M}}$,

$$(\alpha+\beta-J)\, e^{-\beta\mathcal{L}} - (\alpha-\beta-J)\, e^{\beta\mathcal{L}} = -2(\alpha-J)\sinh(\beta\mathcal{L}) + 2\beta\cosh(\beta\mathcal{L}). \tag{B.10}$$

The same can be done to each of the three remaining elements, resulting in

$$\tilde{\mathbf{M}} = 2e^{\alpha}\begin{Bmatrix} -\sinh(\beta L_f) & -\sinh(\beta\mathcal{L}) \\ -\alpha\sinh(\beta L_f) - \beta\cosh(\beta L_f) & -(\alpha-J)\sinh(\beta\mathcal{L}) + \beta\cosh(\beta\mathcal{L}) \end{Bmatrix}. \tag{B.11}$$

Therefore, the determinate condition is that

$$0 = (\alpha-J)\sinh(\beta\mathcal{L})\sinh(\beta L_f) - \beta\cosh(\beta\mathcal{L})\sinh(\beta L_f) \tag{B.12}$$

$$- \alpha\sinh(\beta\mathcal{L})\sinh(\beta L_f) - \beta\sinh(\beta\mathcal{L})\cosh(\beta L_f). \tag{B.13}$$

The remaining terms with α cancel and because both terms containing cosh can be combined using an angle addition identity,

$$0 = J\sinh(\beta\mathcal{L})\sinh(\beta L_f) + \beta\sinh(\beta L_e). \tag{B.14}$$